Carbon Based Nano-Composite Interfaces for Electro-Catalysis

Ahn, Sun Yhik

Award date:
2016

Awarding institution:
University of Bath

Carbon Based Nano-Composite Interfaces for Electro-Catalysis

Sunyhik Ahn

A thesis submitted for the degree of Doctor of Philosophy

University of Bath

Department of Chemistry

March 2016

Sunyhik Ahn

Thesis Abstract

Electrochemical processes suffer from a number of challenges that needs to be overcome for widespread industrial adaptation. The need for an excess amount of inert supporting electrolyte in conventional three electrode set-ups with a single electrolyte medium makes synthetic applications uneconomical in both resource and sustainability aspects, and adds further complexities when the resulting product needs to be purified from the mixture which may also include the electro-catalyst. From an electro-analytical stand-point, altering the sample with the addition of high concentrations of electrolyte salt can have unpredictable chemical effects which may be difficult to account for in the analysis. The following results of the thesis addresses these issues by i) utilising triple-phase boundary systems where the electro-active species are kept in a separate phase from the source of electrons and ions, ii) introducing methods of heterogenising the electro-catalyst from the reaction mixture by immobilising in immiscible oils or polymers of intrinsic microporosity, and iii) offer practical application of such systems through the use of economical and technically unsophisticated methodologies.

In the introduction the concept of an Integrated Chemical System is introduced where components with different functions can be synergistically combined and arranged to achieve a more complex output. In the context of electrochemistry, modifying electrodes with materials to add or improve activity, stabilise performance and to substitute more expensive materials, is desirable for enhanced control over the activity of an electrode. The first chapter begins with a general overview of various electrode modification strategies pioneered throughout the last few decades as an introductory narrative for the approach taken in the thesis. Integrated Chemical Systems synthesized and investigated in the thesis are as follows. In chapter 3, electrospun carbon nanofiber based triple-phase boundary systems are utilised for ion-transfer voltammetry across the liquid-liquid interface. Chapter 4 introduces a more conveniently prepared carbon microsphere-polystyrene composite, where the carbon is mechanically held together into a porous structure by an electrically insulating polymer binder. The porous carbon structure is demonstrated to be an effective host for organic oil analysis, under a triple-phase boundary set-up. Chapter 5 is also a study of a carbon-polymer of intrinsic microporosity composite, the polymer functions as a binder as well as a porous host for electro-catalytic guest molecules. Chapters 6 and 7 presents a novel hydrodynamic technique and its use in modulating mass transport in solution, which can be used as a diagnostic tool to study electrode processes at both modified and unmodified electrodes. Chapter 7 demonstrates the method's utility through a mechanistic analysis of the organic free radical catalyst utilised in chapter 5.

It is the hoped that the series of studies presented in the thesis addresses the issues with electrochemical processes at least in part through utilising economic materials and simple methodologies. Whilst the final outcome and devices presented are not fully optimised, they demonstrate a proof-of-principle of the main advantages of employing the modified electrodes. In future, better materials are needed to address the weaknesses of the composites investigated in the thesis to extract the full benefits offered by the electrochemical approach of chemical synthesis and analysis.

Acknowledgements

I am grateful towards Professor Frank Marken who inspired me to get involved in academic research. Frank's passion and generosity is well-known by everyone who has worked with him. His intellectual leadership and tremendous support during my undergraduate and postgraduate studies made my experiences in Bath stimulating and enjoyable.

I had the pleasure of working with several talented collaborators throughout my PhD; notably Dr Antoine Buchard (University of Bath), Dr Steven Bull, Dr Boyang Mao (University of Bath), Viet Nguyen (University of Cambridge), Prof. Alan Bond (Monash University), Prof. Niel Mckeown (University of Edinburgh) and Dr John Mitchels. I am grateful towards Dr Martin Niedziolka (Polish Academy of Sciences), Dr Adrian Fisher (University of Cambridge) and Dr Jungsik Kim (Loughborough University) for giving me an opportunity to visit their research laboratories.

I would also like to thank members of the Marken group both past and present; Dr John Watkins, Dr Jonathan Halls, Dr Sara Dale, Dr Chris Hotchen, Dr Elena Madrid, Dr Andrew Gross, Dr Daping He, James Webber, and Yuanyang Rong for making the lab an enjoyable and stimulating place to work. I am particularly grateful to John for guiding me through an inspiring summer project while I was an undergraduate student, which significantly influenced my career decisions. John's advice and guidance on research and career development continued years after he left the group. I am indebted to two excellent visiting researchers; Dawid Kaluza's (Polish Academy of Sciences) persistence and positivity in tackling collaborative research challenges was hugely encouraging, and Adam Kolodziej's (University of Birmingham) contagious enthusiasm for membrane electrochemistry made long days in the lab more enjoyable. I am also grateful to Dr Karthik Somasundaram (National University of Singapore) for his patience and diligence in simulating the 'rocking' disc electrode set-up.

I am grateful towards my parents Taeyoon Ahn and Myongsin Kim for their unwavering support throughout my studies and research, they are my greatest mentors and supporters. Finally, I acknowledge the University of Bath and Inochem Ltd for support for a studentship.

Contents

Chapter 1. Introduction to Modified Electrodes

Abstract

This introduction is a broad overview of approaches made in modifying solid macro-electrodes. Examples of electro-catalytic applications where modification of the electrode offers enhanced functionalities and performance stability are given. A key aspect of the introduction lay in linking the role of the modifying substance on the overall functionality of the electrode. A combination of simple modifiers can result in electro-chemical systems with complex functions which fits under a broad concept known as Integrated Chemical Systems. Examples of Integrated Chemical Systems are organised into two main sections. Section 1.1 deals with electrodes architectures with solid phase modifiers; which includes discussions on nanoparticle electro-catalysts, polymer films, carbon paste and more complex architectures involving porous 'host' materials. Section 1.2 deals with electrodes modified with immiscible liquid phase substances, with examples of applications in electro-catalysis across liquid-liquid interfaces, and electro-analysis at the triple-phase boundary. The mechanism of interfacial charge transport in both the solid and liquid phases is also discussed. It is hoped that this general overview will provide the appropriate narrative which underpins the logic behind the design and investigation of Integrated Chemical Systems presented in this thesis.

Contents

1.1 Modification of Carbon Electrodes with Solid Electro-catalytic Particles and Films

Until the mid-1970s most electrochemical measurements utilized unmodified carbon, silver, mercury or platinum electrodes. The aim of intentionally modifying the surface of the electrodes came from the desire to impart enhanced functionalities and improved performance and stability onto the electrode. One of the earliest examples was conducted by Lane and Hubbard in 1973 that utilized a platinum electrode with quinone functionalized olefins chemisorbed to it [1]. The referenced study utilizes the olefins which irreversibly adsorb onto platinum as an anchor for a variety of other chelating substrates with electrochemical properties. Division of function into different structural components allows systematic development of complex functionalities, and can be compared with evolved biological organelle structures found in nature. For example, the chloroplast which is a biological macrostructure that evolved to convert sunlight into chemical energy, is made of a combination of individual components with a specific function. Components in the chloroplast organelle includes Photosystem I and II which absorbs electromagnetic radiation of certain wavelengths, molecules that transports electrons/holes, enzymes that oxidize water molecules, proton pumps that develop a potential gradient across the membrane and molecules that store chemical energy. Each component is arranged in a particular way inside the thylakoid membrane medium such that they interact together to deliver a complex function. Such a system is sometimes referred to as an 'Integrated Chemical System' (ICS), which is defined as a 'heterogeneous, multiphase system involving several different components designed and arranged for specific functions or to carry out specific reactions or processes. Often the different components will be organized structurally and will show synergistic effects. Usually it is the interaction of the components of the ICS that determines its properties' [2]. Synergistic effects between two or more components are difficult to predict, but having a systematic approach to imparting complex functionalities is desirable for practical purposes. Modifying electrodes allow the user to i) introduce additional electrochemical reactivity not accessible to the bare substrate electrode, ii) enhance electrochemical reaction rates (electro-catalysis), iii) allow greater selectivity in electrochemical reactions and iv) can also offer the electrode a layer of chemical/physical protection.

Carbon as a material is an excellent conductor with superb compatibility with organic substrates, and has found wide utility in electrochemistry due to its non-metallic identity, mechanical stability and wide availability. Vitreous carbon (or glassy carbon) and highly ordered pyrolytic graphite electrodes are one of the most common macro-electrodes utilized in electrochemistry. There has been an explosion in research in carbon with hierarchical structures at the micro and nanoscale, with the

development of carbon nanofibers in 1976 [3], carbon fullerene in 1985 [4], carbon nanotubes in 1991 [5], and the recent carbon nanosheets or graphene [6]. The nano-scale structures gives the material a high surface area which is desirable as the activity of the material is greater due to increased mass transport to the materials surface. Along with enhanced mechanical properties, the nano-structures also affect the material's electronic properties; significant improvements in rates of charge transport, electron transfer and surface properties has been extensively reported especially for graphene and carbon nanotubes. There has been an explosion in literature reports on the application of nano-carbon materials in electrode processes, either as a support material for enhanced charge transfer or mechanical stability and as the catalyst itself. This combined with the relative cheapness and wide availability of carbon, makes it an attractive choice as an electrode material.

This introductory chapter aims to deliver a broad overview on different strategies of modifying electrodes to impart complex functionalities, with a particular emphasis on the modification of carbon. The chapter has been divided into two main sections; the first dealing with modification through deposition/addition of a solid phase material on the electrode surface, and the second dealing with the deposition of liquid phase modifiers. Detailed reviews on modification methodologies are not elaborated in much detail as the main results of the thesis utilises only the simplest methods with the exception of carbon nanofiber synthesis (which is described in more detail in chapter 3). Pioneering examples of work on modified electrodes will be briefly reviewed, with an emphasis on linking its enhanced function to the modified structures and the synergy that results. The theoretical aspect necessary to appreciate the enhanced functionalities are touched upon briefly here, and will be expanded in more detail in chapter 2 (Introduction to the Fundamentals of Electrochemistry) and the relevant results chapters. It is hoped that this general overview will provide the appropriate narrative which underpins the logic behind the design and investigation of Integrated Chemical Systems presented in this thesis. The application of Intergrated Chemical Systems presented in this thesis focuses on systems that allow heterogenisation of chemical components required for electrochemical processes such as the electrolyte, and redox mediator and electro-analyte into separate phases. Separating chemical components often results in greater technical complexity in application and analysis but can be desirable in industrial processes where products of electrolysis needs to be purified before use or further processing. The usefulness for this approach will be elaborated in section 1.4 which outlines the scope of the thesis.

1.1.1 Modification with Solid Particles

Modifying a solid electrode surface with solid nanoparticles of a different chemical identity can impart additional chemical functionality to the electrode such as electro-catalytic activity. Modifying electrodes with nanoparticles to act as electro-catalysts has the following advantages: i) nanoparticles have a high surface area to volume ratio, hence ii) nanoparticles experience a greater rate of mass transport than bulk materials, iii) the surface properties of the nanoparticles are different to their bulk form and in some cases exhibit enhanced catalytic activity, iv) gives specific control over the electrode environment, and v) can be a more economic method of utilizing catalyst materials. There are too many reports on nanoparticle electrochemistry for a truly holistic review on the area, the following sections will only highlight examples that are well established and relevant to the main topic of the thesis.

Metallic nanoparticles deposited on solid substrates

The most commonly utilized metal nanoparticle electro-catalysts are transition metals such as gold, silver, platinum, copper, and palladium. Carbon is the preferred electrode substrate for the deposition of metal nanoparticles due to its wide potential window, range of hardness commercially available, relative cheapness, and its non-metallic identity. Metals are excellent conductors of electricity, and are often described as a rigid network of metallic nuclei bathed in a sea of electrons. When the oxidation number of the metallic nuclei is altered (by oxidation or reduction) the transport of charge into the material must be compensated for by either the transport of an opposite charge into the material or by the expulsion of an equivalent charge out of the material to maintain electro-neutrality. Hence the issue of charge transport in and out of the material becomes important when considering electron transfer processes. The ease of oxidation and reduction can be limited by the nature of the charge compensating species present in the electrolyte solution surrounding the electrode. An outline of the four different charge balancing mechanisms are given in Figure 1.1 below.

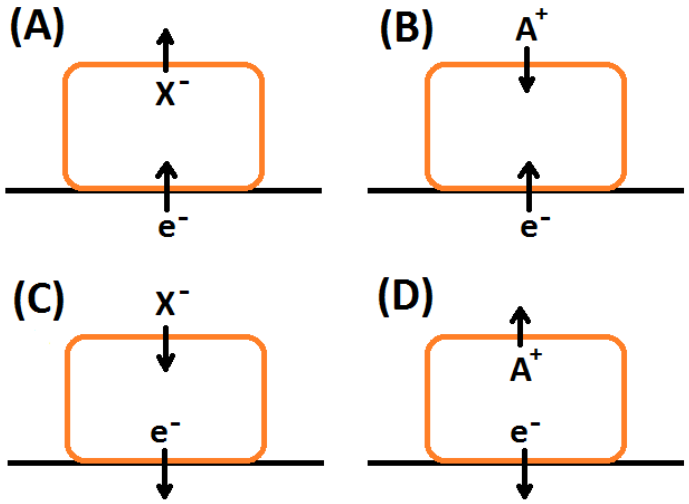

Figure 1.1. Diagram showing a microparticle (orange) deposited on an electrode surface (black) submerged in an electrolyte solution, with electron transfer coupled to ion transfer. A) Reduction coupled to the expulsion of an anion (X^-) from the microparticle into the electrolyte. B) Reduction coupled to cation (A^+) insertion into the microparticle. C) Oxidation coupled to insertion of an anion (X^-) into the microparticle. D) Oxidation coupled to expulsion of a cation (A^+) from the microparticle.

A broad overview of the electrochemical applications of metal nanoparticle modified electrodes are summarized in table 1.1. Many examples listed utilize nano-carbon materials such as nanotubes and graphene oxide as the support material. Compared to immobilizing nanoparticles on a bulk carbon material such as glassy carbon, use of modified nano-carbon substrates has often been shown to improve sensitivity in detecting electro-analytes. This is partially attributed to the nanostructures improving the surface area of the electro-catalyst by resisting Ostwald ripening effects, which is limited by the physical separation of metal nanoparticles across independent carbon structures (in contrast to nanoparticles neighbouring each other on a flat planar surface). Hence the distribution of nanoparticles are key to its performance. A related factor is the size of the nanoparticles; along with the effects of surface area (per given mass), the diameter of nanoparticles affects its surface electron energy, such that its electrochemistry and reactivity can be tuned by varying its size [7]. Tuning the size of the nanoparticles with precision can be technically challenging, but can be done to optimize electro-catalytic activity on a given substrate.

An electro-catalyst is a substance that lowers the activation energy required for an electrochemical process, without being consumed or altered. The mechanism of electro-catalytic mediation is a complex matter that is covered in section 2.4. A good example of integrating electro-catalytic particles

onto carbon structures for enhanced activity is platinum nanoparticles immobilized on carbon black. Platinum has demonstrated high catalytic activity for key chemical processes such as oxygen reduction, methanol oxidation, and 'cracking' hydrocarbons. Carbon black is an industrial porous carbon powder material which provides a high surface area to immobilize nanoparticles on. Chemical processing methods can be adjusted to tune the diameter of platinum nanoparticles on the carbon black supports and this has been found to have significant impact on its activity [8]. Optimization of nanoparticle sizes and its chemical interaction with the carbon black has been proven to dramatically increase the activity of the catalyst, to partially off-set the high cost of platinum. Mounting platinum nanoparticles onto carbon nanotubes has also been reported to further enhance electro-catalytic activity [9]. Carbon nanotubes offer more precise control over the platinum nanoparticles sizes as the nanotube host diameters are more uniformly distributed than the pores on carbon black. This translates to significant gains in activity per mass of platinum as shown below in Figure 1.2 for oxygen reduction. Despite this use of carbon black as a support material still remains attractive due to the ease at which it can be synthesized, and its relatively low price.

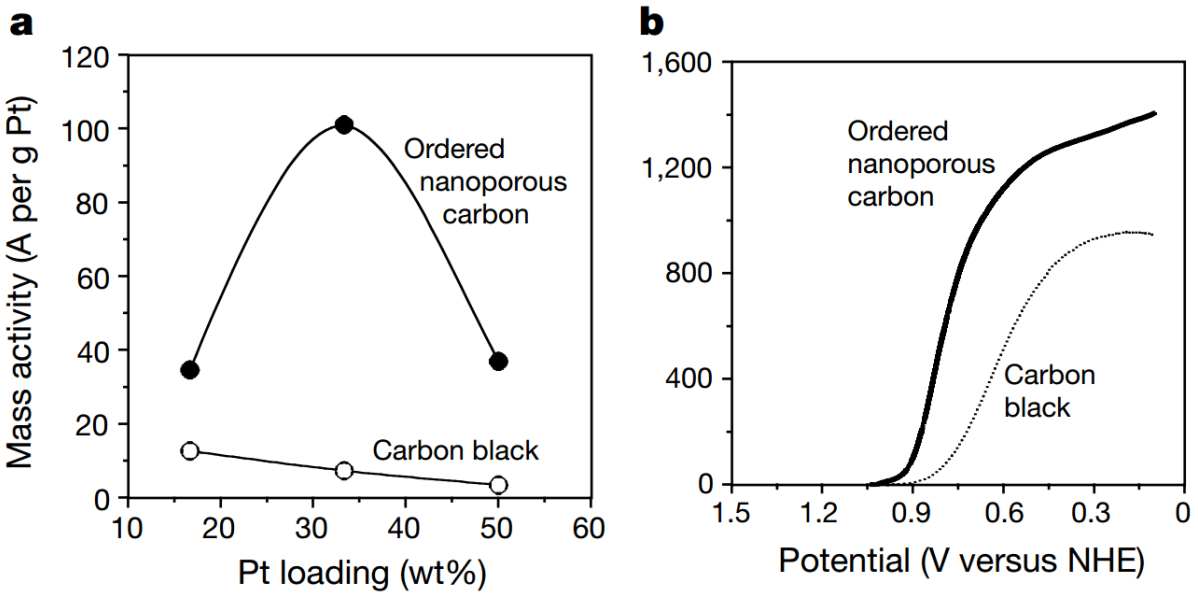

Figure 1.2. Electro-catalytic activities of Platinum/carbon catalysts for O_2 reduction. A) Activity of catalyst measured in oxygen saturated 0.1M $HClO_4$ at a rotating disc electrode rotating at 10000rpm held at a potential of +0.9 V vs. NHE. B) Linear sweep voltammetry recorded at 50 mVs^{-1} on a rotating disc electrode rotating at 10000rpm of 33 wt% Pt on carbon supports. Reprinted by permission from Macmillan Publishers Ltd: Nature [9], copyright (2001).

The distribution of nanoparticles is also important; to fully benefit from increased mass transport from its nano-scaled structures, each nanoparticle must be separated by enough distance such that its

diffusion layer thickness does not overlap with its neighbour [10]. There are sophisticated techniques designed to yield uniformly distributed nanoparticles with a low distribution of particles sizes [11],[12]. Most examples shown in the table below make do without such precision in synthesis, as performance gains compared to its bulk form can be significant even without full optimization at the nanoscale. Electronic effects arising of the interaction of the carbon nano-substrates with the metal nanoparticles can also enhance the rate of electro-catalysis. Such effects are broadly reported as 'synergistic effects', though the precise source of the enhancement is often unspecified.

Table 1.1. Examples of electrochemistry on electrodes modified with metal nanoparticles.

Metal nanoparticle	Substrate	Application
Gold	Glassy carbon	O_2 reduction/H_2O_2 generation [13]
	Glassy carbon	Methanol oxidation [14]
	Glassy carbon	Arsenic (III) detection [15]
	ITO	Mercury detection [16]
	Graphene Oxide	Ascorbic acid detection [17]
Silver	Glassy carbon	H_2O_2 detection [18]
	Glassy carbon	Chloride detection [19]
	Carbon nanotubes & carbon paste	Ascorbic acid and Dopamine [20]
	Graphene Oxide	E. Coli bacteria detection [21]
	Glassy carbon	Tryptophan [22]
Platinum	Graphene on glassy carbon	H_2O_2 detection [23]
	Graphene on glassy carbon	Dopamine, Uric acid and Ascorbic acid [24]
	Boron doped diamond	Oxygen detection [25]
	Electrospun indium oxide	H_2S detection [26]
	Nanoporous carbon	Oxygen reduction [9]
	Reduced graphene oxide	Methanol oxidation [27]
Copper	Boron doped diamond	Nitrate detection [28]
	Multi-walled carbon nanotubes	Glucose detection [29]
	Carbon paste electrodes	Amino acid detection [30]
Palladium	Single-walled carbon nanotubes	Glucose detection [31]

	Carbon nanofibers Graphene oxide	Hydrazine detection [32] Ethanol oxidation [33]

The impact of modifying catalysts on the electrochemistry of substrate electrodes can be dramatic as demonstrated with the case of hydrogen peroxide shown in Figure 1.3. Hydrogen peroxide exhibits slow electron transfer kinetics on electrode materials such as glassy carbon, to the extent that Faradaic activity is not observed within the potential window utilized by the study. It is only after modification with silver nanoparticles [18] or platinum [23] that electrochemical detection becomes feasible. Modification with silver nanoparticles dramatically improves the electron transfer kinetics of hydrogen peroxide reduction into water, such that much faster rates of conversion (observable as an increase in reductive current) are possible. The cited report states the benefits of utilizing silver over platinum as lower cost of material, excellent material stability and being less prone to poisoning effects. Due to many transition metals relative scarcity and high cost, there are many studies aimed at finding alternative materials to replace it or to further optimize the material's performance by incorporating other materials with it and forming Integrated Chemical Systems.

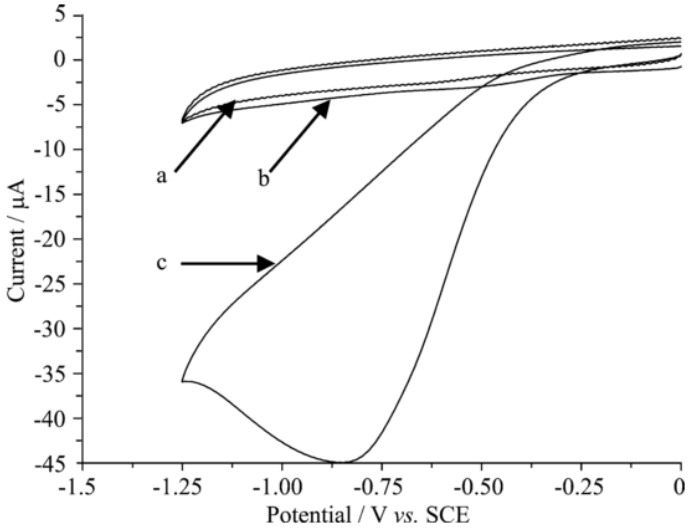

Figure 1.3. The voltammetric response of (a) a bare glassy carbon electrode to 1 mmol L^{-1} hydrogen peroxide, (b) a modified glassy-carbon electrode to blank phosphate buffer and (c) a modified glassy carbon electrode to 1 mmol L^{-1} hydrogen peroxide. All experiments were carried out in phosphate buffer (0.05 mol L^{-1}, pH 7.4) and run at a scan rate of 50 mVs^{-1}. The glassy-carbon surface was modified by deposition of silver for 1 min at +0.5 V vs. Ag from a 5 mmol L^{-1} AgNO3/ 0.1 mol L^{-1} TBAP/MeCN solution, after which the silver was stripped for 5 min at +0.5 V vs. Ag in the same solution. Reprinted from [18] with permission of Springer. Copyright (2005), Science+Business Media New York.

Organic micro-crystals deposited on solid substrates

Electrochemistry of non-metallic solids can be investigated by depositing directly onto solid electrode surfaces, provided that it is insoluble in the electrolyte solution it is submerged in. Non-metallic particles tend not to have metallic properties of electric conduction; hence electron conduction inside the material can be relatively slow (though ionic conduction can be fast). Voltammetry of immobilized particles (VIM) is a simple technique where a small amount (sub-microgram quantities) can be immobilized on the electrode surface for voltammetric characterization. Graphite electrodes are a common electrode substrate on which voltammetry of immobilied particles are carried out on due to its softness and ease of refreshing its surface. This approach has been used for the detection of cocaine [34], pesticides [35], and cannabinoids [36]. As the redox active microcrystals are immobilized directly on the electrode surface, electron transfer can occur directly onto the microcrystals without it having to diffuse through the solvent medium. But unlike metals that conduct electrons readily, non-metallic compounds facilitate electron transfer via a charge hopping mechanism, where electrochemical charge generated by electron transfer is propagated by self-mediated redox between neighbouring species. Electron transfer is coupled to the transfer of ions to maintain electro-neutrality. This often results in the electrochemistry of microparticles being confined to surfaces where there is optimal access to ions. Self-mediating charge hopping processes can be modelled as diffusion [37], hence even when the microcrystals are immobilized directly on the electrode surface, slow electrochemical charge propagation can result in voltammograms that appear to be diffusion limited. The issue of charge transport in organic microparticles described here is common to non-metallic electrode modifiers such as polymer films which are described in section 1.1.2.

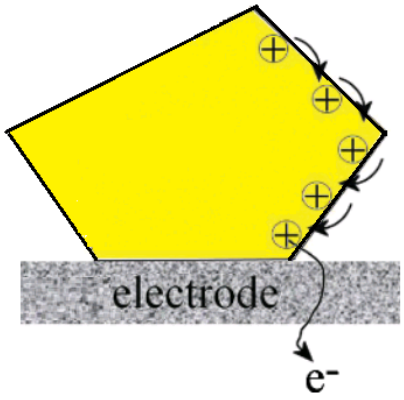

Figure 1.4. Illustration of a solid microcrystal immobilised on a solid electrode surface. Electrochemical charge propagates through a self-mediating hopping mechanism coupled to ion transfer from the surrounding electrolyte into the solid crystal.

Metal-Organic Frameworks

Voltammetry of immobilized particles can be conducted on electro-analytes present in porous solids such as Metal-Organic frameworks (MOFs) immobilized on the electrode. MOFs can be deposited on the electrode as both particles and films. MOFs are a class of material that comprises of a metal centre coordinated to multiple organic molecules that forms a bridge to a neighbouring metal centre, whilst forming a cavity in between (see Figure 1.5A below). MOFs are chemically stable structures with a surface area up to 7000 m^2g^{-1} reported [38]. MOFs can be electrochemically active itself if the metal centres and/or the bridging ligands are redox active. This offers a lot more possibilities to tune the chemical structure and properties of MOFs compared to other porous materials such as zeolites and clays. Electrochemically inactive MOFs can also be post-synthetically modified to host electrochemically active guest molecules in its pores [39]. Post-synthetic modification of MOFs is a convenient method of introducing a variety of electrochemical functionalities to a given MOF structure. MOFs have already been demonstrated to be effective at gas separations [40], gas storage [41], drug delivery vectors [42] and hosts for catalysts [43]. Combining electrochemical functionality with properties of MOFs such as high gas adsorption capacity, porosity (which offers size selectivity) and heterogeneous catalytic activity (of either or both the metal and the organic ligand) can lead to synergistic gains in functionality and performance.

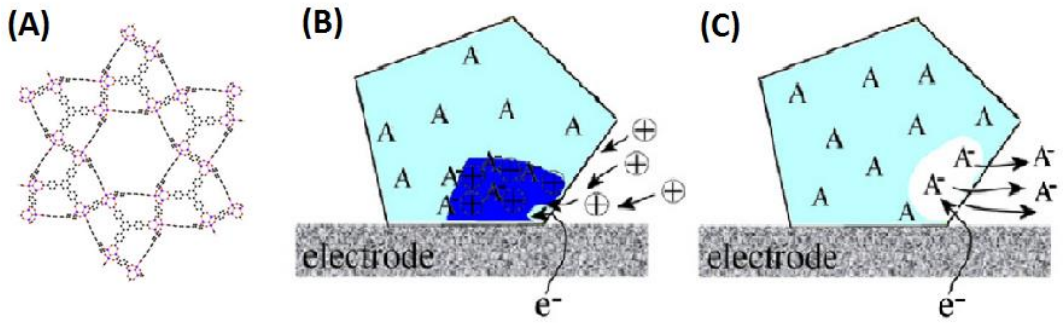

Figure 1.5. A) Structure of UMCM-1 MOF showing the crystalline structure of metal centres bound together with organic ligands. B) Illustration of electroactive species A imbedded into an inert porous MOF structure, electron transfer is coupled to ion transfer from the aqueous solution into the MOF. C) Similar to case B, but electron transfer results in the charged product being expelled out of the MOF structure to maintain electro-neutrality. Reprinted from [44], copyright (2013), with permission from Elsevier.

Electrochemical charge conduction in MOFs require transport of ions in and out of the pores. But the rate of ion transport in MOFs isn't always efficient as demonstrated in a recent report [44]. The cited

study utilized redox inactive UMCM-1 MOF [45] post-synthetically modified with redox active alizarin red S dye. Despite the large pore size and the high mobility of protons, the magnitude of currents observed was consistent with a process confined to the surface of the MOF implying poor ion transport in the MOF structure. Evidence for electrochemically induced dye expulsion with irreversible decay of currents observed in voltammetry suggest that the MOF structure may be structurally broken by build-up of electrostatic forces. Similar issues have been reported for MOF structures that are electrochemically active; commercially available Basolite F300 (Iron based) MOF immobilised on an graphite electrode also exhibited preference for electrochemically induced iron expulsion as opposed to proton migration into the MOF structure [46]. The labile nature of metal-organic bonds make the structure sensitive to its immediate chemical environment, and in the cases cited above prone to structural decay which makes it unsuitable for mediating electro-catalytic processes. But there are examples of electro-catalytic MOFs which exhibit high and sustained turnover rates with lasting structural stability such as in oxygen evolution reactions [47], hydrogen evolution reactions [48], [39] and carbon dioxide reduction [49]. It is clear that when considering a host for electro-catalysts, issues such as electrochemical charge conductivity needs to be considered together with structural stability and performance stability.

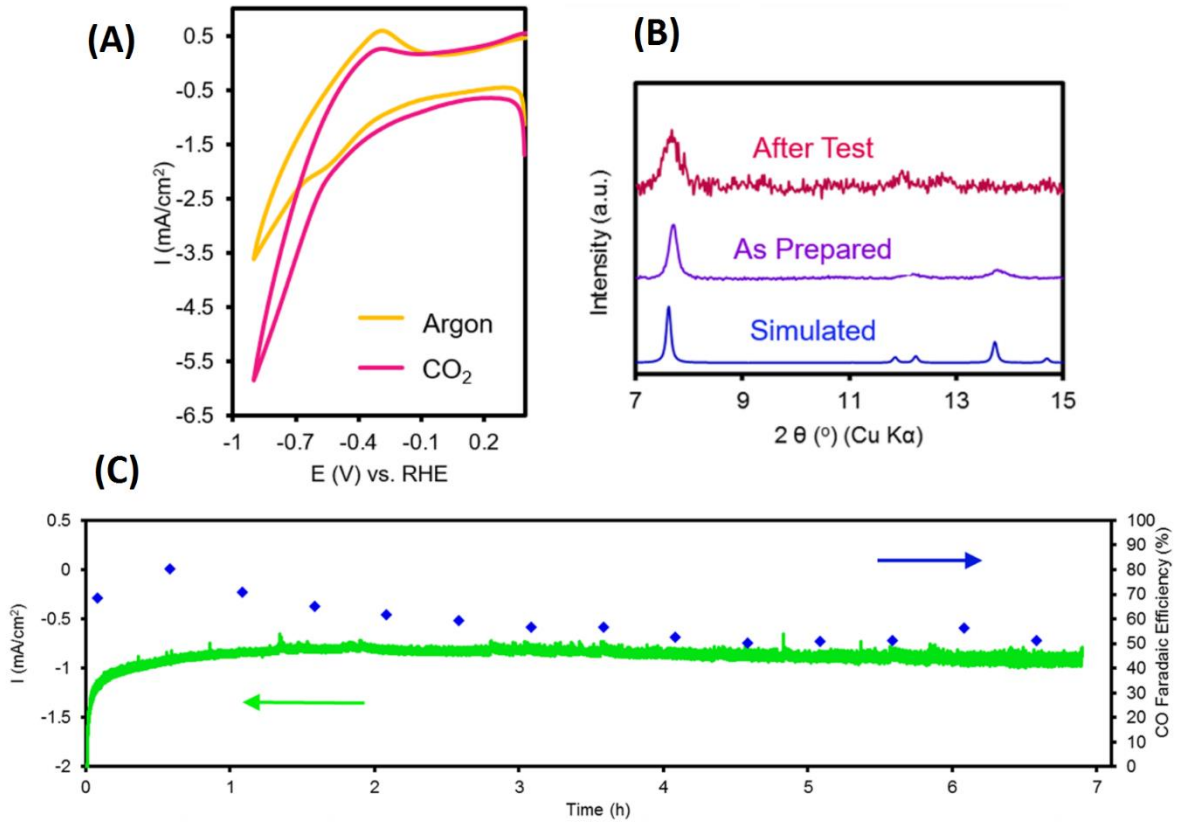

Figure 1.6. Activity of metal-organic framework (MOF) $Al_2(OH)_2$4,4',4'',4'''-(porphyrin-5,10,15,20-tetrayl)tetrabenzoate)-Cobalt in 0.5 M aqueous potassium carbonate solution. A) Cyclic voltammograms of carbon disc electrode modified with a thin film of MOF in an argon saturated electrolyte solution in comparison with a carbon dioxide rich solution. B) XRD analysis of the MOF structures before and after experiments with comparisons to simulations. C) Chronoamperometry held at -0.7 V vs. RHE indicating the stability of the MOF film, with the diamond shaped dots representing the Faradaic efficiency of carbon monoxide generation. Adapted with permission from [49]. Copyright (2015) American Chemical Society.

A recent example of electro-catalytic carbon dioxide reduction in MOF thin films deposited using Atomic Layer Deposition (ALD) technique is shown in Figure 1.6 [49]. The voltammograms in Figure 1.6A clearly shows the electro-catalytic reduction of carbon dioxide, which can be sustained for hours without noticeable decay in activity. The process was found to be diffusion limited, and the authors suggest that it is the migration of counter charged ions from the electrolyte into the film that is the limiting process. The advantage to utilising resource intensive techniques such as ALD is that the MOF layers can be synthesized with nano-scale precision. The cited report studied the activity of MOF films with thicknesses of 0.5nm to 70nm, and optimized it along with the catalyst loading for high rates of mass/charge transport in the film. Stability of the MOF structures allow more complex electrochemical analysis of the catalytic process mediated within in that allows a more in-depth understanding of the rate limiting process.

1.1.2 Modification with Solid Films

Polymer films

Redox polymers can be immobilized onto the electrode surface using a variety of methods such as drop-casting [50], spin coating [51], electrochemical precipitation [52] and adsorption from solution [53]. These methods are relatively simple and technically less demanding compared to depositing single monolayers. Depositing thicker layers of polymer has the advantage of improved stability of the polymer framework and a larger reagent loading capacity which can give larger electrochemical responses. There are cases where the electro-active component of the polymer film is covalently bonded to the polymer framework such as ferrocene polymers [48], and cases where the electro-active component is non-covalently attached to the framework. In the case the guest electro-active species is not bonded to the polymer, the polymer framework's stability does not necessarily offer

improved stability of the electro-active species' electrochemistry. The nature of bonding between the guest molecule and the polymer host can be through ionic interactions, physisorption, or mechanical immobilization.

Electro-active polymer films such as ferrocene polymers [54] and o-quinone [55] have a high density of redox active centres, and mediate rapid electrochemical charge conduction through a charge hopping mechanism. There are polymers such as polypyrrole [56] that exhibit metal-like conduction band structures that allow electron conduction more efficiently. Other polymers such as polyvinylpyridine [57] and nafion [58] are redox-inactive but conduct electrochemical charge through fast ion transport and exchange. Electrochemistry in redox-inactive polymer films that are insulating is only possible when there are redox active guests embedded in its structure, in which case electrochemical charge is propagated through a hopping mechanism. An example of electro-catalysis on a polymer film modified electrode is demonstrated by Kao and Kuwana [59], who embedded platinum nano-particles on a film of poly(vinylacetic acid) on a glassy carbon electrode. The platinum serves as electro-catalysts for hydrogen evolution and oxygen reduction, while the poly(vinylacetic acid) is an electrically insulating polymer film used as a host for the nano-particle catalyst. The electro-catalytic activity of the embedded platinum nano-particles is clearly observed as shown in Figure 1.7 below. The overpotential required for hydrogen evolution is decreased by 700 mV, and oxygen reduction decreased by 800 mV, compared to the activity on a bare glassy carbon electrode.

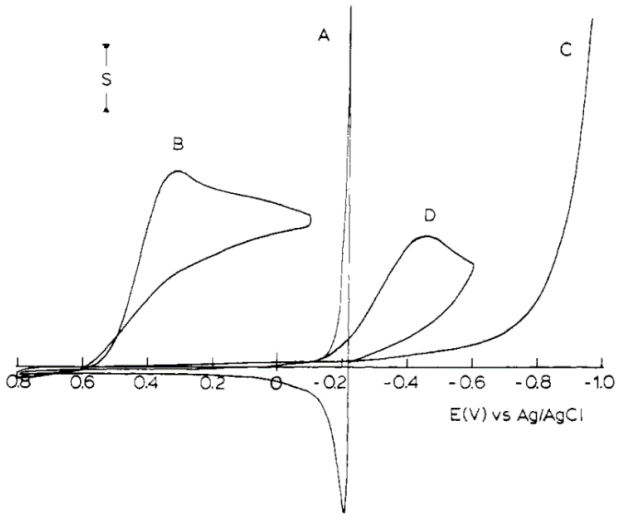

Figure 1.7. Cyclic voltammograms run at $10mVs^{-1}$ in 1 M aqueous sulphuric acid of (A) hydrogen evolution and (B) oxygen reduction at a platinum nano-particle embedded poly(vinylacetic acid) film on glassy carbon electrode. (C) is the hydrogen evolution and (D) is oxygen reduction at an unmodified glassy carbon electrode. Adapted with permission from [59]. Copyright (1984) American Chemical Society.

Modifying an electrode surface with a polymer film (both redox active and inactive) can have the following benefits; i) it can be used to immobilize a catalyst on the electrode [60], ii) in the case where nanoparticles are embedded, offers resistance against Ostwald ripening effects [61], iii) medium allows incorporation of multiple substances for synergistic effects with relative ease [62], [63], iv) the film can protect the electrode material [64], v) the film offers another layer of selectivity [65], vi) the film introduce surface roughness increasing the effective area [66] and vii) the film can act as a pre-concentration media. Though in the case an electro-catalyst is added to the polymer, there may be a loss of catalytic activity due to the addition of a physical barrier between the substrate and the catalyst.

The theoretical treatment of the mechanisms involved in electro-catalysis in films has been thoroughly investigated, such that it is possible to identify and optimize the rate limiting process through a series of diagnostics presented by Saveant [67], Murray [68],[69] and Albery [70],[71]. Quantitative analysis (of catalytic rate constants and electrochemical charge hopping rates) is possible if basic properties of the film such as thickness and density and the catalyst concentration are known. The Albery-Hillman approach to analysing electro-catalysis in modified electrodes is elaborated in more detail in Chapter 5. Typical rates of charge hopping in polymer films given as a diffusion coefficient are in the $10^{-12\sim13}$ cm^2s^{-1} range which is much slower than diffusion in liquid solutions [69].

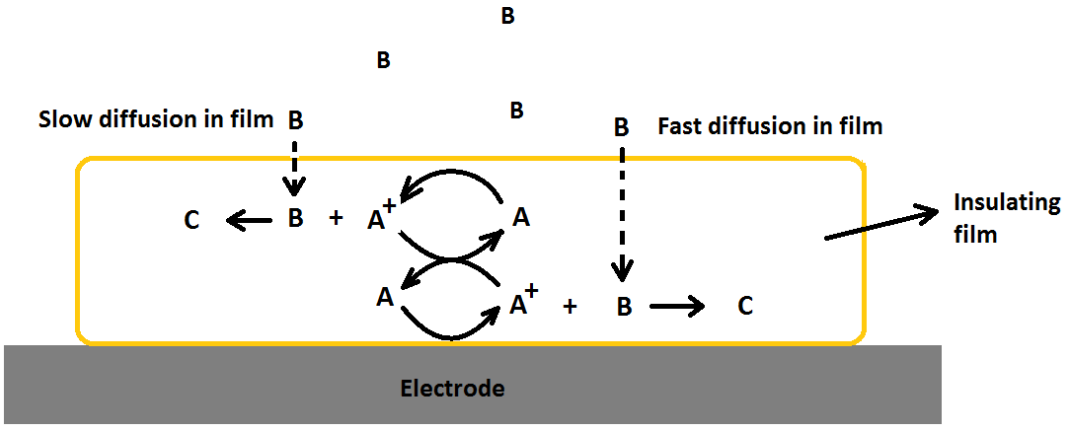

Figure 1.8. Electro-catalyst 'A' immobilised in an inert polymer film. Electrochemical charge propagates through a charge hopping mechanism coupled to ion transfer into the film (ions not shown). Site of electro-catalysis depends on the diffusion coefficient of substrate species 'B' in the polymer film.

Metal based films

Deposition of a metal film onto another metal based electrode material (or carbon) is useful when the deposited material is not mechanically durable enough to function as a stand-alone electrode and requires a mechanical support structure. Functionalizing the surface of a substrate with a thin layer of metal can also be economically desirable when the deposited metal is scarce or expensive. Some materials can be conveniently deposited through electrochemical methods. An example of this is Alumina (Al_2O_3) which is electro-deposited in aqueous phosphoric acid solution [72]. This simple method forms a film that contains parallel cylindrical nanopores with a distribution of diameters (see Figure 1.9). Average pore size and film thickness can be controlled to a degree by varying the electro-deposition potential and duration respectively. Alumina itself is electrically insulating, and has been used as templates for growth of nanostructured materials. The previously cited study found that depositing poly(4-vinyl pyridine) soaked in Ferrocyanide redox species along the walls of the nanopores would exhibit enhanced electrochemical charge propagation compared to the polymer film on its own. The role of alumina nano-pore structure in the composite material may be improving the access of charge balancing ions to the polymer film as well as providing a degree of directional guidance for propagation the electrochemical charge.

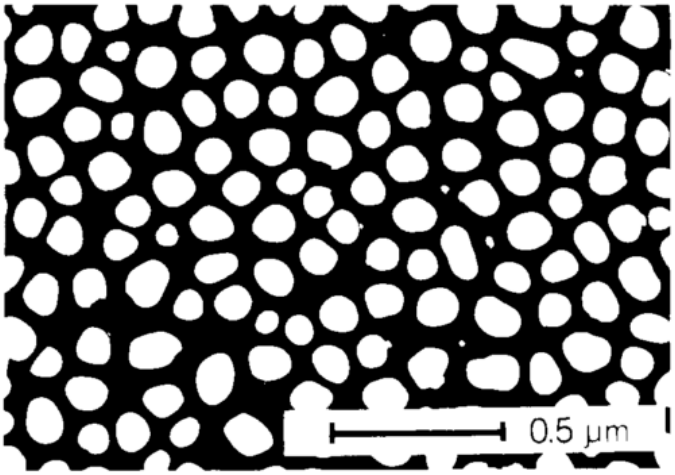

Figure 1.9. Transmission electron micrograph of a 5000 angstrom thick Aluminium Oxide layer which was electro-deposited in 4% H_3PO_4 solution with Aluminium substrate. Adapted with permission from [72]. Copyright (1985) American Chemical Society.

Another example of a well-known metal film-polymer composite is the deposition of porous platinum films on Nafion membrane [73]. This can be prepared by holding the solid Nafion membrane in

between a solution of K_2PtCl_6 and a solution of a reducing agent; the reducing agent diffuses through the Nafion and causes the platinum to reduce into solid deposits which eventually grows into a porous thin film. Having a layer of Nafion sandwiched in between two porous thin films of platinum forms a solid polymer electrolyte cell useful for water electrolysis. The role of Nafion in the composite structure is to mediate rapid ion conduction whereas platinum is a catalyst for both oxygen reduction and hydrogen oxidation. Similar approaches have been taken to form solid polymer electrolyte cells using copper [74] and silver [75] metals. The combination of the electro-catalytic activity of platinum and the fast ion-transport mediating Nafion membrane allows the device to function as an effective water electrolyser.

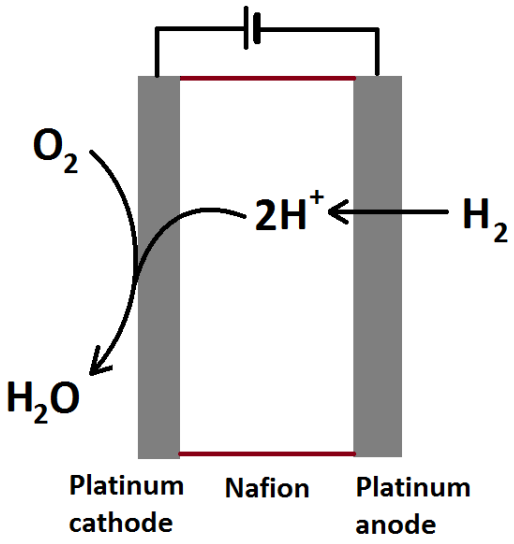

Figure 1.10. An illustration of Nafion membrane sandwiched by porous platinum films. The platinum films mediates electrochemical hydrogen oxidation and oxygen reduction, while the Nafion membrane allows rapid proton conduction. Individual elements form an integrated chemical system that is effective at water electrolysis.

Carbon paste electrode

Carbon paste electrodes first reported by Adams in the 1958 [76] are binary mixtures of carbon powder and a non-electrolytic organic liquid. The consistency of the paste material is dependent on its specific composition, but is usually kept relatively thick and viscous for ease of use. Most of the carbon paste electrodes have been made combining graphite powder with paraffin oils such as trademarked products Nujol or Uvasol [77], [78]. Nujol and Uvasol are non-polar pasting liquids that are chemically inert, insulating, non-volatile and water-immiscible. Use of another solvents such as silicone oils [79] and ionic liquids [80] have been reported. The graphite particles form an electrically connected network with a thin film of the binder covering its surface [81]. In this composite structure, the graphite powder delivers the conductivity required for electrochemical reactions, while the binder can be used to tune the mechanical stability and malleability of the material. The main advantages of the Carbon Paste electrode is that it is cheap, easily prepared, easily modified and easily refreshed. The Carbon Paste once homogenized is typically filled into glass or Teflon tubes with a metal wire establishing the electrical contact between the paste and the potentiostat.

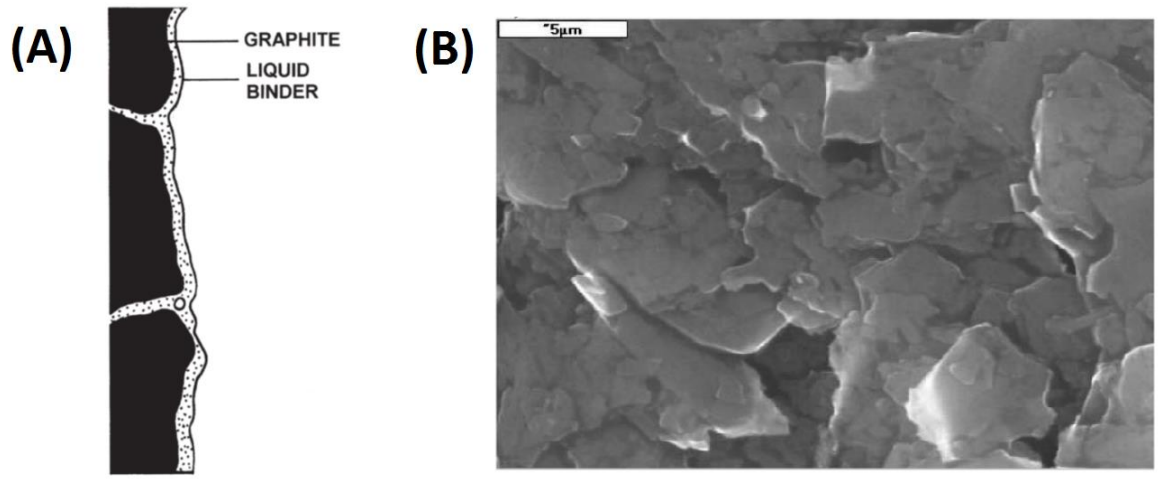

Figure 1.11. A) A schematic drawing of an unmodified carbon paste electrode [78], copyright (2001) reprinted with permission from Taylor & Francis group. B) SEM image of the surface of an unmodified carbon paste electrode [82]. Copyright (2008), reprinted with permission from John Wiley & Sons, Inc.

Use of bare Carbon Paste electrodes in detecting Gold [83], Silver [84], Iron [85], Iodide [86] and Azide ions [87] have been reported. The relative ease in which Carbon Paste electrodes can be modified for additional chemical and electro-chemical functionalities has resulted in many applications which are

reviewed and covered in breadth in [77] and [78]. To pick a few examples, Carbon paste electrodes modified with heptyl sulfonic acid utilized for detection of silver has been reported to have a detection limit of 3 x 10^{-12} M [88], which is a significant improvement over the detection limit of 2 x 10^{-7} M reported in [84] for an unmodified Carbon paste electrode (though the exact measuring technique differs). Carbon paste electrodes modified with biological molecules such as glucose oxidase can be used for detection of more complex molecules such as glucose [89]. Use of glucose oxidase enzyme (a biological catalyst) allows highly selective detection of glucose within the potential window accessible to the electrode material without degradation. The direct transfer of electrons from the biological enzyme to the electrode material is inefficient due to the insulating protein layer surrounding the active site [90], hence a bridging species (such as colloidal gold particles and rhodium particles) has been utilized to enhance electron transfer between the two sub-components. The role of the bridging species is clearly demonstrated in Figure 1.12 below, where a significant increase in electro-catalytic current is observed with its addition to the system. The additional steps required in the reported studies involve mixing in solutions of the metal particles during the preparation steps. Hence despite the complexity involved, use of such Integrated Chemical Systems for enhanced functionalities remain an attractive prospect as the level of technical difficulty in electrode preparation remains low.

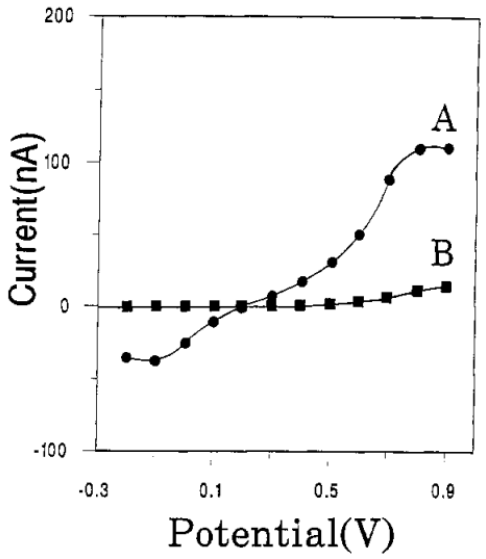

Figure 1.12. Hydrodynamic voltammograms at a rotating disc electrode at 300rpm in 0.05 M phosphate buffer with 2 mM glucose for A) rhodium dispersed carbon paste/glucose oxidase electrode and B) carbon paste/glucose oxidase electrode. Reprinted with permission from [89]. Copyright (1994) American Chemical Society.

1.2 Modification of electrodes with liquids

1.2.1 Modification with Immiscible Liquid Films

The first reported electrochemical system where an immiscible liquid film was deposited on a solid electrode was by Shi and Anson [91], [92]. A thin layer of nitrobenzene was deposited onto a graphite electrode, which was submerged in an aqueous solution of perchloric acid (see Figure 1.13). The nitrobenzene would act as a barrier between the electrode and electro-active species insoluble in nitrobenzene. However when a hydrophobic electro-active species such as ferrocenium is dissolved in the nitrobenzene, clear voltammetric peaks were observed despite the nitrobenzene not being supported with intentionally added electrolyte. Further addition of ferrocyanide to the aqueous phase resulted in an electro-catalytic increase in the ferrocenium reduction signal as the ferrocyanide re-oxidizes the ferrocene back to ferrocenium through interfacial electron transfer (coupled to ion transfer). This is one of the first examples of electro-catalytic electron transfer across an immiscible liquid-liquid boundary.

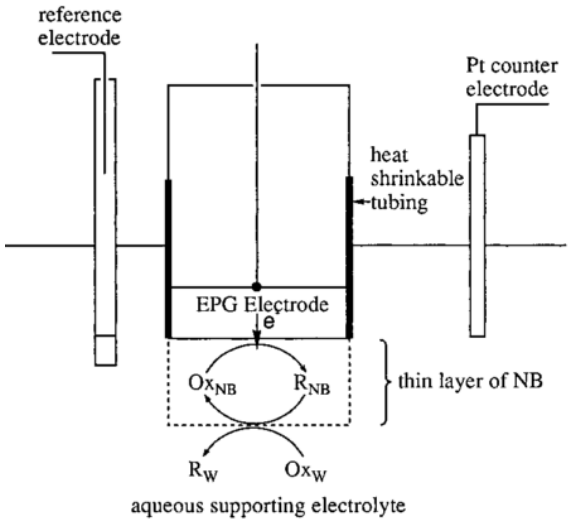

Figure 1.13. A schematic of a liquid film modified electrode submerged in an aqueous electrolyte solution. With redox species O and R, with subscript 'NB' denoting presence in the nitrobenzene phase, and subscript 'W' denoting presence in the aqueous phase. Reprinted with permission from [93]. Copyright (1998) American Chemical Society.

Stability of the films depends on the immiscibility and volatility of the films, it was found that nitrobenzene and benzonitrile worked well whereas more volatile solvents such as dichloromethane did not. Other solvents films deposited include n-octanol [94] and 2-nitrophenyloctyl ether [95]. Redox

probes such as decamethylferrocene or lutetium bis(tetra-tertbutylphthalocyaninato) were used to study electron transfer and coupled ion transfer across the liquid-liquid interface. Conducting electrochemistry utilising a thin film deposited on the electrode was seen as a convenient method through which liquid-liquid interfacial processes could be studied. Compared to the conventional liquid-liquid set-up (see Figure 1.14A), a smaller volume of organic liquid could be used, voltammetry could be conducted using a three-electrode set-up (as opposed to four), and the organic liquid does not necessarily need to be supported by an excess of inert electrolyte.

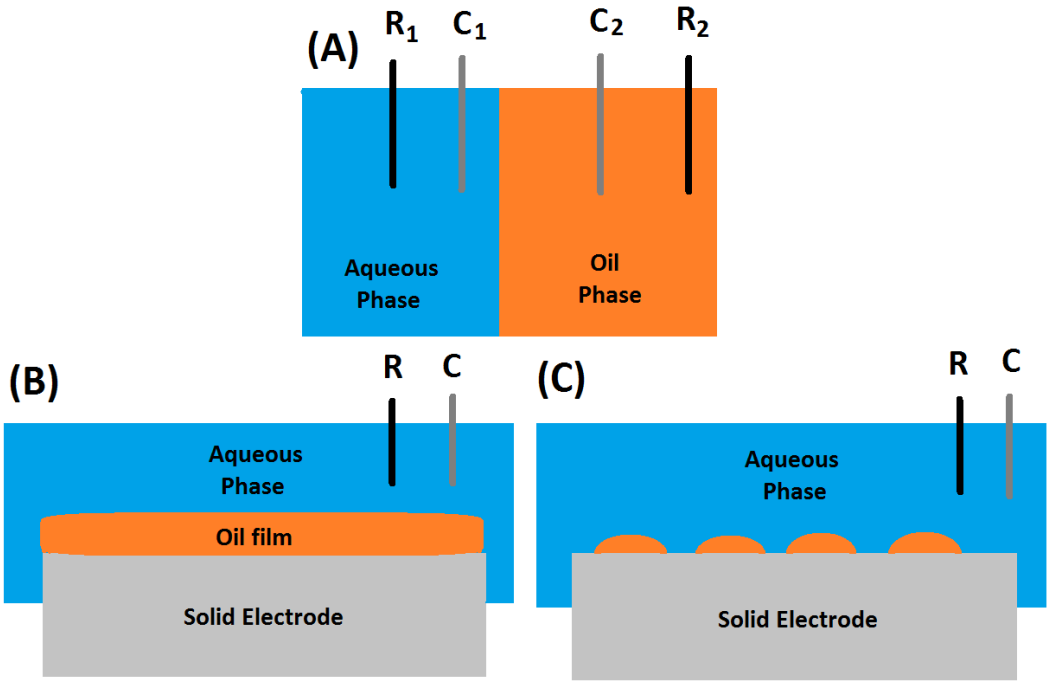

Figure 1.14. Illustration of different types of liquid-liquid interfaces. A) Liquid-liquid interface with a four electrode set-up. B) Solid electrode modified with an oil film (three electrode set-up). C) Solid electrode modified with an array of oil micro-droplets (three electrode set-up). 'R' denotes the reference electrode and 'C' denotes the counter electrode.

The importance of the ion-transfer step coupled to the electron transfer was highlighted by numerous studies. In the study by Quentel, a thin film of n-octanol with lutetium bis(tetra-tertbutylphthalocyaninato) species was deposited on a graphite electrode [94]. The voltammetric study revealed that the onset potential of the redox species shifted according to the standard transfer potential of the ion present in the aqueous phase (see Fig. 1.15), which implies that the ion transfer step is the limiting process. Quental used the set-up to estimate the Gibb's energy of interfacial ion transfer, a similar study was repeated for a thin film deposit of nitrobenzene as well [96]. The

theoretical aspect of interfacial electron and ion transfer will be dealt with in more detail in section 2.3.1.

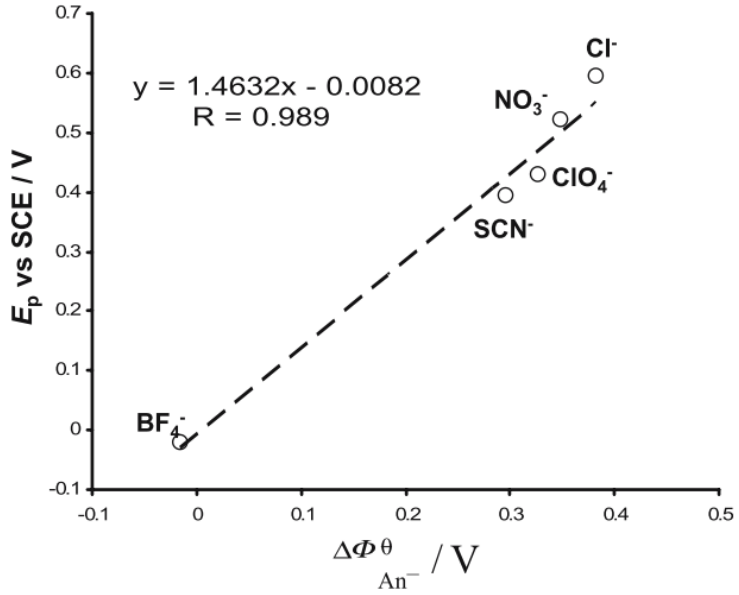

Figure 1.15. A graph illustrating the dependence of the peak potential (E_p) of lutetium bis(tetra-tertbutylphthalocyaninato) dissolved in n-octanol film deposited on a graphite electrode, on the standard anion transfer potential [94]. With permission of Springer, Copyright (2007), Science+Business Media New York.

1.2.2 Modification with Immiscible Liquid Droplets

Redox active liquid droplets can be conveniently deposited on a solid electrode surface by pipetting directly onto the electrode surface. To avoid complete coverage of the electrode, the liquid is often co-deposited with a volatile solvent medium that evaporates off leaving an array of micro-droplets. Micro-droplets on the electrode surface can be electrochemically characterized provided that they remain immobilized and are insoluble in the electrolyte solution. A lot of work on redox active oils based on a tetra-N-alkylated para-phenylenediamine structure has been carried out to demonstrate the concept [97]. The redox active oil is highly hydrophobic and hence immiscible in water, and tends not to crystalize or freeze into a solid. The mechanism of electron and ionic charge transport in droplets is similar to that in liquid films. Electron transfer from the electrode to the oil is coupled to the transfer of ions from the neighbouring aqueous electrolyte to maintain electro-neutrality. Electrochemical activity is initiated at the point ions, redox active species and the source of electrons

meet (called the triple-phase boundary) and the charge propagates through the droplet by the diffusion of charged species in the liquid. Triple-phase boundary processes will be discussed in more detail in section 2.3.

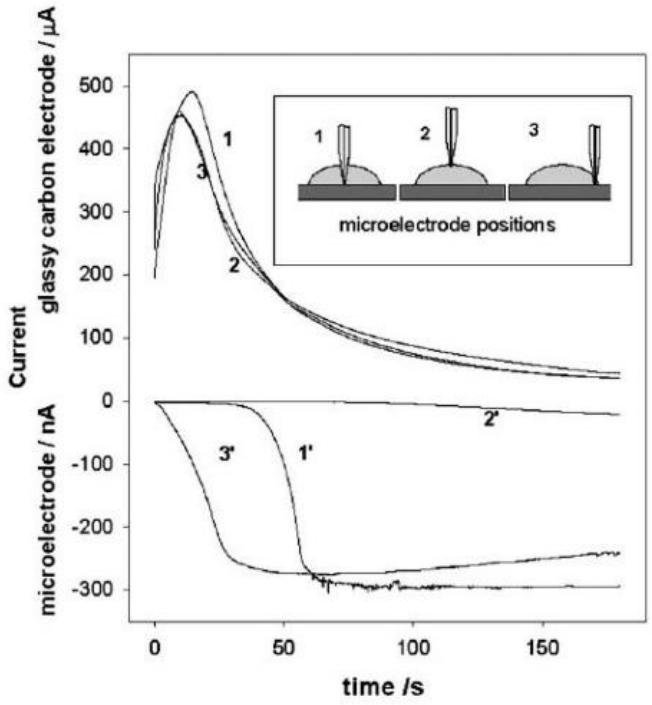

Figure 1.16. The top graph shows chronoamperograms for oxidation of ferrocene at a glassy carbon electrode. The bottom graph shows the corresponding chronoamperograms for the reduction of ferrocene^{+} at a platinum microelectrode. Ferrocene is dissolved in a nitrobenzene droplet immobilized on a glassy carbon electrode which is submerged in an aqueous solution of $LiClO_4$ (0.1M). Reprinted from [98], copyright (2002), with permission from Elsevier

Electrochemistry of immobilized droplets was studied in detail by Scholz [98] and co-workers. In this case, ferrocene is dissolved in an inert oil (nitrobenzene) which is deposited on the electrode surface. The platinum microelectrode shown in Figure 1.16 tracks the spread of electrochemical charge through an insulating liquid droplet at various interfacial boundaries. Electron transfer is only active around the triple-phase boundary at short time-frames but as charged species diffuse through the inert oil it gains ionic conductivity and soon electrochemistry at both oil||water and the oil||electrode boundary is observed. As electron transfer must be coupled to ion transfer, the redox potential is dependent on the nature of electrolyte ions present in the aqueous phase [99]. The energy barrier of ion transfer into a given liquid can be probed by the shift in the onset potential of electron transfer. Scholz and coworkers devised a method to elucidate the Gibbs energy of interfacial ion transfer using

this concept [100]. This was presented as a novel alternative to measuring the hydrophobicity of molecular compounds comparable to doing solvent separations (to obtain the octanol-water partition coefficients).

Other applications of microdroplets deposited on the electrode surface include enantiomerically selective sensing. Use of a chiral oil L-menthol with decamethylferrocene dissolved in it would exhibit different energy barriers towards the two enantiomers of tryptophan [101]. As shown in the square wave voltammograms in Figure 1.17 below, the oxidation peaks potential of decamethylferrocene is dependent on the chirality of the ion being inserted into the menthol oil phase. The difference in peak potential corresponds to a difference in ion-insertion energy of the two enantiomers, and exhibits consistent results when an oil droplet of the opposite chirality is selected.

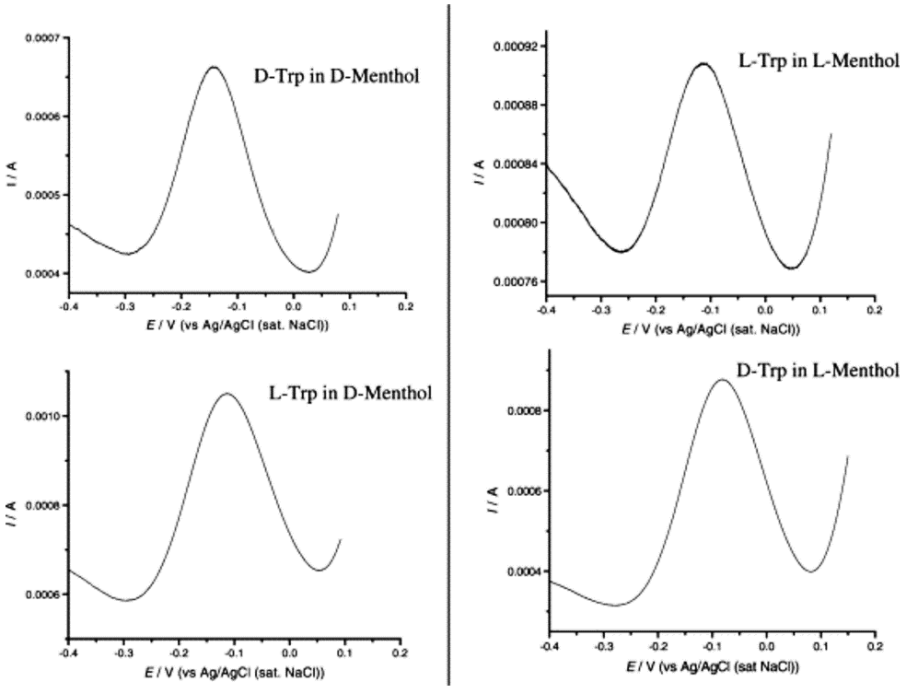

Figure 1.17. Square wave voltammograms recorded at 100 Hz with an amplitude of 50mV of L-menthol and D-menthol droplets with 0.1 M decamethylferrocene dissolved immobilized on a graphite electrode. The modified electrode is submerged in an aqueous solution of 1 M NaOH with 1 M sodium salt of L-Tryptophan and D-Tryptophan. Reprinted from [101], copyright (2002) with permission from Elsevier.

A key aspect of utilizing immiscible liquid systems in the context of electro-catalysis and electro-synthesis lays in the possibility of separating the catalyst from the substrate in two immiscible phases.

Electron transfer across the interface of two immiscible liquids for heterogeneous catalysis has been reported for example in hydrogen evolution reactions [102], [103]. Heterogeneous catalysis can be desirable for industrial applications as it makes separating and purifying the product cheaper and more convenient. Due to the possibility of interfacial ion transfer at the liquid-liquid interface, it is possible to conduct electrochemistry in liquid phases without intentionally added electrolyte salts [104], [105]. The electrochemistry of such a set-up will initially be confined at the triple-phase boundary as shown by the study by Scholz in Figure 1.16 and hence benefits from an electrode geometry that has a large surface area (e.g. nano-structured or porous environments). The possibility of running electrolyte free electro-synthetic conversions is an attractive prospect from a sustainability point of view due to its atom economy. It is also convenient to be able to carry out oil based electro-analysis without having to alter the sample with electrolyte salts.

1.3 Summary and Outlook

Modification of bare metal and carbon electrodes allows additional functionalities to be imparted onto the electrode which had significant impact on the field of electro-analysis and electro-catalysis in the past 40 years. Modification of electrodes with additional chemical components can be thought of as building an Integrated Chemical System, where the role of each component is combined linearly or synergistically to deliver a more complex electrochemical function. As outlined in this brief introduction, a variety of different materials can be deposited on the electrode surface to form Integrated Chemical Systems. Examples of the modification of solid carbon electrodes with electro-catalytic metallic and non-metallic nanoparticles were given in section 1.1.1. This was later expanded to the addition of more complex functionalities such as incorporation of a host film such as a polymer or porous metal-organic-framework onto which the electro-catalysts can be added for enhanced stability and synergistic effects. Electrochemical processes on electrodes modified with liquid droplets and films is also discussed briefly with the usefulness of the separation of the electro-analyte from other components such as the electrolyte salt highlighted with a few examples.

Enhanced functionalities gained through the addition of multi-component modifiers comes at a cost of more complex electrochemical analysis of phenomena such as electrochemical charge propagation and substrate partitioning and diffusion in multiple phases. The mode of electrochemical charge

propagation in modified phases differs depending on the material properties. Metals and metal-like substances conduct charge through electron conduction. Whereas redox active non-metal modifiers tend to conduct charge through a hopping mechanism (or diffusion in the case of liquids). Generally, charge conduction in non-metallic substances tends to be slower and less efficient than in metals. Yet there is growing demand to look for alternatives to transition metal based materials due to their scarcity and high cost. The purpose of this introduction is to provide a broad overview of examples of different approaches to modifying electrodes to impart complex functionalities, and to set the theme for the approach taken in this thesis.

1.4 Scope of this Thesis

This thesis presents a series of projects aimed at enhancing electrochemical processes and functionalities through the use of modified carbon electrodes. The purpose of applying Integrated Chemical Systems in this thesis is to demonstrate partial solutions to technical barriers in the way of wide-spread use of electrochemical technologies in industry. Electrochemistry offers several advantages in performing chemical synthesis or analysis over conventional methods such as (i) applied potential can be tuned for chemical selectivity, (ii) applied potential and charge passed can be used to control extent of reaction, (iii) reaction rate can be controlled by fixing the current, (iv) use of pure electrons (current) as a reagent can allow high atom economy, (v) as the rate of electron transfer is not significantly dependent on temperature, electrochemical reaction conditions can usually be kept mild at room temperature and pressure, and (vi) in cases harmful substances or mediators need to be used, such species can sometimes be electrochemically generated in-situ in a controlled environment which minimise risk to the facility and the environment. Despite these advantages, it is known that electrochemical methods are not widely utilised in industry [106]–[108]. Technical barriers in the way of implementing widespread industrial electrochemical technologies has been discussed as high costs due to the need for specialist equipment and cells, but more fundamentally the need for electrolyte salts and in cases redox mediators that increases processing costs due to the need to separate and purify the final product. A partial solution to the latter issue that has been previously explored by the Marken group, is the use of triple-phase boundary systems. Triple-phase boundary systems has been shown to allow electro-synthetic reactions to occur in phases without intentionally added electrolytes through interfacial ion-transfer processes. Keeping the electro-active species separate from the electrolyte by immobilising in an immiscible liquid phase has the benefit of negating the need for

further purification for extraction or further processing, which is not only convenient but can be economical. Triple-phase boundary formed by two liquid phases meeting on a solid electrode surface is usually quite a small area; in the case of a liquid droplet immobilised on flat solid surface bathed in another immiscible liquid, the triple-phase boundary is the circumference the droplet forms on the electrode surface. The key challenge in implementing triple-phase boundary systems lay with finding a material that can function as an electrochemical interface for effective mediation of ion-transfer processes.

Chapter 3 expands on previous work by Watkins et.al. [104], [105] where carbon nanofibers were utilised as an electrode material in a triple-phase boundary electro-synthetic microreactors. Carbon nanofibers are synthesized as an electrode material that is highly porous, has a high surface area and is amphiphilic, which makes it ideal for electrochemistry at liquid-liquid interfaces. Densely packed randomly arranged nanofiber membranes dramatically enhances the triple-phase boundary formed between two immiscible liquids. The chapter details a synthetic method for carbon nanofiber synthesis that consumes significantly less energy and time that conventional methods reported in literature through 'graphenisation'. Application of the electrochemical microreactors incorporated with the modified carbon nanofibers is demonstrated through ion-transfer voltammetry of manganese porphyrin immobilised in an immiscible oil.

Chapter 4 is a study based on a more conveniently prepared carbon microsphere-polymer composite, where the carbon is mechanically held together into a porous structure by an electrically insulating polymer binder. The porous carbon structure is demonstrated to be an effective host for organic oil analysis, under a triple-phase boundary set-up. Chapter 5 is also a study of a carbon-polymer composite, but here the polymer of intrinsic microporosity has the role of a binder as well as a porous host for electro-catalytic guest molecules. Host-guest effects are investigated and a mechanistic understanding of the rate limiting process in the electro-catalytic scheme is gained through the application of Albery and Hillman's model on modified electrodes [70]. The rigidity of the polymer host offers structural stability, while its nano-porous structure acts as a selective membrane. Chapters 6 and 7 present a novel hydrodynamic technique and its use in modulating mass transport in solution, which can be used as a diagnostic tool to study electrode processes at both modified and unmodified electrodes. Chapter 7 demonstrates the method's utility through a mechanistic analysis of homogeneous electro-oxidation of alcohols using an organic free-radical catalyst.

The thesis aims to present novel approaches to modifying electrodes for enhanced performance in electro-analysis and electro-catalysis utilising a variety of modifying nanomaterials. The key theme with the approach taken involves heterogenising components necessary for electrochemical reactions in separate phases such that the need for further separations and processing is reduced. With triple-phase boundary systems, the electro-analyte is kept separate from the electrolyte solution by immobilising in an immiscible liquid. In the case of heterogeneous catalysis, the free radical redox mediator is also prevented from mixing into the electrolyte solution by immobilising in a composite polymer film. This is accomplished through novel use of composite materials, hence the focus is placed on i) the role of modifying materials on the electrode function and ii) fundamental aspects of electrochemical processes.

1.4 References

[1] R. Lane and A. Hubbard, “Electrochemistry of chemisorbed molecules I. Reactants connected to electrodes through olefinic substituents,” *J. Phys. Chem.*, vol. 77, no. 11, pp. 1401–1410, 1973.

[2] A. J. Bard, "*Integrated chemical systems: A chemical approach to nanotechnology*," John Wiley & Sons, Inc., 1994.

[3] A. Oberlin, M. Endo, and T. Koyama, “Filamentous growth of carbon through benzene decomposition,” *J. Cryst. Growth*, vol. 32, no. 3, pp. 335–349, 1976.

[4] H. W. Kroto, J. R. Heath, S. C. O’Brien, R. F. Curl, and R. E. Smalley, “C 60: buckminsterfullerene,” *Nature*, vol. 318, p. 162, 1985.

[5] S. Iijima, “Helical microtubules of graphitic carbon,” *Nature*, vol. 354, p. 56, 1991.

[6] K. S. Novoselov, A. K. Geim, S. V. Morozov, D. Jiang, Y. Zhang, S. V. Dubonos, I. V. Grigorieva, and A. A. Firsov, “Electric Field Effect in Atomically Thin Carbon Films,” *Science (80)*, vol. 306, p. 666, 2004.

[7] M. Scanlon, P. Peljo, M. A. Mendez, E. A. Smirnov, and H. Girault, “Charging and discharging at the nanoscale: fermi level equilibration of metallic nanoparticles,” *Chem. Sci.*, pp. 2705–2720, 2015.

[8] F. Coloma, F. Rodrõ, A. Sepu, A. Inorga, A. Sepúlveda-Escribano, and F. Rodríguez-Reinoso, “Platinum catalysts supported on carbon blacks with different surface chemical properties,” *Appl. Catal. A Gen.*, vol. 173, no. 2, pp. 247–257, 1998.

[9] S. H. Joo, S. J. Choi, I. Oh, J. Kwak, Z. Liu, O. Terasaki, and R. Ryoo, “Ordered nanoporous arrays of carbon supporting high dispersions of platinum nanoparticles.,” *Nature*, vol. 412, no. 6843, pp. 169–172, 2001.

[10] T. J. Davies and R. G. Compton, “The cyclic and linear sweep voltammetry of regular and random arrays of microdisc electrodes: Theory,” *J. Electroanal. Chem.*, vol. 585, no. 1, pp. 63–82, 2005.

[11] B. H. Kim, N. Lee, H. Kim, K. An, Y. Il Park, Y. Choi, K. Shin, Y. Lee, S. G. Kwon, H. Bin Na, J. G. Park, T. Y. Ahn, Y. W. Kim, W. K. Moon, S. H. Choi, and T. Hyeon, “Large-scale synthesis of uniform and extremely small-sized iron oxide nanoparticles for high-resolution t(1) magnetic resonance imaging contrast agents.,” *J. Am. Chem. Soc.*, vol. 133, no. 32, pp. 12624–12631, 2011.

[12] J. Park, K. An, Y. Hwang, J. G. Park, H. J. Noh, J. Y. Kim, J. H. Park, N. M. Hwang, and T. Hyeon, "Ultra-large-scale syntheses of monodisperse nanocrystals.," *Nat. Mater.*, vol. 3, no. 12, pp. 891–895, 2004.

[13] M. O'Connell, J. R. Lewis, and A. J. Wain, "Electrochemical imaging of hydrogen peroxide generation at individual gold nanoparticles," *Chem. Commun.*, no. 111, 2015.

[14] J. Hernández, J. Solla-Gullón, E. Herrero, A. Aldaz, and J. M. Feliu, "Methanol oxidation on gold nanoparticles in alkaline media: Unusual electrocatalytic activity," *Electrochim. Acta*, vol. 52, no. 4, pp. 1662–1669, 2006.

[15] R. Baron, B. Šljukić, C. Salter, A. Crossley, and R. G. Compton, "Electrochemical detection of arsenic on a gold nanoparticle array," *Russ. J. Phys. Chem. A*, vol. 81, no. 9, pp. 1443–1447, 2007.

[16] N. Ratner and D. Mandler, "Electrochemical Detection of Low Concentrations of Mercury in Water Using Gold Nanoparticles," *Anal. Chem.*, vol. 87 (10), pp. 5148-5155, 2015.

[17] J. Song, L. Xu, R. Xing, Q. Li, C. Zhou, D. Liu, and H. Song, "Synthesis of Au/graphene oxide composites for selective and sensitive electrochemical detection of ascorbic acid," *Sci. Rep.*, vol. 4, p. 7515, 2014.

[18] C. M. Welch, C. E. Banks, A. O. Simm, and R. G. Compton, "Silver nanoparticle assemblies supported on glassy-carbon electrodes for the electro-analytical detection of hydrogen peroxide," *Anal. Bioanal. Chem.*, vol. 382, no. 1, pp. 12–21, 2005.

[19] H. S. Toh, C. Batchelor-mcauley, K. Tschulik, and R. G. Compton, "Electrochemical detection of chloride levels in sweat using silver nanoparticles: a basis for the preliminary screening for cystic fibrosis.," *Analyst*, vol. 138, no. 15, pp. 4292–7, 2013.

[20] J. Tashkhourian, M. R. H. Nezhad, J. Khodavesi, and S. Javadi, "Silver nanoparticles modified carbon nanotube paste electrode for simultaneous determination of dopamine and ascorbic acid," *J. Electroanal. Chem.*, vol. 633, no. 1, pp. 85–91, 2009.

[21] Y. Wan, Y. Wang, J. Wu, and D. Zhang, "Graphene oxide sheet-mediated silver enhancement for application to electrochemical biosensors," *Anal. Chem.*, vol. 83, no. 3, pp. 648–653, 2011.

[22] J. Li, D. Kuang, Y. Feng, F. Zhang, Z. Xu, M. Liu, and D. Wang, "Green synthesis of silver nanoparticles-graphene oxide nanocomposite and its application in electrochemical sensing of tryptophan," *Biosens. Bioelectron.*, vol. 42, no. 1, pp. 198–206, 2013.

[23] S. Guo, D. Wen, Y. Zhai, S. Dong, and E. Wang, "Platinum nanoparticle ensemble-on-rapid synthesis, and used as new sensing," ACS Nano, vol. 4, no. 7, pp. 3959–3968, 2010.

[24] C. L. Sun, H. H. Lee, J. M. Yang, and C. C. Wu, “The simultaneous electrochemical detection of ascorbic acid, dopamine, and uric acid using graphene/size-selected Pt nanocomposites,” *Biosens. Bioelectron.*, vol. 26, no. 8, pp. 3450–3455, 2011.

[25] L. Hutton, M. E. Newton, P. R. Unwin, and J. V. Macpherson, “Amperometric oxygen sensor based on a platinum nanoparticle-modified polycrystalline boron doped diamond disk electrode,” *Anal. Chem.*, vol. 81, no. 3, pp. 1023–1032, 2009.

[26] W. Zheng, X. Lu, W. Wang, Z. Li, H. Zhang, Z. Wang, X. Xu, S. Li, and C. Wang, “Assembly of Pt nanoparticles on electrospun In2O3 nanofibers for H2S detection,” *J. Colloid Interface Sci.*, vol. 338, no. 2, pp. 366–370, 2009.

[27] Y. Li, W. Gao, L. Ci, C. Wang, and P. M. Ajayan, “Catalytic performance of Pt nanoparticles on reduced graphene oxide for methanol electro-oxidation,” *Carbon N. Y.*, vol. 48, no. 4, pp. 1124–1130, 2010.

[28] C. M. Welch, M. E. Hyde, C. E. Banks, and R. G. Compton, “The detection of nitrate using in-situ copper nanoparticle deposition at a boron doped diamond electrode.,” *Anal. Sci.*, vol. 21, no. 12, pp. 1421–1430, 2005.

[29] X. Kang, Z. Mai, X. Zou, P. Cai, and J. Mo, “A sensitive nonenzymatic glucose sensor in alkaline media with a copper nanocluster/multiwall carbon nanotube-modified glassy carbon electrode,” *Anal. Biochem.*, vol. 363, no. 1, pp. 143–150, 2007.

[30] H. Heli, M. Hajjizadeh, A. Jabbari, and A. A. Moosavi-Movahedi, “Fine steps of electrocatalytic oxidation and sensitive detection of some amino acids on copper nanoparticles,” *Anal. Biochem.*, vol. 388, no. 1, pp. 81–90, 2009.

[31] L. Meng, J. Jin, G. Yang, T. Lu, H. Zhang, and C. Cai, “Nonenzymatic electrochemical detection of glucose based on palladium-single-walled carbon nanotube hybrid nanostructures,” *Anal. Chem.*, vol. 81, no. 17, pp. 7271–7280, 2009.

[32] H. Zhang, J. Huang, H. Hou, and T. You, “Electrochemical detection of hydrazine based on electrospun palladium nanoparticle/carbon nanofibers,” *Electroanalysis*, vol. 21, no. 16, pp. 1869–1874, 2009.

[33] X. Chen, G. Wu, J. Chen, X. Chen, Z. Xie, and X. Wang, “Synthesis of ‘clean’ and well-dispersive pd nanoparticles with excellent electrocatalytic property on graphene oxide,” *J. Am. Chem. Soc.*, vol. 133, no. 11, pp. 3693–3695, 2011.

[34] S. Komorsky-lovric, I. Galic, and R. Penovski, “Voltammetric determination of cocaine microparticles,” *Electroanalysis*, vol. 389, pp. 219–223, 1999.

[35] S. J. Reddy, M. Hermes, and F. Scholz, “The application of abrasive stripping voltammetry for a simple and rapid screening of pesticides,” *Electroanalysis*, vol. 8, pp. 955–958, 1996.

[36] I. Novak, M. Mlakar, and Š. Komorsky-Lovrić, “Voltammetry of immobilized particles of cannabinoids,” *Electroanalysis*, vol. 25, no. 12, pp. 2631–2636, 2013.

[37] D. M. Oglesby, S. H. Omang, and C. N. Reilley, “Thin layer electrochemical studies using controlled potential or controlled current.,” *Anal. Chem.*, vol. 37, no. 11, pp. 1312–1316, 1965.

[38] O. K. Farha, I. Eryazici, N. C. Jeong, B. G. Hauser, C. E. Wilmer, A. a. Sarjeant, R. Q. Snurr, S. T. Nguyen, a. Ö. Yazaydin, and J. T. Hupp, “Metal-organic framework materials with ultrahigh surface areas: Is the sky the limit?,” *J. Am. Chem. Soc.*, vol. 134, no. 36, pp. 15016–15021, 2012.

[39] A. Morozan and F. Jaouen, “Metal organic frameworks for electrochemical applications,” *Energy Environ. Sci.*, vol. 5, no. 11, p. 9269, 2012.

[40] J. Li, J. Sculley, and H. Zhou, “Metal organic frameworks for separations,” Chem. Reviews, 112 (2), pp. 869–932, 2012.

[41] T. A. Makal, J. R. Li, W. Lu, and H. C. Zhou, “Methane storage in advanced porous materials,” *Chem. Soc. Rev.*, vol. 41, no. 23, p. 7761, 2012.

[42] P. Horcajada, T. Chalati, C. Serre, B. Gillet, C. Sebrie, T. Baati, J. F. Eubank, D. Heurtaux, P. Clayette, C. Kreuz, J.-S. Chang, Y. K. Hwang, V. Marsaud, P.-N. Bories, L. Cynober, S. Gil, G. Férey, P. Couvreur, and R. Gref, “Porous metal–organic-framework nanoscale carriers as a potential platform for drug delivery and imaging,” *Nat. Mater.*, vol. 9, no. 2, pp. 172–178, 2010.

[43] A. M. Spokoyny, D. Kim, A. Sumrein, and C. A. Mirkin, “Infinite coordination polymer nano- and microparticle structures,” *Chem. Soc. Rev.*, vol. 38, no. 5, p. 1218, 2009.

[44] J. E. Halls, S. D. Ahn, D. Jiang, L. L. Keenan, A. D. Burrows, and F. Marken, “Reprint of proton uptake vs. redox driven release from metal-organic- frameworks: Alizarin red S reactivity in UMCM-1,” *J. Electroanal. Chem.*, vol. 710, pp. 2–9, 2013.

[45] B. Mu, P. M. Schoenecker, and K. S. Walton, “Gas adsorption study on mesoporous metal-organic framework UMCM-1,” *J. Phys. Chem. C*, vol. 114, no. 14, pp. 6464–6471, 2010.

[46] K. F. Babu, M. A. Kulandainathan, I. Katsounaros, L. Rassaei, A. D. Burrows, P. R. Raithby, and F. Marken, “Electrocatalytic activity of BasoliteTM F300 metal-organic-framework structures,” *Electrochem. commun.*, vol. 12, no. 5, pp. 632–635, 2010.

[47] C. Wang, Z. Xie, K. E. DeKrafft, and W. Lin, “Doping metal organic frameworks for water oxidation, carbon dioxide reduction, and organic photocatalysis,” *J. Am. Chem. Soc.*, vol. 133, pp. 13445–13454, 2011.

[48] B. Nohra, H. El Moll, L. M. Rodriguez Albelo, P. Mialane, J. Marrot, C. Mellot-Draznieks, M. O’Keeffe, R. Ngo Biboum, J. Lemaire, B. Keita, L. Nadjo, and A. Dolbecq, “Polyoxometalate-based metal organic frameworks (POMOFs): Structural trends, energetics, and high electrocatalytic efficiency for hydrogen evolution reaction,” *J. Am. Chem. Soc.*, vol. 133, no. 34, pp. 13363–13374, 2011.

[49] N. Kornienko, Y. Zhao, C. S. Kley, C. Zhu, D. Kim, S. Lin, C. J. Chang, O. M. Yaghi, and P. Yang, “Metal–organic frameworks for electrocatalytic reduction of carbon dioxide,” *J. Am. Chem. Soc.*, 137, pp.14129-14135, 2015.

[50] L. L. Miller and M. R. Van De Mark, “Electrode surface modification via polymer adsorption,” *JACS*, vol. 834, pp. 639–640, 1978.

[51] H. Tachikawa and L. R. Faulkner, “Electrochemical and solid-state studies of phthalocyanine thin film electrodes.,” *J. Am. Chem. Soc.*, vol. 100, no. 13, pp. 4379–4385, 1978.

[52] A. Merz and A. J. Bard, “A stable surface modified platinum electrode prepared by coating with electroactive polymer,” *J. Am. Chem. Soc.*, vol. 100, no. 10, pp. 3222–3223, 1978.

[53] N. Oyama and F. C. Anson, “Polymeric ligands as anchoring groups for the attachment of metal complexes to graphite electrode surfaces,” *J. Am. Chem. Soc.*, vol. 101, no. 13, pp. 3450–3456, 1979.

[54] S. Chao, J. L. Robbins, and M. S. Wrighton, “A new ferrocenophane surface derivatizing reagent for the preparation of nearly reversible electrodes for horse heart ferri-/ferrocytochrome,” J. Am. Chem. Soc., no. 3, pp. 181–188, 1983.

[55] A. Lau and L. Miller, “Electrochemical behavior of a dopamine polymer. Dopamine release as a primitive analog of a synapse,” *J. Am. Chem. Soc.*, vol. 30, no. 2, pp. 5271–5277, 1983.

[56] K. K. Kanazawa, A. F. Diaz, R. H. Geiss, W. D. Gill, J. F. Kwak, J. A. Logan, J. F. Rabolt, and G. B. Street, “Organic metals: polypyrrole, a stable synthetic metallic polymer,” *J. Chem. Soc. Chem. Commun.*, no. 19, p. 854, 1979.

[57] N. Oyama, F.C. Anson, “Electrostatic binding of metal complexes to electrode surfaces coated with highly charged polymeric films,” *J. Electrochem. Soc.*, vol. 127, no. 1, p. 249, 1980.

[58] H. S. White, J. Leddy, and A. J. Bard, “Polymer films on electrodes. 8. Investigation of charge-transport mechanisms in Nafion polymer modified electrodes,” *J. Am. Chem. Soc.*, vol. 104, no. 18, pp. 4811–4817, 1982.

[59] W. H. Kao and T. Kuwana, “Electrocatalysis by electrodeposited spherical platinum microparticles dispersed in a polymeric film electrode,” *J. Am. Chem. Soc.*, vol. 106, no. 3, pp. 473–476, 1984.

[60] J. Wang, M. Musameh, and Y. Lin, “Solubilization of carbon nanotubes by Nafion toward the preparation of amperometric biosensors,” *J. Am. Chem. Soc.*, vol. 125, no. 9, pp. 2408–2409, 2003.

[61] D. He, Y. Rong, Z. Kou, S. Mu, T. Peng, R. Malpass-Evans, M. Carta, N. B. McKeown, and F. Marken, “Intrinsically microporous polymer slows down fuel cell catalyst corrosion,” *Electrochem. commun.*, vol. 59, pp. 72–76, 2015.

[62] Y. Zou, C. Xiang, L. X. Sun, and F. Xu, “Glucose biosensor based on electrodeposition of platinum nanoparticles onto carbon nanotubes and immobilizing enzyme with chitosan-SiO2 sol-gel,” *Biosens. Bioelectron.*, vol. 23, no. 7, pp. 1010–1016, 2008.

[63] Y. Wang, W. Wei, J. Zeng, X. Liu, and X. Zeng, “Fabrication of a copper nanoparticle/chitosan/carbon nanotube-modified glassy carbon electrode for electrochemical sensing of hydrogen peroxide and glucose,” *Microchim. Acta*, vol. 160, no. 1–2, pp. 253–260, 2008.

[64] J. M. Bolts, A. B. Bocarsly, M. C. Palazzotto, E. G. Walton, N. S. Lewis, and M. S. Wrighton, “Chemically derivatized n-type silicon photoelectrodes. Stabilization to surface corrosion in aqueous electrolyte solutions and mediation of oxidation reactions by surface-attached electroactive ferrocene reagents,” *J. Am. Chem. Soc.*, vol. 101, no. 6, pp. 1378–1385, 1979.

[65] B. F. Watkins, J. R. Behling, E. Kariv, and L. L. Miller, “A chiral electrode,” *J. Am. Chem. Soc.*, vol. 97, no. 12, pp. 3549–3550, 1975.

[66] Ş. Ulubay and Z. Dursun, “Cu nanoparticles incorporated polypyrrole modified GCE for sensitive simultaneous determination of dopamine and uric acid,” *Talanta*, vol. 80, no. 3, pp. 1461–1466, 2010.

[67] S. J. M. Andrieux C.P., Dumas-Bouchiat J.M., “Catalysis of electrochemical reactions at redox polymer electrodes: Kinetic model for stationary voltammetric techniques,” *J. Electroanal. Chem.*, vol. 131, pp. 1–35, 1982.

[68] R. D. Rocklin and R. W. Murray, "Kinetics of electrocatalysis of dibromoalkyl reductions using electrodes with covalently immobilized metallotetraphenylporphyrins”, J. Phys. Chem., 85, pp. 2104–2112, 1981.

[69] P. Daum and R. W. Murray, “Charge-transfer diffusion rates and activity relationships during oxidation and reduction of plasma-polymerized vinylferrocene films,” *J. Phys. Chem.*, vol. 85, no. 4, pp. 389–396, 1981.

[70] W. J. Albery and A. R. Hillman, “Transport and kinetics in modified electrodes,” *J. Electroanal. Chem. Interfacial Electrochem.*, vol. 170, no. 1–2, pp. 27–49, 1984.

[71] W. J. Albery and M. G. Boutelle, “The mechanism of Faradaic reactions at the thioine coated electrode,” *J. Electroanal. Chem.*, vol. 182, p. 99, 1985.

[72] C. J. Miller and M. Majda, “Microporous aluminium oxide films at electrodes,” *J. Am. Chem. Soc.*, vol. 107, no. 5, pp. 1420–1421, 1985.

[73] D. W. DeWulf and A. J. Bard, “Application of nafion/platinum electrodes (solid polymer electrolyte structures) to voltammetric investigations of highly resistive solutions,” *J. Electrochem. Soc.*, vol. 135, no. 8, p. 1977, 1988.

[74] D. W. Dewulf and A. J. Bard, “The electrochemical reduction of CO2 to CH4 and C2H4 at Cu/Nafion electrodes (solid polymer electrolyte structures),” *Catal. Letters*, vol. 1, no. 1–3, pp. 73–79, 1988.

[75] S. Mazur and S. Reicht, “Electrochemical growth of metal interlayers in polyimide film,” *J. Phys. Chem.*, vol. 90, pp. 1365–1372, 1986.

[76] R. N. Adams, “Carbon paste electrodes,” *Anal. Chem.*, vol. 30, p. 1576, 1958.

[77] I. Švancara, K. Vytřas, K. Kalcher, A. Walcarius, and J. Wang, “Carbon paste electrodes in facts, numbers, and notes: A review on the occasion of the 50-years jubilee of carbon paste in electrochemistry and electroanalysis,” *Electroanalysis*, vol. 21, no. 1, pp. 7–28, 2009.

[78] I. Švancara, K. Vytřas, J. Barek, and J. Zima, “Carbon paste electrodes in modern electroanalysis,” *Crit. Rev. Anal. Chem.*, vol. 31, no. 4, pp. 311–345, 2001.

[79] R. N. Adams, *Electrochemistry at solid electrodes*. New York: Marcel Dekker, 1969.

[80] H. Liu, P. He, Z. Li, C. Sun, L. Shi, Y. Liu, G. Zhu, and J. Li, “An ionic liquid-type carbon paste electrode and its polyoxometalate-modified properties,” *Electrochem. commun.*, vol. 7, no. 12, pp. 1357–1363, 2005.

[81] I. Svancara, M. Hvizdalova, K. Vytpas, and K. Kalcher, “A microscopic study on carbon paste electrodes,” pp. 61–65, 1996.

[82] A. Bobrowski, A. Królicka, and E. Łyczkowska, “Carbon paste electrode plated with lead film. Voltammetric characteristics and application in adsorptive stripping voltammetry,” *Electroanalysis*, vol. 20, no. 1, pp. 61–67, 2008.

[83] K. Vytras and J. Konvalina, “New possibilities of potentiometric stripping analysis based on ion-pair formation and accumulation of analyte at carbon paste electrodes. preliminary note,” *Electroanalysis*, vol. 10, no. 11, pp. 787–790, 1998.

[84] D. E. Schildkraut, P. T. Dao, J. P. Twist, A. T. Davis, and K. a. Robillard, “Determination of silver ions at submicrogram-per-liter levels using anodic square-wave stripping voltammetry,” *Environ. Toxicol. Chem.*, vol. 17, no. 4, pp. 642–649, 1998.

[85] A. Komersová, M. Bartos, K. Kalcher, and K. Vytras, “Trace iron determination in aminoisophthalic acid using differential-pulse cathodic stripping voltammetry at carbon paste electrodes.,” *J. Pharm. Biomed. Anal.*, vol. 16, no. 8, pp. 1373–1379, 1998.

[86] I. Svancara, J. Konvalina, K. Schachl, K. Kalcher, and K. Vytras, “Stripping voltammetric determination of iodide with synergistic accumulation at a carbon paste electrode,” *Electroanalysis*, vol. 10, no. 6, pp. 435–441, 1998.

[87] A. R. Samo, M. Y. Khahawer, S. A. Arbani, and G. A. Qureshi, “Quantitation of azide and lead in lead azide by voltammetric method,” *J. Chem. Soc. Pak.*, vol. 15, no. 3, pp. 187–190, 1993.

[88] I. Svancara, K. Kalcher, W. Diewald, and K. Vytras, “Voltammetric determination of silver at ultratrace levels using a carbon paste electrode with improved surface characteristics,” *Electroanalysis*, vol. 8, no. 4, pp. 336–342, 1996.

[89] J. Wang, J. Liu, L. Chen, and F. Lu, “Highly selective membrane-free, mediator-free glucose biosensor,” *Anal. Chem.*, vol. 66, no. 21, pp. 3600–3603, 1994.

[90] S. Liu and H. Ju, “Reagentless glucose biosensor based on direct electron transfer of glucose oxidase immobilized on colloidal gold modified carbon paste electrode,” *Biosens. Bioelectron.*, vol. 19, no. 3, pp. 177–183, 2003.

[91] C. Shi and F. C. Anson, “Electron transfer between reactants located on opposite sides of liquid/liquid interfaces,” *J. Phys. Chem. B*, vol. 103, no. 30, pp. 6283–6289, 1999.

[92] C. Shi and F. C. Anson, “A simple method for examining the electrochemistry of metalloporphyrins and other hydrophobic reactants in thin layers of organic solvents interposed between graphite electrodes and aqueous solutions.,” *Anal. Chem.*, vol. 70, no. 15, pp. 3114–8, 1998.

[93] C. Shi and F. C. Anson, “Simple electrochemical procedure for measuring the rates of electron transfer across liquid/liquid interfaces formed by coating graphite electrodes with thin layers of nitrobenzene,” *J. Phys. Chem. B*, vol. 102, no. 49, pp. 9850–9854, 1998.

[94] F. Quentel, V. Mirčeski, and M. L'Her, "Electrochemical study of the thermodynamics and kinetics of hydrophilic ion transfers across water | n-octanol interface," *J. Solid State Electrochem.*, vol. 12, no. 1, pp. 31–39, 2007.

[95] F. Quentel, V. Mirčeski, C. Elleouet, and M. L'Her, "Studying the thermodynamics and kinetics of ion transfers across water-2-nitrophenyloctyl ether interface by means of organic-solution-modified electrodes," *J. Phys. Chem. C*, vol. 112, no. 39, pp. 15553–15561, 2008.

[96] F. Quentel, V. Mirceski, and M. L'Her, "Lutetium bis(tetra-tert-butylphthalocyaninato): A superior redox probe to study the transfer of anions and cations across the water/nitrobenzene interface by means of square-wave voltammetry at the three-phase electrode.," *J. Phys. Chem. B*, vol. 109, no. 3, pp. 1262–7, 2005.

[97] C. E. Banks, T. J. Davies, R. G. Evans, G. Hignett, A. J. Wain, N. S. Lawrence, J. D. Wadhawan, F. Marken, and R. G. Compton, "Electrochemistry of immobilised redox droplets: Concepts and applications," *Phys. Chem. Chem. Phys.*, vol. 5, no. 19, p. 4053, 2003.

[98] M. Donten, Z. Stojek, and F. Scholz, "Electron transfer - ion insertion electrochemistry at an immobilised droplet: Probing the three-phase electrode-reaction zone with a Pt disk microelectrode," *Electrochem. commun.*, vol. 4, no. 4, pp. 324–329, 2002.

[99] U. Schröder, J. Wadhawan, R. G. Evans, R. G. Compton, B. Wood, D. J. Walton, R. R. France, F. Marken, P. C. B. Page, and C. M. Hayman, "Probing thermodynamic aspects of electrochemically driven ion-transfer processes across liquid|liquid interfaces: Pure versus diluted redox liquids," *J. Phys. Chem. B*, vol. 106, no. 34, pp. 8697–8704, 2002.

[100] F. Scholz, Š. Komorsky-Lovrić, and M. Lovrić, "A new access to gibbs energies of transfer of ions across liquid|liquid interfaces and a new method to study electrochemical processes at well-defined three-phase junctions," *Electrochem. commun.*, vol. 2, no. 2, pp. 112–118, 2000.

[101] F. Scholz, R. Gulaboski, V. Mirčeski, and P. Langer, "Quantification of the chiral recognition in electrochemically driven ion transfer across the interface water/chiral liquid," *Electrochem. commun.*, vol. 4, no. 8, pp. 659–662, 2002.

[102] I. Hatay, B. Su, F. Li, R. Partovi-Nia, H. Vrubel, X. Hu, M. Ersoz, and H. H. Girault, "Hydrogen evolution at liquid-liquid interfaces," *Angew. Chemie - Int. Ed.*, vol. 48, no. 28, pp. 5139–5142, 2009.

[103] W. Adamiak, J. Jedraszko, O. Krysiak, W. Nogala, J. C. Hidalgo-acosta, H. H. Girault, and M. Opallo, "Hydrogen and hydrogen peroxide formation in trifluorotoluene − water biphasic systems," J. Phys. Chem. C, 118, pp. 23154-23161, 2014.

[104] J. D. Watkins, J. E. Taylor, S. D. Bull, and F. Marken, “Mechanistic aspects of aldehyde and imine electro-reduction in a liquid–liquid carbon nanofiber membrane microreactor,” *Tetrahedron Lett.*, vol. 53, no. 26, pp. 3357–3360, 2012.

[105] J. D. Watkins, S. D. Ahn, J. E. Taylor, S. D. Bull, P. C. Bulman-Page, and F. Marken, “Liquid–liquid electro-organo-synthetic processes in a carbon nanofibre membrane microreactor: Triple phase boundary effects in the absence of intentionally added electrolyte,” *Electrochim. Acta*, vol. 56, no. 19, pp. 6764–6770, 2011.

[106] G. G. Botte, “Electrochemical manufacturing in the chemical industry,” *Electrochem. Soc. Interface*, Fall, pp. 49–50, 2014.

[107] M. A. Matthews, “Green electrochemistry. examples and challenges,” *Pure Appl. Chem.*, vol. 73, no. 8, pp. 1305–1308, 2001.

[108] H. Wendt, “Electrochemistry, 2. Inorganic electrochemical processes,” *Ullmann’s Encycl. Ind. Chem.*, pp. 1–42, 2012.

Chapter 2. Introduction to the Fundamentals of Electrochemistry

Contents

2.1 Fundamentals

2.1.1 Thermodynamics [1,2,3]

Electrochemical potential

Chemical potential is the work required to transfer one mole of a given molecule *a* from a vacuum into a phase, while keeping temperature and pressure constant. The chemical potential of a single chemical component can be expressed using the equation shown in equation 2.1.

$$\mathrm{G} = \mathrm{U} + \mathrm{pV} - \mathrm{TS} \qquad \text{(eq.2.1)}$$

G is the Gibbs energy, U is the internal energy of the phase, p is pressure, V is volume, T is temperature and S is the entropy. Equation 2.2 shows the same equation written as a differential.

$$\mathrm{dG} = \mathrm{Vdp} - \mathrm{SdT} \qquad \text{(eq.2.2)}$$

The Gibbs energy of an ideal gas where pV=nRT at constant temperature (dT=0) can be expressed as shown in equation 2.3.

$$\mathrm{dG} = \mathrm{nRT}\frac{dp}{P} \quad \text{(eq.2.3)}$$

The dependence of the Gibbs energy of n moles of an ideal gas on the change in pressure from p_a to p_b can be expressed as shown below.

$$\Delta\mathrm{G} = G_a - G_b = nRT \int_{p_b}^{p_a} \frac{dp}{p} = nRT \ln\frac{p_a}{p_b} \qquad \text{(eq. 2.4)}$$

Gibbs energy is often expressed relative to the standard Gibbs energy (G^0) which is the Gibbs energy of one mole of a gas at 1 bar pressure.

$$\mathrm{G} = G^0 + RTln\left(\frac{P}{bar}\right) \quad \text{(eq. 2.5)}$$

The chemical potential (μ) can also be written as shown below, here $\mu^0$is the standard chemical potential of one mole of gas at 1 bar pressure.

$$\mu = \mu^0 + RTln\left(\frac{P}{bar}\right) \quad \text{(eq. 2.6)}$$

When considering systems with more than one chemical component an additional term is introduced to the Gibbs energy differential equation to account for their chemical potential. Here the μ_i is the chemical potential of component n_i.

$$\mathrm{dG} = \mathrm{Vdp} - \mathrm{SdT} + \sum_i \mu_i dn_i \quad \text{(eq.2.7)}$$

Given a reaction $\mathrm{Aa} + \mathrm{Bb} \rightleftharpoons \mathrm{Cc} + \mathrm{Dd}$ where A,B,C and D are the stoichiometric coefficient of species a,b,c and d which are ideal gases, the Gibbs energy of change going from reactant to product at constant temperature and volume can be written as shown below, where $\mathrm{d}\xi$ corresponds to the extent of reaction.

$$\mathrm{dG} = (C\mu_c + D\mu_d - A\mu_a - B\mu_b)\mathrm{d}\xi \qquad \text{(eq. 2.8)}$$

$$\Delta_r G' = \frac{dG}{d\xi} = (C\mu_c + D\mu_d - A\mu_a - B\mu_b) \qquad \text{(eq. 2.9)}$$

Assuming ideal gases such that equation 2.6 can be applied gives the expression below.

$$\Delta_r G' = \Delta_r G^0 + RTln\left[\frac{(\frac{P_c}{bar})^C(\frac{P_d}{bar})^D}{(\frac{P_a}{bar})^A(\frac{P_b}{bar})^B}\right] \qquad \text{(eq. 2.10)}$$

When the species are at an equilibrium such that equation 2.11 can be applied, where $\Delta_r G' = 0$.

$$\mathrm{A}\mu_a + B\mu_b = C\mu_c + D\mu_d \qquad \text{(eq. 2.11)}$$

Hence $\Delta_r G^0$ is the Gibbs energy of change at equilibrium.

To extend this thermodynamic treatment of gases onto a pure liquid, it is assumed that the liquid is in equilibrium with its vapour such that the chemical potential of the vapour equals that of the liquid.

$$\mu_i(l) = \mu_i(g) = \mu_i^0(g) + RTln(\frac{P_i}{bar}) \qquad \text{(eq. 2.12)}$$

Solutions or liquids with more than one component, are assumed to be ideal solutions which follows Raoult's law shown below.

$$\mathrm{P} = x_1 P_1^* + x_2 P_2^* \qquad \text{(eq. 2.13)}$$

Here P is the total vapour pressure, x_1 is the mole fraction of component 1 and P_1^* is the vapour pressure of pure component 1. The chemical potential of liquid species 'i' in solution is then given by equation 2.14.

$$\mu_i(soln) = [\mu_i^0(g) + RTln\left(\frac{P_i^*}{bar}\right)] + \mathrm{RTln}x_i \qquad \text{(eq. 2.14)}$$

Chemical potentials of dilute solutions of solids dissolved in the liquid phase are expressed as shown in equation 2.15. Here $\mu_i^{\emptyset}$ is the standard chemical potential for the given system, x_i is the concentration of solute in solution and γ_i is the activity coefficient. The activity coefficient accounts for non-ideal behaviour of solutes in solution which arises from solute-solute interactions.

$$\mu_i = \mu_i^{\emptyset} + RTlnx_i\gamma_i \quad \text{(eq. 2.15)}$$

The electrochemical potential ($\mu_i^{electrochemical}$) of species i is a combination of the chemical potential with electrostatic considerations, which is the work done for a charge to cross into a charged phase from vacuum.

$$\mu_i^{electrochemical} = \mu_i + z_iF(\chi + \Psi) \quad \text{(eq.2.15)}$$

Here μ_i is the chemical potential of species i, z_i is the ionic charge of species i, F is the Faraday constant χ is the electrostatic term linked to the crossing of the dipole interfacial layer, and Ψ is the electrostatic term linked to the charge of the phase. The sum of Ψ and χ is referred to as the inner potential(ϕ) of a given phase.

The electrochemical potential of an electron can be interpreted as the work required to add a mole of electrons to a metal, and is expressed as shown in equation 2.16.

$$\mu_{e-}^{electrochemical,M} = \mu_{e-}^{M} + z_{e-}F\chi^M + z_{e-}F\Psi^M = \alpha_{e-}^{M} - F\Psi^M \quad \text{(eq. 2.16)}$$

Here, μ_{e-}^{M} is the chemical potential of an electron in the metal phase (denoted by the superscript m), z is the charge of the electron (= -1).

$$\alpha_{e-}^{M} = -\Phi_{e-}^{M} \quad \text{(eq. 2.17)}$$

Φ is the work required to extract a mole of electrons from the Fermi level of an uncharged metal which is essentially the opposite of chemical potential. The Fermi level is defined as the energy of the Highest Occupied Molecular Orbital (HOMO) at 0 K. The effect of temperature on the electrochemical potential of metals is negligible.

When two metals come in contact, there is a redistribution of electrons such that the electrochemical potential of the electrons in the two metal phases equal each other.

$$\mu_{e-}^{electrochemical,M1} = \mu_{e-}^{electrochemical,M2}$$

$$\Psi^{M1} - \Psi^{M2} = -(\Phi_{e-}^{M1} - \Phi_{e-}^{M2})/F \qquad \text{(eq.2.18)}$$

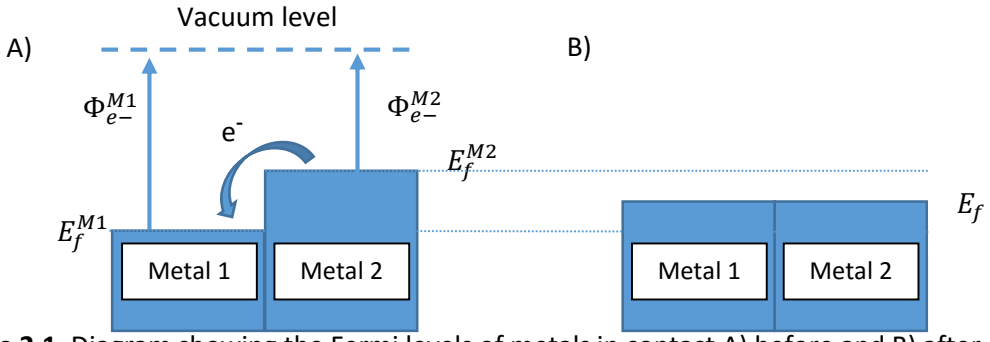

Figure 2.1. Diagram showing the Fermi levels of metals in contact A) before and B) after equilibrium.

$\Psi^{M1} - \Psi^{M2}$ is the Volta potential difference between two metals which can be calculated if the work function of the two metals are known.

Electrochemical equilibria: The Nernst Equation

In the above example, the electrochemical potential of two metals in contact became equal as a result of electron redistribution. In this section, the thermodynamic aspect of electron transfer between a given redox species dissolved in solution and a metal (a working electrode) is considered.

Equation 2.19 below shows the ferro/ferri-cyanide species in equilibrium, where subscript 'l' and 'm' denotes the phase the species is in liquid and metal respectively.

$$Fe(CN)_{6(l)}^{3-} + e_M^- \rightleftharpoons Fe(CN)_{6(l)}^{4-} \qquad \text{(eq. 2.19)}$$

At an equilibrium the electrochemical potential of species on the right hand side equals that on the left hand side.

$$\mu_{Fe(III)}^{electrochemical,s} + \mu_{e-}^{electrochemical,M} = \mu_{Fe(II)}^{electrochemical,s}$$

Substituting in equation 2.15 and rearranging yields the equation below.

$$F(\phi_M - \phi_s) = \mu_{Fe(III)} + \mu_{e-} - \mu_{Fe(II)} \qquad \text{(eq. 2.20)}$$

$$\phi_M - \phi_s = \frac{\Delta\mu^o}{F} + \frac{RT}{F}\ln\left(\frac{[Fe(CN)_6^{3-}]}{[Fe(CN)_6^{4-}]}\right) \qquad \text{(eq. 2.21)}$$

$$\Delta\mu^o = \mu_{Fe(III)}^o + \mu_{e-} - \mu_{Fe(II)}^o \qquad \text{(eq. 2.22)}$$

The equation written in its general form for a reaction involving transfer of n electrons is shown below in equation 2.23.

$$E = E_f^o + \frac{RT}{nF} ln\left(\frac{[product]^p}{[reactant]^r}\right) \qquad \text{(eq. 2.23)}$$

$$E_f^o = E^o + \frac{RT}{nF} ln\left(\frac{\gamma_{product}^p}{\gamma_{reactant}^r}\right) \qquad \text{(eq. 2.24)}$$

Here E is the applied potential ($\phi_M - \phi_s$), superscripts 'p' and 'r' are the stoichiometric coefficients of the product and reactant respectively, γ is the activity coefficient of the species in a given solvent, E^o is the standard electrode potential measured relative to the normal hydrogen electrode, and E_f^o is the formal potential which is specific to the electrolyte and solvent system utilised. Equation 2.21 is known as the Nernst equation. It relates the concentration of the potential determining redox species to the potential difference. So given an applied potential V, one can use the Nernst equation to predict the direction of electrochemical reaction but not necessarily how fast the reaction will occur, as electron transfer kinetics is a separate matter. It is important to note that these thermodynamic relations rely on the redox species being in equilibrium. Hence the issue of reversibility of an electrochemical reaction becomes significant.

For an electrochemical system at equilibrium, applying a voltage of +a volts relative to the formal potential of the redox species causes oxidation of A to B as shown below. The system is considered chemically reversible if applying a voltage of –a volts (again relative to the formal potential) results in a reversal of the oxidation i.e. reforming A without forming any other products.

$$\mathrm{A} - e^- \rightleftharpoons \mathrm{B} \qquad \text{(eq. 2.25)}$$

Thermodynamic reversibility is when a small reversal in driving force (which in the case above is the applied potential) causes the process to reverse its direction i.e. the system is always at an equilibrium. Most electrochemical processes occur at finite rates, hence it is not practical to work under thermodynamically reversible conditions. Experimental electrochemists rely on the Nernst equation (eq.2.21) to judge whether an electrochemical system is reversible. Often a system that is perturbed at a given rate can be approximated by equations that assume equilibrium conditions provided that the kinetics is fast enough such that response to the perturbation is rapid.

Reference Electrode

Expressing standard electrode potentials relative to a single given reference redox system such as the normal hydrogen electrode is a convenient method of comparing the relative ease of oxidation or reductions. Common reference systems used to measure the redox potential of a given species are outlined below. (hydrogen, calomel, silver, ferrocene with potentials relative to the Normal Hydrogen Electrode).

$H^+ + 2e^- \rightleftharpoons 0.5H_2$ at a platinum electrode; the Normal Hydrogen electrode (NHE)

$0.5Hg_2Cl_{2(s)} + e^- \rightleftharpoons 2Hg_{(l)} + Cl^-_{(aq)}$; Saturated Calomel electrode (SCE) 0.242 V vs. NHE

$\mathrm{AgCl} + e^- \rightleftharpoons Ag_{(s)} + Cl^-_{(aq)}$; in saturated Cl^- solution, 0.199 V vs. NHE.

$Cp_2Fe^+ + e^-_{(m)} \rightleftharpoons Cp_2Fe$; potential dependent on solvent composition.

The reference system is maintained at a constant electrochemical potential by limiting the current to very low values (ca. picoamps), such that the concentration of the potential determining species is essentially unchanged. Having a reference electrochemical potential that is stable and constant becomes important when studying electrode kinetics as the potential difference driving the electron transfer process must be accurately measured. Typical electrochemical measurements are recorded utilizing a three electrode set up; a working electrode whose potential is set with respect to a chosen reference electrode and a counter electrode which draws most of the current.

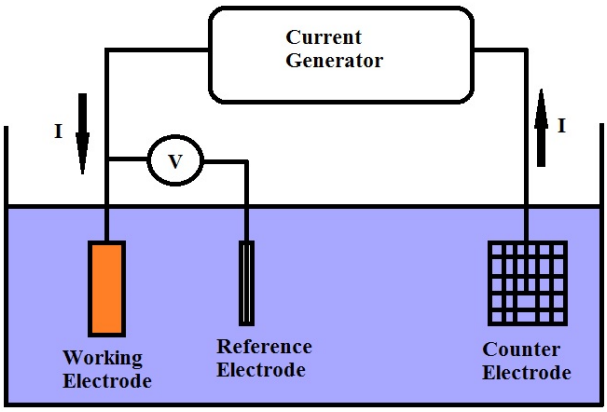

Figure 2.2. A simplified diagram of a three-electrode cell. V is the voltmeter, and I is the current.

The exception to this is the ferrocene/ferrocenium reference redox couple which are dissolved in non-aqueous media together with the redox species of interest. This reference system is usually utilized for studying reactions sensitive to the presence of water which rules out the use of silver/silver chloride and the calomel reference electrode. Here there are only two electrodes present which is the working electrode and the counter electrode; the counter electrode also acts as the reference electrode in this case. The chemical composition of the electrolyte surrounding the counter/reference electrode will change as a result of electron transfer, resulting in the shifting of the reference electrochemical potential. As a result the onset of oxidation and reduction of a given species will appear to shift along a potential axis over time. The shift in reference potential can be measured by tracking the shift of the redox potential of ferrocene/ferrocenium. Irrespective of the numerical value of the potential (V) at which electron transfer occurs, it is reported with respect to the redox potential of the ferrocene/ferrocenium couple which is defined as the zero point.

This two electrode set-up can also be utilized in set-ups where the total current passed through the system is very small such that the chemical potential of the electrolyte surrounding the counter/reference electrode is not changed significantly. A silver wire can be used in this case to form a pseudo-reference system with trace amounts of chloride ions present in solution forming AgCl. As the reference potential does not shift significantly, the set-up can be utilized without having to use a separate reference redox system like ferrocene/ferrocenium.

The counter electrode is set up such that the same current is forced to flow through it as the working electrode. This current is controlled by the electronics of the potentiostat which applies the necessary

potential to drive the required current. The potentiostat utilized for most voltammetric measurements presented in the thesis is a microAutolab series III (Metrohm, UK) that has a compliance voltage of +-12V, but there are commercially available potentiostats with a compliance voltage upto +-100V. It is clear from this discussion that considerations for energetic efficiencies of electrochemical processes requires a holistic approach where processes occurring at the counter electrode are also accounted for.

2.1.2 Kinetics [1,2,3]

Marcus theory of Electron transfer

The potential energy of a redox species present in a solution above 0 K is affected by various factors such as the chemical interaction between it and the solvent molecules, bond stretching, bending, rotating, and vibrating due to kinetic energy, and in some cases excitation due to electromagnetic radiation. Hence the chemical potential energy of the species is not discrete but is distributed, and can be expressed using a simplified energy curve as shown below which models one-dimensional bond vibration as a harmonic oscillator.

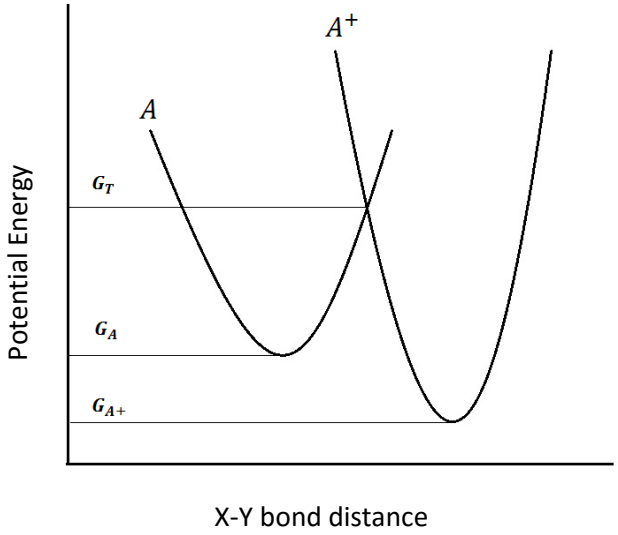

Figure 2.3. Energy profile diagram of species A and A^+ based on a simple harmonic oscillator model. G_A is the potential energy of A in the ground state, G_T is the potential energy of the transition state, and G_{A+} is the potential energy of the product.

The second curve to the right shows how the potential energy shifts as a result of electron transfer. The Frank-Condon Principle tells us that electron tunnelling is fast occurring in around 10^{-15} seconds, which is a hundred times faster than the timeframe of molecular vibration. The molecule is essentially stationary when electron transfer occurs, so transitions from A to B can only occur through vertical lines on the diagram. The only point in which transition from A to B can occur while conserving energy is the point at which the two potential energy curves overlap. The potential energy of the transition point defines the activation energy required for electron transfer to occur. The activation energy for electron transfer will be the transition point energy minus the ground state energy of A ($E_a = G_T - G_A$).

Using this simplified illustration, one can see that the activation energy required for electron transfer will be lower when the two potential energy curves are shifted closer together, which corresponds to a situation where electron transfer results in a small change in molecular conformation. This interpretation can be expanded to state that the activation energy required for electron transfer is lower for transitions that result in a small change in molecular structure, electronic arrangement and solvent rearrangement. Such transformations are likely to have fast electron transfer kinetics. Given a well-defined harmonic oscillator model of a redox species it is possible to quantitatively predict the activation energy, with good correlation to experimentally observed kinetics [4]. Such approaches works best for symmetrical species where consideration of one reaction coordinate can be reasonably approximated to represent the entire molecule. A more general approach to kinetics is described in the section below.

Butler-Volmer Kinetics

A generic redox species in equilibrium and its energy profile is shown below in equation 2.26 and Figure 2.4; where x and y are the charges on species a and b, and k_c and k_a are the reaction rate constants.

$$a^z + e^- \underset{k_a}{\overset{k_c}{\rightleftarrows}} b^{(z-1)} \qquad \text{(eq. 2.26)}$$

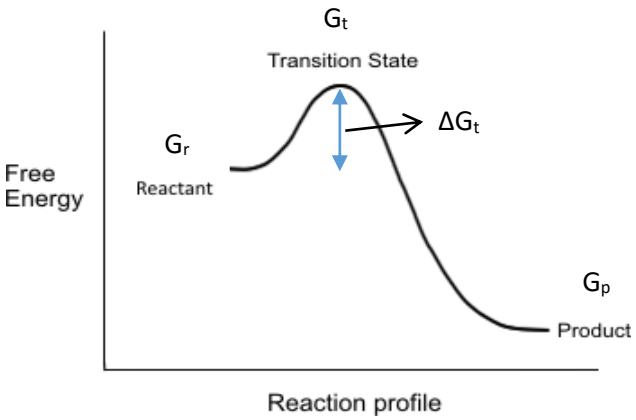

Figure 2.4. A reaction profile of an exergonic reaction

The chemical kinetics can be expressed using transition state theory which is expressed below in equation 2.27.

$$k_c = A_c exp\left(\frac{-\Delta G_t}{RT}\right) \qquad \text{(eq. 2.27)}$$

Where A_c is a constant and ΔG^t is the activation energy for the reaction.

$$\Delta G_t = G_t - G_r \qquad \text{(eq. 2.28)}$$

Substituting $\mathrm{G} = \text{constant} + \mathrm{nF}\phi_s$ into the above yields the equation below.

$$k_c = k_c^0 exp\left(\frac{-\alpha F(E-E_f^0)}{RT}\right) \qquad \text{(eq. 2.29)}$$

α is the transfer coefficient which gives information on the transition state and is usually assumed to be 0.5. F is the Faraday constant, $E - E_f^0$ is the overpotential experienced by the redox species, R is the ideal gas constant and T is temperature. In the case where the rate of mass transport is high compared to the rate of charge transfer, the kinetics of charge transfer is said to be electrochemically irreversible or quasi-reversible. The net flux (j given in units of $molcm^{-2}s^{-1}$) of electroactive species towards the electrode can be written as shown below. For an electrochemically irreversible case, [a] and [b] represent the surface concentration of species a and b on the electrode surface, i.e. the mass transport of both species towards the electrode is assumed to be infinitely high.

$j = k_c[a] - k_a[b]$ (eq. 2.30)

The current that results is expressed by equation 2.31.

$I = FAj$ (eq. 2.31)

Where I is the current (Cs^{-1}), F is the Faraday constant and A is the electrode area (cm^2). Finally substituting equation 2.29 into 2.30 yields the Butler-Volmer equation.

$$j = k_c^0 exp\left(\frac{-\alpha F(E-E_f^0)}{RT}\right)[a] - k_a^0 exp\left(\frac{(\alpha-1)F(E-E_f^0)}{RT}\right)[b] \quad \text{(eq. 2.32)}$$

As j is directly proportional to the current, we can conclude that the current increases exponentially with the potential difference applied provided that the concentration of the species remains constant.

Tafel plot

Taking the Butler-Volmer expression, one can see that either of the two exponential terms will dominate depending on which potential is applied. At reducing potentials the Butler-Volmer expression simplifies to equation 2.33 while at oxidative potentials the expression simplifies to equation 2.34.

$$j = k_c^0 exp\left(\frac{-\alpha F(E-E_f^0)}{RT}\right)[a] \quad \text{(eq. 2.33)}$$

$$j = k_a^0 exp\left(\frac{(\alpha-1)F(E-E_f^0)}{RT}\right)[b] \quad \text{(eq. 2.34)}$$

As j is directly proportional to the current (I), taking the natural log of both sides of the equation yields the expressions below.

$$\ln|I_{red}| = \frac{-\alpha FE}{RT} + constant \quad \text{(eq 2.35)}$$

$$\ln|I_{ox}| = \frac{(\alpha-1)FE}{RT} + constant \quad \text{(eq. 2.36)}$$

Plotting the natural log of current versus potential is what is known as a Tafel plot. The linear plot should have a constant gradient from which the transfer coefficient α can be found. The transfer coefficient should range from a value of 0 to 1, and is usually close to 0.5.

Tafel plots can be particularly useful in analysing multistep electron transfer processes such as the one shown below.

$a^z + e^- \rightleftarrows b^{(z-1)}$ (eq. 2.37)

$b^{(z-1)} + e^- \rightleftarrows c^{(z-2)}$ (eq. 2.38)

Assuming that the current is limited purely by charge transfer kinetics (by inducing high mass transport rates through hydrodynamic methods), either of the two electron transfer processes can be rate limiting. When the first electron transfer step is rate limiting, a transfer coefficient of around 0.5 is expected. However in the case where the second electron transfer step is the limiting process (i.e. the first electron transfer step is fast and is at an equilibrium), the current will follow the expression given below. So the Tafel slope will yield a value of around 1.5, clearly distinguishing it from the first limiting step.

$$\ln|I_{red}| = \frac{-\alpha FE}{RT} + constant \quad \text{(eq. 2.39)}$$

2.1.3 Mass Transport [1,2,3]

There are three main components that contribute towards mass transport (or the flux, J), as expressed below by the Nernst-Planck equation for species j.

$$J_j(x) = -D_j \frac{\partial C_j(x)}{\partial x} - \frac{z_j F}{RT} D_j C_j \frac{\partial \phi(x)}{\partial x} + C_j \upsilon(x) \quad \text{(eq. 2.40)}$$

D is the diffusion coefficient, c is concentration, x is distance, z is ionic charge of species j, F is the Faraday constant, R is the ideal gas constant, T is temperature, $\frac{\partial \phi}{\partial x}$ is the potential difference, and υ is the solution velocity at point x towards the electrode surface. The first term in the equation is an expression for diffusion, the second term is the expression for migration of charged species and the third term is for convection.

Migration

Migration is the movement of charged species induced by a potential gradient. Interfaces of electron transfer builds up charge locally as it facilitates electron transfer, which results in migration of ions from electrostatic attraction/repulsion. Given a system undergoing electrolysis as shown below, the net contribution toward mass transport of redox species towards the electrode will be a combination of migration and diffusion (provided care is taken not to induce convection).

In order to simplify the analysis and interpretation of current measurements, effects of migration and diffusion need to be considered separately. Addition of excess inert electrolyte salts to the solution serves to carry most of the charge resulting from electron transfer. The electrolyte salt is redox inactive within the potential window of measurement. The proportion of charge carried is related to the relative concentration of each species, the inert electrolyte is usually added in excess of 100 times the amount of redox species present. So the current that results from the flux of redox active species towards the electrode surface can be approximated to be purely diffusion limited (provided care is taken not to induce convection).

Diffusion

Diffusion is a passive process of redistribution of matter in a given media from a polarised towards a homogenous distribution as a result of random motion of matter. The rate of diffusion will be faster the more polarised the distribution of matter, this is expressed in Fick's first law (written for a 1-dimensional case) shown below.

$$-J_a(x,t) = D_0 \frac{\partial C_a(x,t)}{\partial x} \qquad \text{(eq. 2.41)}$$

Where J is the flux of species a, at distance x, time t, D is the diffusion coefficient, and c is the concentration.

Fick's second law (written for a 1-dimensional case) expresses the change in concentration of species a with time.

$$\frac{\partial C_a}{\partial t} = D_a \left(\frac{\partial^2 C_a(x,t)}{\partial x^2}\right) \qquad \text{(eq. 2.42)}$$

Fick's second law is a differential equation which can be solved with the following boundary conditions; when t = 0, c = c* for all x where c* is the bulk concentration, when t > 0, x = 0, c = 0 and when t > 0, x $\longrightarrow \infty$, c = c*. The precise derivation can be found in literature [2]; the result is what is known as the Cottrell equation.

$$I = \frac{nFA\sqrt{D}c^*}{\sqrt{\pi t}} \qquad \text{(eq. 2.43)}$$

The Cottrell equations states that in a mass transport limited case, the flux of redox species A (which is proportional to the current) decreases as a function of $t^{-0.5}$. It applies to electrodes with relatively large planar geometries that can be approximated by 1-dimensional mass transport. Figure 2.5A below shows how the concentration gradient becomes shallower as species A becomes depleted from the surface of the electrode. A shallow concentration gradient results in slower diffusional mass transport towards the electrode surface. This is why the current at a fixed oxidizing/reducing potential will decay as a function of time as shown in Figure 2.6B. As the current-time plot on the right shows, the current decay pattern is identical for species with different diffusion coefficients. But species that diffuse faster (higher diffusion coefficient) gives higher flux hence higher currents.

(A)

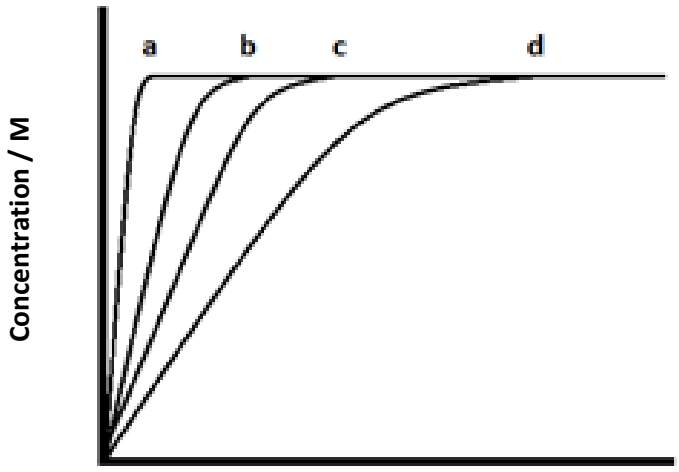

(B)

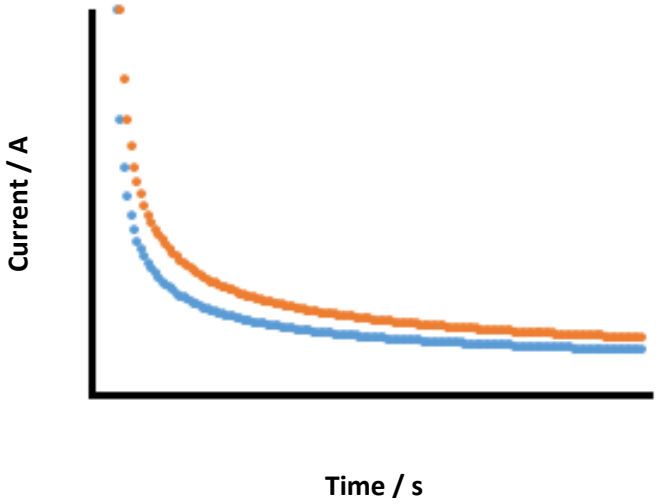

Figure 2.5. (A) Concentration profiles shown as a function of perpendicular distant away from the electrode surface at a) t=0.001, b) t=0.005, c) t=0.01 and d) t=0.05 seconds. (B) Current versus time plot showing a decay in current in a mass transport limited case assuming 1D semi-infinite diffusion. Top graph: D= 1×10^{-9} m^2s^{-1} and bottom graph: D= 5×10^{-10} m^2s^{-1}.

As $t \longrightarrow \infty$ the Cottrell current predicts that the current tends to zero, but this is never realised experimentally. There is a point where this diffusion only model breaks down, and effects of natural convection comes into play. The rigidity of the electrode results in a stagnant layer of liquid of a finite thickness, if the timeframe of measurement is set such that the concentration of redox active species depletes within this stagnant layer, there will be effects of convection visible in the experimental data. This natural convection is a result of changes in densities brought about from electrochemical transformations. In order to interpret data with diffusion only models, timeframes of measurements must be set such that the diffusion layer does not grow past this stagnant layer. Diffusion layer thicknesses typically range from 10-100μm.

There are situations where the diffusion layer thickness is manipulated by intentionally added convection. There are several refined hydrodynamic techniques which allows the diffusion layer thickness to be controlled accurately, such as the rotating disc electrode technique and electrochemical flow cells. A broad overview on hydrodynamic electrochemical techniques will be discussed in section 2.2.4.

2.2 Electrochemical Techniques

2.2.1 Chronoamperometry [1,2,3,4]

Redox species in solution

As briefly discussed in section 2.1.3, measuring the current as a function of time at a fixed potential (known as chronoamperometry) can reveal information related to the mass transport properties of the electro-analyte. Given a reversible redox species freely diffusing in solution with fast electron transfer kinetics as shown below, that oxidizes at a potential E_{ox}, an overpotential is applied such that the limiting factor in the oxidation process becomes the mass transport of species 'a' towards the electrode.

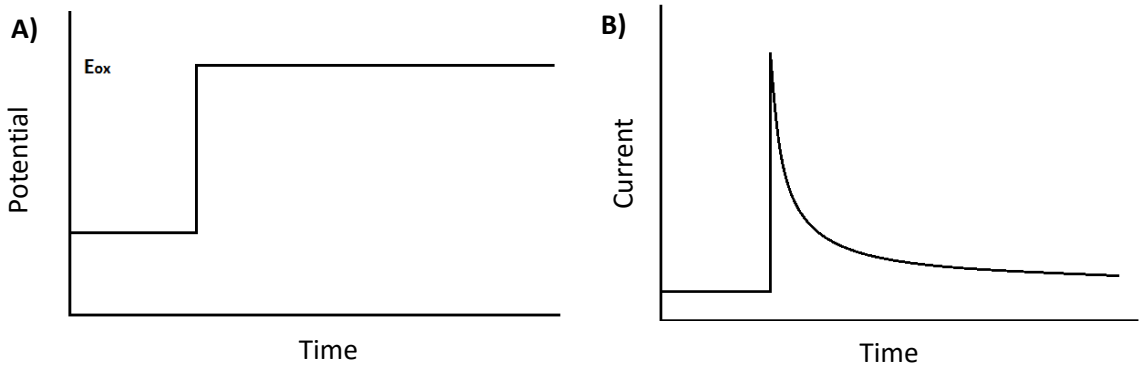

Figure 2.6. A) Time vs. potential graph showing the potential step. B) Time vs. current graph showing the decay in current as a function of time at a fixed potential.

It was shown in section 2.1.3 that a 1D mass transport limiting case (planar macroelectrodes) can be modelled using the Cottrell equation (eq. 2.44), shown below is the current plotted as a function of $t^{-0.5}$.

$$\mathrm{I} = \frac{nFA\sqrt{D}c^*}{\sqrt{\pi t}} \qquad \text{(eq. 2.44)}$$

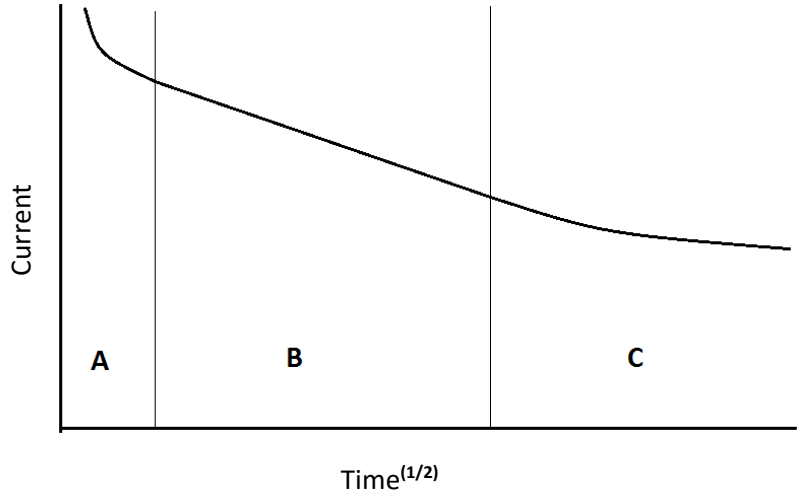

Figure 2.7. Square root of time vs. current. A) Significant contributions from double layer charging, B) Cottrell decay region and C) Effects of natural convection.

At short time frames of 10s of milliseconds, there are significant contributions from charging of the electrochemical interface [2] that results in currents that is not limited by mass transport hence does not follow a Cottrell decay pattern. Such charging processes are known as non-faradaic processes; the amount of charge passed is not proportional to the amount of electron transfer reactions initiated. This will be discussed in the next section 2.2.2. It follows that faradaic processes are electron transfer reactions that yields reduction/oxidation products proportional to the amount of electric charge passed through the system (this is known as Faraday's law). It is important to remove the first 10-20ms of data points when attempting to run simulations to fit chemical parameters (such as the diffusion coefficient, concentration or electrode area) to experimental results so that only the faradaic component of current is fitted. At longer times the current does not decay as a function of $t^{-0.5}$, this is when the onset of natural convection or 'edge effects' breaks the diffusion only model.

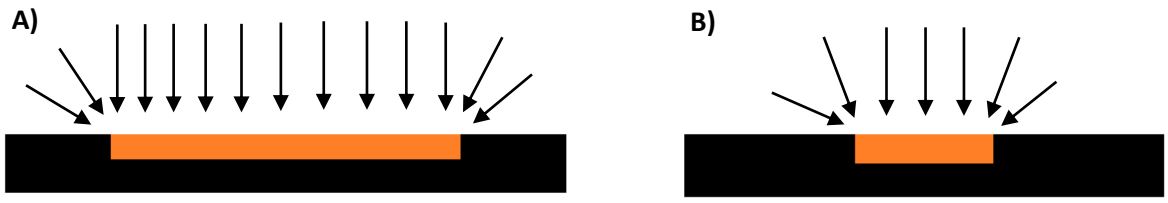

Figure 2.8. Illustration of A) macrodisc and B) microdisc electrode with planar diffusion (1D) and edge diffusion (2D). Relative contribution of 2D diffusion is more significant for the microdisc electrode.

Use of micro-disc electrodes for chronoamperometric measurement requires a different treatment as the mode of diffusion cannot be accurately approximated by just considering 1D mass transport. The circumference of the disc, or the edge experiences mass transport from two dimensions as shown above in figure 2.8, and so the rate of transport towards the edges are greater. It was found that disc electrodes with diameters smaller than 25μm start deviating significantly from the 1D model. Steady state currents that results from micro-disc electrodes with a diameter less than 25μm follows the expression shown below [5], where n is the number of electrons transferred per molecule, F is the Faraday constant, D is the diffusion coefficient, c is the concentration and r is the radius of the micro-disc electrode. Computational simulation packages that are able to simulate 2D diffusion models may be used to analyse transient currents.

$$I = 4nFDcr \qquad \text{(eq. 2.45)}$$

Redox species immobilized in an insulating film on the electrode surface

Redox species immobilized in an insulating film (e.g. polymers) on the electrode surface propagates electrochemical charge by a hopping mechanism where the electroactive species self-mediates the reduction and oxidation throughout the bulk of the film. Electrochemical charge hopping which involves the hopping of electrons or holes coupled to the transport of ions (that balance charge), have successfully been modelled as a diffusive process [6]. The rate of electrochemical charge propagation can be measured through chronoamperometric measurements. The model assumes that the diffusion coefficient and the activity of the ion is constant throughout the film, though it has been found that presence of heterogenous regions in the film that may breach that condition does not break the model as long as the dimensions of the heterogenous regions are relatively small compared to the overall film thickness [7]. Oglesby modelled charge propagation through such films as a Cottrell current limited by exhaustion of electroactive species in a film of a finite film thickness [8].

$$I_{(l,t)} = \frac{nFA\sqrt{D}c}{\sqrt{\pi t}} \times \sum_{k=0}^{\infty}(-1)^k \left[exp\left(\frac{-k^2l^2}{Dt}\right) - exp\left(\frac{-(k+1)^2l^2}{Dt}\right)\right] \qquad \text{(eq. 2.46)}$$

Here I is the current, n is the number of electrons transferred per molecule, A is the electrode area, D is the diffusion coefficient, c is the concentration, t is time, k are integers going from 0 to infinity, and l is the film thickness.

2.2.2 Cyclic Voltammetry [1,2,3,4]

Cyclic voltammetry measures the current as the potential is varied at a linear rate (scan rate, ν) between two specified potentials. The figure below graphically illustrates this point; the gradient of the lines will give the scan rate ν in units of Vs^{-1}. Electronic potentiostats will increase the potential in a series a small steps, this is known as stair-case voltammetry.

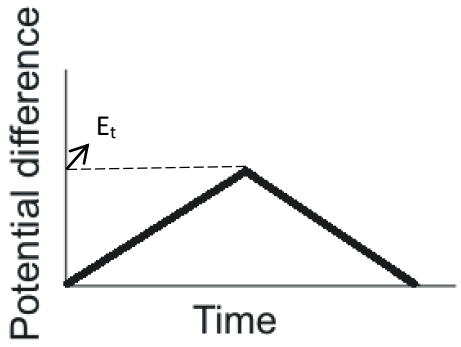

Figure 2.9. Potential E is increased linearly with time until E_t where the potential is cycled back again to its starting value.

The current response of an electrode submerged in a liquid in the absence of redox active species results in capacitive currents. A capacitor is a device or an object that will store charge when a current is applied, and then release the charge when the charging current is stopped. The electrochemical interface between a metal electrode surface and the electrolyte solution behaves like a capacitor. As a potential is applied the electrode becomes charged and attracts a single layer of charged counter ions that adsorbs onto the surface, this layer is called the Inner Helmholtz plane (IHP), see below in figure 2.10. Due to the adsorbed ions the closest distance non-adsorbed ions can approach the electrode is the radius of non-adsorbed ion plus the diameter of the solvent molecule, this distance is called the Outer Helmholtz plane (OHP). The separation of charge between the metal electrode surface and ions in solution is the basis on which the capacitive behaviour of electrochemical interfaces is rationalized. Ions in the OHP interacts with the charged metal via long-range electrostatic forces, and is distributed not as a single 2-dimensional layer but a 3-dimensional one due to thermal agitation. This layer is known as the diffuse layer, and its thickness depends on the concentration of the electrolyte in solution and also the applied potential.

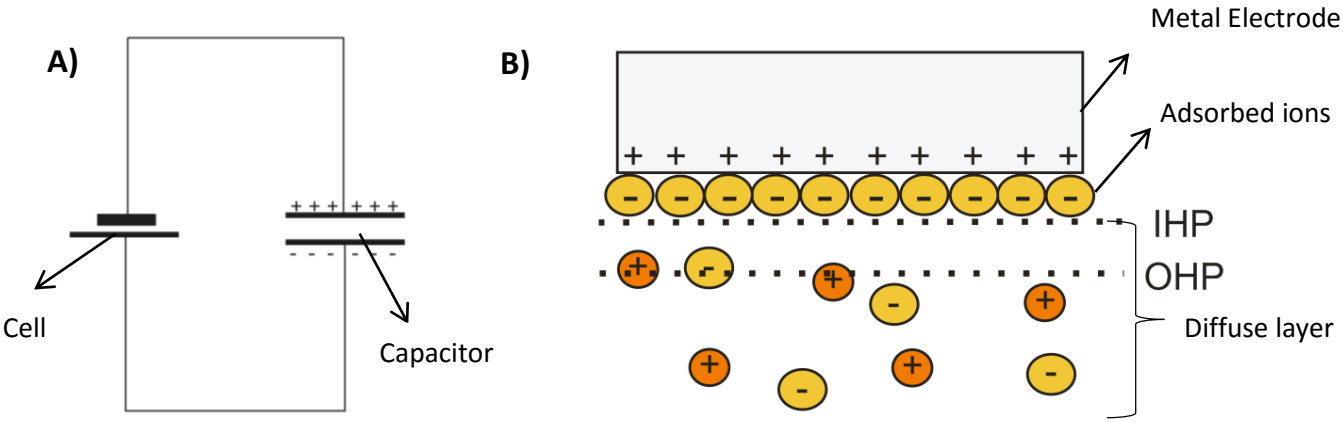

Figure 2.10. A) Circuit diagram of a capacitor connected to a source. B) Diagram of the double layer charging model; the electrochemical interface behaves like a capacitor. Note the coloured spheres represents ions surrounded by solvation molecules.

Faradaic processes are electron transfer processes occurring for redox active species in the diffuse layer, where the amount of charge transferred is equal to the amount of chemical species reduced/oxidized. The potential exerted by the metal electrode onto the electrolyte solution decreases as a function of distance (see Fig. 2.11). Hence the redox active species approaching this double layer will experience a lower potential difference than the total potential difference between the metal electrode and the solution. Having high concentrations of inert supporting electrolyte salts in solution compacts the diffuse layer, such that the potential gradient is relatively steep. This acts to minimize the loss in potential difference (or potential drop) experienced by redox active species diffusing close to the OHP. Below is a brief outline of how this manifests itself on a cyclic voltammogram.

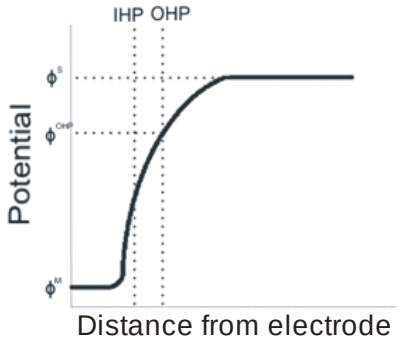

Figure 2.11. Change in potential with distance away from the electrode surface. The potential difference experienced by the redox active species on the OHP will be less than ($\phi^M - \phi^S$). ϕ^M is the potential of the electrode and ϕ^S is the potential of the electrolyte solution.

The potential (E) being sweeped at a scan rate (ν) for a duration of t seconds can be expressed as equation 2.47.

$E = \nu t$ (eq. 2.47)

The electrode not only behaves as a capacitor but also a resistor; this is expressed in the equation below where the former term represents the resistor element and the latter the capacitor element.

$E = iR_s + q/C_d$

$\nu t = iR_s + q/C_d$ (eq. 2.48)

Where i is the current, R is the resistance, q is charge and C is capacitance. Integrating with boundary conditions of q = 0 when t = 0 yields equation 2.49.

$i = \nu C_d[1 - \exp(-t/R_sC_d)]$ (eq. 2.49)

Following the equation, plotting current as a function of time as it is cycled between two potentials at a fixed scan rate of ν yields the patterns shown below.

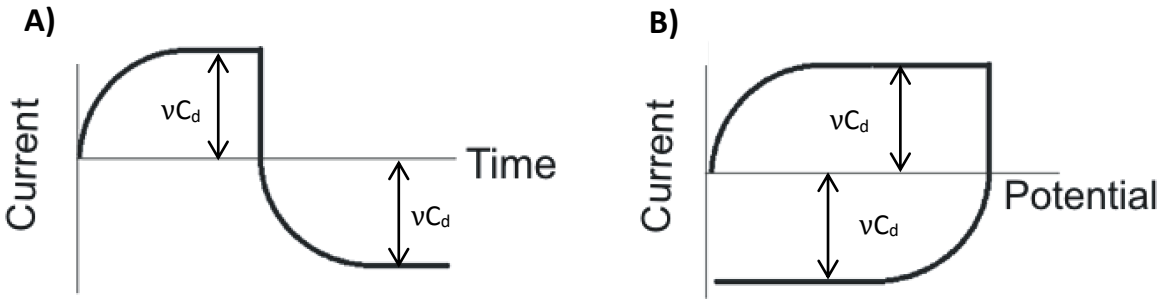

Figure 2.12. A) Change in current with time when E=νt (see figure 2.8). Current reaches a maximum value of νC_d before changing signs as the potential is cycled back. B) Change in current with potential; a cyclic voltammogram with no redox active species shows only capacitive behaviour.

Figure 2.13 below shows electrochemically reversible faradaic redox peaks which by definition has fast electrode kinetics. Faradaic currents are observed once a potential greater than the formal potential ($E^{0\prime}$) is applied. The current initially increases exponentially as a function of applied potential as predicted by the Nernst equation, until it reaches a peak current. From this point on the rate of substrate conversion exceeds the rate at which it can be replenished by diffusion, and so the current changes to a mass transport limited case and exhibits a Cottrell decay where the current decays as a function of $t^{-0.5}$.

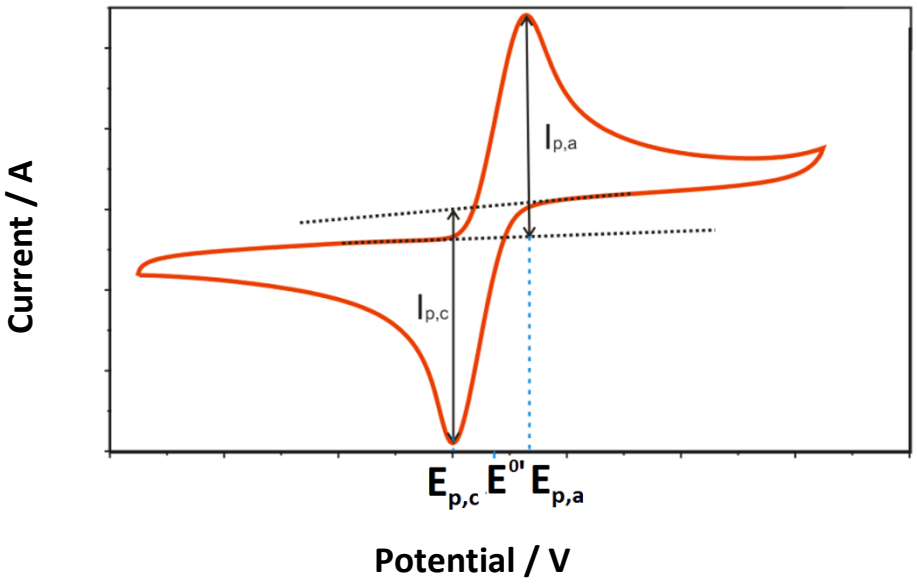

Figure 2.13. A cyclic voltammogram of a reversible redox reaction.

Peak current: Diffusion limited case

The peak cathodic/anodic current can be given by the Randles-Sevcik expressions shown below. Peak currents for an electrochemically reversible system is given below in equation 2.50.

$I_p = -0.445 n^{3/2} F A c_{bulk} \sqrt{FvD/RT}$ (eq. 2.50)

Here n is the number of electrons transferred per redox molecule, F is the Faraday constant, A is the electrode area, c_{bulk} is the bulk concentration of electrolyte, v is the scan rate, D is the diffusion coefficient, R is the ideal gas constant and T is the temperature. Peak current is a function of the square root of scan rate v. This expression is useful as it can be used to estimate the diffusion coefficient from a simple experiment. This can be achieved by plotting the peak current versus the square root of scan rate, a linear plot would be indicative of a diffusion based process.

When the system departs from electrochemical reversibility and becomes irreversible the peak current expression must be adjusted and is shown below.

$I_p = -0.496 \sqrt{\alpha}\ n^{3/2} F A c_{bulk} \sqrt{FvD/RT}$ (eq. 2.51)

α is the transfer coefficient, usually approximated to be around 0.5. Hence the peak current of an electrochemically irreversible system is expected to be lower than that of a reversible system.

Peak currents: thermodynamically limited case

Given a redox species adsorbed onto the electrode surface, which shows reversible electrochemistry and has fast electron transfer kinetics, the limiting factor will be the applied potential. The peak current (i_p) in this case is expressed by equation 2.52.

$$i_p = \frac{n^2F^2vVc}{4RT} \qquad \text{(eq. 2.52)}$$

The voltammetry of surface adsorbed species can be distinguished from species diffusing in solution by plotting the peak current as a function of scan rate. Adsorbed species will exhibit a linear increase in current as a function of scan rate.

Measuring reversibility

The peak cathodic and anodic potential (E_{pc} and E_{pa}) of a reversible system in solution undergoing redox at a macro-electrode (planar diffusion) is given by the two expressions below.

$$E_{pc} = E^{0\prime} + 1.109\frac{RT}{nF} - \frac{RT}{nF}\ln\frac{D_{ox}^{1/2}}{D_{red}^{1/2}} \qquad \text{(eq. 2.53)}$$

$$E_{pa} = E^{0\prime} - 1.109\frac{RT}{nF} - \frac{RT}{nF}\ln\frac{D_{ox}^{1/2}}{D_{red}^{1/2}} \qquad \text{(eq. 2.54)}$$

Where $E^{0\prime}$ is the formal potential of the redox system. A good way of testing reversibility is by measuring the peak potential separation. Following the above equations, when n=1 and T=298.15K.

$$E_{pc} - E_{pa} = 2(1.109\ \frac{RT}{nF}) \approx \frac{57}{n}mV \qquad \text{(eq. 2.55)}$$

What is also noteworthy about the expression above (eq. 2.54) is that the peak potentials are a function of the ratio of the oxidized and reduced species' diffusion coefficients. This is illustrated in the simulated cyclic voltammograms below (fig. 2.14). When $D_{ox} \approx D_{red}$ the $(E_{pc} - E_{pa})/2$ can be used to approximate the formal potential ($E^{o\prime}$). But this may not always be the case so the centre is commonly refered to as the mid-point potential.

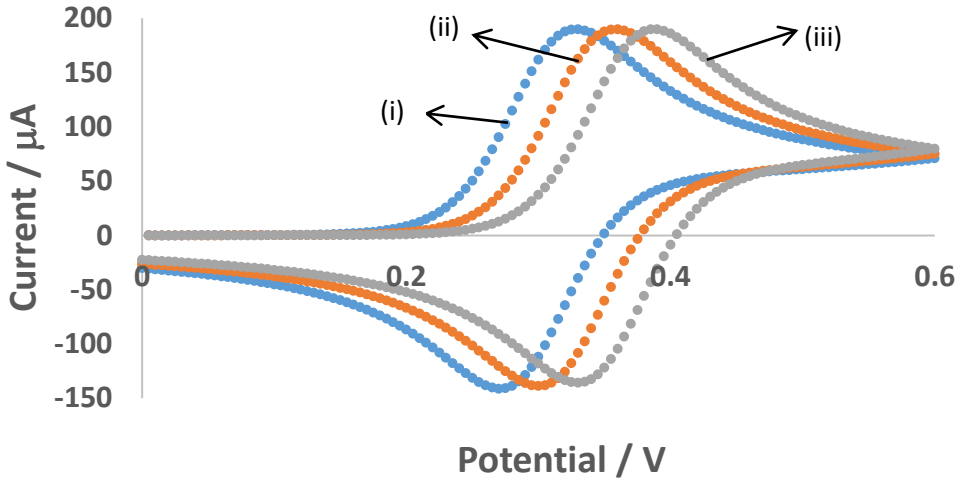

Figure 2.14. Simulated cyclic voltammograms at 0.1 Vs^{-1}; A=1cm^2, n=1, k_e=10000 cms^{-1}, c=0.001 M and D_{red} = 5×10^{-10} m^2s^{-1}. (i) D_{ox} = 5×10^{-10} m^2s^{-1}, (ii) D_{ox} = 5×10^{-11} m^2s^{-1} and (iii) D_{ox} = 5×10^{-12} m^2s^{-1}.

Electrochemical reversibility is defined as a situation where the electron transfer kinetics is rapid relative to the rate of mass transport of redox active species. The effect of reducing the electron transfer kinetics (k_e) while maintaining a constant diffusion coefficient (D) is illustrated below in figure 2.15. Whereas the mid-point potential remains similar as the ratio of diffusion coefficients of reduced and oxidized species remain the same, the gap between the peak currents increase as the ratio of k_e:D increases (becomes more irreversible).

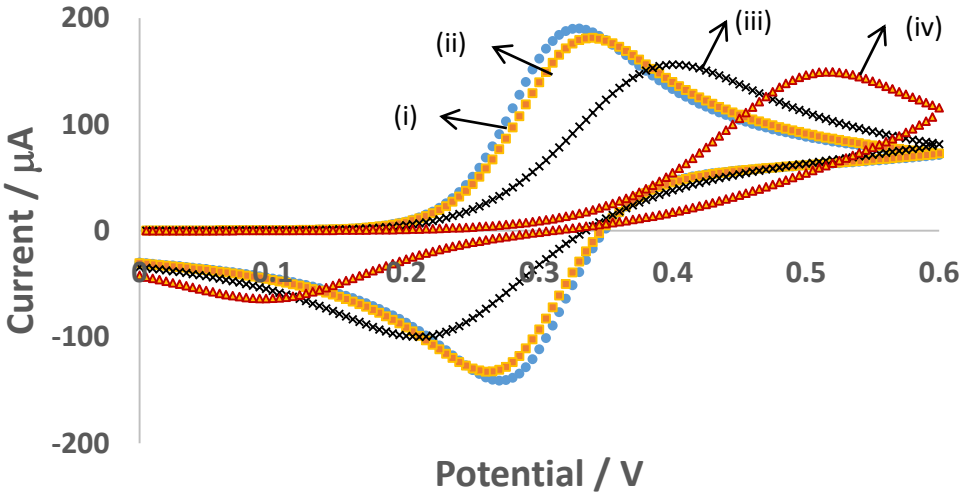

Figure 2.15. A cyclic voltammograms of quasi-reversible redox reaction from simulation using DigiElch softare; scan rate at 100 mVs^{-1}, D=5×$10^{-6}$$cm^2s^{-1}$ (both reduced and oxidized species), Electrode area=1 cm^2, (i) k_c^0=10000 cms^{-1} (i) k_c^0 = 0.01 cms^{-1} (i) Blue, k_c^0=0.001 cms^{-1} (i) k_c^0=0.0001 cms^{-1}

2.2.3 Square Wave Voltammetry [1,2,3,4]

Square wave voltammetry can be seen as a combination of chronoamperometry and cyclic voltammetry; the technique involves measuring the change in current as a function of a series of potential steps that are held for a longer period than it is for cyclic voltammetry (see fig. 2.16).

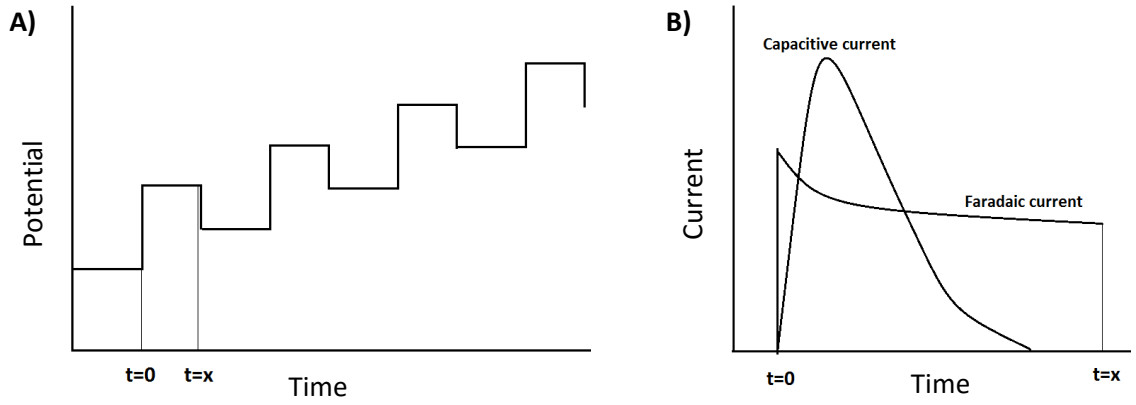

Figure 2.16. A) Square wave potential applied as a function of time, where t=x is where the sample current is measured. B) Current as a function of time; sample is taken at t=x where contributions from capacitive current is relatively small.

The aim of this method is to improve the resolution of the faradaic current versus the capacitive current, and this is achieved by carefully choosing the sample time such that the contribution of the capacitance towards the total current is small. In section 2.2.1; chronoamperometry, the Cottrell decay of the faradaic current was discussed along with the need to discard the first few milliseconds of the current versus time curve due to the effects of capacitive charging. The potential step in square wave voltammetry is selected to be long enough to outlast the effects capacitive charging. Square wave voltammetry is a good method to measure faradaic currents of species in low concentrations (10^{-8} M), where it offers superior resolution compared to conventional stair-case voltammetry. It is also used when the redox potential of a given species need to be known accurately (for example when determining the Gibb's energy of ion transfer across a liquid-liquid interface) as capacitance can in certain situations skew the position of the peak potential.

2.2.4 Hydrodynamic Techniques

Hydrodynamic techniques involve increasing mass transport of redox active species towards the electrode surface by intentionally induced convection. There are too many methods through which convection can be introduced to a liquid based electrochemical system; it was found by a recently study that unintentional factors such as temperature gradients in the lab or having a flow of gas blowing over the electrolyte surface can induce experiment altering convective effects [9]. The methods of interest are ones that can induce convection in a uniform manner that can be controlled with relative ease, and allows quantitative analysis of the increased mass transport. Such methods offer much improved resolution of faradaic processes that are mass-transport controlled over capacitance.

It is also convenient if the liquid media of the electrochemical system behave as a Newtonian liquid, which means that the liquid's resistance to flow (viscosity) is a constant that does not vary depending on the stress imparted onto it, such that a solution stirred with force y flowing at a velocity of i, will flow at a velocity of (5 x i) when a force of (5 x y) is applied. The effect of increased convective mass transfer can be observed as long as the electron transfer kinetics is faster than the rate of mass transport. At sufficient high mass-transport rates, the kinetically limited current can be found.

Rotating disc electrode

The rotating disc electrode is a mechanical set-up which induces convection in a liquid based electrochemical system by uni-directional rotation of a symmetric cylindrical electrode that is centred on the centre of rotation. It is the most common intentionally utilized hydrodynamic technique, for which a quantitative convection model has been developed and successfully applied.

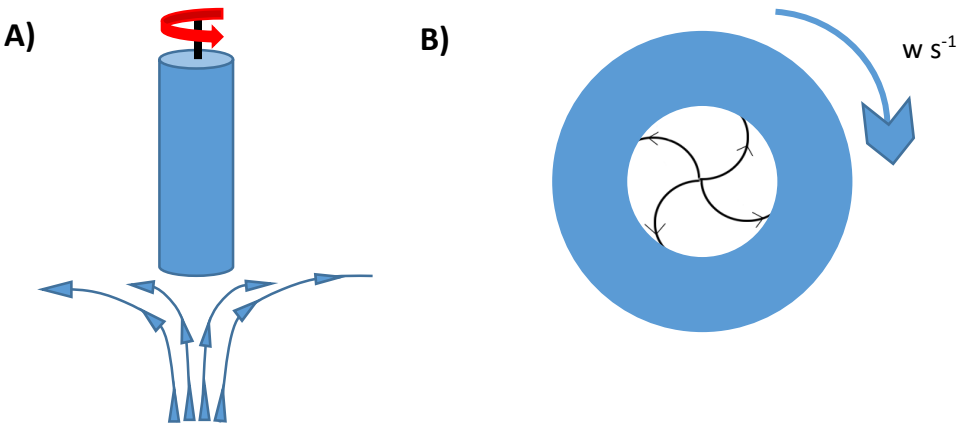

Figure 2.17. Diagram of rotating disk electrode in motion. A) Rotation of the cylindrical electrode causes convection of the liquid electrolyte solution as shown by the arrowed lines; bringing the flow towards the electrode from below. B) Electrode surface face on with the convection flow pattern shown by the arrows; flows from the centre of rotation towards the outside edge.

The velocity profile of the fluid near the rotating disc electrode is roughly illustrated in Figure 2.17. There is a combination of mass transport in a vertical direction perpendicular to the electrode surface and in a horizontal direction parallel to the electrode surface. As shown in Fig. 2.17b there is also an angular component to the fluid flow as a result of the rotating motion. The steady state velocity profile for laminar flow conditions has been derived by von Karman and Cochran [10].

$$V_y = (\omega v)^{0.5}\left(-0.51(\tfrac{\omega}{v})y^2 + \tfrac{1}{3}(\tfrac{\omega}{v})^{\frac{3}{2}}y^3 - 0.103(\tfrac{\omega}{v})^2 y^4 + \cdots\right) \quad \text{(eq. 2.56)}$$

Where V_y is the velocity component perpendicular to the electrode surface, ω is the angular rotation velocity of the electrode, v is the kinematic viscosity of the solution, and y is the distance away from the electrode. The equation shows that the velocity profile perpendicular to the electrode surface is independent of the velocity along the radial direction of the electrode and the angular velocity as well. Hence the steady state convective-diffusion equation can be simplified to equation 2.57.

$$V_y\left(\frac{\partial C_o}{\partial y}\right) = D_o\frac{\partial^2 C_o}{\partial y^2} \qquad \text{(eq. 2.57)}$$

Levich approximates V_y to only the first term in the expansion shown in eq. 2.56. Substituting the simplified V_y into the above expression yields the Levich equation (consult [1,4] for the mathematical derivation).

$$i = 0.62nFAD_o^{2/3}\omega^{1/2}\upsilon^{-1/6}c \qquad \text{(eq. 2.58)}$$

The Levich equation is accurate for most common solvents such as water, but the model deviates from experimental data for viscous solutions (it over estimates). For such systems the full velocity profile expression must be utilized which yields the following expression reported by Newman [11]. The denominator contains the ratio between v and D, which is called the Schmidt number. The Schmidt number has no units, the additional terms in the denominator can be thought of as a reciprocal sum that 'adjusts' the numerical constant in the Levich term.

$$i = \frac{0.62nFAD_o^{2/3}\omega^{1/2}v^{-1/6}c}{1+0.298v^{-1/3}D^{1/3}+0.145v^{-2/3}D^{2/3}} \qquad \text{(eq. 2.59)}$$

The steady state current under rotating disc conditions will be proportional to the square root of the angular rotation rate. This will be true provided a) the electrochemical system is given enough time to reach the steady state, b) the kinetics of electron transfer is fast compared to the rate of mass transport, c) the liquid electrolyte can be approximated to behave as a Newtonian fluid and is in laminar flow conditions and d) the electrode is symmetrically centred around the centre of rotation. There are quantitative methods to account for conditions where d) does not hold [12], but it is known that a slight offset does not cause serious deviations from the Levich model.

Rotating ring disc electrode

The rotating ring-disc electrode technique is identical to the rotating disc electrode except that a symmetrical ring shaped electrode is rotated instead of a disc. The two techniques are often used in conjunction as shown in Figure 2.18A. Due to the radial flow of electrolyte from the centre of the disc electrode outwards, the ring disc electrode is often used to detect the product of a reversible electron transfer reaction. Such a set-up is generally known as a collector-generator, while the generator produces the electrochemically active products, the collector is held at a potential that reduces/oxidizes the product. Having a very small gap between the disc and the ring-disc electrode allows detection of intermediate species that has small lifetimes.

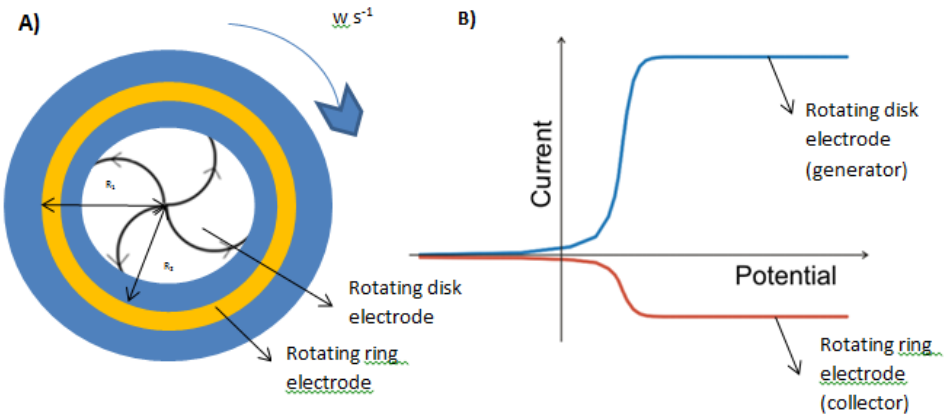

Figure 2.18. A) Illustration of the electrode surface of a rotating ring electrode (RRE) used in tandem with rotating disk electrode (RDE). Curved lines with arrows indicate the flow of electrolyte due to rotation. B) Cyclic voltammograms of a collector generator system with the RDE acting as a generator and the RRE acting as the collector electrode.

The ring electrode can also be used on its own. A Levich type model is shown in equation 2.60.

$$i = 0.62\pi nF(r_3^3 - r_2^3)^{2/3} D_o^{2/3} \omega^{1/2} \upsilon^{-1/6} c \qquad \text{(eq. 2.60)}$$

The ring has a greater proportion of the electrode area being edge sites compared to the disc shape, and edge sites experience a greater rate of mass transport. As a result ring-disc electrodes yields a higher current than a disc of the same area rotated at the same rate, and the difference becomes greater as the ring-disc electrode becomes thinner. A well defined symmetrical ring-disc electrode is technically challenging to synthesize so tends to be an expensive piece of kit.

Hydrodynamic modulation voltammetry (HMV)

HMV is a technique that further enhances the resolution of mass transport controlled faradaic processes from background interferences such as capacitance and reaction of surface adsorbed species. This is achieved by modulating the rate of convection such that the mass transport controlled component of the faradaic current is modulated as well, thereby allowing a further refinement of it from other background processes. Hydrodynamic modulation of the rotating disc electrode [13], pulsed flow cells [14] and pulsed rotating disc technique [15] has been reported.

Hydrodynamic modulation of the rotating disc electrode (HMRDE) usually involves a sinusoidal variation in rotation speed centred on a fixed rotation rate. The concentration profile of species in solution was found to adjust slowly to the change in rotation speed compared to the rapid change in the fluid velocity profile [16], hence the modulation frequency must be kept low compared to the centre rotation rate. The modulation amplitude (A) is usually kept at 1% of the centre rotation speed (ω_c). The alternating current that results can be demodulated using a lock-in amplifier, which gives the corresponding direct current output with the background processes filtered out. The technique can be used to detect species at sub-micromolar concentrations.

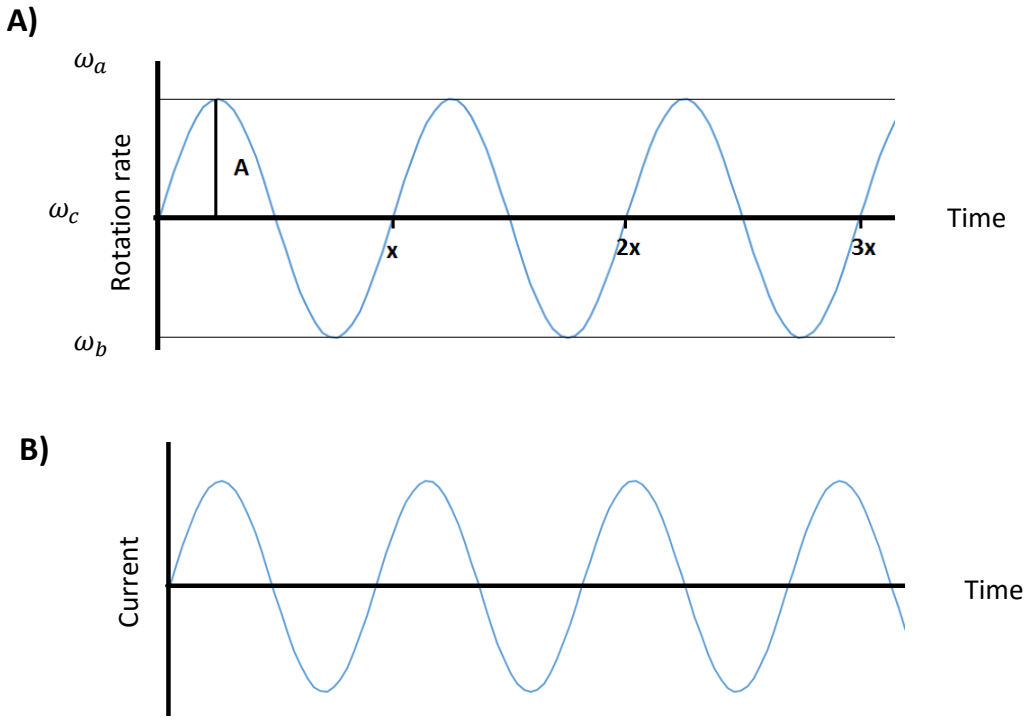

Figure 2.19. A) Sinusoidal modulation of rotation speed as a function of time B) Resulting alternating limiting current, which can be demodulated into dc form using a lock-in amplifier.

Vibrating electrodes

There are many reports of vibrating electrodes of various geometries; such as discs [17], plates [18], spheres [19], cylinders [20] and wires [21]. Methods of inducing vibration include ultra-sonication [19], cranks [20], speakers [17], and electromagnetic vibrators [22]. The mode of mechanical movement induced varies from motion parallel and perpendicular to the plane of the electrode surface, with angular components to consider as well. Cross comparisons and rationale linking modes of vibration

to observed mass transport effects in a precise manner is difficult with such variations in the methods of vibration. But it has been found that vibrating the electrode perpendicularly with respect to the plane of the electrode surface, results in larger rates of mass transport compared to parallel vibrations due to the onset of turbulent fluid motions [24].

Attempts to quantitatively model turbulent flow induced by perpendicular wire vibration has been reported [23]. Where the limiting current is expressed as a function of the Reynolds number, which in the general form is written as equation 2.61.

$$\mathrm{Re} = \frac{vL\rho}{\eta} \qquad \text{(eq. 2.61)}$$

Where v is the flow rate, L is the characteristic length, ρ is the density of the liquid and η is the viscosity of the medium. The Reynolds number is used to estimate whether a fluid is experiencing laminar flow or turbulent flow. The Reynolds number expressed for the motion caused by a wire vibrating with frequency f and amplitude a and a hydrodynamic diameter of d_e is given by equation 2.62.

$$Re_v = \frac{2afd_e}{v} \qquad \text{(eq.2.62)}$$

The limiting current for a range of Reynold numbers (from 5-120) has been modelled by fitting with experimental data and is generally expressed as equation 2.63.

$$I_l = kRe_v^x \qquad \text{(eq. 2.63)}$$

Where k is a constant and x has been fitted to be a numerical value ranging from 0.52-0.96 depending on the electrode. Due to the onset of turbulent fluid motion the rate of mass transport to the electrode using the vibrating wire electrode reported in the study is incredibly rapid. A Reynolds number of 100 achieved while maintaining the vibration frequency of 240 Hz yielded a current density equivalent to a rotating disc electrode set-up with over 416 Hz (rotations per second).

Turbulent hydrodynamic electrochemical systems have shown a lot of promise in providing high resolution of mass-transport limited faradaic processes from other background processes by

increasing the rate of mass transport to the electrode surface even more effectively than laminar flow hydrodynamic systems. Modelling of convective mass transport induced by a variety of methods has been attempted by fitting with experimental data, but given the complexity of motion and variety vibrating methods (often not clearly defined) a unifying quantitative model based on fluid dynamics is difficult to realise.

2.3 Voltammetry at liquid-liquid interfaces

2.3.1 Fundamentals of Liquid-Liquid Ion Transfer Voltammetry [3]

Ionic equilibria between two immiscible liquids

Given an ionic species j, in equilibrium between two immiscible liquids (water and toluene) in contact with each other.

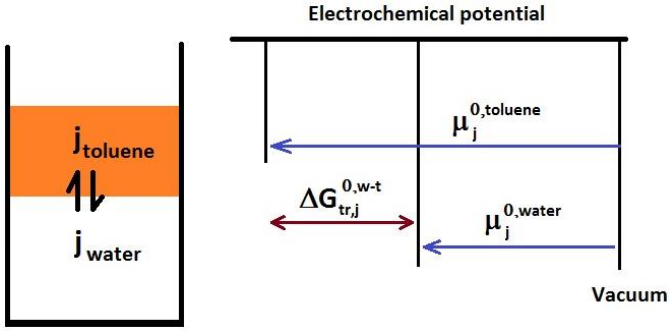

Figure 2.22. Species j in equilibrium between toluene and water. Species j will tend towards the phase with a lower electrochemical potential.

$$\Delta G_{tr,j}^{o,w\rightarrow t} = \mu_j^{o,toluene} - \mu_j^{o,water} \qquad \text{(eq. 2.64)}$$

$\Delta G_{tr,j}^{o,w\rightarrow t}$ is the standard Gibbs transfer energy of species j going from water into toluene, and μ^o is the standard chemical potential of species a in the given phase. The electrochemical potential of species j in water for example is written as shown in equation 2.65.

$$\mu_j^{electrochemical} = \mu_j^{o,water} + RTlna_j^{water} + z_jF(\phi^{water}) \qquad \text{(eq. 2.65)}$$

Where α is the activity of species j in water, z is the ionic charge, F is the Faraday constant and ϕ is the inner potential of a given phase. The Galvani potential difference between the two phases with species j in equilibrium is written as (a form of the Nernst equation) shown below.

$$\Delta_w^t\phi = \phi^t - \phi^w = \Delta_w^t\phi_j^o + \frac{RT}{z_jF} ln\left(\frac{a_j^t}{a_j^w}\right) \qquad \text{(eq. 2.66)}$$

$\Delta_w^t\phi_j^o$ is the standard transfer potential which can be expressed as the Gibbs energy of transfer by the expression below.

$$\Delta_w^t\phi_j^o = \frac{\Delta G_{tr.j}^{o,w\to t}}{z_jF} \qquad \text{(eq. 2.67)}$$

When considering a two ions of opposite charge in equilibrium distributed across two phases, the electro-neutrality principle applies where the concentration of each species must equal that of the counter ion. The Galvani potential difference for ionic species m^+ and n^- partitioned across water and toluene is known as the distribution potential and is written as shown below in equation 2.68.

$$\Delta_w^t\phi = \frac{\Delta_w^t\phi_{m+}^o + \Delta_w^t\phi_{n-}^o}{2} + \frac{RT}{2F} ln\left(\frac{\gamma_{m+}^t\gamma_{n-}^w}{\gamma_{m+}^w\gamma_{n-}^t}\right) \qquad \text{(eq. 2.68)}$$

Where γ is the activity coefficient which tends to 1 in dilute solutions, making the second term in the equation negligible. The potential of both phases can be manipulated by the use of a four electrode set-up where there is a reference electrode and a counter electrode in each phase, interfacial ion transfer in either direction can be induced by applying the necessarily potential difference.

Redox equilibria between two immiscible liquids

For a reversible redox species facilitating electron transfer across the interface of two immiscible liquids as shown in the Figure below, where electron transfer occurs from a species in the toluene phase to species present in the water phase.

$$A_{water} + B_{toluene}^- \rightleftharpoons A_{water}^- + B_{toluene} \qquad \text{(eq. 2.69)}$$

$$C_{toluene}^+ \rightleftharpoons C_{water}^+ \qquad \text{(eq. 2.70)}$$

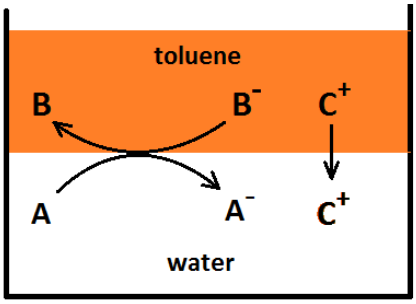

Figure 2.23. Interfacial electron transfer coupled to ion transfer to maintain electro-neutrality.

As there is a net build-up of charge as a result of electron transfer, interfacial ion transfer must be coupled to electron transfer to maintain electro-neutrality. The Nernst equation written for the electron transfer (ET) equilibrium is shown in equation 2.71 below.

$$\Delta_t^w \phi_{ET} = \Delta_t^w \phi_{ET}^o + \frac{RT}{nF} ln \left(\frac{a_{A^-}^{water} a_B^{toluene}}{a_A^{water} a_{B^-}^{toluene}} \right) \qquad \text{(eq. 2.71)}$$

Where $\Delta_t^w \phi_{ET}^o$ is the standard redox potential for the interfacial electron transfer from the toluene phase into the water phase.

$$\Delta_t^w \phi_{ET}^o = \frac{\mu_{A^-}^w + \mu_B^t - \mu_A^w - \mu_{B^-}^t}{nF} \qquad \text{(eq. 2.72)}$$

Equation 2.72 can be written in Gibbs energy terms.

$$\Delta_t^w \phi_{ET}^o = \frac{\Delta G_{tr,B}^{o,w \to t} - \Delta G_{tr,A}^{o,w \to t}}{nF} \qquad \text{(eq. 2.73)}$$

The Nernst equation written for the interfacial ion transfer (IT) is expressed as shown in equation 2.74.

$$\Delta_t^w \phi_{IT} = \Delta_t^w \phi_{C^+}^o + \frac{RT}{z_{C^+} F} ln \left(\frac{a_{C^+}^w}{a_{C^+}^t} \right) \qquad \text{(eq. 2.74)}$$

The standard potential of the interfacial ion transfer coupled electron transfer process is written as the sum of the two as shown below.

$$\Delta_t^w \phi = \Delta_t^w \phi_{ET} + \Delta_t^w \phi_{IT} \qquad \text{(eq. 2.75)}$$

Hence the potential required to drive interfacial electron transfer is determined by the nature of electrolyte ions present in the both liquid phases (see Fig. 2.24). Liquid-liquid systems offer the benefits of being able to keep the electron donor in a separate phase to the electron acceptor, which can be useful in cases where the product of electron transfer needs to be separated and purified (e.g. electro-catalytic conversions). The challenge with this system lies with the restrictions related to solvent and electrolyte selection; which needs to maintain immiscibility while being able to accommodate a common electrolyte ion at a significant excess of the redox species in both phases, and offer a potential window large enough not to interfere with the target faradaic process. Although the potential of interfacial electron-transfer are not affected by interfacial area, keeping the interface stable for consistent currents can also be technically challenging when working with organic solvents with high volatility and low viscosity.

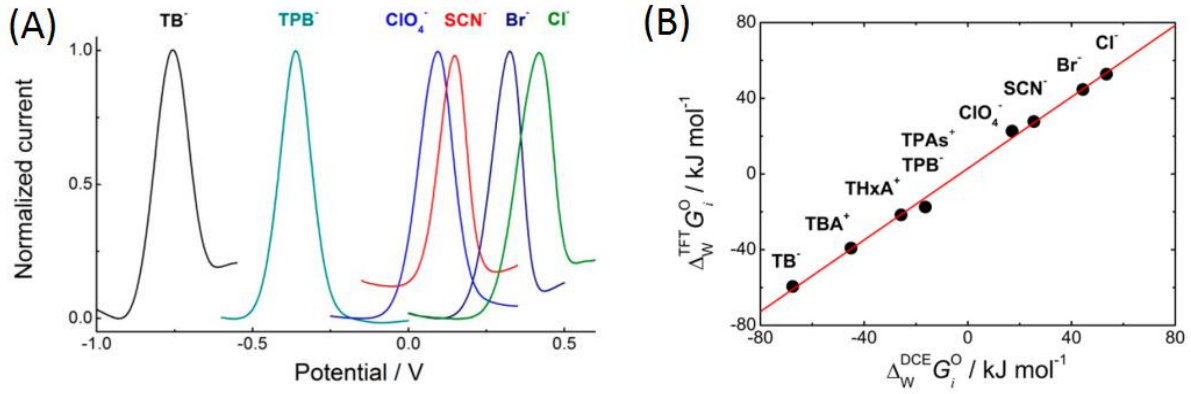

Figure 2.24. A) Normalized square wave voltammetry of decamethylferrocene in trifluorotoluene in contact with aqueous solution with different transfer ions. B) Gibbs energy of ion transfer coupled to redox of decamethylferrocene. Reprinted with permission from [25]. Copyright (2014) American Chemical Society.

2.3.2 Triple Phase Boundary Electrochemistry

A triple phase boundary (or three phase boundary) is the interface of three separate phases coming in contact with each other. In the context of this report, it is the interface between two immiscible liquids and a solid working electrode. The triple phase boundary is not one dimensional as even immiscible liquids tends to mix near the interface. A typical organic | water interface is dynamic with

solvents penetrating into each other at the microscopic level, that on average has a mixed phase of ca. 10 angstroms thick. In the simplest case of an immiscible droplet of oil immobilized on a solid electrode surface, which is altogether submerged in an aqueous solution, the triple-phase boundary is the circumference of the droplet on the electrode surface.

Unlike in liquid-liquid systems, the triple phase boundary system can be studied utilizing a three electrode set-up, where the reference and counter electrode is in the aqueous phase. Electron transfer at the working electrode can occur at either of the two phases; if the redox active species is in the water, its reduction/oxidation is coupled to a process at the counter electrode and the immiscible oil does not play a role in the system. However if the redox species is present in the oil phase, we approach a case similar to the liquid-liquid system where electron transfer from the working electrode to the oil phase results in a charge imbalance that requires an interfacial ion transfer from the aqueous phase into the oil phase. When the ionic conductivity of the oil phase is low (i.e. does not contain any intentionally added electrolytes), the ion-transfer coupled electron transfer is initially confined to the triple phase boundary.

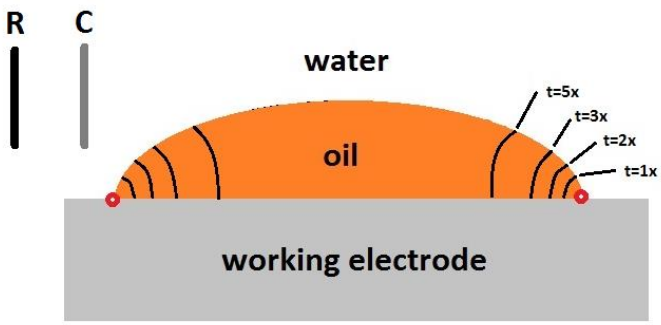

Figure 2.24. Triple phase boundary diagram. Ion transfer coupled to electron transfer spreads the ionic conductivity region with increasing time.

Once the electron transfer reaction is allowed to run for a period of time, there will be a flux of ions from the aqueous phase into the oil phase which will increase the ionic conductivity of the oil, eventually to a point where electron transfer region expands from the triple phase boundary into the oil droplet to form a 2-dimensional electrode-oil boundary. Electron transfer from the electrode into the oil is coupled to ion transfer at the water | oil boundary [26]. The same thermodynamic considerations can be applied to triple-phase boundary systems as with liquid-liquid systems as outlined in the previous section. But the timeframe of measurement must be kept short such that the

potential of the oil phase does not change significantly during the duration of the electrochemical measurement. Care must be taken especially when the oil droplets being studied have a small volume. Square wave voltammetry is often utilized in these cases as it offers better faradaic resolution compared to normal voltammetry at short-time measurements (faster scan rates).

The advantages the triple phase boundary holds over liquid-liquid systems is that i) measurements can be carried out with a three-electrode set-up, ii) the oil phase does not require addition of inert electrolyte salts, iii) point ii has the added benefits in electro-synthetic set-ups where the converted product can be extracted as a salt of the transferred ionic species, with minimal contaminants, iv) the required volume of the organic phase is very small compared to the liquid-liquid case and v) working with volatile organic solvents can be carried out with ease provided it is immiscible with the neighbouring liquid.

2.4 Electrocatalysis

The definition of a catalyst is a substance that enhances the rate of a chemical process without being consumed. The catalyst does not alter the net change in Gibbs energy, but lowers the activation energy required thereby increasing the kinetics of the reaction. With respect to electrochemistry, there are two cases which will be discussed in this section.

ECE mechanism and catalysis on electrodes

In this case, the electron is delivered to the chemical system through an electrode as outlined in the Figure 2.25 below. The initial electron transfer from the electrode to solution species A reduces it to species B. B undergoes a rapid chemical conversion to C, which is then reduced at the electrode to form species D. The general term for this process is known as an ECE mechanism; an electrochemical step followed by a chemical step followed by another electrochemical step.

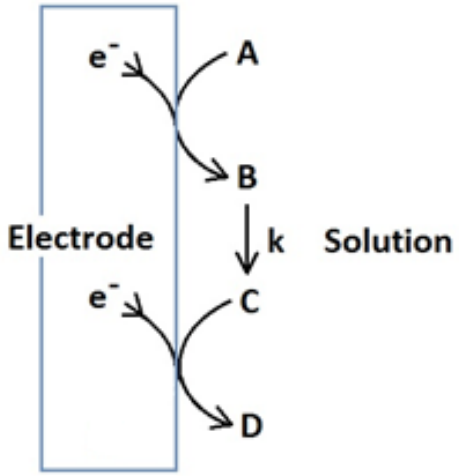

ECE mechanism

$A + e^- \rightleftharpoons B$	electrochemical step
$B \rightarrow C$	chemical step
$C + e^- \rightleftharpoons D$	electrochemical step

Figure 2.25. Schematic of an ECE mechanism.

Also commonly observed are catalytic effects from the metal electrode itself; where the electrons are consumed as part of the catalytic cycle but use of certain metals allows the reduction/oxidation to occur at a lower potential compared to other electrode materials. Metals that form favourable interactions with the substrate such that its rate limiting transition state is stabilized, can lower the activation energy of the process and enhance kinetics. An example of this is the platinum electrode which is known to facilitate hydrogen evolution reaction effectively (see Figure 2.26). Compared to silver and mercury electrodes, proton reduction into hydrogen occurs at a lower potential.

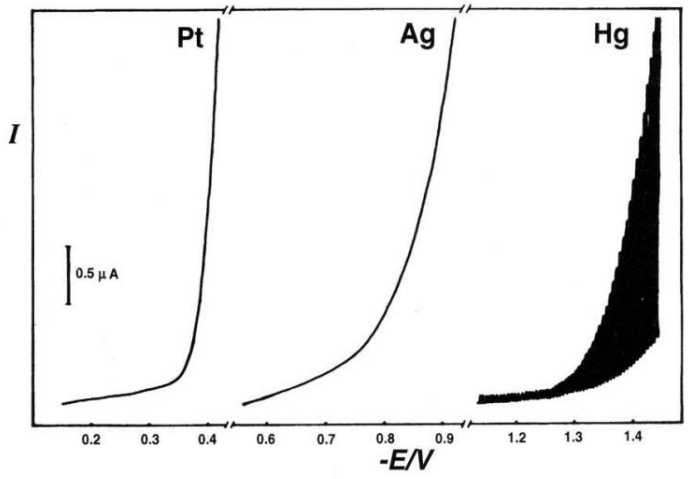

Figure 2.26. I-E curves in H_2SO_4 aqueous solutions at pH 3.21 obtained with platinum, silver, and mercury electrodes. Reprinted with permission from [27]. Copyright (1994) American Chemical Society.

Redox catalysts

Redox active catalysts are species that act as electron/hole shuttle between the electrode and the substrate. The active catalyst B is electrochemically generated by reducing A, catalyst B donates the electrons to solution based substrate E which is reduced to F. The net effect is E reduced to F by catalyst B which is continuously regenerated by the applied potential (electrons are consumed). The catalyst mediated reduction of E occurs at a lower potential than the direct reduction of E at the electrode. This is an example of a homogenous EC' catalytic mechanism, it is also possible to get heterogeneous EC' catalysis.

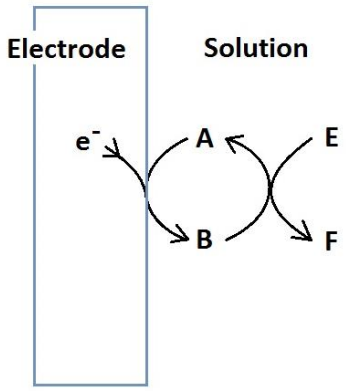

EC' mechanism

$A + e^- \rightleftharpoons B$ electrochemical step

$B + E \rightarrow F + A$ chemical step

Figure 2.27. Schematic of an EC' mechanism.

As species A is being continuously regenerated at the electrode surface and consuming electrons, the EC' mechanism can be monitored through the use of a potentiostat which counts the number of electrons consumed as a function of time at a given potential. Assuming that there are no other interfering reactions, it is possible to extract quantitative kinetic data from experimental data with the aid of simulation software such a DigiElch.

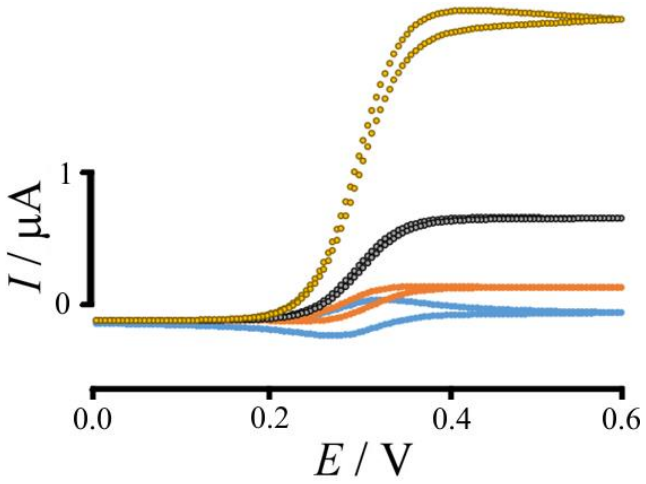

Figure 2.28 Simulated cyclic voltammograms run at 50 mVs^{-1}. Assuming fast electron transfer kinetics, the rate limiting process was the chemical C' step. From bottom to top; k = 0, k = 100, k = 1000, and k = 10000 $M^{-1}s^{-1}$ and K_{eq}= 1 x 10^{15}. 1D semi-infinite diffusion model utilized with an electrode area of 1 cm^2, $D_{A/B}$= 5 x 10^{-10} m^2s^{-1}, $D_{E/F}$ = 1 x 10^{-9} m^2s^{-1}, [red] = 0.001 M and [E] = 0.1 M.

When the rate of the C' step is set to zero, the cyclic voltammetry shows a reversible redox system where the oxidation peak and reduction peak have a ratio of one to one (assuming an ideal case). When the kinetics of C' is set to 10, the oxidative current loses its peak shape and gives a steady state current. As species B is consumed in the catalytic process there is no corresponding reduction peak. There is an increase in the current when the catalytic C' step kicks in as species A is regenerated once oxidized. One can easily distinguish between an EC' mechanism and an EC mechanism in which the 'C' step generates an electro-inactive product by observing the difference in current magnitudes (EC' is larger). When the kinetics of the catalytic step is relatively low, the reaction between catalyst B and substrate E is kinetically limited, hence the limits of mass transport (which manifests itself as a Cottrell decay in current in the k = 0 case) are not observed. It is only at higher kinetic rates that mass transport limits start affecting the voltammetry. At k = 10000 the catalytic current is no longer at a steady state as the rate of mass transport of E is slower than the rate at which it is consumed by the catalysis. The voltammetry becomes more peak like as mass transport limits become more significant. Mass transport of substrate E is determined by factors such as concentration of E, diffusion coefficient of E, and convection.

2.5 References

[1] A. J. Bard and L. R. Faulkner, "*Electrochemical methods,*" John Wiley & Sons, 1980.

[2] R. G. Compton and C. E. Banks, "*Understanding voltammetry*," Imperial College Press, 2007.

[3] H. H. Girault, "*Analytical and physical Electrochemistry*," EPFL Press, 2004.

[4] J. Albery, "*Electrode kinetics*," Oxford University Press, 1975.

[5] Y. Saito, "A theoretical study on the diffusion current at the stationary electrodes of circular and narrow band types," *Rev. Polarogr.*, vol. 15, no. 6, pp. 177–187, 1968.

[6] P. Daum, J. R. Lenhard, D. Rolison, and R. W. Murray, "Diffusional charge transport through ultrathin films of radiofrequency plasma polymerized vinylferrocene at low temperature," *J. Am. Chem. Soc.*, vol. 102, no. 14, pp. 4649–4653, 1980.

[7] P. Daum and R. W. Murray, "Charge-transfer diffusion rates and activity relationships during oxidation and reduction of plasma-polymerized vinylferrocene films," *J. Phys. Chem.*, vol. 85, no. 4, pp. 389–396, 1981.

[8] D. M. Oglesby, S. H. Omang, and C. N. Reilley, "Thin layer electrochemical studies using controlled potential or controlled current.," *Anal. Chem.*, vol. 37, no. 11, pp. 1312–1316, 1965.

[9] J. Urban, A. Zloczewska, W. Stryczniewicz, and M. Jönsson-Niedziolka, "Enzymatic oxygen reduction under quiescent conditions - the importance of convection," *Electrochem. commun.*, vol. 34, pp. 94–97, 2013.

[10] V. G. Levich, *Physicochemical hydrodynamics*. Prentice-Hall, Englewood Cliffs, 1962.

[11] J. Newman, "Schmidt number correction for the rotating disk," *J. Phys. Chem.*, vol. 70, no. 4, pp. 1327–1328, 1966.

[12] C. M. Mohr, "Mass transfer to an eccentric rotating disk electrode," *J. Electrochem. Soc.*, vol. 122, no. 7, p. 928, 1975.

[13] B. Miller and S. Bruckenstein, "Theoretical and experimental study of hydrodynamically modulated current-potential curves at rotating disk electrodes under conditions of mixed electron and mass transfer control," *J. Electrochem. Soc.*, vol. 121, no. 12, p. 1558, 1974.

[14] S. L. Boyer, "Submicromolar concentration measurements with tubular electrodes," vol. 43, no. 12, pp. 1538–1540, 1971.

[15] W. J. Blaedel and R. C. Engstrom, "Investigations of the ferricyanide-ferrocyanide system by pulsed rotation voltammetry," *Anal. Chem.*, vol. 50, pp. 476–479, 1978.

[16] K. Tokuda, "The frequency response of limiting currents to sinusoidal speed modulation at a rotating disk electrode," *J. Electrochem. Soc.*, vol. 122, no. 10, p. 1316, 1975.

[17] J. J. Podesta, G. F. Paus, and A. J. Arvia, “Ionic mass transfer at horizontals disc electrodes under longitudinal vibration,” *Electrochim. Acta*, vol. 19, no. 9, pp. 583–589, 1974.

[18] L. C. Blackman and R. Wall, “Vibration-enchanced corrosion of metals,” *Nature*, vol. 202, pp. 285–286, 1964.

[19] W. E. Rowe, “Changes in an electrode process brought about by small-scale acoustic streaming,” *J. Acoust. Soc. Am.*, vol. 39, no. 5A, p. 965, 1966.

[20] C. V. R. Raju, G. J. V. J. Raju, and C. V. Rao, *Indian J. Technol.*, vol. 5, p. 305, 1967.

[21] A. J. Lindsey, “Vibrating micro-electrodes in polarography. the relationship between diffusion current and frequency and amplitude of vibration,” *J. Phys. Chem.*, no. 2, pp. 439–442, 1952.

[22] F. Oehme and D. Noack, *Chem. Technol.*, vol. 7, p. 270, 1955.

[23] K. W. Pratt and D. C. Johnson, “Vibrating wire electrodes-I. Literature review, design and evaluation,” *Electrochim. Acta*, vol. 27, no. 8, pp. 1013–1021, 1981.

[24] G. Facsko and I. Radoi, *Bul. Sti. Teh. Inst. Pliteh. Timisoara*, vol. 14, p. 519, 1971.

[25] W. Adamiak, J. Jedraszko, O. Krysiak, W. Nogala, J. C. Hidalgo-acosta, H. H. Girault, and M. Opallo, “Hydrogen and hydrogen peroxide formation in trifluorotoluene − water biphasic systems,” J. Phys. Chem. C, 118, pp. 23154-23161, 2014.

[26] M. Donten, Z. Stojek, and F. Scholz, “Electron transfer - Ion insertion electrochemistry at an immobilised droplet: Probing the three-phase electrode-reaction zone with a Pt disk microelectrode,” *Electrochem. commun.*, vol. 4, no. 4, pp. 324–329, 2002.

[27] D. Marin, F. Mendicuti, and C. Teijeiro, “An electrochemistry experiment: hydrogen evolution reaction on different electrodes,” *Mod. student Lab.*, vol. 71, no. 11, pp. 4–5, 1994.

Chapter 3. Triple Phase Boundary Electrochemistry in Electrospun Carbon Nanofibres

Abstract

Low temperature carbonisation (500 ^{o}C) of poly-acrylonitrile nanofibres electrospun into a nano-web-like deposit on tin-doped indium oxide (ITO) substrates (or as free-standing membrane over glass capillaries) yields active carbon film electrodes, but with only relatively low electrochemical activity. Without resorting to higher carbonisation temperatures, substantial improvements in both electrical conductivity and electron transfer reactivity are observed after "surface-graphenisation". Voltammetry is reported for (i) the aqueous phase hydroquinone/benzoquinone redox system and (ii) the biphasic oil | aqueous ion transfer redox system tetraphenylporphyrinato-Mn(III/II) in 4-phenyl-(3-propyl)-pyridine).

Keywords: graphene, electrospinning, carbonisation, carbon nanofibre, voltammetry, membrane, sensor.

Acknowledgements

Dr. Boyang Mao and Dr. Sofia Pascu are gratefully acknowledged for the synthesis and supply of graphene oxide used in this study.

This work was adapted from

S. D. Ahn, B. Mao, S. I. Pascu, A. Vuorema, J. M. Mitchels and F. Marken, Electroanalysis, 26, p.69-75, Copyright (2014). John Wiley & Sons.

Contents

3.1 Introduction

3.1.1 Carbon Nanofiber Electrodes: Triple-Phase Boundary Electrochemistry

Electrochemistry offers a method of inducing chemical change by directly transferring electrons to a substrate without the use of additional oxidative/reductive reagents which makes it possible to achieve higher atom economy than with conventional synthetic methods. In a typical electrochemical set-up where a single liquid phase is in contact with a solid electrode, an excess of inert electrolyte salt is added to the liquid for efficient transfer of electrons from the electrode to the solute substrate. Separating the electro-synthetic product from the electrolyte is a necessary step that can be technically challenging and also uneconomical. Triple-phase boundary systems offer a partial solution to this issue. In this study a triple-phase boundary is defined as the point where two immiscible liquids come in contact with a solid electrode. By having two immiscible liquid phases in contact with each other, one supported with intentionally added electrolyte and one without, it is possible to induce electrochemical reactions in the unsupported phase with interfacial ion-transfer. Such a system benefits from i) not requiring extraction of excess electrolyte ions from the product solution, ii) relatively high atom economy due to lack of electrolyte ions used in the organic phase, iii) opportunities for heterogeneous catalysis and iv) scope for efficient flow-cell type designs in the future. In studies [1] and [2] commercially purchased randomly aligned carbon nanofibers were used as porous electrodes incorporated into a micro-reactor (see Figure 3.1) which increases the triple-phase boundary due to its large surface area resulting from its nano-structures. Carbon nanofibers are excellent electronic conductors with high mechanical stability and good compatibility with organic substrates. They also exhibit amphiphilic properties that makes it suitable for mediating electrochemical processes at liquid-liquid interfaces. Bulk conversion of aldehydes and amines at the milligram scale with high yields were demonstrated in organic phases without intentionally added electrolyte.

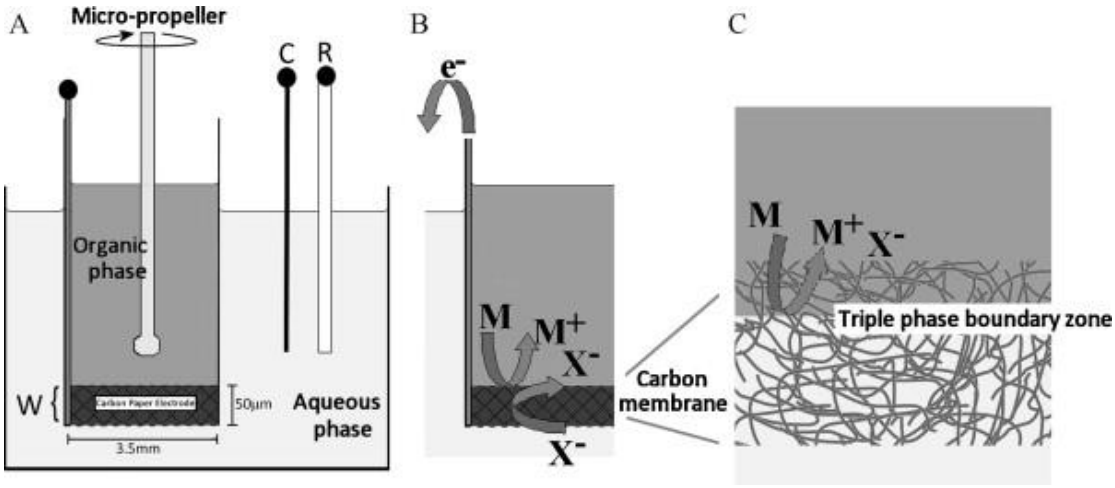

Figure 3.1. (A) Schematic cartoon drawing of an electrochemical cell with working, counter, and reference electrode (labelled W, C, and R respectively) in the aqueous phase and an immiscible organic phase separated by a carbon nanofibre membrane. (B) Schematic drawing of an oxidation process at the carbon membrane working electrode, which is accompanied by the transfer of an anion from the aqueous into the organic phase. (C) Expanded view of the triple phase boundary reaction zone within the carbon membrane. Reprinted from [1], copyright (2011) with permission from Elsevier.

Though the studies based on commercial carbon nanofibres reported some success, there were limitations due to slow mass transport within the carbon nanofiber layers. Here attempts are made to synthesize carbon nanofibers such that its structure, properties and thickness can be tuned for the purpose of mediating efficient triple-phase boundary processes. A well-known method of carbon nanofiber synthesis which involves electrospinning polymer nanofibers followed by carbonisation in a heated vacuum furnace is adapted following literature recipes. An additional pre-carbonisation modification step is introduced that drastically reduces the energy required to carbonise the polymer while maintaining desired properties for electrochemical processes.

3.1.2 Carbon Nanofiber Synthesis I: Electrospinning Nanofibers

While there are several methods of electrospinning reported [3], the most common form of this technique involves slowly extruding a volume of liquid out through a conducting capillary (typically less than 1mm diameter) that is charged with kilovolts. There is a build-up of electrostatic charge in the liquid that causes it to push out of the capillary and form what is

known as the Taylor's cone [4]. The coulombic force is resisted by the liquid's surface tension and its viscoelastic properties. In the case where there is high level of liquid cohesion, the applied potential causes the liquid to shoot out and form nanofibers. If the liquid cohesion isn't strong, the liquid will shoot out and disperse into fine nano-droplets. The latter case is referred to as electrospraying and has utility in mass spectrometers where liquid samples are vaporised and ionized.

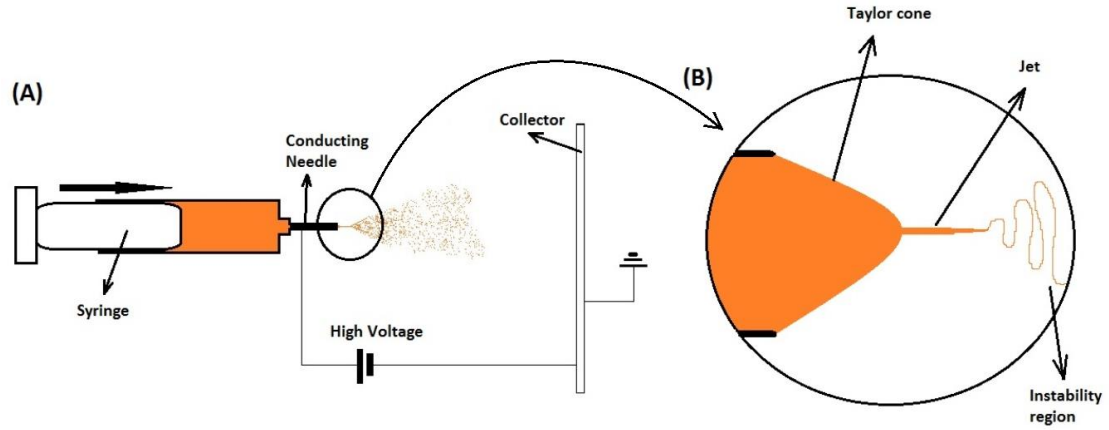

Figure 3.2. A schematic drawing of A) Electrospinning set-up and B) Taylor's cone.

In electrospinning, when a sufficiently high voltage is applied to the needle, a jet of liquid shoots out of the Taylor's cone which then elongates rapidly down to a nanometer scale diameter. The micro/nanofibers undergoes a rapid whipping motion that makes it appear that there are multiple threads of fibres shooting out of the liquid jet. High frame rate video analysis has shown that there is in fact only one fibre coming out of the end of the Taylor's cone at any given time [5]. The nanofibers are deposited on the collector in a random orientation, though it is possible to get alignment of the nanofibers by having the collector rotate at a high speed. Factors that affect the properties of the nanofibers deposited are i) solvent volatility, ii) molecular weight of the substrate, iii) substrate concentration in the solvent, iii) applied voltage, iv) temperature, v) atmospheric conditions such as humidity and gaseous composition, and vi) needle-collector distance. Due to the number of factors involved it is difficult to control the exact diameter of the electrospun nanofibers, there is normally a distribution of fibre dimensions whose average can be tuned by varying the factors listed above through trial and error.

Polymer and solvent selection

The most widely utilized polymer substrate for the purposes of synthesizing carbon nanofibers is poly-acrylonitrile (PAN), as it gives a high carbon yield after carbonisation. Viscose rayon [6], mesophase pitch [7], cotton, polystyrene [8], polybenzimidazole [9], polyethylene [10], Chitosan [11] and many more materials have been reported in literature as carbon precursors though only the first two materials on the list (along with PAN) have been used for commercial electrospinning.

The most common solvent for electrospinning PAN is dimethylformamide (DMF), it is a polar aprotic solvent with a density similar to water and a relatively high boiling point (152 ^{O}C). DMF is considered dangerous particularly to females as it has been linked to birth defects. It readily absorbs through the skin as well as inhalation, and tends to accumulate in the body. Dimethyl sulfoxide (DMSO), which has similar physical properties to DMF has been successfully utilized for electrospinning PAN [12]. Though the solvent itself is harmless and in fact had medical applications in the past, it readily absorbs through the skin with contaminants and industrial toxins that may be dissolved in it.

A key property of the solvent is its dielectric constant and dipole moment, which are good indicators of its susceptibility towards an applied electric field. Solvents with higher dielectric constants will be able to harness a greater coulombic force from an electric field, which results in a higher rate of nanofiber production (greater productivity). Boiling points are also important as it affects the solvent content of the fibres as it is shooting through the air towards the collector. The viscoelastic properties and the surface tension of the liquid fibre will be affected by the solvent content, which regulate how much the fibre can stretch before the polymer becomes too rigid. These factors along with the time duration the fibres are allowed to be in the air determines the fibre diameters.

Systematic studies have been carried out to optimise solvent selections; one approach was to use binary solvent systems to replace solvents that exhibit high productivity but are undesirable due to health and safety issues and cost. Binary solvent systems have been successfully utilized for electrospinning [13], the key solvent properties studied in this

particular report was hydrogen bonding, dispersion forces and polar interactions. This specific study aimed to electrospin polystyrene, but the approach can be taken for other polymers as well. The morphology of the fibres were found to be porous due to phase separations causing uneven distribution of the polymer. Porosity in nanofibers can be advantageous as the increase in active surface area can be significant, but the downside is that the fibres will be mechanically weaker than smooth nanofibers.

3.1.3 Carbon Nanofiber Synthesis II: Carbonisation of Polymer Nanofibres

Carbonisation is a process where the non-carbon elements present in the polymer nanofibers are removed from the structure by the application of thermal energy. The most common method is heating in a furnace (with an inert atmosphere or a vacuum), but there are other methods reported such as heating with microwaves [14] and use of deep-eutectic molten salt systems [15]. Utilizing microwaves is an energy efficient method of carbonising polymers, and is rapid. The problem lies with the fact that the process is too rapid, it is difficult to optimize the method to produce high quality carbon nanofibers as the rate of carbonisation results in the fibres snapping and forming a material that is mechanically brittle. Literature reports of heating polymer nanofibers in the furnace commonly emphasize the need to maintain a low temperature ramp rate during carbonisation [16]. Many also include a separate stabilization step where the polymer fibres are heated at a low temperature in an oxygen atmosphere before being exposed to higher temperatures [17]. Utilizing molten salt systems also does not offer a way to gently heat the fibres, so whereas it may be well suited for carbonizing materials that does not have long range structure (such as carbon nano-particles) it is not suitable for carbonizing nanofibers.

The stabilization step involve heating the PAN nanofibers at 280 ^{O}C in an oxygen atmosphere typically for an hour. It is generally agreed that this step allows the nitrile groups in the adjacent PAN chains to cyclize to form 6 membered rings as shown below [19,21].

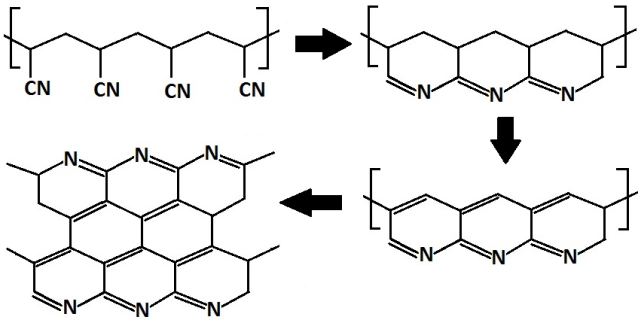

Figure 3.3. PAN cyclization and carbonisation.

The carbonisation step in the furnace involves heating the polymer substrate at temperatures up to 3000 ^{O}C [20]. The process involves the removal and evaporation of various nitrogen functionalities to leave behind graphitic carbon [21]. This must be carried out in an atmosphere not containing oxygen as it would lead to the combustion and loss of carbon as oxides. Carbonisation is carried out in a controlled atmosphere with pure argon, nitrogen or under vacuum. The products of the carbonisation step is commonly studied using Raman spectroscopy which is a technique that probes the vibrational energy of a molecule by measuring inelastic scattering effects with a laser. Depth of laser penetration (which is essentially the sampling depth) depends on the wavelength and the optical properties of the medium, and is typically in the range of microns. Carbon structures yields Raman peaks at 1350 cm^{-1} and 1580 cm^{-1} which corresponds to D and G peaks respectively. Highly ordered pyrolytic graphite (HOPG) exhibits a single peak at 1582cm^{-1}, the relative intensities of the D and G peaks show how disordered the carbon material is. X-ray crystallography is also used to measure crystallinity of the material; the in-plane crystal size yields information on how ordered the material is with larger crystal sizes implying longer range order. PAN nanofibers treated at temperatures lower than 1000 ^{O}C has the properties of amorphous carbon whereas treatments at 2800 ^{O}C, results in graphitic carbon [20]. Care is taken to keep the temperature ramp rate relatively low to prevent the nanofibers from snapping [16], typical ramp rates are kept between 1-5 ^{O}Cmin^{-1}. There are studies where the heat ramping rates aren't reported [22,23].

3.1.4 Carbon Nanofiber Synthesis III: Pre-Carbonisation Modification of Polymer Nanofibers

It is clear that current methods for producing carbon nanofibers though reliable are very energy and time intensive. An approach for improved efficiency is to modify the polymer substrate prior to carbonisation to lower the temperature required to yield carbon materials with the desired properties. Chemical modifications can improve carbonisation efficiency by i) catalysing the ring-cyclization process and the chemical steps required to remove nitrogen functionalities, and ii) become carbonized at a lower temperature itself to form a surface layer of graphitized carbon at a lower a temperature than PAN.

Addition of $FeCl_2$ [24], $CoCl_2$ [25], and hydrazine hydrate [26] has been reported to improve the material properties of the carbon material when added to the PAN prior to carbonisation. Whereas use of itaconic acid [27], ethylene diamine [28], $KMnO_4$ [29], and $CoSO_4$ [30] have been reported to reduce the time or heat energy required for the stabilisation process. Due to difficulties in monitoring the carbonisation process directly in-situ over hundreds of degrees Celsius, the mechanism of catalysis is not well understood. The cited studies justifies the use of modifiers through a before and after comparison approach, which does not contribute to the fundamental understanding of the chemical aspect of carbonisation. Use of metal based modifiers or catalysts for synthesis of carbon based electrode materials are undesirable as it will likely result in contamination.

Graphene Oxide (GO)

There are many reports on the use of graphene oxide (GO) as a precursor for graphitic films for applications in electrochemical systems. GO is multi-layered graphene with various oxygen functional groups such as tertiary alcohols, esters and epoxy groups that interrupts the delocalized π-electron system essentially making it an insulator. GO is commonly synthesized using the Hummer's method which involves the chemical exfoliation of graphite into smaller platelets [31,32]. GO is usually present as a distribution of various platelet widths, diameters and oxygen functionality concentrations.

There are several methods through which oxygen can be removed; such as heat annealing [33,34], chemical reductions [35,36] and electrochemical reductions [37,38,39]. Such methods reduce the C:O ratio from as low as 2:1 to typically 12:1, though ratios as high as 246:1 have been reported [40]. The electronic properties of reduced graphene oxide (rGO) resembles graphite. Presence of oxygen functional groups interrupts the conjugated π-systems and reduces both the charge mobility and density of the material; the highest conductivity reported on thermally reduced rGO is about two orders of magnitude lower than that of pure graphene [40,41,42]. Regardless, use of GO as a precursor appeals due to its relative cheapness and ease in handling and processing. There has been a growing interest in applications of rGO as modified electrodes [43,44] and in novel composite materials with electrochemical activity [45,46].

This study reports the use of i) celestine blue dye and ii) graphene oxide, employed as a pre-carbonisation modifier for poly-acrylonitrile nanofibres which are then carbonised by heating in a furnace. The materials are characterized and utilized as an electrode material for both aqueous phase electrochemistry and triple-phase boundary processes. The large surface area of randomly aligned carbon nanofibers are expected to be an effective electrochemical interface for triple phase boundary processes. The aim of this study is to develop an energy efficient method for synthesizing carbon nanofibers suitable for triple-phase boundary electrochemistry for applications in electrosynthesis and electroanalysis.

3.2 Experimental Method

3.2.1 Reagents

Dimethylsulphoxide (DMSO) (99.5%, Sigma Aldrich), poly-acrylonitrile (PAN) with M_w of (150,000 $gmol^{-1}$, Sigma-Aldrich), phosphoric acid (85%, Fisher Scientific), Hydroquinone (99%, Aldrich), 4-phenyl-(3-propyl)-pyridine (97%, Aldrich), 5,10,15,20-Tetraphenyl-21*H*,23*H*-porphine manganese(III) chloride (95%, Sigma Aldrich) were used as purchased. Silver conductive paint from Radiospares (RS) components and Ambersil silicone sealant (Silicoset 151) from Amber Chemical Company were used as purchased. Graphene oxide a GO suspension in ethanol:H_2O (2:1) was made from graphite powder following a modified Hummers method [32].

3.2.2 Instrumentation

For voltammetry studies, a microAutolab II potentiostat system (EcoChemie, Netherlands) was employed with a KCl-saturated calomel reference electrode (SCE, Radiometer). Working electrodes were based on tin-doped indium oxide (ITO) coated glass, (Image Optics, Basildon) which were cut to 50 mm × 10 mm area, and also borosilicate glass capillary tubes with an outer diameter of 1 mm and inner diameter of 0.6 mm. The counter electrode was a platinum wire of 0.5 mm diameter. Electrolyte solutions were de-aerated using BOC Pureshield argon. Electro-spinning was performed using an Easyspin system (Lineari, Italy). Samples were then placed into a quartz tube with a diameter of 3 cm (Springham, UK) and vacuum carbonized in a Thermoscientific tube furnace type F21100 under oil-pump vacuum ca. 10^{-3} Torr. Electron microscopy images were obtained on a JEOL FESEM6301F system and Raman spectra were measured with a Renishaw inVia Raman Microscope at 532nm.

3.2.3 Procedure: Electrospinning

Electro-spinning was carried out following a literature procedure [12]. Briefly, PAN was dissolved in DMSO by stirring at room temperature for 24 hours to form a 4 % wt. solution. The homogenous solution was ejected out of a syringe with an internal needle diameter of 0.8 mm at a rate of 200 µL/h. The needle was aligned horizontally with the stationary aluminium collector at a distance of 20 cm. The ITO coated glass slides were placed flat on the aluminium conductor normal to the needle tip. A voltage of 10 kV was applied to the needle tip and electro-spinning was carried out at 20 +/- 2 ^oC). ITO slides were coated for 30 minutes.

Free-standing membranes were prepared by peeling off and mounting PAN nanofibre films initially coated onto the aluminium collector for 60 minutes. The free-standing membranes were wrapped onto the end of borosilicate glass capillary tubes.

3.2.4 Procedure: Modification of Poly-acrylonitrile nanofiber films

PAN nanofibers are modified with i) Celestine blue dye or ii) graphene oxide. For the modification of PAN nanofiber with Celestine blue (CB), a saturated solution of celestine blue (CB) dye (0.02g/ml) was made up in 0.01M $H_2SO_{4(aq)}$. PAN nanofibre network was modified by submerging in CB solution for 60 minutes. Excess dye was gently rinsed off in deionized water then dried at 60 ^oC for 30 minutes. For the modification of PAN nanofiber with graphene oxide (GO), PAN nanofibers were submerged into a GO suspension in ethanol/H_2O (2:1) for 60 minutes, followed by drying (evaporating the solvents at 60 ^oC for 30 minutes.

3.2.5 Procedure: Carbonisation of Modified Poly-acrylonitrile nanofibres

Carbonisation of the PAN nanofibre network in both cases was carried out *in vacuo* (ca. 10^{-3} Torr oil pump) by heating at a rate of 3 ^oC min^{-1} to the peak temperature 500 ^oC, which was held for 60 minutes before allowing the sample to cool *in vacuo*. There were no separate stabilization steps involved.

Figure 3.4. Electrode preparation method shown for modification utilizing graphene oxide. A) PAN nanofiber film deposited on ITO and B) Free standing PAN membrane supported on a borosilicate glass capillary.

3.2.6 Procedure: Triple Phase Boundary Electrochemistry

As reported previously [47], a solution of TPPMn(III)Cl (TPPMnCl) and 80 mg 4-phenyl-(3-propyl)-pyridine (PPP) in 10 cm^3 acetonitrile was prepared. Evaporation of this solution onto the electrode or membrane resulted in the formation of PPP oil phase deposits containing ca. 61 mM TPPMn(III).

3.3 Results and Discussions

3.3.1 ''Surface-Graphenisation'' on Carbonized Electrospun Nanofiber Electrodes I: Characterisations

The FESEM images in Figure 3.5A and B show that unmodified carbon nanofibers have uniform thickness (no beading), that have a distribution of fibre diameters (shown in Figure 3.6). Poly-acrylonitrile (PAN) nanofibers lose mass and volume after carbonisation as non-carbon elements are evaporated. PAN nanofibers have an average diameter of 183nm which decreases to 157nm after carbonisation, which corresponds to a ca. 30% loss in volume. Addition of celestine blue (CB) forms a layer of carbonised material surrounding the nanofibers as shown in Figure 3.5D&E, forming new surfaces between the nanofibers. FESEM images of PAN modified with graphene oxide (GO) 3.5F+G&H reveal that GO is distributed unevenly across the surface of the PAN nanofibers. Large GO flakes deposits over larger gaps (ca. 1μm) between fibres, whereas smaller flakes appear to wrap around individual nanofibers resulting in rough surface structures (nanometer scale) not visible on unmodified carbon nanofibers.

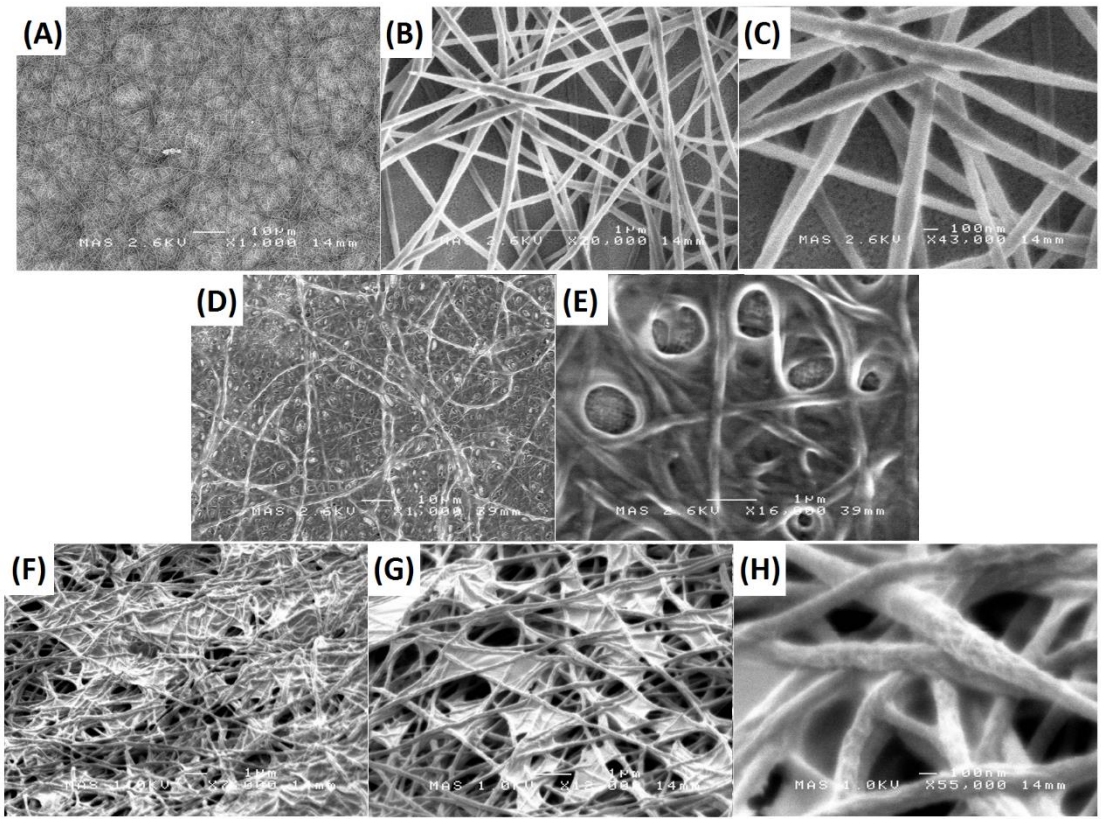

Figure 3.5. FESEM images of carbonised PAN nanofibers (ES-C); A) x1000 magnification, B) x20,000 magnification and C) 43,000 magnification. Carbonised PAN nanofibers modified with Celestine blue (ES-CB-C); D) x1000 magnification and E) x16,000 magnification. Carbonised PAN nanofibers modified with graphene oxide (ES-GO-C) F) x7000 magnification, G) x12,000 magnification and H) x55,000 magnification.

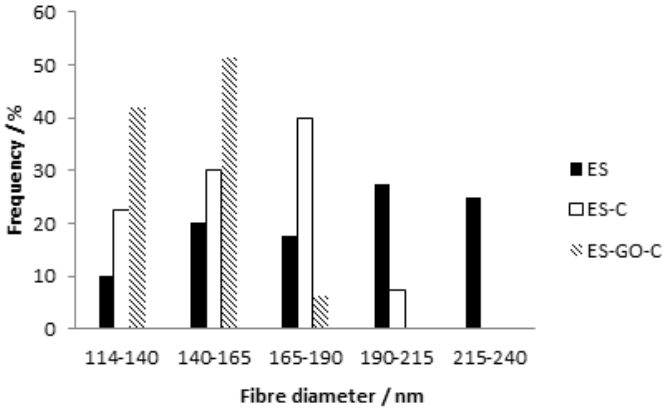

Figure 3.6. Bar chart of fibre diameter distribution determined by ImageJ software analysis.

Raman data of the carbonised PAN nanofibers (see Figure 3.8) show a relatively large D peak (relative to the G peak) indicative of amorphous carbon. There is an increase in the G peak in regions rich with reduced graphene oxide. A typical sampling depth of the Raman technique

is in the order of microns. The small increase is consistent with a thin layer of reduced graphene oxide deposited on the surface of amorphous carbon [48].

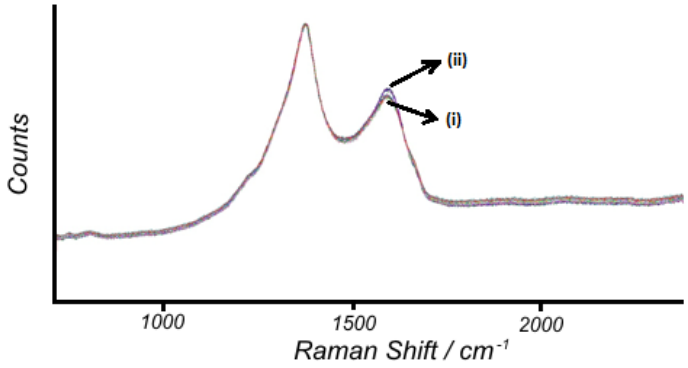

Figure 3.7. RAMAN spectra recorded at 532nm, overlay of 5 spectra of i) carbonised PAN nanofibers and ii) GO modified PAN nanofibers.

3.3.2 "Surface-Graphenisation" on Carbonised Electrospun Nanofiber Electrodes II.: Aqueous Phase Redox Processes

Figure 3.8A shows a comparison of voltammetric responses in a -0.7 to +0.8 V vs. SCE potential window. The bare ITO substrate is shown to make an insignificant contribution to the background current. The comparison of ES-C (electrospun poly-acrylonitrile nanofibers carbonised) and ES-GO-C (electrospun poly-acrylonitrile nanofibers modified with graphene oxide carbonised) electrode materials demonstrates a doubling of capacitive current, which is mainly due to the additional surface area from the graphitic layer. Addition of CB onto the carbon nanofibers also increases the capacitive current but not as much as with GO. The voltammetric response for a GO-C electrode (only graphene oxide carbonised on ITO) is shown to contribute to the capacitive current.

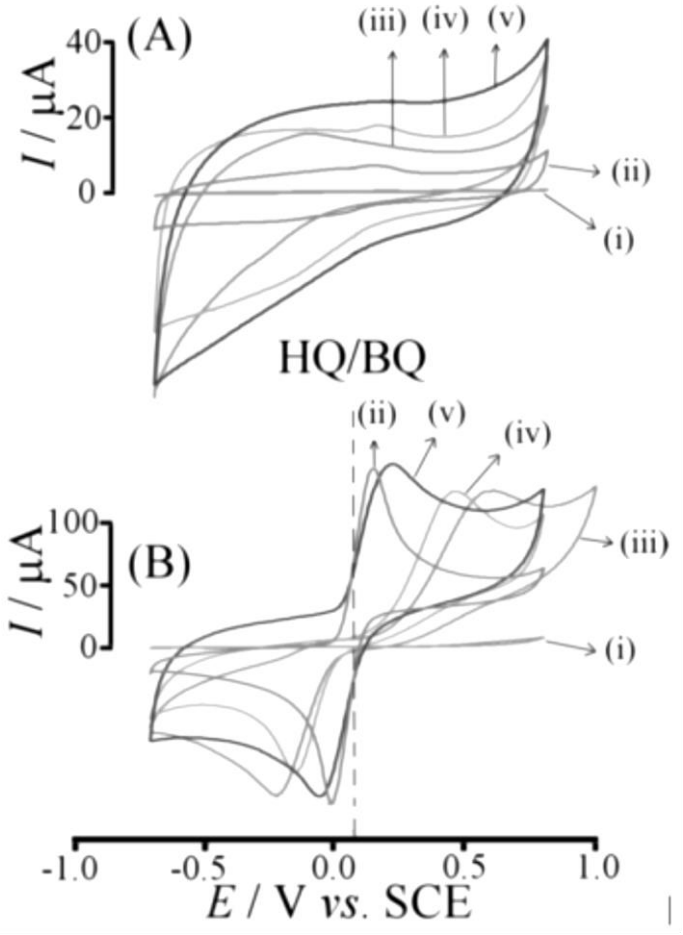

Figure 3.8 (A) Cyclic voltammograms (scan rate 0.05 Vs^{-1}) in aqueous 0.1 M phosphate buffer pH 7 and (B) in 1 mM hydroquinone in 0.1 M phosphate buffer pH 7 for (i) bare ITO, (ii) GO-C electrodes, (iii) ES-C electrodes, (iv) ES-CB-C electrodes, and (v) ES-GO-C electrodes.

Next, the 2-electron 2-proton oxidation of hydroquinone to benzoquinone is employed to reveal interfacial reactivity. On a bare ITO electrode (see Figure 3.8Bi) this oxidation is kinetically slow [49] and not observed in the -0.7 to +0.8 V vs. SCE potential window. Data in Figure 3.8Biii show that the low temperature carbonised ES-C electrode is active, but with a substantial separation of oxidation and back-reduction peak indicating slow electron transfer kinetics. With “surface graphenisation” a much improved voltammetric response is obtained (Figure 3.8Bv). The GO-C electrode (Figure 3.8Bii, a graphite layer on ITO) shows the best peak-to-peak separation consistent with fast electron transfer and high conductivity at a flat electrode surface. ES-CB-C (Figure 3.8Biv) is the intermediate case, where a slight improvement in the electron transfer kinetics is observed. Graphene oxide must graphitize to

a greater degree than celestine blue in the carbonisation temperatures used in the study; visually, the GO modified nanofibers appears more reflective than CB modified fibres after carbonisation, reinforcing this point. Use of graphene oxide as a pre-carbonisation modifier is preferred due to its superior performance and also due to difficulties in controlling the amount of CB deposited on the nanofibers. The additional material deposited in between the nanofibers when modifying with CB may reduce the porosity of the material which is disadvantageous for triple-phase boundary processes.

3.3.3 "Surface-Graphenisation" on Carbonised Electrospun Nanofiber Electrodes III.: Redox Processes at the Electrode | Organic | Aqueous Triple Phase Boundary

Triple phase boundary redox processes within nano-carbon membranes are important for both gas | liquid and liquid | liquid interfaces. Applications have been suggested in "clean electrosynthesis" [1,2] without supporting electrolyte and in electroanalysis [50,51], for examples in oils [52]. The TPPMn(III/II) redox system in 4-(3-phenylpropyl)-pyridine (PPP) has been employed previously as a model case [53]. The inset in Figure 3.9 summarises the overall redox process: (TPP)Mn(II) is oxidised to the $(TPP)Mn(III)^+$ cation, which is associated with transfer of the aqueous anion (here perchlorate, ClO_4^-) across the liquid | liquid interface to maintain charge neutrality.

The capacitive background responses for GO-C and ES-C in Figure 3.9A appear to be almost additive to give the response for the ES-GO-C electrode immersed in aqueous 0.1 M $NaClO_4$. With the oil phase deposited (10 nL 61 mM (TPP)MnCl in PPP, see Figure 3.9B), the anticipated Mn(II/III) redox signal is obtained on all three types of electrodes. The peak-to-peak separation on ES-C is only slightly wider probably indicative of resistivity. The charge under reduction or oxidation peaks can be estimated as 30 μC which is half of the value (of 60 μC) estimated for complete conversion of the redox system in the oil phase. When more oil is added (see Figure 3.9C) the relative conversion at 0.05 Vs^{-1} is further decreased indicative of the presence of larger oil droplets where conversion is slower. The results suggest that the oils are able to penetrate into the nanofiber network just as effectively independent of the type of carbon deposit.

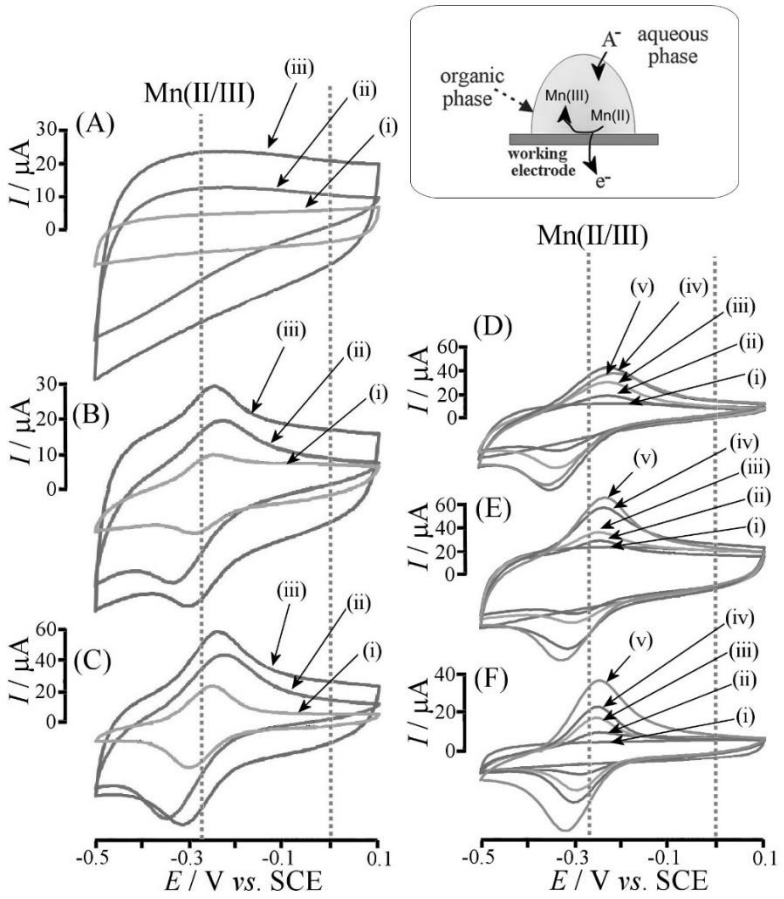

Figure 3.9 Left: Cyclic voltammograms (scan rate 0.05 Vs^{-1}) for (i) GO-C, (ii) ES-C, and (iii) ES-GO-C electrodes immersed in 0.1 M $NaClO_4$ and for (A) bare electrodes, (B) 10 nL and (C) 40 nL microdroplet deposits of 61 mM (TPP)Mn(III)Cl in PPP. Right: Cyclic voltammograms (scan rate 0.05 Vs^{-1}) for (D) ES-C, (E) ES-GO-C, and (F) GO-C electrodes immersed in 0.1 M $NaClO_4$ and for (i) 0, (ii) 10, (iii) 20, (iv) 40, and (v) 80 nL microdroplet deposits of 61 mM (TPP)Mn(III)Cl in PPP. Inset: Schematic drawing of the coupled electron transfer – anion transfer process at the triple phase boundary.

Data in Figure 3.9D-F are for different amounts of oil phase on the three types of nano-carbon electrodes. In all cases an increase is observed reaching a limit when too much oil is coated over the electrode and the triple phase boundary reaction zone is diminished.

3.3.4 "Surface-Graphenisation" on Carbonised Electrospun Nanofiber Electrodes IV.: Free-Standing Carbon Membrane Electrodes for Redox Processes at the Electrode | Organic | Aqueous Triple Phase Boundary

As the carbonisation temperature has been reduced to 500 °C, relatively inexpensive template materials can be used to form carbon nanofibers with miniaturized dimensions. Free-standing carbon nanofibre membrane electrodes supported on the end of a borosilicate glass capillary tube are utilized for liquid | liquid triple phase boundary voltammetry experiments. The electrodes are prepared by peeling off PAN nanofibre material from an aluminium target and sealing it around the end of a glass capillary tube before carbonisation. Figure 3.10A shows photographs of the PAN coating before and after carbonisation. The top-view shows the graphite-like appearance of the ES-GO-C membrane with variation in membrane thickness across the capillary diameter.

Figure 3.10B shows capacitive current responses without oil deposits. When oil is filled into the capillary the Mn(III/II) redox system is again detected. In these experiments the ES-C membrane did not yield any Faradaic current responses within the potential range, probably due to substantial resistance. But the ES-GO-C membrane gave well-defined redox activity as shown in Figure 3.10C. The Mn(III/II) redox peaks are significantly wider apart than those in Figure 3.10E, probably due to stunted charge mobility that results from a lack of conducting support (ITO) and the longer path to the electrode surface.

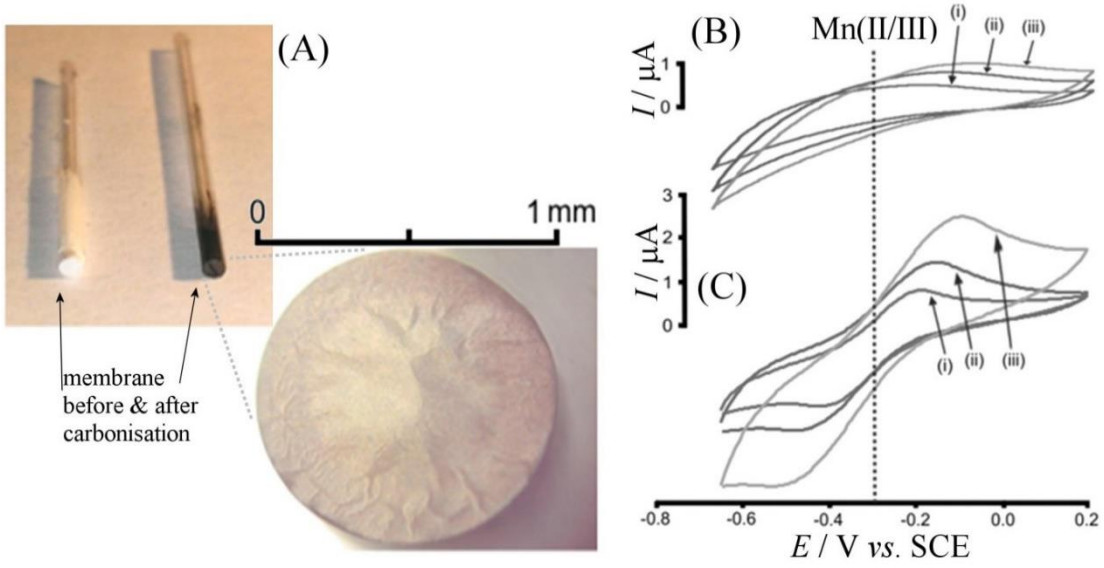

Figure 3.10. (A) Photographs of PAN nanofibre membrane applied to a 1 mm diameter borosilicate capillary before and after carbonisation. The top view of the membrane shows a graphitic appearance and non-uniform thickness. (B) Cyclic voltammograms (scan rate (i) 2 (ii) 5, (iii) 10 mVs^{-1}) for free ES-GO-C membrane mounted on borosilicate capillary tube immersed in 0.1 M $NaClO_4$. (C) As before but with the electrode surface saturated with 61 mM (TPP)Mn(III)Cl in PPP.

The data provide proof-of-principle evidence for the application of electro-spun nano-carbon materials in triple phase boundary electrochemistry. Future improvements will be possible by optimizing the membrane thickness and the amount of graphene oxide applied to the membrane surface. Potential applications are in novel electro-analytical triple phase boundary probes (smaller diameter capillaries down to nano-pipettes) and in disposable oil analysis tools. When used in arrays or on scaffolds, the nano-carbon membrane will also allow new types of biphasic micro-reactor electrosynthesis to be developed.

3.4 Conclusion

It has been shown that electro-spun poly-acrylonitrile nanofibres can be carbonised to useful thin film carbon nanofibre membrane electrodes under mild (500 ^oC) conditions without the need of a separate stabilisation step. Further improvements in both conductivity and reactivity are possible by “surface-graphenisation” (applying a graphene oxide coating before carbonisation). Electrodes of this type will be useful for thin film membrane electrodes in particular for triple phase boundary electrochemical systems based on oil microdroplet deposits (e.g. in oil analysis). Generally the ES-GO-C architecture shows promise for utility in triple-phase boundary electro-synthetic set-ups. But even with the substantial savings in time and energy made with the new synthetic method, electrospinning and carbonisation remains a relatively time consuming method of producing electrode materials. In the next chapter a convenient method of producing porous carbon electrodes based on carbon microspheres and polystyrene composite is demonstrated for applications in oil analysis.

3.5 References

[1] J.D. Watkins, S. D. Ahn, J. E. Taylor, S. D. Bull, P. C. Bulman-Page, F. Marken, "Liquid-liquid electro-organo-synthetic processes in a carbon nanofibre membrane microreator: Triple phase boundary effects in the absence of intentionally added electrolyte," Electrochimica Acta 56, 6764-6770, (2011)

[2] J. D. Watkins, J. E. Taylor, S. D. Bull, F. Marken, "Mechanistic aspects of aldehyde and imine electro-reduction in a liquid-liquid carbon nanofiber membrane microreactor," Tetrahedron Lett. 53, 3357-3360, (2012).

[3] F. Cengiz, I. Krucinska, E. Gliscinska, M. Chrzanowski, F. Goktepe, "Comparative Analysis of Various Electrospinning Methods of Nanofibre Formation," Fibres Text East Eur 17, 13-19 (2009).

[4] G. Taylor, "Disintegration of Water Drops in Electric Field," Proc. R. Soc. Lon. Ser.-A 280, 383, (1964).

[5] D. H. Reneker, A. L. Yarin, H. Fong, S. Koombhongse, "Bending instability of electrically charged liquid jets of polymer solutions in electrospinning," J. Appl. Phys. 87, 4531-4547, (2000).

[6] J. B. Donnet, "Carbon fibers," 3rd edn, (Dekker, 1998).

[7] T. Matsumoto, "Mesophase pitch and its carbon-fibers," Pure Appl. Chem. 57, 1553-1562, (1985).

[8] S. V. Volkov, V. M. Ogenko, L. V. Dubrovina, O. V. Holdun, "Solutions of polystyrene as a carbonization precursor for the matrix synthesis of carbon nanostructures," Nato Security Sci. A, 521-528, (2007).

[9] R. B. Sandor, "Polybenzimidazole (Pbi) as a Matrix resin precursor for carbon carbon composites (Reprinted)," Sampe Quart 22, 23-28 (1991).

[10] G. S. Bhat, D. Zhang, "Influence of processing variables on the structure and properties of polyethylene-based carbon-fibers. Processing and fabrication of advanced materials," pp. 367-378 (1994).

[11] M. Bengisu, E. Yilmaz, Oxidation and pyrolysis of chitosan as a route for carbon fiber derivation. Carbohyd Polym 50, 165-175, (2002).

[12] Z. Kurban, A. Lovell, D. Jenkins, S. Bennington, I. Loader, A. Schober, N. Skipper, Turbostratic graphite nanofibres from electrospun solutions of PAN in dimethylsulphoxide. Eur Polym J 46, 1194-1202, (2010).

[13] C. J. Luo, M. Nangrejo, M. Edirisinghe, A novel method of selecting solvents for polymer electrospinning. Polymer 51, 1654-1662, (2010).

[14] X. Y. Zhang, S. K. Manohar, Microwave synthesis of nanocarbons from conducting polymers. Chem Commun, 2477-2479, (2006).

[15] X. Wang, C. Hu, Y. Xiong, H. Liu, G. Du, X. He, Carbon-nanosphere-supported Pt nanoparticles for methanol and ethanol electro-oxidation in alkaline media. J Power Sources 196, 1904-1908, (2011).

[16] J. Rafique, J. Yu, X. X. Zha, K. Rafique, Fabrication of ultra thin and aligned carbon nanofibres from electrospun polyacrylonitrile nanofibres. B Mater Sci 33, 553-559 (2010).

[17] I. Karacan, G. Erdogan, The Role of Thermal Stabilization on the Structure and Mechanical Properties of Polyacrylonitrile Precursor Fibers. Fiber Polym 13, 855-863, (2012).

[18] N. Grassie, R. Mcguchan, Pyrolysis of Polyacrylonitrile and Related Polymers .2. Effect of Sample Preparation on Thermal Behaviour of Polyacrylonitrile. Eur Polym J 7, 1091, (1971).

[19] M. A. Aviles, J. M. Gines, J. C. del Rio, J. Pascual, J. L. Perez-Rodriguez, P. J. Sanchez-Soto, Thermal analysis of acrylonitrile polymerization and cyclization in the presence of N,N-dimethylformamide. J Therm Anal Calorim 67, 177-188, (2002).

[20] C. K. Liu, K. Lai, W. Liu, M. Yao, R. J. Sun, Preparation of carbon nanofibres through electrospinning and thermal treatment. Polym Int 58, 1341-1349, (2009).

[21] J. R. Pels, F. Kapteijn, J. A. Moulijn, Q. Zhu, K. M. Thomas, Evolution of Nitrogen Functionalities in Carbonaceous Materials during Pyrolysis. Carbon 33, 1641-1653, (1995).

[22] Y. Wang, J. J. Santiago-Aviles, Large negative magnetoresistance and two-dimensional weak localization in carbon nanofiber fabricated using electrospinning. J Appl Phys 94, 1721-1727, (2003).

[23] Y. Wang, S. Serrano, J. J. Santiago-Aviles, Conductivity measurement of electrospun PAN-based carbon nanofiber. J Mater Sci Lett 21, 1055-1057, (2002).

[24] A. W. Morawski, K. Kalucki, M. Nakashima, M. Inagaki, Modified Carbonization of Polyacrylonitrile by Incorporation of FecCl2 and Fe(No3)(3) Pore Structure. Carbon 32, 1457-1461, (1994).

[25] T. H. Ko, L. C. Huang, The influence of cobaltous chloride modification on physical properties and microstructure of modified PAN fiber during carbonization. J Appl Polym Sci 70, 2409-2415, (1998).

[26] I. Mladenov, M. Ljubcheva, Polyacrylonitrile Fibers Treated by Hydrazine Hydrate as a Basis for the Production of Carbon-Fibers. J Polym Sci Pol Chem 21, 1223-1226, (1983).

[27] Q. Ouyang, L. Cheng, H. J. Wang, K. X. Li, Mechanism and kinetics of the stabilization reactions of itaconic acid-modified polyacrylonitrile. Polym Degrad Stabil 93, 1415-1421, (2008).

[28] I. Karacan, G. Erdogan, The effect of ethylenediamine pretreatment on the molecular structure of thermally stabilized polyacrylonitrile fibers before carbonization. Polym Eng Sci 52, 467-480, (2012).

[29] W. X. Zhang, L. Jie, Effect of post-spinning modification on the PAN precursors and resulting carbon fibers. J Wuhan Univ Technol 21, 44-48 (2006).

[30] W. X. Zhang, Y. Z. Wang, Manufacture of carbon fibers from polyacrylonitrile precursors treated with CoSO4. J Appl Polym Sci 85, 153-158, (2002).

[31] W. S. Hummers, R. E. Offeman, Preparation of Graphitic Oxide. J Am Chem Soc 80, 1339-1339, (1958).

[32] D. C. Marcano, D. V. Kosynkin, J. M. Berlin, A. Sinitskii, Z. Sun, A. Slesarev, L. B. Alemany, W. Lu, J. M. Tour, Improved Synthesis of Graphene Oxide. Acs Nano 4, 4806-4814, (2010).

[33] D. Yang, A. Velamakanni, G. Bozoklu, S. Park, M. Stoller, R. D. Piner, S. Stankovich, I. Jung, D. A. Field, C. A. Ventrice Jr., R. S. Ruoff, Chemical analysis of graphene oxide films after heat and chemical treatments by X-ray photoelectron and Micro-Raman spectroscopy. Carbon 47, 145-152, (2009).

[34] H. A. Becerril, R. M. Stoltenberg, M. L. Tang, M. E. Roberts, Z. Liu, Y. Chen, D. H. Kim, B. Lee, S. Lee, Z. Bao, Evaluation of solution-processed reduced graphene oxide films as transparent conductors. Acs Nano 2, 463-470, (2008).

[35] G. X. Wang, J. Yang, J. Park, X. Gou, B. Wang, H. Liu, J. Yao, Facile synthesis and characterization of graphene nanosheets. J Phys Chem C 112, 8192-8195, (2008).

[36] S. Stankovich, D. A. Dikin, R. D. Piner, K. A. Kohlhaas, A. Kleinhammes, Y. Jia, Y. Wu, S. T. Nguyen, R. S. Ruoff, Synthesis of graphene-based nanosheets via chemical reduction of exfoliated graphite oxide. Carbon 45, 1558-1565, (2007).

[37] M. F. Zhu, C. Q. Zeng, J. S. Ye, Graphene-Modified Carbon Fiber Microelectrode for the Detection of Dopamine in Mice Hippocampus Tissue. Electroanal 23, 907-914, (2011).

[38] A. Viinikanoja, Z. J. Wang, J. Kauppila, C. Kvarnstrom, Electrochemical reduction of graphene oxide and its in situ spectroelectrochemical characterization. Phys Chem Chem Phys 14, 14003-14009, (2012).

[39] H. L. Guo, X. F. Wang, Q. Y. Qian, F. B. Wang, X. H. Xia, A Green Approach to the Synthesis of Graphene Nanosheets. Acs Nano 3, 2653-2659, (2009).

[40] S. F. Pei, H. M. Cheng, The reduction of graphene oxide. Carbon 50, 3210-3228, (2012).

[41] S. Bae, H. Kim, Y. Lee, X. Xu, J. Park, Y. Zheng, J. Balakrishnan, T. Lei, H. R. Kim, Y. I. Song, Y. J. Kim, K. S. Kim, B. Ozyilmaz, J. Ahn, B. H. Hong, S. Iijima, Roll-to-roll production of 30-inch graphene films for transparent electrodes. Nat Nanotechnol 5, 574-578, (2010).

[42] Q. Su, S. Pang, V. Alijani, C. Li, X. Feng, K. Mullen, Composites of Graphene with Large Aromatic Molecules. Adv Mater 21, 3191, (2009).

[43] L. Y. Chen, Y. H. Tang, K. Wang, C. B. Liu, S. L. Luo, Direct electrodeposition of reduced graphene oxide on glassy carbon electrode and its electrochemical application. Electrochem Commun 13, 133-137, (2011).

[44] Y. Z. Chang, G. Y. Han, M. Y. Li, F. Gao, Graphene-modified carbon fiber mats used to improve the activity and stability of Pt catalyst for methanol electrochemical oxidation. Carbon 49, 5158-5165, (2011).

[45] S. Chen, J. W. Zhu, X. D. Wu, Q. F. Han, X. Wang, Graphene Oxide-MnO2 Nanocomposites for Supercapacitors. Acs Nano 4, 2822-2830, (2010).

[46] H. Zhang, X. J. Lv, Y. M. Li, Y. Wang, J. H. Li, P25-Graphene Composite as a High Performance Photocatalyst. Acs Nano 4, 380-386, (2010).

[47] M. J. Bonne, C. Reynolds, S. Yates, G. Shul, G. Niedziolka, M. Opallo, F. Marken, The electrochemical ion-transfer reactivity of porphyrinato metal complexes in 4-(3-phenylpropyl)pyridine vertical bar water systems. New J Chem 30, 327-334, (2006).

[48] Z. P. Zhou, X. F. Wu, Graphene-beaded carbon nanofibers for use in supercapacitor electrodes: Synthesis and electrochemical characterization. J Power Sources 222, 410-416, (2013).

[49] M. Amiri, S. Shahrokhian, F. Marken, Ultrathin carbon nanoparticle composite film electrodes: Distinguishing dopamine and ascorbate. Electroanal 19, 1032-1038, (2007).

[50] R. Gulaboski, F. Scholz, Lipophilicity of peptide anions: An experimental data set for lipophilicity calculations. J Phys Chem B 107, 5650-5657, (2003).

[51] F. Marken, C. M. Hayman, P. C. B. Page, Chromate and dichromate electro-insertion processes into a N,N,N ',N '-tetraoctylphenylenediamine redox liquid. Electroanal 14, 172-176, (2002).

[52] X. H. Zhang, C. A. Paddon, Y. H. Chan, P. C. Bulman-Page, P. S. Fordred, S. D. Bull, H. C. Chang, N. Rizvi, F. Marken, Voltammetric Antioxidant Analysis in Mineral Oil Samples Immobilized into Boron-Doped Diamond Micropore Array Electrodes. Electroanal 21, 1341-1347, (2009).

[53] S. M. MacDonald, M. Opallo, A. Klamt, F. Eckert, F. Marken, Probing carboxylate Gibbs transfer energies via liquid vertical bar liquid transfer at triple phase boundary electrodes: ion-transfer voltammetry versus COSMO-RS predictions. Phys Chem Chem Phys 10, 3925-3933, (2008).

Chapter 4. Triple Phase Boundary Electrochemistry in Carbon-Polystyrene Composite Electrodes

Abstract

Oil analysis for the case of quinizarin in methyl laurate is demonstrated with a disposable carbon microsphere – polystyrene composite electrode. Randomly packed glassy carbon microspheres (2-12 mm diameter) held together with a polystyrene binder (ca. 0.1% by weight) are immobilized onto a pencil lead electrode and used for electrochemical oil analysis. Oxidation and reduction of quinizarin are observed as triple-phase boundary processes at the immiscible oil | water | carbon interface. Pore-filling with oil is optimised for voltammetric detection and fluorescence spectroscopy is employed to support the mechanistic analysis based on voltammetry. Future applications for a wider range of oils and additives are proposed.

Keywords: Carbon microspheres, surface tension, oil analysis, quinizarin, anti-oxidant, biofuel, sensor.

This work was adapted from

S. D. Ahn, D. Kaluza, M. Jonsson-Niedziolka, J. M. Mitchels and F. Marken, Electroanalysis, 27, p.1043-1049, Copyright (2015), John Wiley & Sons.

Contents

4.1 Introduction

Carbon as an electrode material is desirable due to its electronic conductivity, mechanical stability, thermal stability, relative abundance and good compatibility with organic molecules. Bulk carbon materials such as glassy carbon (vitreous carbon), graphite and boron-doped diamond are few of the most widely utilized electrode materials. There has also been an explosion in research on carbon materials with fine structures at the micro and nano-scale such as carbon nanofibers, carbon nanotubes, fullerenes, carbon nano/microspheres and graphene. In this study a cost efficient and easy-to-make (potentially disposable) porous carbon electrode is fabricated to facilitate triple-phase boundary electrochemistry. The composite is formed from glassy carbon microspheres (2 to 12 μm diameter) bound together with polystyrene (ca. 0.1% wt). Glassy carbon microspheres have been employed previously in electroanalysis [1], support material for electrocatalysis [2] and supercapacitors [3]. Unlike carbon nanotubes or graphene it does not exhibit catalytic activity on its own. Carbon materials are often combined with polymers to form composites for enhanced stability and functionalities. A few examples of carbon-polymer composites utilized for electroanalysis are outlined in table 4.1 below.

Table 4.1. Examples of carbon-polymer composites used for electroanalysis.

Carbon Material	**Polymer**	**Analyte**	**Limit of Detection (M)**	**Reference**
Multi-walled carbon nanotubes	Chitosan	Dopamine	1.9×10^{-7}	[4]
		Morphine	2.4×10^{-7}	[1]
		Sudan I	3.0×10^{-8}	[5]
	Nafion	Ondasetron	3.1×10^{-8}	[6]
	Poly (3,4-ethylene dioxythiophene)	Hydroquinone	3.0×10^{-7}	[7]
		Nitrobenzene	8.3×10^{-8}	[8]
		Dopamine	2.0×10^{-8}	[9]
	Chitin	Cholesterol	1.0×10^{-9}	[10]
	Poly (methacrylic) acid	Allopurinol	6.9×10^{-9}	[11]
Reduced Graphene Oxide	Poly(aminobenzene sulphonic acid)	DNA	3.7×10^{-17}	[12]
	Polypyrrole	NO2-	1.0×10^{-7}	[13]
	Polystyrene	Dopamine	5.0×10^{-6}	[14]
	Poly(o-phenylene diamine)	Chlorotetracycline	1.0×10^{-5}	[15]

Chitosan is an electrically insulating material as is polystyrene; these materials are used to mechanically immobilize and stabilise the catalyst such that its activity arising from nanostructures is preserved under experimental conditions. Such materials may have additional benefits such as anti-fouling effects, increase in active surface area, and it may also act as a pre-concentration medium for the electroanalyte. Utilizing Nafion, which is an ionic conductor as a support material can actually enhance electrocatalysis, the referenced study above suggest there is synergy between the nafion support and the carbon nanotubes that enhance the electron transfer kinetics. Use of conducting polymers such as poly(3,4-ethylenedioxythiophene) and polypyrrole is also known to improve the electron transfer kinetics. Many of the polymer composites can be conveniently prepared through mixing and drop-casting directly onto the electrode. Here, polystyrene is used as an inert structural binder to form a porous conducting structure with carbon microspheres. There are previous studies on polystyrene-based carbon composite materials with graphite [16] and with carbon nanofibres [17] which has been utilized for electro-analytical purposes. Polystyrene is utilized here due to its excellent mechanical properties and low price. In [20], the thermo-plastic nature of polystyrene was exploited to produce pellet electrodes with 66 wt% polystyrene content at 200 ^{0}C. In contrast here only 0.1 wt% polystyrene is applied without heat treatment as an ambient binder. A relatively low wt% was used to preserve the porosity of the material for effective mediation of triple-phase boundary processes.

Oil analysis based on electroanalytical techniques can be performed (i) with samples diluted in organic solvent media [18], (ii) in surfactant solubilised samples [19], (iii) micro-emulsions [20], or (iv) employing oil phase dispersed in a mesoporous carbon/conductor substrate [21,22] to provide an enhanced electrochemically active oil | electrode | aqueous electrolyte triple-phase boundary interface [23]. A considerable area of development of closely related oil-carbon composite electrodes is in electro-analytical paste electrodes [24]. Areas of application are particularly in anti-oxidant content monitoring [25], in oil quality monitoring [26], biofuel testing [27], and in the quantitative detection of impurities or dye additives such as quinizarin.

Quinizarin (see molecular structure in equation 4.1) is water-insoluble in the ambient pH range and has been shown to be electrochemically active. The dye has been proposed as colorant and anti-corrosion coating for anodised aluminium [28]. Molecular quinizarin adsorbed onto carbon has been shown to catalyse the oxygen reduction process [29,30]. Quinizarin has also been shown to act as a Michael-acceptor when oxidised [31] and this has implications in electroanalytical detection of sulphur species. When examined as DNA groove-binding redox reagent, quinizarin has been shown to act as

fluorescence reporter in biological samples [32] and has been investigated as a model system for anti-cancer drug molecules [33]. The main application of quinizarin is as dye-marker additive in hydrocarbon oils [34,35] for safety and tax reasons.

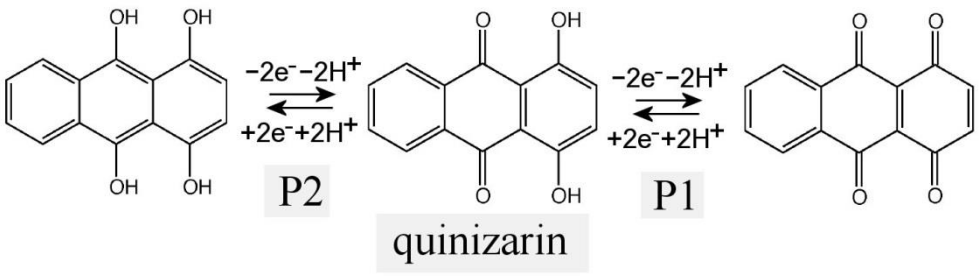

(eq. 4.1)

Methyl laurate is a major component in bio-fuels [36] and employed here as a “model oil” with quinizarin as a ‘’model redox marker’’. The newly developed electroanalytical method based on a carbon microsphere composite electrode could be applied to a wider range of oils containing redox active substances such as anti-oxidants. No electrolyte is added to the oil phase which is deposited directly into a porous carbon electrode made from a composite with glassy carbon microspheres and polystyrene. Figure 4.1 shows a schematic drawing of the electrode with a small amount and with a higher amount of oil deposited. The electrochemical reaction is believed to occur at the triple-phase boundary. A Faradaic current is anticipated as long as the electro-analyte (quinizarin in oil) can diffuse towards the triple-phase boundary, where ions (here protons) present in the neighbouring phase that can balance the build-up of charge resulting from the electron transfer. From an electro-analytical standpoint, not having to alter or prepare the sample before electrochemical analysis is convenient and developing a simple “dip-probe” method could be very useful.

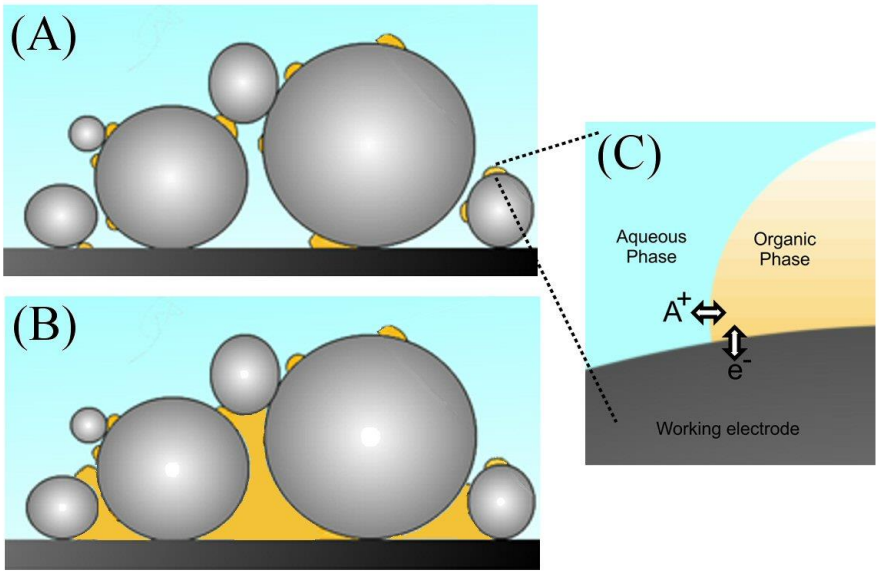

Figure 4.1. Schematic drawings for (A) a carbon microsphere electrode with some oil deposit, (B) a carbon microsphere electrode "flooded" with oil, and (C) a schematic drawing of processes at the triple-phase boundary formed by carbon|oil|aqueous electrolyte.

4.2 Experimental Methods

4.2.1 Reagents

Phosphoric acid (85%, Fisher Scientific), boric acid (99.9995%, Alfa Aesar), acetic acid (99.7%, Aldrich), sodium hydroxide (98%+, Sigma-Aldrich), methyl laurate (97%, Fluka), quinizarin (96%, Aldrich), glassy carbon spherical powder with nominal 2-12 μm diameter (99.95%, Sigma-Aldrich), toluene (99.9%, Sigma-Aldrich), acetonitrile (99%, Sigma-Aldrich), argon (Pureshield, BOC), 0.7 mm diameter 2B graphite pencil lead (Mars micro carbon, Staedtler), and polystyrene (M.W. = 100,000 g mol^{-1}, Aldrich) were purchased and used without further purification. Britton-Robinson buffer was prepared with 0.04 M acetate, 0.04 M borate, and 0.04 M phosphate concentration. Demineralised and filtered water was taken from a Millipore water purification system with not less than 18.2 MΩcm resistivity.

4.2.2 Instrumentation

Voltammetric experiments were performed with a microAutolab III system (Ecochemie, Netherlands) in staircase voltammetry mode. The step potential was maintained at approximately 3 mV. The

counter and reference electrodes were platinum wire and KCl-saturated calomel (SCE, Radiometer), respectively. The working electrode was prepared from a 0.7 mm diameter 2B graphite pencil lead from Staedtler (see below). Solutions were deaerated with argon (Pureshield, BOC). The pH was measured with a glass electrode (3505 pH meter, Jenway). Raman and fluorescence data were obtained on a Renishaw inVia Raman Microscope at 532 nm excitation. Electron microscopy images were obtained on a Jeol 6301F FESEM. All experiments were conducted at a temperature of 20 ± 2 °C.

4.2.3 Procedure: Electrode Fabrication

Glassy carbon spherical powder was dispersed in toluene (0.26 g per cm^3). A separate polystyrene solution in toluene was prepared (0.1 g per cm^3) and 2.6 μL of this added into the carbon dispersion to give 0.1% by weight of polystyrene in the resulting carbon composite. The resulting mixture was pipetted onto the end of a pencil lead (3 μL volume to give 0.78 mg deposit, unless stated otherwise). The toluene was left to evaporate, leaving behind a porous network of glassy carbon microspheres with polystyrene binder visible as a thin film coating of the carbon in scanning electron micrographs (see figure 4.2).

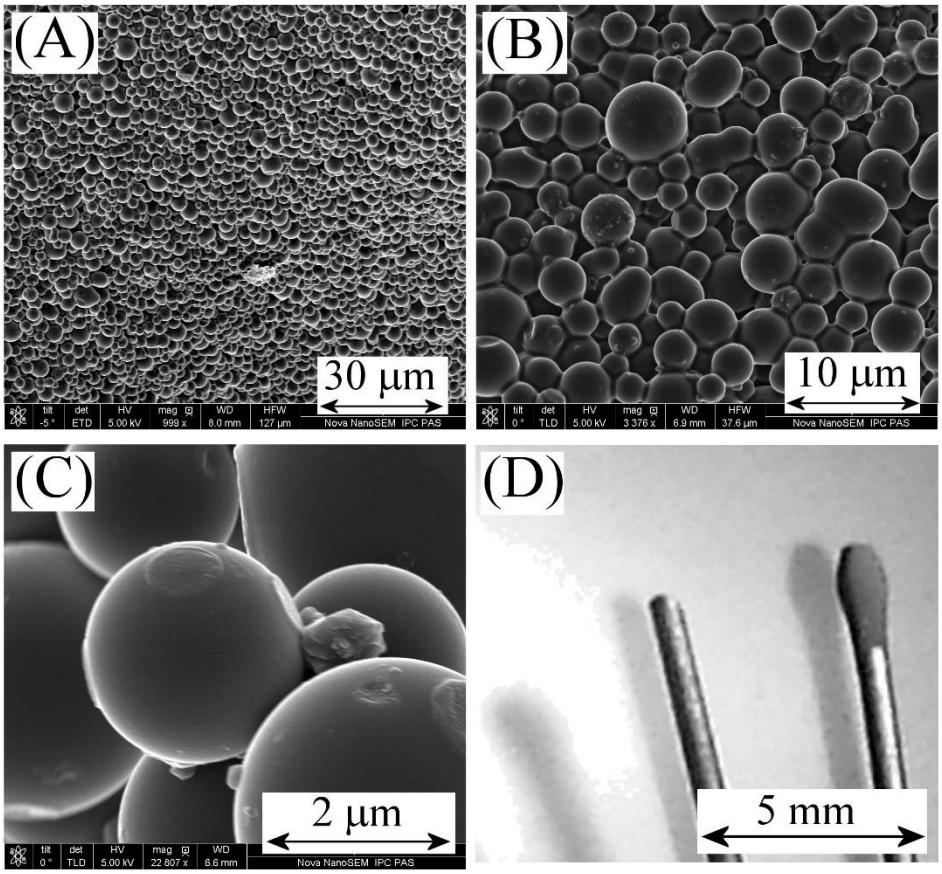

Figure 4.2. (A) Lower magnification and (B,C) higher magnification scanning electron microscopy (SEM) images of the carbon microsphere – polystyrene composite electrode material. (D) Photograph of the uncoated and 0.78 mg carbon microsphere – polystyrene composite coated pencil lead electrode.

4.2.4 Procedure: Triple Phase Boundary Electrochemistry

Quinizarin was dissolved in methyl laurate to give a concentration of 2 mM, which was then diluted with acetonitrile at a ratio of 1:4. The organic solution was pipetted onto the electrode (typically 1.5 μL) and acetonitrile allowed to evaporate to give a final deposit of 0.3 μL methyl laurate containing 2 mM quinizarin. The prepared electrodes were submerged about 1 cm into deaerated aqueous electrolyte solution and left equilibrating for around 5 minutes before each voltammetric measurement.

4.3 Results and Discussions

4.3.1 Carbon Microsphere Composite Voltammetry I: Effect of Methyl laurate

Figure 4.3 shows cyclic voltammograms recorded in buffer solutions over a potential range to reveal information about the capacitance of the electrode with/without carbon microsphere – polystyrene deposits. Perhaps surprisingly, the capacitive currents for a bare pencil lead (Figure 4.3Ai) and for a 0.78 mg carbon microsphere deposit (Figure 4.3Aii) apparently are almost identical (ca. 2 μF). A significant increase in capacitance (Figure 4.3Biii) was only observed after "pre-wetting" in acetonitrile before submerging the electrode in aqueous electrolyte. The polystyrene binder appears to prevent direct wetting of carbon with aqueous electrolyte. However, pre-wetting with the water-miscible solvent allows the electrolyte solution to penetrate into the porous structure. A plot of capacitance versus weight of carbon microsphere deposit (Figure 4.3C) clearly demonstrates this effect. Deposition of methyl laurate into the 0.78 mg carbon microsphere – polystyrene composite also changes the capacitive currents. Figure 4.3D shows how the porous structure is filled with oil. Initially, the capacitance values are low (similar to those for the poorly-wetted carbon microsphere composite), but then the capacitance values increase up to an optimum value (0.3 μL methyl laurate in 0.78 mg carbon) followed by a loss of capacitance when "flooding" occurs at about twice the optimum fill volume. Figure 4.1 shows a schematic drawing of the resulting porous carbon | oil | water interface.

'Pre-wetting' effects on the capacitance of carbon nanofibers were not observed suggesting that polystyrene is responsible for this effect. Although polystyrene is a reasonable binder, the mechanical stability of the carbon microsphere-polystyrene composite is inferior to that of carbon nanofibers. Attempts have been made to produce free standing films of carbon-microsphere-polystyrene composites but the material dispersed when placed at the interface of two immiscible liquids. Application of this particular composite requires a rigid support that can mechanically support the material. Hence application of this particular composite appears more suited for conveniently prepared disposable electrodes.

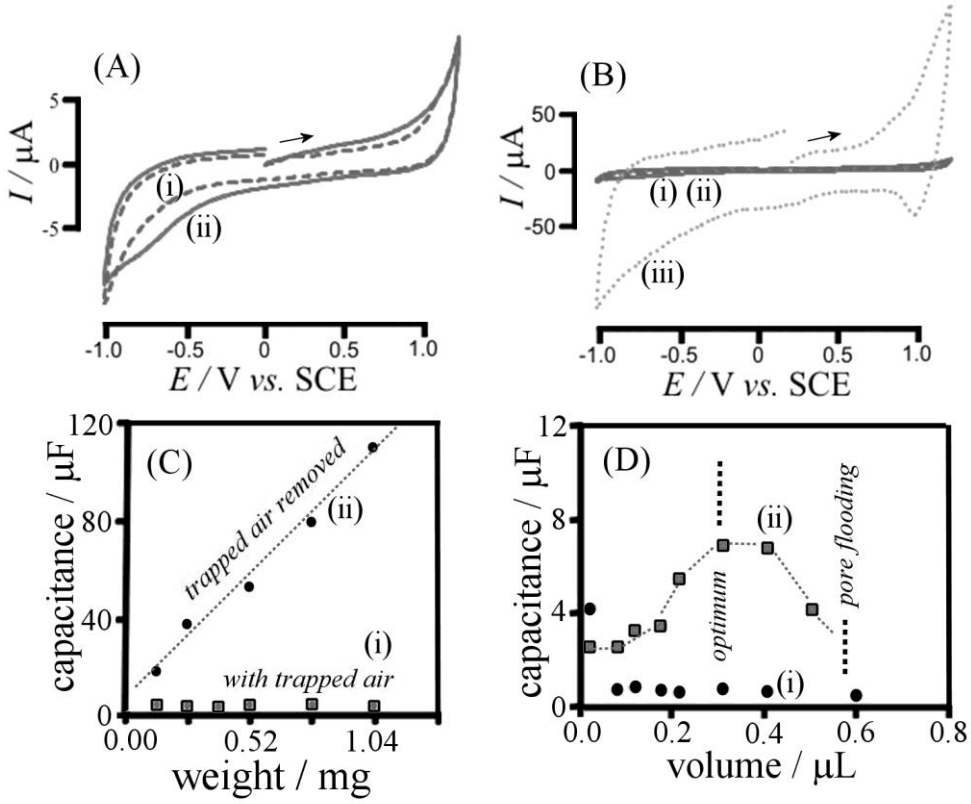

Figure 4.3. (A,B) Cyclic voltammograms (scan rate 1Vs^{-1}) in deaerated Britton-Robinson buffer pH 2.0 of (i) the bare pencil lead electrode, (ii) the pencil lead with 0.78 mg carbon microsphere - polystyrene composite, and (iii) the same but dipped into acetonitrile (to improve wetting) just before immersion into the aqueous phase. (C) Plot of capacitance versus weight of carbon microsphere composite deposit applied (scan rate 0.1 Vs^{-1}) for (i) untreated electrode (ii) electrode dipped in acetonitrile directly before use. (D) Plot of capacitance (determined from cyclic voltammograms at 0.4 Vs^{-1}) versus volume of methyl laurate deposited for (i) the bare pencil lead and (ii) 0.78 mg carbon microsphere – polystyrene deposit.

4.3.2 Carbon Microsphere Composite Voltammetry II: Quinizarin Redox Processes

When quinizarin is added into the methyl laurate oil, two clear redox processes are observed. Figure 4.4A and 4.4B show oxidation process P1 and reduction process P2 at midpoint potentials of +0.77 V vs. SCE and -0.38 V vs. SCE, respectively (see equation 4.1).

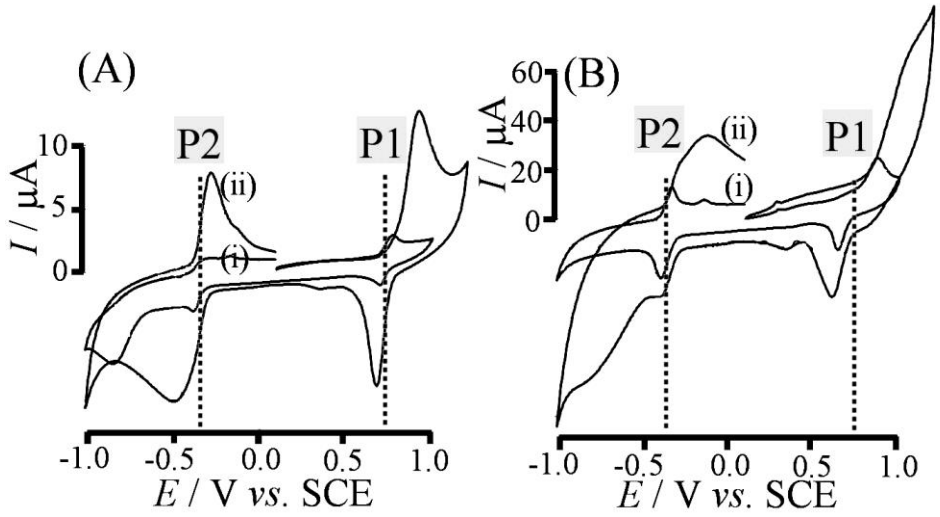

Figure 4.4. Cyclic voltammograms (scan rate (A) 0.05 Vs^{-1} and (B) 1 Vs^{-1}) for (i) solid quinizarin or (ii) 0.3 μL of 2 mM quinizarin in methyl laurate deposited on 0.78 mg glassy carbon microsphere – polystyrene composite and immersed into deaerated Britton-Robinson buffer pH 2.0.

Both processes, oxidation P1 and reduction P2, are observed also when depositing only solid quinizarin into the porous glassy carbon microsphere – polystyrene composite electrode. The presence of ''split peaks'' for both P1 and P2 are indicative of a more complex overall process with more than one reaction pathways. Trace (i) in Figure 4.4 shows the redox behaviour of the solid contrasted with the redox behaviour of the quinizarin in methyl laurate solution in trace (ii). The current response for the solution in oil appears higher and different in particular at lower scan rates. This is due to the diffusion of quinizarin from the bulk oil to the reactive triple-phase boundary (see Figure 4.1). The typical thickness of the carbon microsphere – polystyrene composite deposit is 200 μm (see Figure 4.2D) and therefore with half filling (see Figure 4.3) typically δ = 100 μm diffusion path is available. Methyl laurate has a viscosity of approximately 3 times higher than that of water [37], which suggests a diffusion coefficient of approximately $D = 10^{-10}$ m^2s^{-1} and an estimated diffusion time of $\tau = \frac{\delta^2}{D} = 100$ s, consistent with complete electrolysis requiring several minutes.

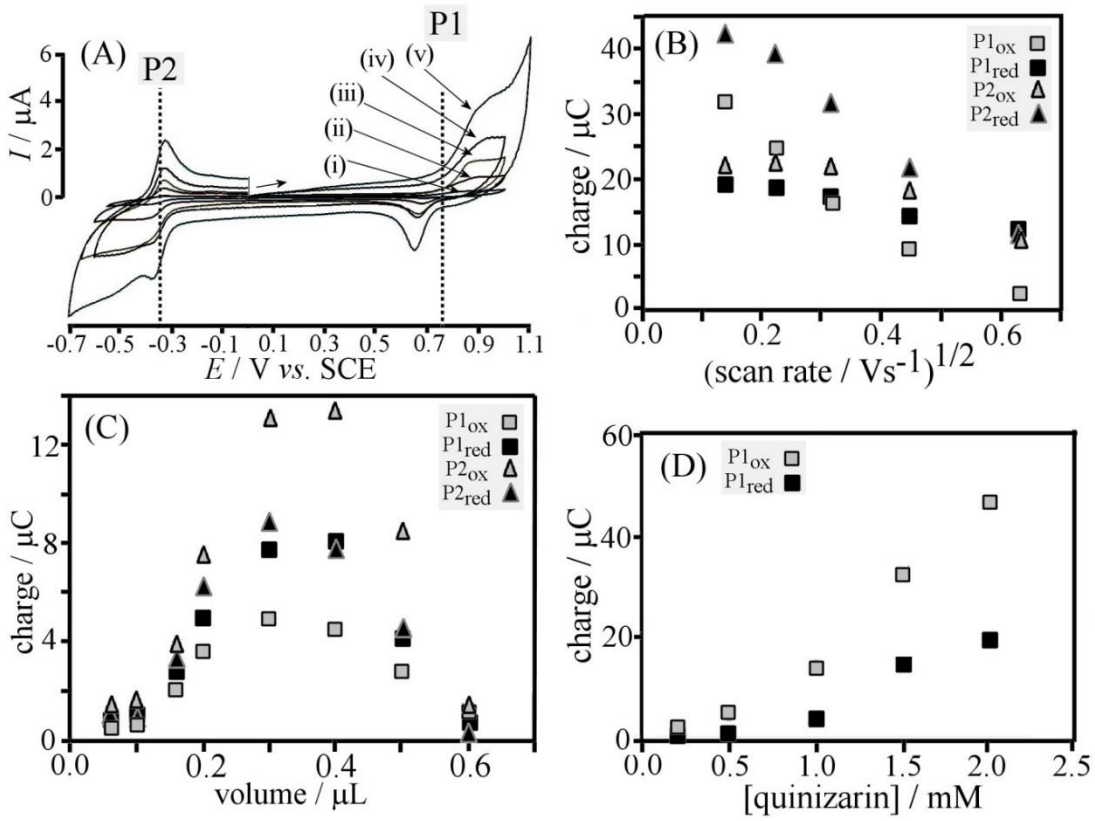

Figure 4.5. (A) Cyclic voltammograms (scan rate (i) 10, (ii) 50, (iii) 100, (iv) 200, and (v) 400 mVs^{-1}) of 0.3 µL 2 mM quinizarin in methyl laurate coated on 0.78 mg carbon microsphere – polystyrene composite deposit. (B) Plot of the approximate charge under the peaks for processes P1 and P2 versus the square root of scan rate. (C) Plot of the approximate charge under the peaks for processes P1 and P2 versus deposition volume (at scan rate 0.4 Vs^{-1}). (D) Plot of the charge under the peaks for process P1 (scan rate 10 mVs^{-1}) versus quinizarin concentration in methyl laurate.

Voltammetric signals of quinizarin in methyl laurate submerged in deaerated Britton-Robinson buffer pH 2.0 are stable, suggesting that chemical decomposition and leaching into the aqueous phase do not occur at significant levels. Figure 4.5A shows a typical set of voltammograms for scan rates from 10 mVs^{-1} to 400 mVs^{-1}. Plot 4.5B shows that approximate charge under the oxidation and reduction peaks when plotted versus the square root of scan rate. The observed charge is not constant (as would be anticipated for complete thin film electrolysis) and shows an approximately linear decrease consistent with a diffusion process in the oil phase. Plot 4.5C shows peak charge data as a function of the volume of methyl laurate deposited. The Faradaic charges for processes P1 and P2 clearly follow the pattern seen in Figure 4.3D for the capacitive current for the "exposed carbon surface". This is in agreement with the hypothesis of a triple-phase boundary process (see Figure 4.1) requiring both the exposed carbon and the liquid|liquid interface for the redox process to happen. Plot 4.5D shows the effect of the quinizarin concentration on the charge under the signal for process P1. There appears to

be some non-linearity in the lower concentration region with an approximate limit of detection currently at approximately at 0.1 mM quinizarin in methyl laurate at a scan rate of 10mVs^{-1} at pH 2.0.

4.3.3 Carbon Microsphere Composite Voltammetry III: pH Effects

Figure 4.6 shows voltammetric data for 2 mM quinizarin oxidation and reduction in methyl laurate as a function of pH. Both oxidation process P1 and reduction process P2 are sensitive to pH and it is possible to estimate the main peak positions as a function of pH (see Figure 4.6C). From linear extrapolation through the midpoint potentials it is possible to see that the slope for the reduction process P2 is 63 mV/pH, which is close to the expected Nernstian value for a 2-electron 2-proton process. For the oxidation process P1 the slope is sub-Nernstian with approximately 39 mV/pH unit, which may be due to an underlying change in the potential across the oil|aqueous phase boundary. A change in the linear behaviour for both processes occurs beyond approximately pH 8 due to the deprotonation (pK_A in water 10 and 11.5 [38]) of the quinizarin under these conditions. For applications in electroanalytical methods, the voltammetric response observed at pH 2.0 gives the most clearly defined signal.

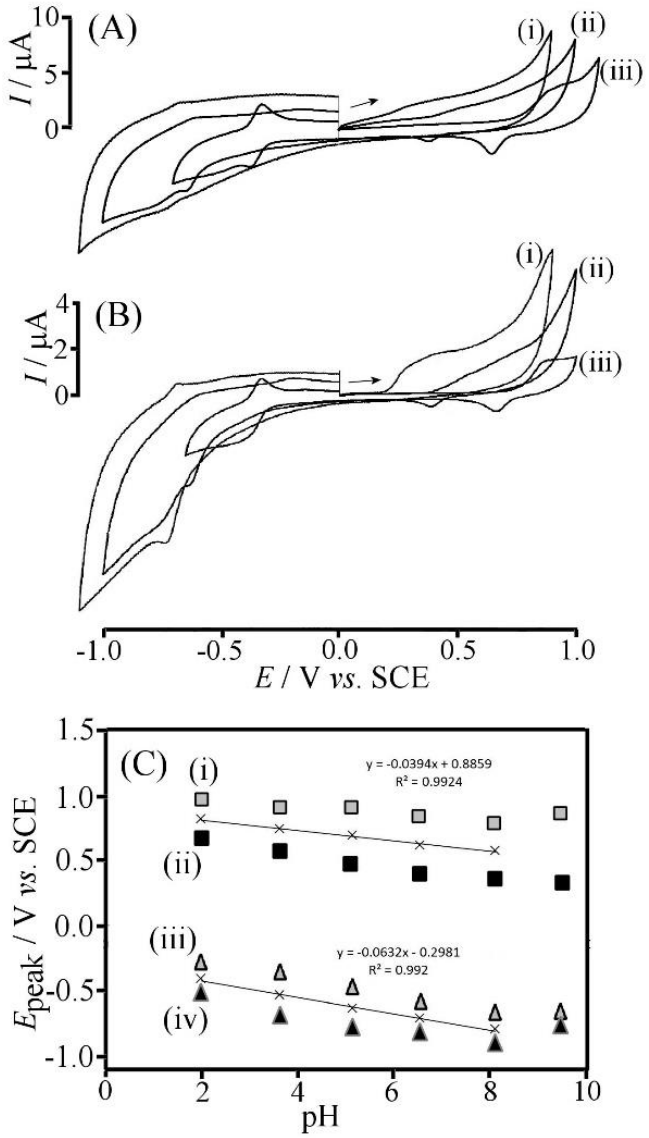

Figure 4.6. Cyclic voltammograms (scan rate (A) 0.4 and (B) 0.1 Vs^{-1}) for 0.3 μL 2 mM quinizarin in methyl laurate deposit on a 0.78 mg composite electrode immersed into deaerated Britton-Robinson buffer at pH (i) 10, (ii) 7.0, and (iii) 2.0. (C) Plot of the peak potentials and midpoint potentials (at scan rate 0.1 Vs^{-1}) versus pH for (i) P1 oxidation, (ii) P1 reduction, (iii) P2 oxidation, and (iv) P2 reduction.

4.3.4 Carbon Microsphere Composite Voltammetry IV: Quinizarin Fluorescence

Figure 4.7 shows a summary of fluorescence and Raman measurements at 532 nm excitation. Methyl laurate does not exhibit any luminescence in its pure form, but quinizarin shows a strong fluorescence in the solid (4.7i) and when dissolved in methyl laurate (4.7ii). This fluorescence is still strong after deposition of the quinizarin in methyl laurate solution onto the carbon microsphere – polystyrene composite electrode (4.7iii). Next, oxidation of quinizarin in methyl laurate was carried out by submerging in Britton-Robinson buffer pH 2.0 and holding at a potential for + 1.0 V vs. SCE for 5 minutes. Fluorescence responses from the sample in contact with aqueous solution were quenched and therefore ex-situ measurements were performed. The resulting fluorescence curve for the oxidised quinizarin in methyl laurate (4.7iv) is very weak and scaled here to also show an underlying Raman signal. The same Raman responses are obtained for only carbon microsphere – polystyrene composite and they are easily identified as the D, G, and 2D bands [39] (572 nm, 581 nm and 620 nm, respectively) for graphitic carbon.

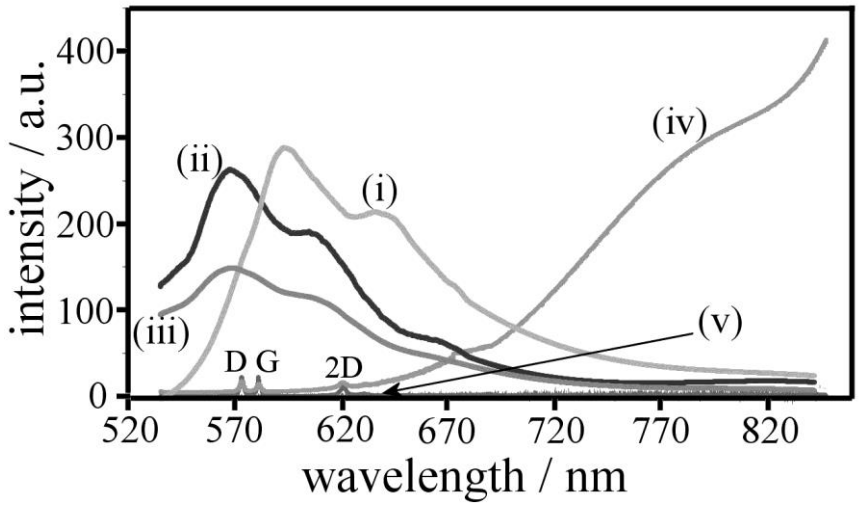

Figure 4.7. Plot showing fluorescence and Raman data for (i) solid quinizarin, (ii) quinizarin dissolved in methyl laurate, (iii) quinizarin in methyl laurate immobilised into carbon microsphere – polystyrene composite before oxidation, (iv) after oxidation, and (v) carbon microsphere composite showing Raman signals. Curves (iv) and (v) were scaled to bring out the Raman features.

The data suggest that quinizarin is dissolved in methyl laurate when immobilised into the porous carbon microsphere – polystyrene composite material and the exhaustive oxidation (5 minutes at +1.0 V vs. SCE) does convert close to all quinizarin in the oil. Therefore oil analysis based on the

electrochemical reaction of the quinizarin dye or similar anti-oxidant additives at the triple-phase boundary at the novel glassy carbon – polystyrene composite electrode is feasible.

4.4 Conclusion

A new type of glassy carbon microsphere – polystyrene composite electrode has been introduced to allow oil sample uptake and electroanalysis under triple-phase boundary conditions. The model case of quinizarin in methyl laurate is investigated and from analysis of the capacitive and Faradaic currents as a function of oil volume it is demonstrated that a volume of 0.3 μL oil in 0.78 mg carbon composite gives optimum voltammetric responses. The use of simple pencil lead substrates and low cost carbon and polymer components as disposable electrode probes can be useful for electro-analytical purposes. The amount of time and energy required for material synthesis compared to carbon nanofibers (see chapter 3) is significantly lower, but the material is not suited for use as a free standing membrane due to its relatively weak structural integrity. In future this method could have wider application for other types of oil and additives.

4.5 References

[1] X. Dai, G.G. Wildgoose, R.G. Compton, “Designer electrode interfaces simultaneously comprising three different metal nanoparticle (Au, Ag, Pd)/carbon microsphere/carbon nanotube composites: progress towards combinatorial electrochemistry,” Analyst, 131, 1241-1247, (2006).

[2] C. Xu, L. Cheng, P. Shen, Y. Liu, “Methanol and ethanol electrooxidation on Pt and Pd supported on carbon microspheres in alkaline media,” Electrochem. Comm., 9, 997-1001 (2007).

[3] H. Kim, M. E. Fortunato, H. Xu, J. H. Bang, K. S. Suslick, “Carbon microspheres as supercapacitors,” J. Phys. Chem. C, 115, 20481-20486, (2011).

[4] A. Babaei, M. Babazadeh, H. R. Momeni, “A sensor for simultaneous determination of dopamine and morphine in biological samples using a multi-walled carbon nanotube/chitosan composite modified glassy carbon electrode,” Int. J. Electrochem. Sci., 6, 1382-1395, (2011).

[5] M. Wu, W. Tang, J. Gu, Q. Wang, P. He, Y. Fang, “Electrochemical detection of Sudan I using a multi-walled carbon nanotube/chitosan composite modified glassy carbon electrode,” Am. J. Anal. Chem., 4, 1-6, (2013).

[6] B Nigovic, M. Sadikovic, M. Sertic, “Multil-walled carbon nanotubes/nafion composite film modified electrode as a sensor for simultaneous determination of ondansetron and morphone,” Talanta, 122, 187-194, (2014).

[7] G. Xu, B. Li, X. Luo, “Carbon nanotube doped poly(3,4-ethylenedioxythiophene) for the electrocatalytic oxidation and detection of hydroquinone,” Sens. Actuators B, 176, 69-74, (2013).

[8] G. Xu, B. Li, X. Wang, X. Luo, “Electrochemical sensor for nitrobenzene based on carbon paste electrode modified with a poly(3,4-ethylenedioxythiophene) and carbon nanotube nanocomposite,” Microchim. Acta, 181, 463-469, (2014).

[9] G. Xu, B. Li, X. T. Cui, L. Ling, X. Luo, “Electrodeposited conducting polymer PEDOT doped with pure carbon nanotubes for the detection of dopamine in the presence of ascorbic acid,” Sens. Actuators B, 188, 405-410, (2013).

[10] Y. Tong, H. Li, H. Guan, J. Zhao, S. Majeed, S. Anjum, F. Liang, G. Xu, “Electrochemical cholesterol sensor based on carbon nanotube@molecularly imprinted polymer modified ceramic carbon electrode,” Biosens. Bioelectron., 47, 553-558, (2013).

[11] B. Rezaei, O. Rahmanian, “Nanolayer treatment to realize suitable configuration for electrochemical allopurinol sensor based on molecular imprinting recognition sites on multiwall carbon nanotube surface,” Sens. Actuators B, 160, 99-104, (2011).

[12] T. Yang, Q. Guan, X. Guo, L. Meng, M. Du, K. Jiao, “Direct and freely switchable detection of target genes engineered by reduced graphene oxide-poly(m-aminobenzenesulfonic acid) nanocomposite via synchronous pulse electrosynthesis,” Anal. Chem., 85, 1358-1366, (2013).

[13] D. Ye, L. Luo, Y. Ding, Q. Chen, X. Liu, “A novel nitrite sensor base on graphene/polypyrrole/chitosan nanocomposite modified glassy carbon electrode,” Analyst, 136, 4563-4569, (2011).

[14] W. Liu, J. Xiao, C. Wang, H. Yin, H. Xie, R. Cheng, “Synthesis of polystyrene-grafted-graphene hybrid and its application in electrochemical sensor of dopamine,” Mater. Lett., 10, 70-73, (2013).

[15] Y. Liu, L. Zhu, Z. Luo, H. Tang, “Fabrication of molecular imprinted polymer sensor for chlortetracycline based on controlled electrochemical reduction of graphene oxide,” Sens. Actuators B, 185, 438-444, (2013).

[16] G. Chen, C. Wu, W. Weng, D. Wu, W. Yan, “Preparation of polystyrene/graphite nanosheet composite,” Polymer, 44, 1781-1784, (2003).

[17] L. Rassaei, M. Sillanpää, M.J. Bonne, F. Marken, “Carbon nanofiber–polystyrene composite electrodes for electroanalytical processes,” Electroanalysis, 19, 1461-1466, (2007).

[18] S.N. Robledo, M.A. Zon, C.D. Ceballos, H. Fernandez, “Qualitative and quantitative electroanalysis of synthetic phenolic antioxidant mixtures in edible oils based on their acid–base properties,” Food Chem., 127, 1361-1369, (2011).

[19] T.A. de Araujo, A.M.J. Barbosa, L.H. Viana, V.S. Ferreira, “Voltammetric determination of tert-butylhydroquinone in biodiesel using a carbon paste electrode in the presence of surfactant,” Coll. Surf. Biointerfaces, 79, 409-414, (2010).

[20] J.D. Watkins, F. Amemiya, M. Atobe, P.C. Bulman-Page, F. Marken, “Liquid vertical bar liquid biphasic electrochemistry in ultra-turrax dispersed acetonitrile vertical bar aqueous electrolyte systems,” Electrochim. Acta, 55, 8808-8814, (2010).

[21] J. Niedziolka, M.A. Murphy, F. Marken, M. Opallo, “Characterisation of hydrophobic carbon nanofiber–silica composite film electrodes for redox liquid immobilisation,” Electrochim. Acta, 51, 5897-5903, (2006).

[22] X.H. Zhang, C.A. Paddon, Y.H. Chan, P.C. Bulman-Page, P.S. Fordred, S.D. Bull, H.C. Chang, N. Rizvi, F. Marken, “Voltammetric antioxidant analysis in mineral oil samples immobilized into boron-doped diamond micropore array electrodes,” Electroanalysis, 21, 1341-1347, (2009).

[23] C.E. Banks, T.J. Davies, R.G. Evans, G. Hignett, A.J. Wain, N.S. Lawrence, J.D. Wadhawan, F. Marken, R.G. Compton, “Electrochemistry of immobilised redox droplets: concepts and applications,” Phys. Chem. Chem. Phys., 5, 4053-4069, (2003).

[24] R.Nissim, R.G. Compton, “Introducing absorptive stripping voltammetry: wide concentration range voltammetric phenol detection,” Analyst, 139, 5911-5918, (2014).

[25] A.J. Blasco, A.G. Crevillen, M.C. Gonzalez, A. Escarpa, “Direct electrochemical sensing and detection of natural antioxidants and antioxidant capacity in vitro systems,” Electroanalysis, 19, 2275-2286, (2007).

[26] A.L. Santos, R.M. Takeuchi, R.A.A. Munoz, L. Angnes, N.R. Stradiotto, "Electrochemical determination of organic compounds in automotive fuels," Electroanalysis, 26, 233-242, (2014).

[27] T. G.G. Barbosa, E.M. Richter, R.A.A. Munoz, "Flow-injection pulsed-amperometric determination of free glycerol in biodiesel at a gold electrode," Electroanalysis, 24, 1160-1163, (2012).

[28] A. Ahmadi, P. Norouzi, M.R. Ganjali, "Study of corrosion resistance of colored anodized aluminum with quinizarin using cyclic voltammetry and impedance measurement methods," Prog. Org. Coatings, 56, 227-233, (2006).

[29] I.B. Dimov, C. Batchelor-McAuley, L. Aldous, R.G. Compton, "The adsorption of quinizarin on boron-doped diamond," Phys. Chem. Chem. Phys., 14, 2375-2380, (2012).

[30] J. Mason, C. Batchelor-McAuley, R.G. Compton, "The adsorption of quinizarin on boron-doped diamond," Phys. Chem. Chem. Phys., 15, 8362-8366, (2013).

[31] D. Nematollahi, A. Sayadi, F. Varmaghani, "Electrochemical study of quinizarin in the presence of arylsulfinic acids: synthesis of new sulfone derivatives of quinizarin," J. Electroanal. Chem., 671, 44-50, (2012).

[32] M.B. Gholivand, S. Kashanian, H. Peyman, "DNA-binding, DNA cleavage and cytotoxicity studies of two anthraquinone derivatives," Spectrocim. Acta A-Mol. Biomol. Spectr., 87, 232-240, (2012).

[33] S. Rossi, C. Tabolacci, A. Lentini, B. Provenzano, F. Carlomosti, S. Frezzotti, S. Beninati, "Anthraquinones danthron and quinizarin exert antiproliferative and antimetastatic activity on murine B16-F1 melanoma cells," Anticancer Research, 30, 445-449, (2010).

[34] R.B. Harrison, L.Y. Heaysman, "Methods for the detection, determination and identification of quinizarin in hydrocarbon oil," Analyst, 86, 566-568, (1961).

[35] K. Field, E.W. Godly, "The determination of quinizarin in hydrocarbon oil," Analyst, 91, 287-289, (1966).

[36] A. Bouaid, M. Martinez, J. Aracil, "Biorefinery approach for coconut oil valorisation: A statistical study," Bioresource Technol., 101, 4006-4012, (2010).

[37] D.S. Viswanath, T.K. Ghosh, "Viscosity of liquids: theory, estimation, experiment, and data," Springer, Berlin, (2007).

[38] G. Fabriciova, J.V. Garcia-Ramos, P. Miskovsky, S. Sanchez-Cortez, "Adsorption and acidic behavior of anthraquinone drugs quinizarin and danthron on Ag nanoparticles studied by Raman spectroscopy," Vibrational Spectroscopy, 34, 273-281, (2004).

[39] R.P. Vidano, D.B. Rischbach, L.J. Willis, T.M. Loehr, "Observation of Raman band shifting with excitation wavelength for carbons and graphites," Solid State Communications, 39, 341-344, (1981).

Chapter 5. Carbon-Polymer of Intrinsic Microporosity Composite Embedded with Redox Active Catalyst

Abstract

Free radical 4-benzoyloxy-2,2,6,6-tetramethylpiperidine-1-oxyl (4B-TEMPO) is water-insoluble and active as an electrocatalyst for primary alcohol oxidations when immobilised at an electrode surface and immersed into an aqueous carbonate buffer solution. To improve the catalytic process, a composite film electrode was developed based on (i) carbon microparticles of 2-12 μm diameter to enhance charge transport and (ii) a polymer of intrinsic microporosity (PIM-EA-TB) with a BET surface area of 1027 m^2g^{-1}. The composite film acts as a highly rigid molecular framework embedded with the free radical catalyst with simultaneous access to aqueous phase and substrate. Catalytic alcohol oxidation in the film follows a mechanism consistent with the substrate reacting near the electrode - film interface (LEk case using Albery-Hillman notation). Reactivity optimisation and screening for a wider range of primary alcohols in conjunction with DFT-based relative reactivity correlation reveals *substrate hydrophobicity* as an important factor for enhancing catalytic currents. The PIM-EA-TB host matrix is proposed to control substrate partitioning and thereby reactivity and selectivity.

Keywords: carbon microspheres, membrane, fuel cell, biofuel, mesoporosity, voltammetry.

Acknowledgements

Dr Antoine Buchard is gratefully acknowledged for running the Density Functional Theory simulations presented in the paper. Dr Mariolino Carta and Prof. Neil McKeown are acknowledged for synthesizing and providing the polymer of intrinsic microporosity.

This work was adaped from

S. D. Ahn, A. Kolodziej, R. Malpass-Evans, M. Carta, N. B. McKeown, S. D. Bull, A. Buchard, and F. Marken, Electrocatalysis, vol. 7, pp. 70-78, (2016). With permission from Springer. Copyright (2016), Science+Business Media New York.

Contents

5.1 Introduction

Green catalytic and electro-catalytic processes are of considerable interest for sustainable development of chemical processes that minimize environmental degradation [1]. Controlling molecular electrocatalyst reactivity within a microporous host environment offers opportunities for (i) improved selectivity due to host – substrate interactions, (ii) increased reactivity due to modified catalyst – substrate interaction, and (iii) control over catalyst density and co-catalyst effects. Electrocatalysis in conventional non-rigid polymer films has been extensively studied [2], [3], [4] but is mechanistically complex with many sub-cases depending on (i) the transport of reactants and products, (ii) the control of pH, (iii) the transport of charge via coupled electron hopping with ion diffusion, (iv) the chemical rate constants, and (v) additional partitioning effects between the bulk reagent phase and the electrocatalytic layer. Here, the case of a polymer of intrinsic microporosity (PIM) [5] acting as a host for electrocatalytically active free radical 4-benzoyloxy-TEMPO is investigated.

TEMPO is a stable nitroxyl based free radical widely utilized in polymer chemistry [6], organic synthesis [7], [8] and electrosynthesis [9]. Recently there have been reports of more unusual applications such as in battery technologies [10] and fuel-cell catalysts [11]. TEMPO undergoes a 1-electron oxidation to $TEMPO^+$ which can be initiated through the use of a sacrificial chemical oxidant or an applied potential. When coupled to an applied potential, TEMPO can mediate transition metal free alcohol oxidations. $TEMPO^+$ stoichiometrically mediates a 2-electron oxidation of alcohols to aldehydes/ketones and becomes reduced to $TEMPO^-$ in the process. The active catalyst $TEMPO^+$ can be regenerated by a 2-electron oxidation of $TEMPO^-$ or through a comproportionation reaction between $TEMPO^-$ and $TEMPO^+$ to reform TEMPO. Electrode kinetics of $TEMPO^-$ oxidation on carbon electrodes is reported to be sluggish [12], while the comproportionation reaction rate is a function of pH and is rapid in alkali conditions [13]. Hence the regeneration of the TEMPO catalyst is complex, with two possible competing processes that are dependent on specific experimental conditions.

The mechanism of TEMPO catalysed alcohol oxidation depends on the pH of the environment. The mechanism first proposed by Semmelhack [14] involves a nucleophilic attack of the alkoxide on to the nitrogen on TEMPO (see fig. 5.3) followed by a hydrogen transfer. TEMPO exhibits selectivity towards primary alcohols in alkali media [15]. In acidic media there is a change in mechanism and a

favoured selectivity towards secondary alcohols [16] but the rate of oxidation is considerably slower than in alkali conditions. In this study, a particularly hydrophobic derivative of the TEMPO catalyst (4-benzoyloxy-TEMPO or 4B-TEMPO) is used as a water-insoluble electrocatalyst immobilised in an intrinsically microporous polymer (PIM) framework.

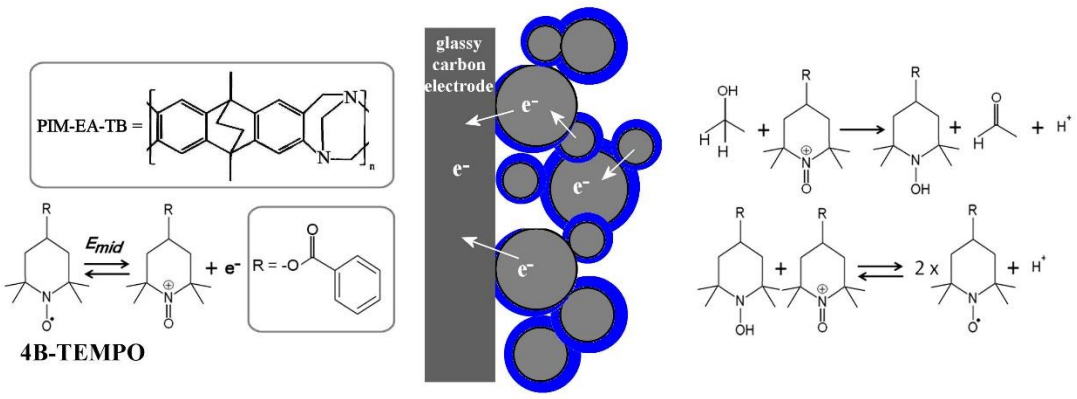

Figure 5.1. Scheme showing (i) the PIM-EA-TB molecular structure, (ii) 4B-TEMPO structure and reactivity, and (iii) a cartoon of the composite film with electrocatalyst embedded in PIM-EA-TB on carbon microspheres.

Polymers of intrinsic microporosity (PIM) provide a new generation of highly rigid microporous materials with (i) excellent processability, (ii) highly rigid pore structures in which guest catalyst molecules can be readily embedded, (iii) good access of solvent and substrate through pores to the catalyst, and (iv) robustness towards corrosion. In previous work by the Marken group, the poly-amine structure PIM-EA-TB [17] has been employed to grow palladium lamellae [18], to act as a host for molecular Fe(II)porphyrinato electrocatalysts [19], and to protect gold nanoparticle catalysts [20]. Recently we have demonstrated proof-of-concept data for the immobilisation of the molecular 4B-TEMPO into a PIM-EA-TB host film for the electrocatalytic oxidation of saccharides [21]. Major limitations in the electrocatalytic process were observed due to low overall currents and a limited reactive interface. Therefore, in this study (i) a three-dimensional electrocatalyst film based on carbon microspheres was developed to increase the reactive interface, (ii) the film thickness and catalyst loading are investigated as process optimisation parameters, and (iii) substrate concentration and its chemical properties are considered as parameters in the overall reaction scheme. It is shown that a wide range of primary alcohols are electrocatalytically oxidised in aqueous carbonate buffer at pH 10.3. As a new feature, the partitioning (accumulation) of the substrate into

the PIM-EA-TB host film is identified as a key step in the heterogeneous electrocatalytic process. In order to dissect molecular electronic versus host-partitioning effects, an approximate DFT model of the reaction is proposed. The rate limiting catalytic step is assumed to be the chemical step involving hydrogen transfer in the TEMPO-alkoxide transition state.

5.2 Experimental methods

5.2.1 Reagents

4-hydroxy-2,2,6,6-tetramethylpiperidine-1-oxyl benzoate (4-benzoyloxy-TEMPO), perchloric acid, dimethylformamide (DMF), sodium hydroxide, sodium bicarbonate, D(+)glucose, sorbitol, methanol, ethanol, 1-propanol, 1-butanol, 1-pentanol, 1-hexanol, benzyl alcohol, 3-pyridinemethanol, 2-pyridinemethanol, 1,3-propandiol, 1,4-dimethanolbenzene and glassy carbon microsphere (2-12um) were purchased from Sigma-Aldrich, TCI Chemicals, or Fisher Scientific and used without further purification. PIM-EA-TB was prepared following a literature protocol [17]. Solutions were prepared with filtered and deionized water of resistivity 18 MΩ cm from a Thermo Scientific water purification system.

5.2.2 Instrumentation

A potentiostat system (Metrohm micro-Autolab II) was employed with a conventional three-electrode cell configuration: a Pt wire as a counter electrode and a KCl-saturated calomel electrode (SCE, Radiometer, Copenhagen) as a reference, and a glassy carbon electrode (BAS) with a diameter of 3 mm as the working electrode.

5.2.3 Procedure: Electrode Preparation

PIM-EA-TB was dissolved in dimethylformamide (DMF) acidified with perchloric acid (ca. 0.5% volume) to make up a stock solution with a concentration of 30mg/ml. 4B-TEMPO stock solution was made up to 28mg/ml in pure DMF. 50μL of PIM stock solution was mixed with 5μL of 4B-TEMPO stock solution, and an additional 45μL of DMF was added with 18mg of solid glassy carbon microspheres. 0.5μL of the resulting mixture was carefully pipetted onto the glassy carbon disc

electrode. The DMF was left to evaporate in a fume hood, and the electrode was used for electrochemical measurements as soon as the DMF evaporated. The final composition of the composite film on the electrode contains 0.71μg of 4B-TEMPO, 7.5μg of PIM, and 179μg of glassy carbon micro-particles. Figure 5.2 shows typical scanning electron micrographs. Pre-conditioning potential cycles (10 cycles at $10mVs^{-1}$) prior to voltammetric measurements were necessary to generate reproducible redox peaks.

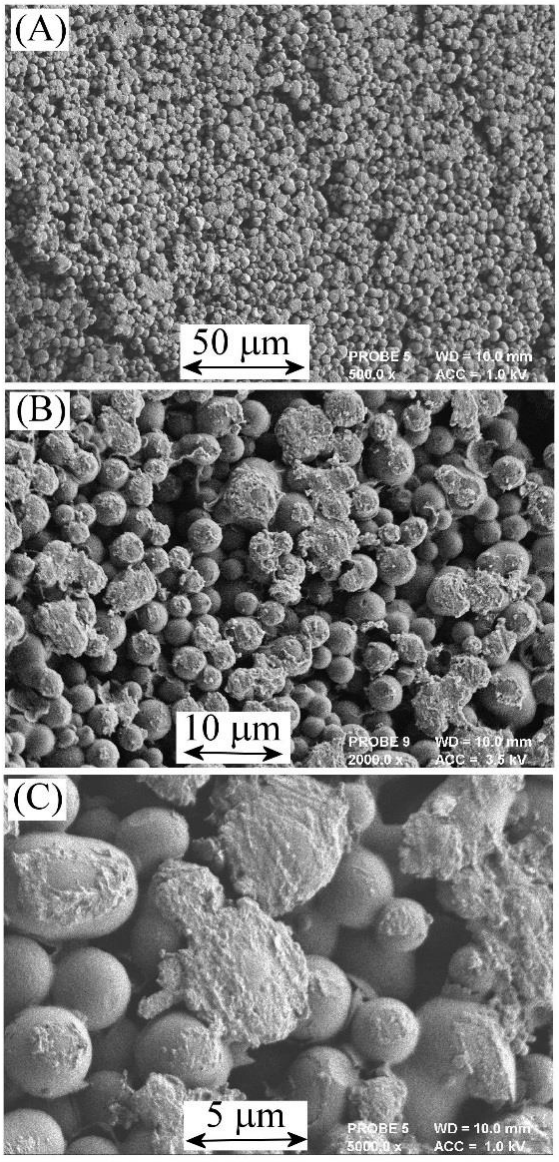

Figure 5.2. SEM images for the composite film with 0.75 μg 4-benzoyloxy-TEMPO/ 7.5 μg PIM-AT-TB/ 179 μg carbon microparticles giving a porous film of approximately 50 μm thickness on a 3 mm diameter electrode. The thickness of the PIM-EA-TB layer around each carbon microparticle is estimated to be 50 nm.

5.2.4. Density Funtional Theory (DFT) Calculation of Kinetic Barriers

The reaction between oxidised 4B-TEMPO$^+$ cation, $NaCO_3^-$ anion and various primary alcohols was examined using DFT calculations. Calculations were performed with Gaussian09 suites of code [23] and protocol rB3LYP/6-311++G(d,p)/SCRF= (cpcm,solvent=water)/ temperature=298.15. The nature of all the stationary points as minima or transition states were verified by calculations of the vibrational frequency spectrum. All transition states were characterized by normal coordinate analysis revealing precisely one imaginary mode corresponding to the intended reaction, and verified by Intrinsic Reaction Coordinates. As expected, the oxidation of alcohols to aldehydes by 4B-TEMPO$^+$ is highly thermodynamically favoured. Calculations also revealed the key hydride transfer step to occur via a cyclic transition state, with an activation barrier low enough for the reaction to happen readily at room temperature. Table 5.1 shows the calculated free enthalpy barriers of this transition state for a series of alcohols. Figure 5.3 illustrates the proposed reaction mechanism. A two-electron transfer occurs formally as hydride transfer from the primary alcohol to the TEMPO$^+$ oxygen.

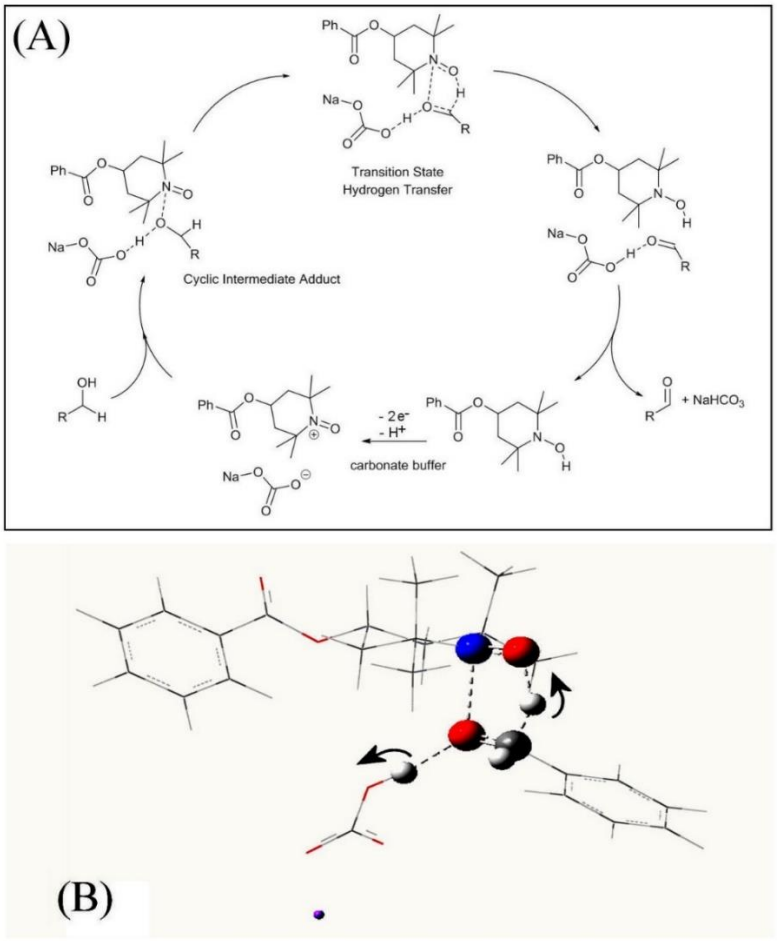

Figure 5.3. (A) Postulated reaction mechanism with cyclic transition state for the hydride transfer. (B) Molecular structure of DFT calculated transition state for the hydrogen transfer step between benzyl alcohol and 4B-TEMPO (red: oxygen, blue: nitrogen, grey: carbon, white: hydrogen, purple: sodium; light blue: displacement vectors of the TS imaginary frequency). Image obtained with GaussView 5.0.8.

A summary of the calculated barriers in kJ mol^{-1} is given in Table 5.1. For molecules with multiple primary alcohol moieties, only one calculation was performed. Additional octanol-water partitioning constant data ($logP_{OW}$) are included in this table.

Table 5.1. Summary of DFT calculation results in terms of the approximate activation barrier for the two-electron transfer process converting a primary alcohol to an aldehyde. Additional data for the logarithm of the octanol-water partion coefficient ($logP_{OW}$) were attained from ACD labs.

	Substrate	**log(P_{OW})**	**DFT energy barrier / kJmol^{-1}**
(i)	α-D-glucose	-2.5	19.0
(ii)	D-sorbitol	-2.0	11.2
(iii)	1,3-propanediol	-1.07	18.5
(iv)	methanol	-0.72	15.2
(v)	ethanol	-0.31	20.3
(vi)	propan-1-ol	0.34	19.9
(vii)	butan-1-ol	0.78	20.1
(viii)	pentan-1-ol	1.65	18.8
(ix)	hexan-1-ol	1.94	19.0
(x)	4-pyridine-methanol	0.06	13.6
(xi)	3-pyridine-methanol	0.03	14.4
(xii)	1,4-benzenedimethanol	0.67	9.42
(xiii)	benzylalcohol	1.26	13.1

5.3 Results and Discussion

5.3.1 Reactivity of 4B-TEMPO Embedded in PIM-EA-TB/Carbon Microsphere Films I.: Charge Transport

The effect of glassy carbon microparticles of nominal 2 to 12 μm diameter on the electrochemical reactivity of 4B-TEMPO immobilised at a 3 mm diameter glassy carbon electrode is dramatic. Figure 5.4A shows cyclic voltammetry data for 4B-TEMPO deposited on its own, when embedded into PIM-EA-TB, and when embedded into PIM-EA-TB with glassy carbon microparticles. The current increased by an order of magnitude with the presence of microparticles, consistent with an increase in the surface area and improved flow of electrons, ions and electrolyte through the film (see scheme in Figure 5.1).

In Figure 5.4B and 5.4C the effect of scan rate on voltammetric currents is compared in PIM films with/without carbon microparticles and a further important effect is observed. In the 4B-TEMPO – PIM-EA-TB film (Figure 5.4B) a reversible oxidation – reduction redox process is seen at ca. E_{mid} = +0.63 V vs. SCE. The charge under the oxidation and reduction peaks are scan rate dependent, they both decrease at faster scan rates. The double logarithmic plot in Figure 5.4B has a slope of approximately -1/2 which is consistent with a diffusion controlled charge transport process within the 4B-TEMPO – PIM-EA-TB film. In contrast, a similar plot of data for the 4B-TEMPO – PIM-EA-TB – carbon microparticle film shows a transition to thin film behaviour (complete film electrolysis) at a scan rate of approximately 20 mVs^{-1} (Figure 5.4C). The approximate time for complete electrolysis in this film is therefore given by dimensional analysis as $\tau = \frac{RT}{v_{trans}F} \approx 1s$ (with the gas constant, *R*, the absolute temperature, *T*, the Faraday constant, *F*, the film thickness, δ, and the electrochemical charge diffusion coefficient, *D*). Transport of charges in the film may be dominated either by inter-molecular hopping of electrons (starting at the electrode surface) or by ion diffusion (from the solution phase).

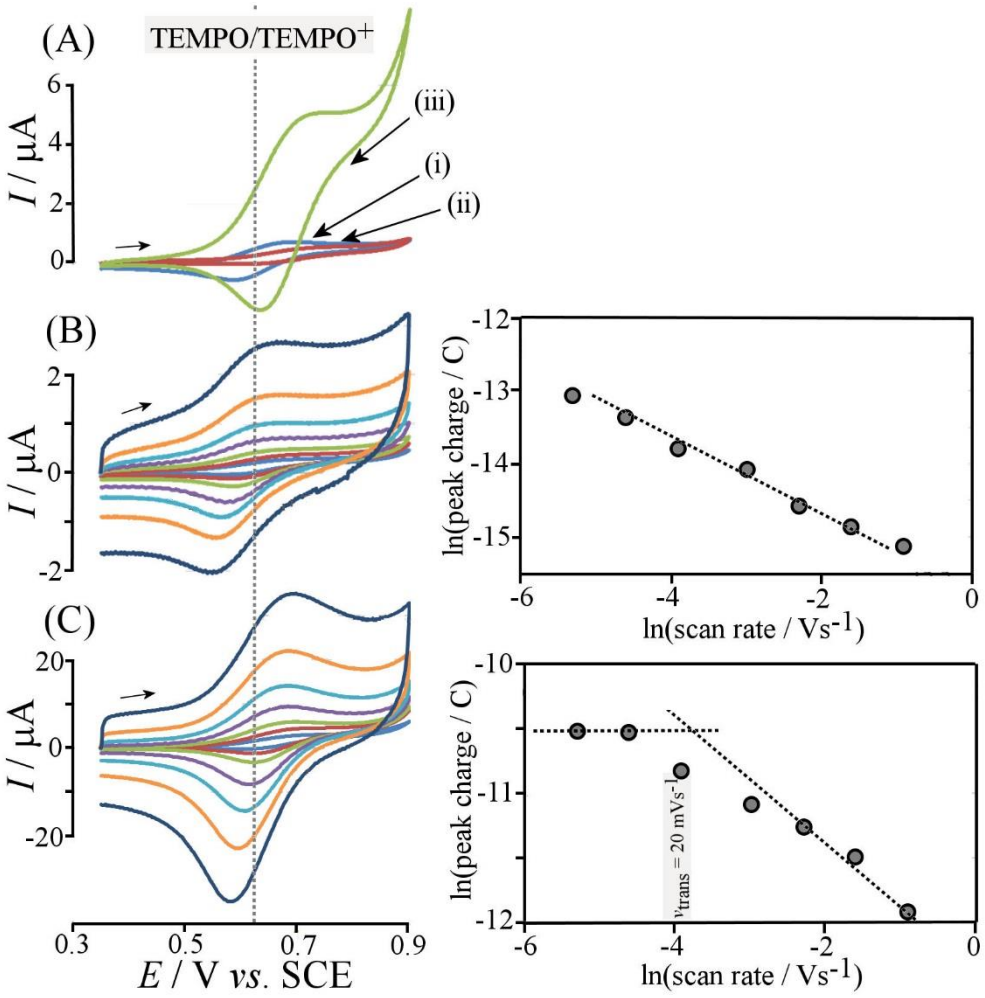

Figure 5.4. (A) Cyclic voltammograms (scan rate 10 mVs^{-1}; in 0.1 M carbonate buffer pH 10.3) for 0.75 µg of 4B-TEMPO immobilised on a 3 mm diameter glassy carbon electrode (blue), immobilised within 7.5 µg PIM-EA-TB (red), and immobilised in 7.5 µg PIM-EA-TB + 179 µg carbon microparticles (green). (B) Cyclic voltammograms (scan rates (i) 5, (ii) 10, (iii) 20, (iv) 50, (v) 100, (vi) 200, and (vii) 400 mVs^{-1}) for 0.75 µg 4B-TEMPO. Inset shows peak charge versus scan rate. (C) As before for 7.5 mg 4B-TEMPO. Inset shows peak charge versus scan rate.

The transport of charges in the composite film is likely to be complicated, with the amount of 4B-TEMPO in the film affecting the mechanism of the process. Assuming a diffusion-like charge propagation mechanism, it is possible to estimate the oxidative charge diffusion coefficient from $\tau = \frac{\delta^2}{\pi D}$ as $D \approx 10^{-15}$ m^2s^{-1} (based on $\delta \approx 50$ nm, see Figure 5.2), which is consistent with typical charge hopping processes [22]. Assumptions made are that all of the 4B-TEMPO deposited are evenly distributed in the PIM film, and that its diffusion coefficient remains constant for the duration of electrochemical measurements.

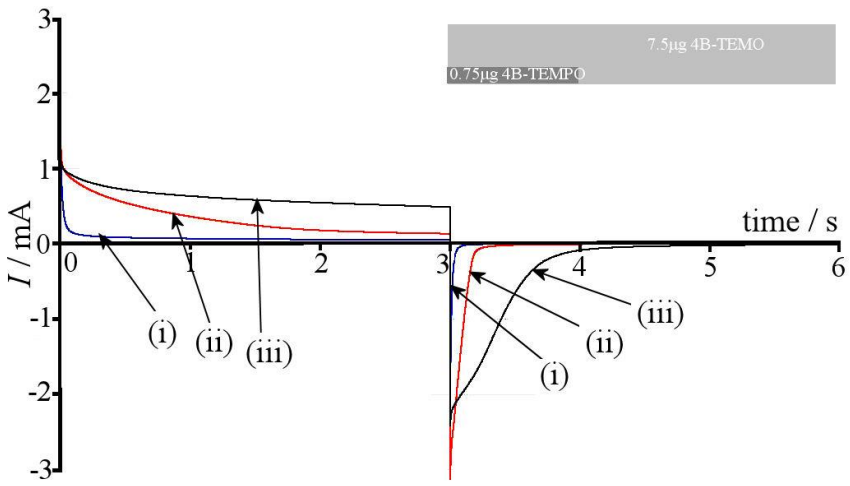

Figure 5.5. Chronoamperometry data for the oxidation (0.9 V vs. SCE) and back-reduction (0.0 V vs. SCE) of (i) 0.0, (ii) 0.75, and (iii) 7.5 µg of 4B-TEMPO immobilised in 7.5 µg PIM-EA-TB with 179 µg glassy carbon microparticles (2-12 µm diameter) immersed in 0.1 M carbonate buffer pH 10.3. The pale grey and dark grey areas correspond to the charge anticipated to flow for 7.5 µg and 0.75 µg 4B-TEMPO conversion respectively.

Further complexity in the charge transport is revealed in chronoamperometry data (Figure 5.5). The applied potential was initially stepped up to an oxidation potential of +0.9 V vs. SCE followed by a step down to 0.0 V vs. SCE. Without 4B-TEMPO (trace i) only short charging currents are recorded. With 0.75 µg 4B-TEMPO immobilised, oxidation of 4B-TEMPO occurs within a couple of seconds. The back-reduction appears to be somewhat faster (see trace ii) and associated with less charge. For 7.5 µg 4B-TEMPO immobilized in 7.5 µg PIM-EA-TB (see trace iii) the oxidation appears to be slower, but the back-reduction again occurs within a one second period and with a shape more typical of a moving reaction boundary than that of a Cottrellian diffusion process. The excess anodic current (also visible as background anodic current in the cyclic voltammetry data shown in figure 5.4) is currently not fully understood, but the 4B-TEMPO oxidation response appears chemically reversible and stable enough for electro-catalytic processes to be driven.

5.3.2 Reactivity of 4B-TEMPO Embedded in PIM-EA-TB/Carbon Microsphere Films II.: D(+)-Glucose Oxidation

The oxidation of glucose can serve as an important model system to assess the electrocatalytic activity of immobilised 4B-TEMPO. In a recent study it has been shown that this process while feasible, exhibited relatively low catalytic efficiency [21]. Here, the effect of introducing glassy carbon microparticles on the electrocatalytic current is investigated. The effect of pH on 4B-TEMPO is shown in figure 5.7A. There is a decrease in peak current with an increase in pH of the carbonate buffer from 9.3 to 10.3 and to 11.3. This trend could be due to the pH affecting charge transport. It is known that TEMPO catalysts in homogeneous solutions produce higher catalytic currents in more alkaline conditions, however when immobilised, additional detrimental effects are possible. This is demonstrated in Figure 5.7D where the effect of glucose concentration and pH are summarised. The plot shows a typical increase in catalytic current (see Figure 5.7C) with glucose concentration but also a loss of activity when the solution is too alkaline. This can be attributed to either slower charge transport or loss of catalyst due to side reactions as suggested by Brown et al. [12]. A solution pH of 10.3 appears to be a good compromise and is therefore used for most of the experiments performed in this study.

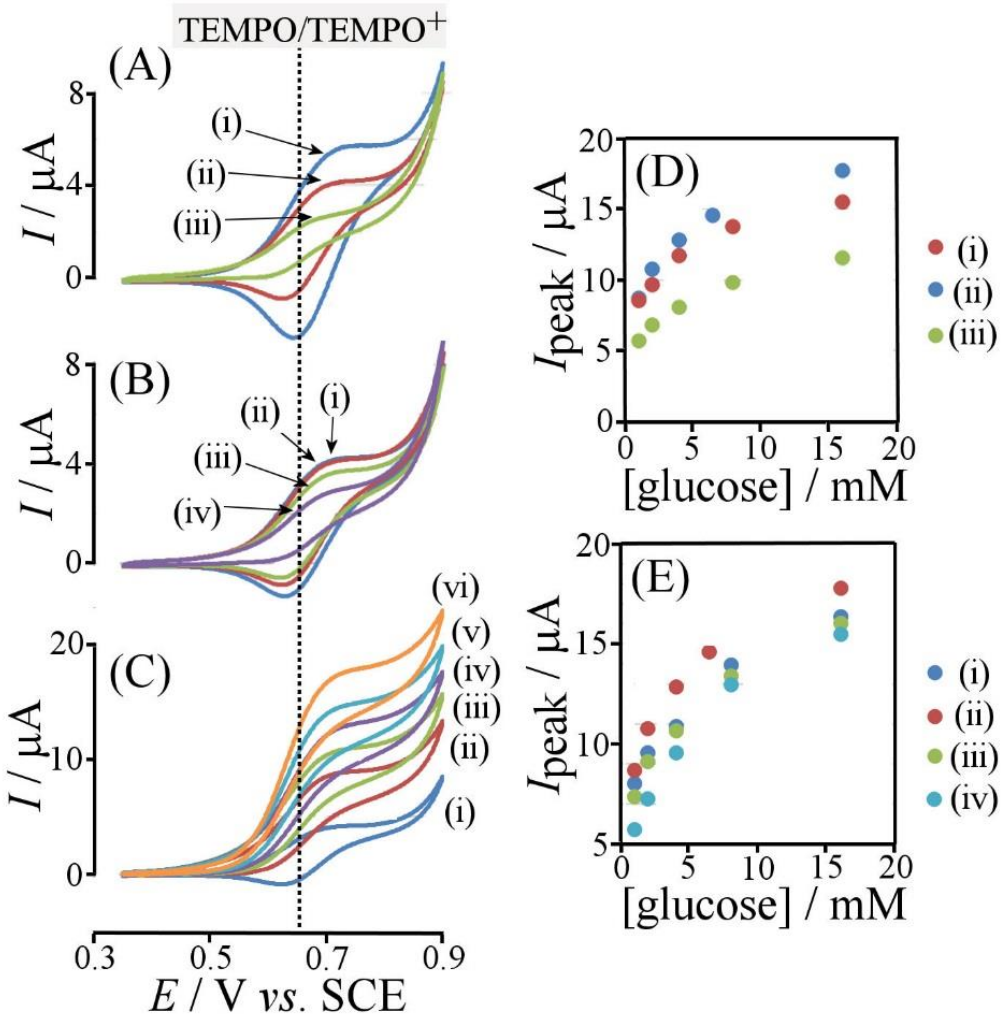

Figure 5.7. (A) Cyclic voltammograms (scan rate 10 mVs^{-1}; in 0.1 M carbonate buffer with pH (i) 9.3, (ii) 10.3, and (iii) 11.3) for 0.75 μg 4B-TEMPO/ 7.5 μg PIM-EA-TB/ 179 μg carbon microparticles immobilised on a 3 mm diameter glassy carbon disk electrode. (B) As above but at pH 10.3 in (i) 0.05, (ii) 0.1, (iii) 0.2, and (iv) 1.0 M carbonate buffer. (C) As above in 0.1 M carbonate buffer at pH 10.3 with addition of (i) 0, (ii) 1, (iii) 2, (iv) 4, (v) 8, and (vi) 16 mM glucose. (D) Plot of peak currents versus glucose concentration at pH (i) 9.3, (ii) 10.3, and (iii) 11.3. (E) Plot of peak current versus glucose concentration at pH 10.3 for (i) 0.05, (ii) 0.1, (iii) 0.2, and (iv) 1.0 M carbonate buffer.

The effect of adding carbon microparticles into the catalyst film is significant with an order of magnitude increase in glucose oxidation. The effect of ionic strength is demonstrated in Figure 5.7B and 5.7E. Charge transport appears to be impeded by increasing ionic strength. Measurements in the presence of glucose suggest that a good compromise is reached at 0.1 M carbonate buffer. There appears to be a non-linear increase in catalytic current with glucose concentration for all conditions studied, suggesting a saturation effect of the substrate in the film or on the catalyst. Next, the effect of 4B-TEMPO concentration in the catalytic film is investigated.

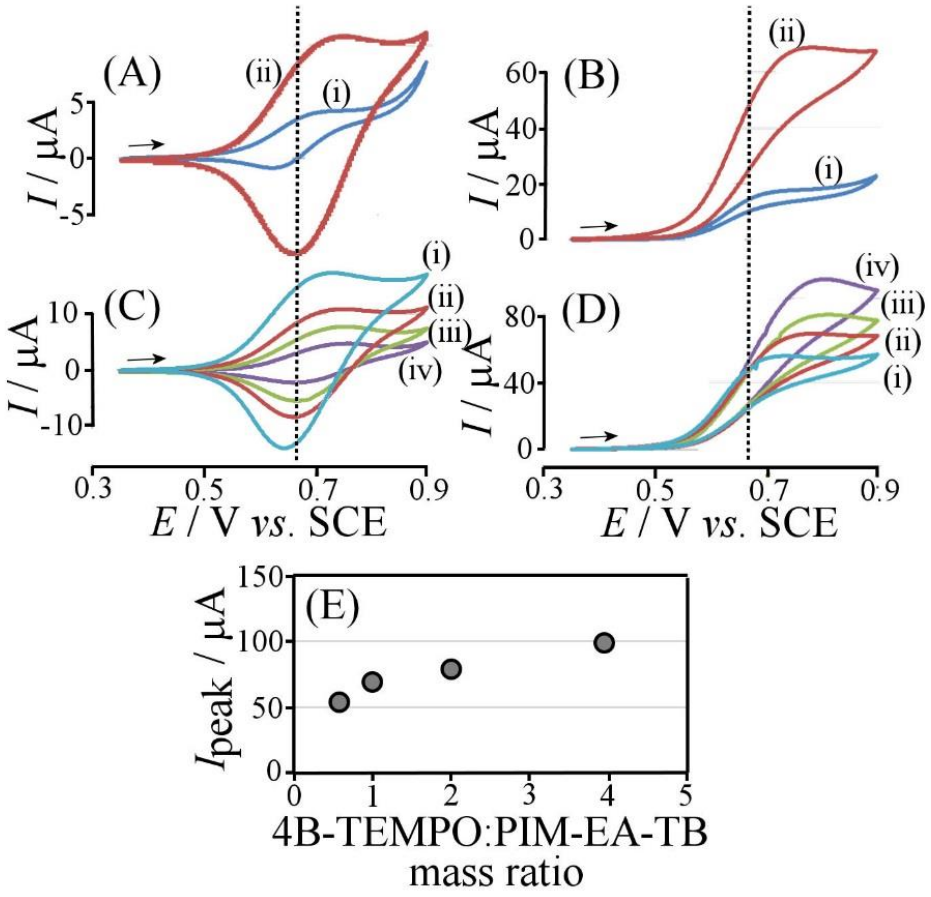

Figure 5.8. (A) Cyclic voltammograms (scan rate 10 mVs^{-1}; in 0.1 M carbonate buffer pH 10.3) with 7.5 µg PIM-EA-TB and 179 µg carbon microparticles and with (i) 0.75 µg 4B-TEMPO and (ii) 7.5 µg 4B-TEMPO at a 3 mm diameter glassy carbon electrode. (B) As above but with 16 mM glucose. (C) As above but with 0 mM glucose, with 7.5 µg 4B-TEMPO, and with (i) 12.7, (ii) 7.5, (iii) 3.7, and (iv) 1.9 µg PIM-EA-TB. (D) As above but with 16 mM glucose. (E) Plot of the peak current versus 4B-TEMPO:PIM-EA-TB mass ratio indicating that a lower 4B-TEMPO concentration lowers the catalytic efficiency.

Figure 5.8 shows that increasing the amount of 4B-TEMPO by 10 times (with the amount of PIM-EA-TB and carbon microparticles fixed) increases both the Faradaic current in the absence of glucose and the catalytic current in the presence of glucose significantly. Increasing the concentration of TEMPO by reducing the amount of PIM-EA-TB (with a fixed amount of 4B-TEMPO and carbon microparticles) has a less dramatic effect. In this case, catalytic glucose oxidation currents can be increased but the electrode also becomes unstable possibly due to the saturation of the PIM framework leading to the loss of catalyst due to crystallisation or leaching into the solution phase. A 4B-TEMPO:PIM-EA-TB mass ratio of approximately 1:1 results in stable currents and is therefore a good compromise.

5.3.3 Reactivity of 4B-TEMPO Embedded in PIM-EA-TB/Carbon Microsphere Films III.: Primary Alcohol Oxidation

Figure 5.8A shows cyclic voltammograms in the presence of four different primary alcohols: (i) 4 mM ethanol, (ii) 4 mM glucose, (iii) 4 mM 3-pyridinemethanol, and (iv) 4 mM benzyl alcohol. The catalytic current changes significantly depending on the substrate used, indicating that the rate limiting process is dependent on the properties of the substrate. A plot of the catalytic current with substrate concentrations fixed at 4 mM versus the logarithmic octanol-water partition coefficient (see Figure 5.8C) shows a degree of correlation in particular for a given class of substrates such as the n-alkyl alcohols.

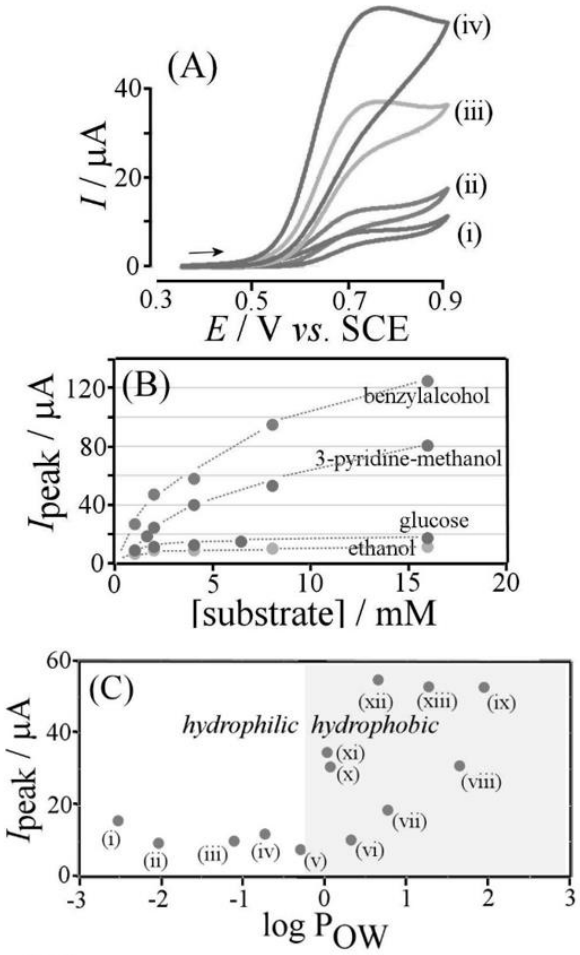

Figure 5.8. (A) Cyclic voltammograms (scan rate 10mVs^{-1}; in 0.1 M carbonate buffer pH 10.3) with 0.75 μg 4B-TEMPO + 7.5 μg PIM-EA-TB + 376 μg carbon microparticles on a 3 mm diameter glassy carbon electrode in the presence of (i) 4 mM ethanol, (ii) 4 mM glucose, (iii) 4 mM 3-pyridine-methanol, (iv) 4 mM benzylalcohol. (B) Plot of peak current versus substrate concentration. (C) Plot of peak current versus logP_{OW} (octanol-water partitioning coefficients) for 4 mM of (i) glucose, (ii) sorbitol, (iii) 1,3-propanediol, (iv) methanol, (v) ethanol, (vi) 1-propanol, (vii) 1-butanol, (viii) 1-

pentanol, (ix) 1-hexanol, (x) 4-pyridine-methanol, (xi) 3-pyridine-methanol, (xii) 1,4-benzene-dimethanol, and (xiii) benzylalcohol.

Assuming a homogenous film at steady state conditions, the transport of electrons and reactants in the catalytic film can be modelled through analytical models derived by Albery and Hillman [2] and Saveant [3]. The reaction location depends on the relative rates of transport of electrochemical charge and substrate through the film. The main cases and their corresponding analytical models are outlined in the diagram and table below. The case of catalysis directly on the film-electrolyte interface is omitted given the slow rate of electrochemical charge transport. Alcohol oxidation directly on the electrode surface is also not included.

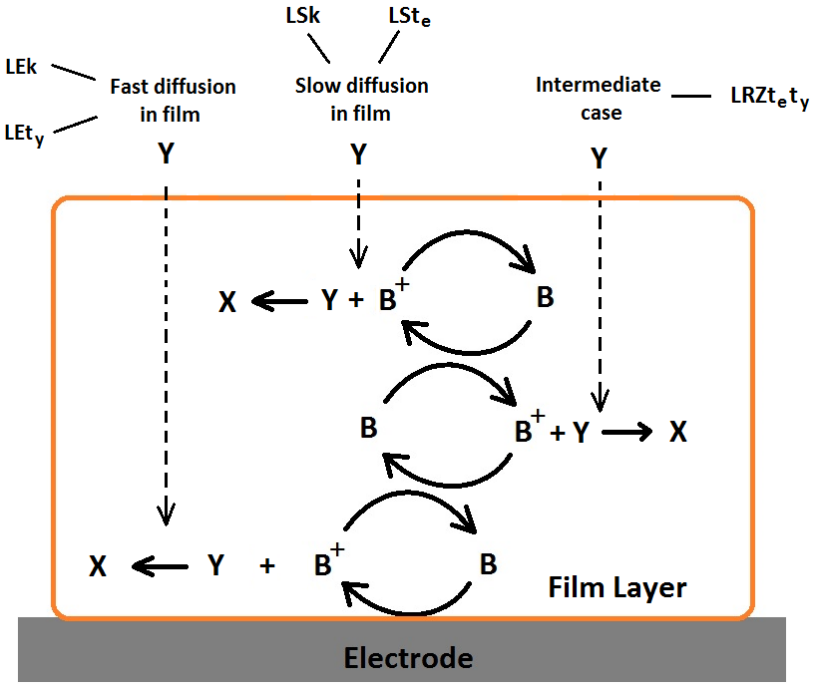

Figure 5.9 Illustration of five electrocatalytic cases in films depending the rate of transport of substrate Y relative to the rate of electrochemical charge propagation (through catalyst B).

Table 5.2. Six different kinetic cases depending on the location of catalytic activity. Following the notation of Albery and Hillman. Case labels; L stands for film layer, S stands for electrolyte solution, E stands for electrode, t with subscript e or y stands for mass transport limits for electrochemical charge and substrate y respectively. k'_{Me} is the electrochemical rate constant and j_0 is the flux of electrons which is directly proportional to current. K is the partition constant into the catalytic film, k is the kinetic rate constant of reaction between catalyst and substrate, b_0 is the concentration of catalyst B at the electrolyte-film interface, D_Y is the diffusion coefficient of substrate Y in the film, L is the film thickness, y_s is the concentration of substrate Y at the electrolyte-film interface, D_e is the diffusion coefficient of electrochemical charge in the film.

Case	Location	k'_{Me}	$j_0 = k'_{Me}y_s$
LSk	Near the film-electrolyte interface (in the film)	$K(kb_0D_Y)^{1/2}$	$y_sK(kb_0D_Y)^{1/2}$
LSt_e		D_eb_0/Ly_s	D_eb_0/L
$LRZt_et_y$	Narrow reaction zone in film	$(D_eb_0/Ly_s)+(KD_Y/L)$	$(D_eb_0/L)+(y_sKD_Y/L)$
LEk	Near the electrode-film interface (in the film)	$Kb_0(D_ek/y_s)^{1/2}$	$Kb_0(y_sD_ek)^{1/2}$
LEt_y		KD_Y/L	y_sKD_Y/L
Lk	Throughout the film layer	$KkLb_0$	y_sKkLb_0

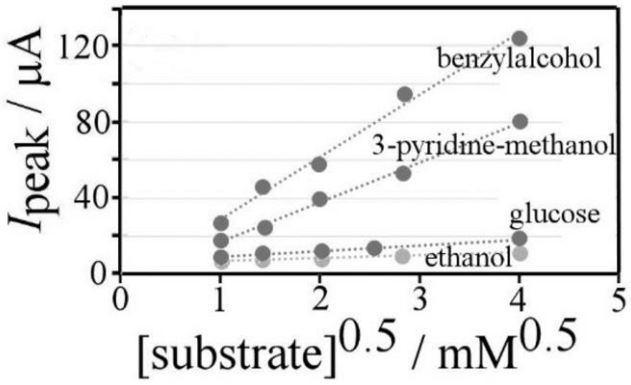

Figure 5.10. A plot of the catalytic current of (i) ethanol (slope=1.52, R^2=0.93, SE=0.596), (ii) glucose (slope=2.95, R^2=0.97, SE=0.703), (iii) 3-pyridinemethanol (slope=20.6, R^2=0.99, SE=2.10) and (iv) benzyl alcohol (slope=32.5, R^2=0.99, SE=5.32) as a function of the square root of substrate concentration.

The model gives the relation between substrate concentration and electron flux j_0 which is directly proportional to the steady state current. The four substrates considered exhibit a square root dependence of substrate concentration on the catalytic current which is consistent with the LEk case. This is where the rate of substrate transport in the film is faster than the rate of electrochemical charge propagation, hence the reaction location is near the electrode-film interface.

5.3.4 Reactivity of 4B-TEMPO Embedded in PIM-EA-TB/Carbon Microsphere Films IV.: Comparisons with Kinetic Simulations from Density Functional Theory

DFT calculations based on the catalytic mechanism first suggested by Semmelhack where the rate limiting step is hydrogen transfer within the cyclic TEMPO-alkoxide transition state (see figure 5.3) is utilized. The activation energy for hydrogen transfer is calculated from which the Arrhenius rate constant can be derived using the equation below.

$$k = Ae^{\frac{-E_a}{RT}} \qquad \text{(eq. 5.1)}$$

Here, k is the rate constant, A is the pre-exponential factor, E_a is activation energy, R is the ideal gas constant and T is the absolute temperature. DFT calculations of the activation energy of hydrogen transfer are shown below in table 5.3 along with the logarithmic octanol/water partition coefficient.

Table 5.3. Hydrogen transfer energy barriers calculated using DFT with corresponding log P and catalytic currents for a given substrate at 4mM concentration in pH 10.3 carbonate buffer.

	Substrate	**log(P_{OW})**	**DFT Barrier (kJ/mol)**	**Arrhenius rate constant**	**Icat /A**
(i)	α-D-Glucose	-2.5	19.0	4.66 x 10^{-4}	1.54 x 10^{-5}
(ii)	D-Sorbitol	-2	11.2	1.10 x 10^{-2}	9.40 x 10^{-6}
(iii)	1,3-propanediol	-1.07	18.4	5.86 x 10^{-4}	1.03 x 10^{-5}
(iv)	Methanol	-0.72	15.2	2.18 x 10^{-3}	1.21 x 10^{-5}
(v)	Ethanol	-0.31	20.3	2.71x 10^{-4}	8.20 x 10^{-6}
(vi)	Propan-1-ol	0.34	19.9	3.26 x 10^{-4}	1.03 x 10^{-5}
(vii)	Butan-1-ol	0.78	20.0	3.07 x 10^{-4}	1.85 x 10^{-5}
(viii)	Pentan-1-ol	1.65	18.8	5.10 x 10^{-4}	3.10 x 10^{-5}
(ix)	Hexan-1-ol	1.94	19.0	4.70 x 10^{-4}	5.28 x 10^{-5}
(x)	4-pyridine-methanol	0.06	13.5	4.22 x 10^{-3}	3.08 x 10^{-5}
(xi)	3-pyridine-methanol	0.03	14.4	3.05 x 10^{-3}	3.40 x 10^{-5}
(xii)	1,4-benzenedimethanol	0.67	9.4	2.25 x 10^{-2}	5.47 x 10^{-5}
(xiii)	Benzylalcohol	1.26	13.0	5.19 x 10^{-3}	5.30 x 10^{-5}

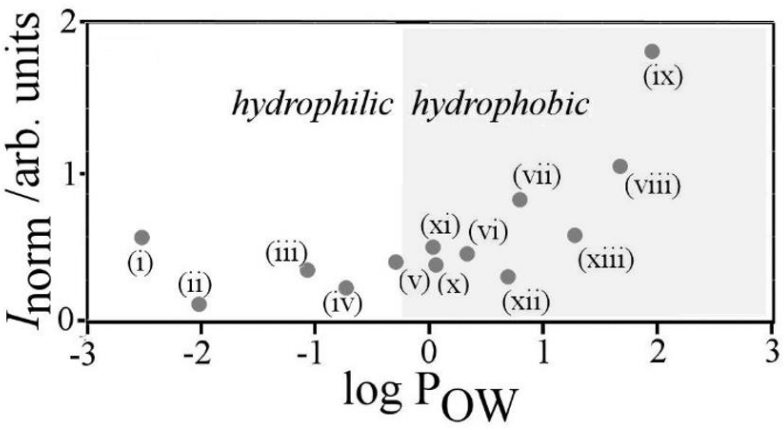

Figure 5.11 Plot of the normalised peak current (peak current divided by the square root of the Arrhenius factor $exp\frac{-E_A}{RT}$ with the kinetic activation barrier E_A) versus logP_{OW} (octanol-water partitioning coefficients) for 4 mM of (i) glucose, (ii) sorbitol, (iii) 1,3-propanediol, (iv) methanol, (v) ethanol, (vi) 1-propanol, (vii) 1-butanol, (viii) 1-pentanol, (ix) 1-hexanol, (x) 4-pyridine-methanol, (xi) 3-pyridine-methanol, (xii) 1,4-benzene-dimethanol, and (xiii) benzyl alcohol. Uncertainty in normalised current estimated to be $\pm$ 3% based on systematic measurement error. Log $P_{o/w}$ values estimated by ACD labs are within $\pm$ 0.3 units [24].

According to the LEk mechanism, the partition coefficient into the film and the catalysis kinetics can also be rate limiting factors. The partition coefficient of the substrate into the PIM-EA-TB catalyst film can be correlated to the octanol-water partition coefficients. In order to deconvolute the PIM-EA-TB host effects on the rate of catalysis, an approximate activation barrier for the reaction of $TEMPO^+$ with primary alcohols has been calculated by DFT methods (see Experimental 5.2.4). Catalytic peak currents are normalised in first approximation by dividing by the square root of the Arrhenius factor $exp\frac{-E_A}{RT}$ in accordance with the LEk mechanism. Deconvoluting chemical kinetic effects from the data clarifies the correlation of increasing catalytic current with hydrophobicity of the substrate. The normalised plot in figure 5.11 shows a strong and systematic effect of the hydrophobicity of the substrate on the electrocatalytic currents. It can therefore be assumed that partitioning of the substrate into the PIM-EA-TB host occurs, thereby increasing the local substrate concentration and enhancing the electrocatalytic process.

5.4 Conclusion

It has been shown that a PIM-EA-TB composite with glassy carbon microparticles can be employed as a three-dimensional electrode with good access of solution phase and substrate to the active catalyst site. In this case, a 4-benzoyloxy-TEMPO catalyst was employed to study the oxidation of primary alcohols to aldehydes in carbonate buffer at pH 10.3 and novel reactivity patterns were observed. Catalytic activity followed the analytical model consistent with the substrate reacting near the electrode - film interface. Factors that limit the catalytic process in the film were identified as the kinetic rate constant of catalysis, partitioning of the substrate into the film and the substrate concentration. Concentration of catalyst and the rate of electrochemical charge hopping were assumed to be constant and independent of substrates present. Deconvoluting the effect of chemical kinetics (estimated with an appropriate DFT model) allow a clear observation of the PIM-EA-TB film selectivity towards hydrophobic substrates.

5.5 References

[1] R. A. Sheldon, "Recent advances in green catalytic oxidations of alcohols in aqueous media," Catal. Today, vol. 247, pp. 4–13, (2015).

[2] W. J. Albery and A. R. Hillman, "Transport and kinetics in modified electrodes," J. Electroanal. Chem. Interfacial Electrochem., vol. 170, no. 1–2, pp. 27–49, (1984).

[3] S. J. M. Andrieux C.P. and Dumas-Bouchiat J.M., "Catalysis of electrochemical reactions at redox polymer electrodes: Kinetic model for stationary voltammetric techniques," J. Electroanal. Chem., vol. 131, pp. 1–35, (1982).

[4] P. Daum and R. W. Murray, "Charge-transfer diffusion rates and activity relationships during oxidation and reduction of plasma-polymerized vinylferrocene films," J. Phys. Chem., vol. 85, no. 4, pp. 389–396, (1981).

[5] N. B. McKeown, "Polymers of intrinsic microporosity," vol. 2012, (2012).

[6] L. Tebben and A. Studer, "Nitroxides: Applications in synthesis and in polymer chemistry," Angew. Chemie - Int. Ed., vol. 50, no. 22, pp. 5034–5068, (2011).

[7] R. A. Sheldon and I. W. C. E. Arenas, "Organocatalytic oxidations mediated by nitroxyl radicals," Adv. Synth. Catal., vol. 346, no. 9–10, pp. 1051–1071, (2004).

[8] R. A. Sheldon, I. W. C. E. Arends, G. J. Ten Brink, and A. Dijksman, "Green catalytic oxidations of alcohols," Acc. Chem. Res., vol. 35, no. 9, pp. 774–781, (2002).

[9] J. T. Hill-Cousins, J. Kuleshova, R. A. Green, P. R. Birkin, D. Pletcher, T. J. Underwood, S. G. Leach, and R. C. D. Brown, "TEMPO-mediated electrooxidation of primary and secondary alcohols in a microfluidic electrolytic cell, ChemSusChem," vol. 5, no. 2, pp. 326–331, (2012).

[10] B. J. Bergner, A. Schürmann, K. Peppler, A. Garsuch, and J. Janek, "TEMPO: A mobile catalyst for rechargeable Li-O2 batteries," J. Am. Chem. Soc., vol. 136, no. 42, pp. 15054–15064, (2014).

[11] D. P. Hickey, M. S. Mccammant, F. Giroud, M. S. Sigman, and S. D. Minteer, "Hybrid enzymatic and organic electrocatalytic cascade for the complete oxidation of glycerol," pp. 23–26, (2014).

[12] R. A. Green, J. T. Hill-Cousins, R. C. D. Brown, D. Pletcher, and S. G. Leach, "A voltammetric study of the 2,2,6,6-tetramethylpiperidin-1-oxyl (TEMPO) mediated oxidation of benzyl alcohol in tert-butanol/water," Electrochim. Acta, vol. 113, pp. 550–556, (2013).

[13] A. Israeli, M. Patt, M. Oron, A. Samuni, R. Kohen, and S. Goldstein, "Kinetics and mechanism of the comproportionation reaction between oxoammonium cation and hydroxylamine derived from cyclic nitroxides," Free Radic. Biol. Med., vol. 38, no. 3, pp. 317–324, (2005).

[14] M. F. Semmelhack, C. R. Schmid, and D. A. Cortés, "Mechanism of the oxidation of alcohols by 2,2,6,6-tetramethylpiperidine nitrosonium cation," Tetrahedron Lett., vol. 27, no. 10, pp. 1119–1122, (1986).

[15] W. F. Bailey, J. M. Bobbitt, and K. B. Wiberg, "Mechanism of the oxidation of alcohols by oxoammonium cations," J. Org. Chem., vol. 72, no. 12, pp. 4504–4509, (2007).

[16] F. Minisci, F. Recupero, A. Cecchetto, C. Gambarotti, C. Punta, R. Faletti, R. Paganelli, and G. F. Pedulli, "Mechanisms of the aerobic oxidation of alcohols to aldehydes and ketones catalysed under mild conditions by persistent and non-persistent nitroxyl radicals and transition metal salts− polar, enthalpic, and captodative effects," European J. Org. Chem., vol. 2004, no. 1, pp. 109–119, (2004).

[17] M. Carta, R. Malpass-Evans, M. Croad, Y. Rogan, J. C. Jansen, P. Bernardo, F. Bazzarelli, and N. B. McKeown, "An efficient polymer molecular sieve for membrane gas separations," Science (80), vol. 339, no. January, pp. 303–307, (2013).

[18] F. Xia, M. Pan, S. Mu, R. Malpass-Evans, M. Carta, N. B. McKeown, G. a. Attard, A. Brew, D. J. Morgan, and F. Marken, "Polymers of intrinsic microporosity in electrocatalysis: novel pore rigidity effects and lamella palladium growth," Electrochim. Acta, vol. 128, pp. 3–9, (2014).

[19] Y. Rong, R. Malpass-Evans, M. Carta, N. B. McKeown, G. A. Attard, and F. Marken, "High density heterogenisation of molecular electrocatalysts in a rigid intrinsically microporous polymer host," Electrochem. commun., vol. 46, pp. 26–29, (2014).

[20] Y. Rong, R. Malpass-Evans, M. Carta, N. B. Mckeown, G. A. Attard, and F. Marken, "Intrinsically porous polymer protects catalytic gold particles for enzymeless glucose oxidation," Electroanalysis, vol. 26, no. 5, pp. 904–909, (2014).

[21] A. Kolodziej, S. D. Ahn, M. Carta, R. Malpass-Evans, N. B. McKeown, R. S. L. Chapman, S. D. Bull, and F. Marken, "Electrocatalytic carbohydrate oxidation with 4-benzoyloxy-TEMPO heterogenised in a polymer of intrinsic microporosity," Electrochim. Acta, vol. 160, pp. 195–201, (2015).

[22] C. Y. Cummings, J. D. Wadhawan, T. Nakabayashi, M. A. Haga, L. Rassaei, S. E. C. Dale, S. Bending, M. Pumera, S. C. Parker, and F. Marken, "Electron hopping rate measurements in ITO junctions: Charge diffusion in a layer-by-layer deposited ruthenium(II)-bis(benzimidazolyl)pyridine-phosphonate- TiO2 film," J. Electroanal. Chem., vol. 657, no. 1–2, pp. 196–201, (2011).

[23] Gaussian 09, Revision A.02, M. J. Frisch, G. W. Trucks, H. B. Schlegel, G. E. Scuseria, M. A. Robb, J. R. Cheeseman, G. Scalmani, V. Barone, B. Mennucci, G. A. Petersson, H. Nakatsuji, M. Caricato, X. Li, H. P. Hratchian, A. F. Izmaylov, J. Bloino, G. Zheng, J. L. Sonnenberg, M. Hada, M. Ehara, K. Toyota, R. Fukuda, J. Hasegawa, M. Ishida, T. Nakajima, Y. Honda, O. Kitao, H. Nakai, T. Vreven, J. A. Montgomery, Jr., J. E. Peralta, F. Ogliaro, M. Bearpark, J. J. Heyd, E. Brothers, K. N. Kudin, V. N. Staroverov, R. Kobayashi, J. Normand, K. Raghavachari, A. Rendell, J. C. Burant, S. S. Iyengar, J. Tomasi, M. Cossi, N. Rega, J. M. Millam, M. Klene, J. E. Knox, J. B. Cross, V. Bakken, C. Adamo, J. Jaramillo, R. Gomperts, R. E. Stratmann, O. Yazyev, A. J. Austin, R. Cammi, C. Pomelli, J. W. Ochterski, R. L. Martin, K. Morokuma, V. G. Zakrzewski, G. A. Voth, P. Salvador, J. J. Dannenberg, S. Dapprich, A. D. Daniels, Ö. Farkas, J. B. Foresman, J. V. Ortiz, J. Cioslowski, and D. J. Fox, Gaussian, Inc., Wallingford CT, (2009).

[24] Advanced Chemistry Development / Labs, “Product and Solutions Catalogue”, pp. 143-163, (2007/2008). Web 19 June 2016. <http://www.acdlabs.pl/portals/1/files/katalogi/physchem.pdf>

Chapter 6. Hydrodynamic Voltammetry at a Rocking Disc Electrode: Theory versus Experiment

Abstract

Rocking disc electrode voltammetry (RoDE) is introduced as an experimentally convenient and versatile alternative to rotating disc voltammetry. A 1.6 mm diameter disc electrode is employed with an overall rocking angle of Θ = 90 degrees applied over a frequency range of 0.83 Hz to 25 Hz. For a set of known aqueous redox systems (the oxidation of $Fe(CN)_6^{4-}$ in 1 M KCl, the reduction of $Ru(NH_3)_6^{3+}$ in 0.1 M KCl, the oxidation of hydroquinone in 0.1 M pH 7 phosphate buffer, the oxidation of I^- in 0.125 M H_2SO_4, and the reduction of H^+ in 1 M KCl) the mass transport controlled limiting current I_{lim} is demonstrated to follow in good approximation the Levich-type expression $I_{\lim} = 0.111\, nFAcD^{2/3}\nu^{-1/6}\sqrt{\Theta f}$ with *n*, the number of electrons transferred per molecule diffusing to the electrode surface, *F*, the Faraday constant, *A*, the geometric area, *c*, the concentration of the active redox species, *D*, the diffusion coefficient, *v*, the kinematic viscosity, Θ is the overall rocking angle in degree, and *f*, the rocking rate in Hz. Quantitative theory is developed based on a two-dimensional (2D) axisymmetric laminar flow model accounting for the conservation of mass, momentum and species along with the kinematic analysis of a four-bar mechanism to obtain the rocking motion. A novel collector-generator system utilizing two electrically separated dual-semi-disc electrodes is also investigated.

Keywords: Hydrodynamic modulation; Plating; Ionic liquid; Convection; Viscosity.

Acknowledgements

Somasundaram K., Nguyen V., Birgersson E., Lee J. Y., and Fisher A. are gratefully acknowledged for designing and running the numerical simulations presented in section 6.2.4 and 6.3.3.

This work was adapted from

Ahn S.D., Somasundaram K., Nguyen H.V., Birgersson E., Lee J.Y, Gao X., Fisher A.C., Frith P.E., Marken F., Electrochemica Acta, 188, 837-844, (2016).

Ahn S.D., Frith P.E., Fisher A.C., Bond A.M., Marken F., Journal of Electroanalytical Chemistry, 722, 78-82, (2014).

Contents

6.1 Introduction

Hydrodynamic electrochemical methods, and in particular the rotating disc electrode, offer an accurate and reliable way of obtaining surface and solution kinetic information for electrochemical redox systems. Accurate control of the rate of mass transport to the electrode surface can be useful for mechanistic analysis of electro-catalytic systems, and has shown utility in diagnosing properties and performance of film modified electrodes [1]. For the rotating disc electrode set-up, steady state voltammetric responses are accurately measured and analysed as a function of the rotation rate. Although more accurate treatments of the hydrodynamic conditions at the rotating disc electrode are known [2], the equation proposed by Levich [3] (see equation 6.1) is generally accepted for the analysis of the mass transport limited current signal.

$$I_{\lim} = 0.62 \frac{nFAD^{2/3}}{v^{1/6}} \sqrt{2\pi f} = 1.55 \frac{nFAD^{2/3}}{v^{1/6}} \sqrt{f} \qquad \text{(eq. 6.1)}$$

In this equation, the mass transport limited current I_{lim} is given by n, the number of electrons transferred per molecule diffusing to the electrode surface, F, the Faraday constant, A, the geometric electrode area, D, the diffusion coefficient, v, the kinematic viscosity, and f, the angular frequency (which is given as radians per second). Many further methods have been developed from the initial concept including for example rotating ring disc measurements [4], hydrodynamically modulated rotating disc voltammetry [5], channel flow electrodes [6], and hydrodynamic electrodes with Couette flow [7] (discussed more in section 2.2.4).

Here, the use of a “rocking” disc electrode where the electrode is semi rotated back and forth about the centre of the disc displacing 90 degrees angle each way (see Figure 6.1) is investigated and contrasted to the conventional rotating disc electrode. Earlier experimental studies by Cummings showed that a “rocking movement” of the electrode or electrochemical cell could lead to uniform mass transport and beneficial electro-deposition conditions very similar to those obtained with a rotating disc electrode [8]. It was argued that such a system has the advantages of technical simplicity as there are no sliding contacts and improved versatility. The study successfully demonstrated that the mass transport limited current increased linearly with the square root of the rocking rate with sufficient electrolyte homogenisation as well as dislodging gas bubbles from the electrode surface.

Given the above observations, it seemed reasonable to assume that the hydrodynamic conditions brought about by the rocking motion can be approximated by a model similar to the Levich equation. This study presents an empirical study of the relation of the steady state limiting current produced by the rocking motion to the variable factors in the Levich equation. It is shown that in spite of the expected turbulent nature of the hydrodynamic conditions at the rocking disc, well-defined steady state voltammetric measurements are possible with future applications in electro-deposition, electroanalysis, or voltammetric investigation of more complex liquids. This chapter attempts the achieve the following; i) an empirical fitting to the mass transport limited current induced by the rocking motion to a Levich style model, which is supported by ii) a numerical simulation approach taken by collaborating researchers who utilised a commercial software package (COMSOL). And finally iii) a novel collector-generator system based on the rocking disc electrode is investigated.

A key difference between the rocking disc electrode and the rotating disc electrode is the oscillatory nature of electrode motion which changes velocity periodically. Hydrodynamic modulation effects are reported in set-ups where there is a periodic variation in the rate of mass transport of the electroanalyte towards the electrode surface. Such effects may be observed under rocking disc conditions as there is a periodic variation in the electrode's angular velocity. Modulating the rate of mass transport can further resolve mass-transport limited faradaic processes from background processes, which improves the sensitivity of electro-analysis of substances down to nano-molar concentrations [5]. It is shown here that although hydrodynamic modulation under rocking conditions remains insignificant, concentration modulation can be achieved in generator-collector configuration with two adjacent semi-disc electrodes.

6.2 Theory

A four-bar mechanism is designed to deliver the rocking motion to the electrode that covers 180 degrees (90 degrees back and forth, see Figure 6.1B) during one rocking cycle. In practice, the new construction obviates the need for contact brushes and simplifies the experimental procedures. However, the hydrodynamic flow caused by the rocking motion is significantly more complex and no analytical solution is currently available. This problem is thus tackled using a numerical approach. This section aims to numerically investigate the performance of RoDE mediating a simple electrochemical reaction and to validate it with experimental results. The mathematical model comprises of the governing transient conservation of mass, momentum and species along with the velocity equations for the rocking motion. The nomenclature for symbols is summarised in Table 6.1 and Table 6.2.

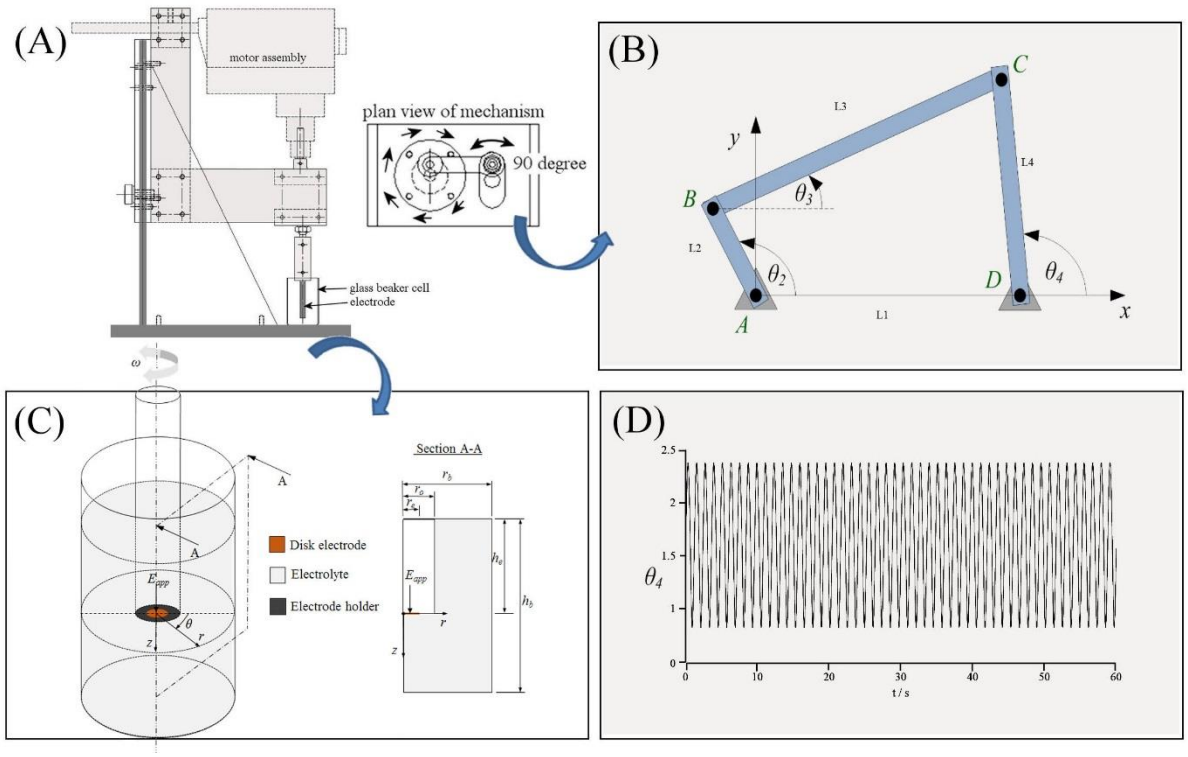

Figure 6.1. (A) Schematic drawing of the motor driven rocking disc electrode system with cell and electrode assembly. (B) Comsol mechanism for converting rotation into rocking motion. (C) Schematic of the rocking system in 3D and 2D axi-symmetric geometries. (D) Rocking motion as defined by the kinematic analysis (at 50 rpm) described by angular parameter θ_4.

Table 6.1. Nomenclature of symbols used in this report.

Symbol	Description
A	disc electrode surface area, m^2
c_i	concentration of species i, mol m^{-3}
c_i^*	bulk concentration of species i, mol m^{-3}
D_i	diffusion coefficient of species i, m^2 s^{-1}
dE/dt	voltage scan rate, V s^{-1}
E_0	initial voltage, V
E_{app}	applied voltage, V
E_{eq}	reference/equilibrium potential, V
F	Faraday's constant, C mol^{-1}
f	body force or inertial force, m s^{-2},
g	acceleration due to gravity, m s^{-2}
h_b	height of beaker, m
h_e	height of electrode holder, m
i_{loc}	charge transfer current density, A m^{-2}
I	current, A
k_a, k_c	anodic and cathodic reaction rate constants, m s^{-1}
N	angular speed, rpm
$\mathbf{N}_i$	flux of species i, mol m^{-2} s^{-1}
n	normal vector, -
n	number of electrons, -
p	pressure, Pa
R	universal gas constant, J mol^{-1} K^{-1}
r	radial coordinate, m
r_b	radius of beaker, m
r_e	radius of disc electrode, m
r_o	radius of electrode holder, m
s_i	stoichiometric coefficient of species I, -
T	temperature, K
t	time, s
u	velocity vector, m s^{-1}
u_r	velocity in r-direction, m s^{-1}
u_ϑ	velocity in θ-direction, m s^{-1}
u_z	velocity in z-direction, m s^{-1}
z	axial coordinate, m
z_i	charge number, -
ϑ	angular coordinate, rad
Θ	total rocking angle, degree
Greek	
α	transfer coefficient, -
η	overpotential, V
μ	dynamic viscosity of the electrolyte, Pa s
ν	kinematic viscosity of the electrolyte, m^2 s^{-1}
ρ	density of the electrolyte, kg m^{-3}
ϕ_l	potential in the electrolyte, V
ω	angular velocity of the rotating electrode, rad s^{-1}
Subscript	
i	Species (O - oxidizing, and R – reducing species)

Table 6.2. Physical parameters.

Parameter	Value
c_O^0	0 mol m^{-3}
c_R^0	1 mol m^{-3}
$\frac{dE}{dt}$	0.01 V s^{-1}
D_i	0.65 x 10^{-9} m^2 s^{-1}
E_0	-0.1 V
E_{eq}	0.21 V
F	96487 C mol^{-1}
h_b	2 x 10^{-2}m
h_e	1 x 10^{-2} m
k_a , k_c	8 x 10^{-5} m s^{-1}
n	1
r_b	3 x 10^{-2} m
r_e	8 x 10^{-4} m
r_o	4 x 10^{-3} m
R	8.314 J mol-1 K^{-1}
s_R	-1
s_O	1
T	298.15 K
ϵ	0.5
μ	10^{-3} Pa s
ρ	10^3 kg m^{-3}
ϕ_l	0 V

Kinematic analysis of the four-bar mechanism yields the velocity equations that are solved numerically to obtain the rocking rate in terms of the rotation rate (see Figure 6.1D). The rocking motion obtained is fed as the boundary condition to the transient conservation of momentum and thus gets coupled. The limiting current corresponding to various "rocking" frequencies will be calculated and compared to both experimental data and the theoretical values from a modified Levich-type equation.

A schematic of the whole device and the mechanism is illustrated in Figure 6.1A. The four-bar mechanism (Figure 6.1B) functions as follows. The bar AB is rotated at regular frequency "ω_2", which can be electronically controlled with a motor. Via the crank BC, this transmits a "back-and-forth" motion to the bar CD. The electrode is attached to the bar CD and its movement then follows that of

the bar. The "rocking" frequency used in subsequent parts of the article will refer to the frequency of bar AB instead of CD. By denoting the angles θ_2, θ_3 and θ_4 as in Figure 6.1B, the following differential equations termed as velocity equations are obtained from kinematic analysis:

$$\frac{d\theta_3}{dt} = \frac{L_2}{L_3}\omega_2 \frac{\sin(\theta_2 - \theta_4)}{\sin(\theta_4 - \theta_3)} \quad \text{(eq. 6.2)}$$

$$\frac{d\theta_4}{dt} = \frac{L_2}{L_4}\omega_2 \frac{\sin(\theta_2 - \theta_3)}{\sin(\theta_4 - \theta_3)} \quad \text{(eq. 6.3)}$$

Here ω_2 is the angular frequency of bar AB in rad/s, L_2, L_3, and L_4 are the lengths of the links as shown in Figure 6.1B. The equations above are subject to appropriate initial conditions for θ_3 and θ_4 from the geometry of the mechanism. The rocking rate is given by equation 6.2 and the Levich equation now will have additional terms other than ω_2. Once the rocking rate $\frac{d\theta_4}{dt}$ is calculated, it is coupled to the fluid and mass transport calculations as outlined below.

Fluid and species transport. A schematic representation of the RoDE experimental setup is shown in Figure 6.1C. The disc electrode is immersed in a large beaker containing an aqueous solution of the electrolyte using an electrode holder made of Teflon. Excess supporting electrolyte is used and a generalised redox process $O + e^- \rightleftharpoons R$ is considered. The continuity equation for incompressible fluids is given by equation 6.4.

$$\nabla \cdot \mathbf{u} = 0 \quad \text{(eq. 6.4)}$$

The momentum conservation for the fluid is given by equation 6.5.

$$\frac{\partial \mathbf{u}}{\partial t} + \mathbf{u} \cdot \nabla \mathbf{u} = -\frac{1}{\rho}\nabla p + \nu \nabla^2 \mathbf{u} + f \quad \text{(eq. 6.5)}$$

The species conservation equation is described by equation 6.6.

$$\frac{\partial c_i}{\partial t} = -\nabla \cdot \mathbf{N}_i + r_i, i = O, R \quad \text{(eq. 6.6)}$$

The flux here is defined in equation 6.7.

$$\mathbf{N}_i = -D_i \nabla c_i - z_i u_i F c_i \nabla \phi_l + \mathbf{u} c_i \qquad \text{(eq. 6.7)}$$

In the above equations, $\mathbf{u}$ is the velocity vector, t is the time, p is the pressure, ρ is the density of the electrolyte, ν is the kinematic viscosity of the electrolyte, c_i is the concentration of the species i, $\mathbf{N}_i$ is the species flux, r_i is the rate of homogenous production of species i, D_i is the diffusion coefficient of species i, z_i is the charge number, u_i is the species mobility, F is the Faraday's constant, and ϕ_l is the potential in the electrolyte. In equation 6.7, the first term on the right hand side denotes the diffusive flux, the second term represents the flux due to migration, and the third term provides the convective flux. For solutions containing an excess of supporting electrolyte, the ionic migration term can be neglected and hence the second term becomes zero. The liquid phase potential is also set to zero. Without chemical reactions in solution and diffusion coefficients assumed constant, the general convective-diffusion (equation 6.8) is obtained.

$$\frac{\partial c_i}{\partial t} = D_i \nabla^2 c_i - \mathbf{u} \cdot \nabla c_i \qquad \text{(eq. 6.8)}$$

For the case of a liquid with a constant density and a constant binary diffusion coefficient, continuity, and the geometry as shown in Figure 6.1C, momentum and species balance equations are transformed into cylindrical coordinates as shown in equations 6.9-6.13 below.

Continuity

$$\frac{1}{r}\frac{\partial}{\partial r}(r u_r) + \frac{1}{r}\frac{\partial u_\theta}{\partial \theta} + \frac{\partial u_z}{\partial z} = 0 \qquad \text{(eq. 6.9)}$$

Momentum conservation (r - component)

$$\rho\frac{\partial u_r}{\partial t} + \rho u_r \frac{\partial u_r}{\partial r} + \rho\frac{u_\theta}{r}\frac{\partial u_r}{\partial \theta} - \rho\frac{u_\theta^2}{r} + \rho u_z \frac{\partial u_r}{\partial z} = -\frac{\partial p}{\partial r} + \mu\frac{\partial}{\partial r}\left[\frac{1}{r}\frac{\partial}{\partial r}(r u_r)\right] + \frac{\mu}{r^2}\frac{\partial^2 u_r}{\partial \theta^2} - \mu\frac{2}{r^2}\frac{\partial u_\theta}{\partial \theta} + \mu\frac{\partial^2 u_r}{\partial z^2} \qquad \text{(eq. 6.10)}$$

Momentum conservation (θ -component)

$$\rho\frac{\partial u_\theta}{\partial t}+\rho u_r\frac{\partial u_\theta}{\partial r}+\rho\frac{u_\theta}{r}\frac{\partial u_\theta}{\partial\theta}+\rho\frac{u_r u_\theta}{r}+\rho u_z\frac{\partial u_\theta}{\partial z}= \\ -\frac{1}{r}\frac{\partial p}{\partial\theta}+\mu\frac{\partial}{\partial r}\left[\frac{1}{r}\frac{\partial}{\partial r}\left(ru_\theta\right)\right]+\frac{\mu}{r^2}\frac{\partial^2 u_\theta}{\partial\theta^2}+\mu\frac{2}{r^2}\frac{\partial u_r}{\partial\theta}+\mu\frac{\partial^2 u_\theta}{\partial z^2} \quad \text{(eq. 6.11)}$$

Momentum conservation (z -component)

$$\rho\frac{\partial u_z}{\partial t}+\rho u_r\frac{\partial u_z}{\partial r}+\rho\frac{u_\theta}{r}\frac{\partial u_z}{\partial\theta}+\rho u_z\frac{\partial u_z}{\partial z}=-\frac{\partial p}{\partial z} \\ +\frac{\mu}{r}\frac{\partial}{\partial r}\left[r\frac{\partial u_z}{\partial r}\right]+\frac{\mu}{r^2}\frac{\partial^2 u_z}{\partial\theta^2}+\mu\frac{\partial^2 u_z}{\partial z^2} \quad \text{(eq. 6.12)}$$

Species conservation

$$\frac{\partial c_i}{\partial t}+u_r\frac{\partial c_i}{\partial r}+\frac{u_\theta}{r}\frac{\partial c_i}{\partial\theta}+u_z\frac{\partial c_i}{\partial z}=D_i\left[\frac{1}{r}\frac{\partial}{\partial r}\left(r\frac{\partial c_i}{\partial r}\right)+\frac{1}{r^2}\frac{\partial^2 c_i}{\partial\theta^2}+\frac{\partial^2 c_i}{\partial z^2}\right] \quad \text{(eq. 6.13)}$$

In the above equations 6.9-6.13, u_r is the radial component of velocity, u_θ is the angular component of the velocity, u_z is the axial component of the velocity, μ is the dynamic viscosity of the fluid, *r* is the radial coordinate, ϑ is the angular coordinate, and *z* is the axial coordinate.

Boundary and initial conditions. At the walls of the beaker ($r=r_b, -h_e\le z\le h_b-h_e$, and $z=h_b-h_e, 0\le r\le r_b$), no slip is specified for the velocity and no flux is specified for the species (equation 6.14).

$$u_r=u_\theta=u_z=0, \mathbf{n}\cdot\mathbf{N}_i=0 \quad \text{(eq. 6.14)}$$

At the surface of the disc electrode ($z=0, 0\le r\le r_e$), redox reactions provide the flux of the oxidized and reduced species (equation 6.15).

$$\mathbf{n}\cdot\mathbf{N}_i=\frac{s_i i_{loc}}{F} \quad \text{(eq. 6.15)}$$

As the electrode disc along with the holder spins at the specified revolutions per minute (rpm), the velocity is specified at these boundaries ($z = 0, 0 \le r \le r_o$ and $r = r_o, -h_e \le z \le 0$) as in equation 6.16.

$$u_r = u_z = 0$$
$$u_\theta = \frac{d\theta_4}{dt} r \qquad \text{(eq. 6.16)}$$

Insulation is specified at the electrode holder boundary as no species flow across the holder occurs ($z = 0, r_e \le r \le r_o$ and $r = r_o, -h_e \le z \le 0$, equation 6.17)

$$\mathbf{n} \cdot \mathbf{N}_i = 0 \qquad \text{(eq. 6.17)}$$

At the top free/open surface of the electrolyte ($z = -h_e, r_o \le r \le r_b$), symmetry boundary conditions are applied for fluid flow and species transport which denotes that there is no normal stress on the fluid here and no flux of species (equation 6.18).

$$\frac{\partial u_r}{\partial z} = \frac{\partial u_\theta}{\partial z} = u_z = 0 \qquad \text{(eq. 6.18)}$$
$$\mathbf{n} \cdot \mathbf{N}_i = 0$$

For the 2D axisymmetric case, axial symmetry is specified at the axis of cylindrical coordinate ($r = 0$, equation 6.19).

$$u_r = u_\theta = \frac{\partial u_z}{\partial r} = 0 \qquad \text{(eq. 6.19)}$$

The pressure is set to be zero arbitrarily at a reference point ($r_0 < r = r_b, z = -h_e$).

$$p = 0 \qquad \text{(eq. 6.20)}$$

At time $t = 0$, the concentration of reduced and oxidised species are defined in equation 6.21.

$$c_i = \begin{cases} c_R^0, i = R \text{ (reducedspecies)} \\ c_O^0, i = O \text{ (oxidizing species)} \end{cases} \qquad \text{(eq. 6.21)}$$

Constitutive relations. The transfer current density is defined by using Butler-Volmer kinetics (equation 6.22).

$$i_{loc} = nF\left(k_a c_R \exp\left(\frac{(1-\beta)\eta F}{RT} \right) - k_c c_O \exp\left(\frac{-\beta\eta F}{RT} \right) \right) \quad \text{(eq. 6.22)}$$

Here the overpotential η is defined as equation 6.23.

$$\eta = E_{app} - \phi_l - E_{eq}. \quad \text{(eq. 6.23)}$$

The voltage applied at the electrode depends on the scan rate and is defined as equation 6.24.

$$E_{app} = E_0 + \frac{dE}{dt}t \quad \text{(eq. 6.24)}$$

The current is the flux at the electrode surface and is defined as equation 6.25.

$$I = \pm nFAD_i \left(\frac{dc_i}{dy} \right)_{y=0}, i = O, R \quad \text{(eq. 6.25)}$$

Where a "+" sign used for the oxidized species and "–" sign for the reduced species respectively.

The expression for the Levich equation for a RDE is given as shown in equation 6.26.

$$i_{Levich,RDE} = 0.62\, nFAc^* D^{\frac{2}{3}} \nu^{-\frac{1}{6}} \sqrt{\omega_2} \quad \text{(eq. 6.26)}$$

Where $c^* = \lim_{z \to \infty} c$ represents the bulk concentration of the oxidized or reduced species for cathodic or anodic limiting currents. For a RoDE, we employ the rocking rate instead of the rotational rate to obtain equation 6.27.

$$i_{Levich,RoDE} = 0.62\, nFAc^* D^{\frac{2}{3}} \nu^{-\frac{1}{6}} \sqrt{\frac{d\theta_4}{dt}} \quad \text{(eq. 6.27)}$$

The time average of the absolute values in the sine term in equation 6.3 along with the given length ratio L_2/L_4 relate the rocking rate to the rotation rate (equation 27). The factor 0.46 (for a total rocking angle 90 degree) is close to L_2/L_4 = 7 mm / 10 mm = 0.7, but can be obtained more accurately numerically from the Comsol model by averaging over time. The rocking rate can be expressed more generally as shown in equation 6.28.

$$\frac{d\theta_4}{dt} = 0.46\,\omega_2 \qquad \text{(eq. 6.28)}$$

Therefore, the Levich-type equation for RoDE (equation 6.29) can be expressed directly (assuming laminar conditions prevail at the electrode surface – solution interface). Furthermore, the effect of the total rocking angle Θ can be predicted with the model and expressed as shown in the Levich-type expression in equation 6.30. The corresponding diffusion layer thickness is given in equation 6.31.

$$i_{Levich,RoDE} = 0.62\,nFAc^*D^{\frac{2}{3}}\nu^{-\frac{1}{6}}\sqrt{0.46\omega_2} = 1.05\,nFAc^*D^{\frac{2}{3}}\nu^{-\frac{1}{6}}\sqrt{f} \qquad \text{(eq. 6.29)}$$

$$i_{Levich,RoDE} = 0.111\,nFAc^*D^{\frac{2}{3}}\nu^{-\frac{1}{6}}\sqrt{\Theta f} \qquad \text{(eq. 6.30)}$$

$$\delta_{RoDE} = \frac{9.0D^{\frac{1}{3}}\nu^{\frac{1}{6}}}{\sqrt{\Theta f}} \qquad \text{(eq. 6.31)}$$

Numerics. The 2D axisymmetric model equations are solved using the commercial finite element solver Comsol Multiphysics 5.1. The system of equations for the rocking mechanism model is implemented using global ODEs in Comsol and solved with a convergence tolerance of 10^{-6}. For fluid flow and species transport, the single phase laminar flow and transport of diluted species modes in Comsol are used. The mesh consists of 7×10^3 and 3.3×10^3 elements for the fluid flow and species transport respectively and the corresponding degrees of freedom (DoF) are 50×10^3 and 7.5×10^3. The solutions were tested for mesh independence. Initially, the rocking motion is solved followed by the fluid flow and species transport in sequence. The computations were carried out in a workstation having two quad-core processors with 64GB RAM.

Simulation results. The case of a redox system with $D = 6.5 \times 10^{-10}$ m^2s^{-1} and $c = 1$ mM is considered with a 1.6 mm diameter disc electrode giving an area of $A = 2 \times 10^{-6}$ m^2. The voltammograms obtained at various rocking rates (here in rpm) agree well with experimental observations at lower rocking rates as shown in Figure 6.2. As expected, the limiting current increases with increasing frequency.

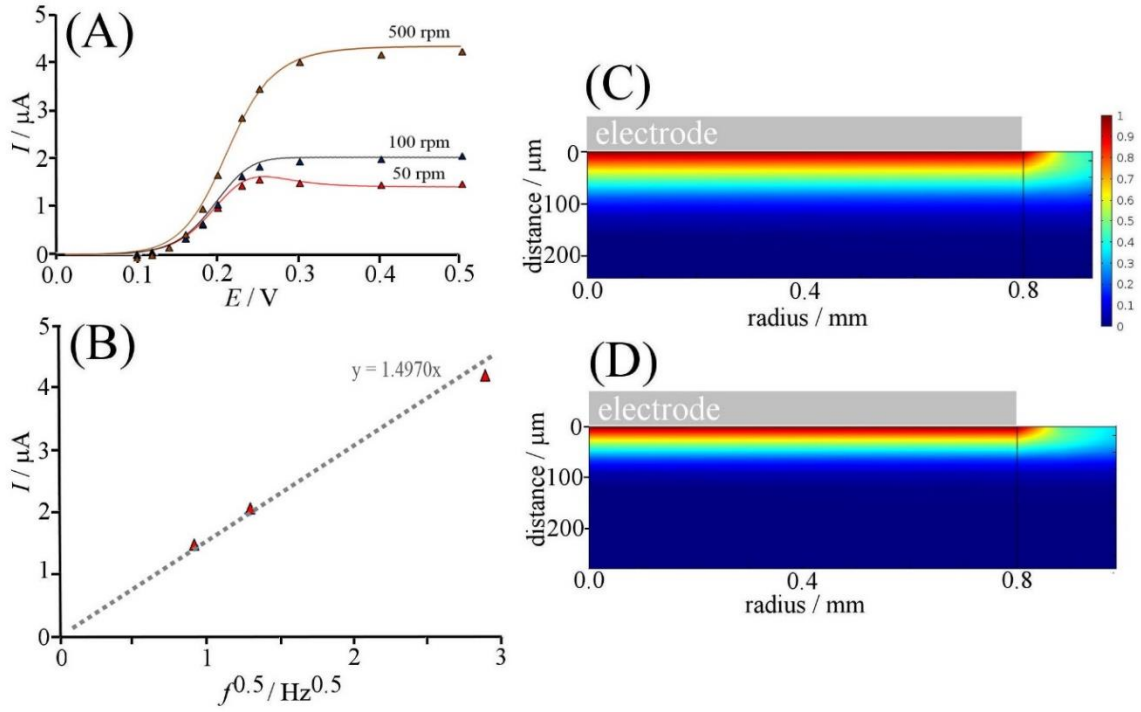

Figure 6.2. (A) Voltammograms (scan rate 10 mVs^{-1}, 1 mM redox active species, $D = 6.5 \times 10^{-9}$ m^2s^{-1}, 1.6 mm diameter disc electrode) at various rocking rates: model predictions (lines) versus experimental data (symbols, *vide infra*). (B) Plot of limiting current versus rocking frequency: model predictions (lines) versus experiments (symbols, *vide infra*). (C,D) Contour maps of the diffusion layer showing the concentration of product at the end of the potential sweep at 0.5 V for (C) 50 rpm and (D) 100 rpm.

6.3 Experimental methods

6.3.1 Reagents

Potassium chloride (99%), sodium perchlorate (98%), 2,2,6,6-tetramethylpiperidine 1-oxyl (TEMPO, 98%), potassium iodide (99%), sulphuric acid (95-98%), and sucrose (99.5%) were obtained from Sigma Aldrich. Hydrochloric acid (30%) was obtained from Fluka, and hexaammine ruthenium (III) chloride (99%) from purchased Strem Chemicals. Reagents were used without further purification. Solutions were prepared in demineralized and filtered water taken from a Thermo Scientific water purification system (Barnstead Nanopure) with 18.2 MΩcm resistivity.

6.3.2 Instrumentation

For voltammetry studies, a microAutolab II potentiostat system (EcoChemie, Netherlands) was employed with a KCl-saturated calomel reference electrode (SCE, Radiometer). For all experiments, the reference electrode was placed in approximately 2 mm distance from the working electrode. The working electrode was a platinum macro-disc electrode with a diameter of 1.6 mm (BAS). The counter electrode was a platinum wire. Rocking motion (90 degrees) of the working electrode (as shown in Figure 6.3) was applied with an IKA Eurostar digital motor through a four-bar mechanism (see Figure 6.2). All experiments were conducted in ambient atmosphere at a temperature of 22+/- 2 ^{o}C.

6.3.3 Dual-semi-disc electrode preparation

The glassy carbon rod was polished down to give two identical half cylinder pieces approximately 30 mm long. An electrical contact was established on one end of both cylinders by attaching a conducting wire with silver epoxy. The two half-cylinders were then inserted into a custom made Teflon sheath (at ca. 100 ^{o}C) to reform a full cylinder (the Teflon sheath was heat-shrunk for a tight fit). The two half cylinders were kept electrically separate with a thin layer (0.05 mm) of PTFE film. A “black wax” (Apiezon) seal was applied and the electrode was then polished with alumina (0.3 micron) to form the dual-semi-disc electrode (see Figure 6.1B) with a diameter of approximately 3.5mm.

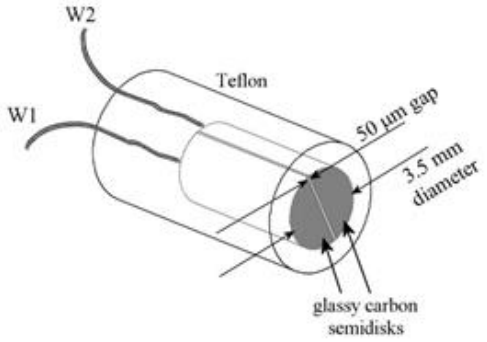

Figure 6.3. A schematic drawing of the dual-semi-disc electrode utilized for collector-generator experiments.

6.4 Results and Discussions

6.4.1 Rocking Disc Electrode Voltammetry I.: Convective Transport and Concentration Effects

For an electrode that is gently rocking at 1.67 Hz (see Figure 6.4A) the effect of scan rate on the shape of the voltammetric response is indicative of the hydrodynamic effect. Only at a low scan rate of 10 mVs^{-1} is the peak response insignificant and a near-steady state voltammogram is obtained. The average diffusion layer thickness under these conditions can be estimated (see equation 6.32).

$$\delta \approx \sqrt{\frac{DRT}{v_{trans}F}} = \sqrt{\frac{6.7\times10^{-10}\times8.31\times293}{0.01\times96485}} = 41\mu m \qquad \text{(eq. 6.32)}$$

An average diffusion layer thickness of ca. 41 μm at a rocking rate of 1.67 Hz is similar to that expected under rotating disc electrode conditions. By increasing the rocking rate the limiting current is increased and therefore the average diffusion layer thickness decreased (see Figure 6.4B). When plotted, the square root dependency of the mass transport limited current on the rocking rate is clearly revealed (see Figure 6.4C). As expected, the transition scan rate v_{trans} is significantly increased at higher rocking rates. The effect of the rocking rate is equivalent to that associated with the rotation rate for rotating disc voltammetry. The voltammetric response scales linearly with $Fe(CN)_6^{4-}$ concentration and a simple comparison of the mass transport limited current with that for rotating disc conditions, assuming $D_{Fe(CN)_6^{4-}} = 6.5 \times 10^{-10}$ m^2s^{-1} [9]) allows rocking rate to be correlated to rotation rate with $f_{RDE} = 0.55\, f_{RoDE}$. This result suggests that the level of mass transport achieved by a 360 degree rotation (in rotating disc experiments) is approximately equal to four 90 degree movements or two full rocking cycles (in rocking disc experiments). This result implies that the average momentum transfer from the rocking electrode to the solution phase is similar to that induced by rotation when normalised over the angle of movement. This comparison of rotating disc and rocking disc characteristics can be further justified based on previous work on the rocking electrode flow pattern [8], [10] which was proposed to be “oscillatory outward” over the electrode surface.

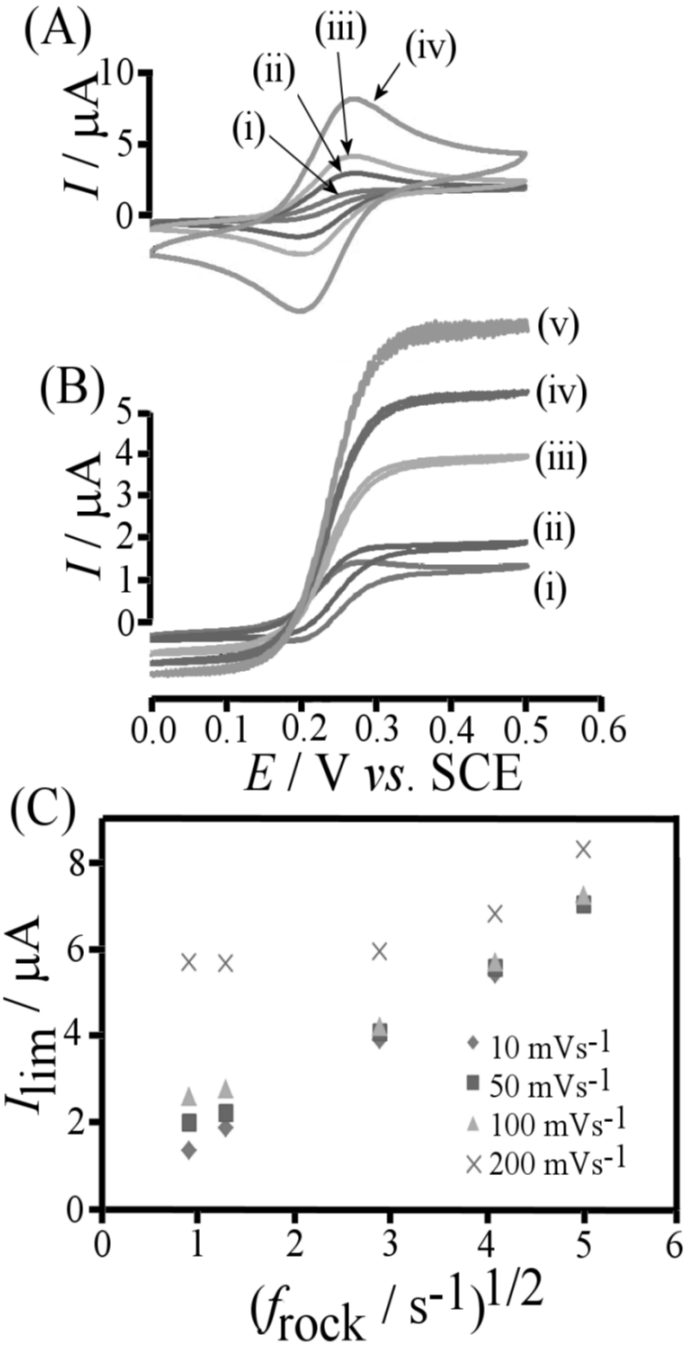

Figure 6.4. (A) Cyclic voltammograms (scan rate (i) 10, (ii) 50, (iii) 100, and (iv) 400 mVs^{-1}) for the oxidation of 1 mM $Fe(CN)_6^{4-}$ in aqueous 1 M KCl at a rocking (1.67 Hz) 1.6 mm diameter platinum disc electrode. (B) Cyclic voltammograms (scan rate 10 mVs^{-1}) obtained at rocking rates of (i) 0.83 Hz, (ii) 1.67 Hz, (iii) 8.3 Hz, (iv) 16.7, and (v) 25 Hz. (C) Plot of the mass transport limited current versus square root of rocking rate.

The effect of varying concentration is demonstrated in Figure 6.5. A plot of the limiting current as a function of concentration is shown for three different rocking rates. The plots demonstrate linearity.

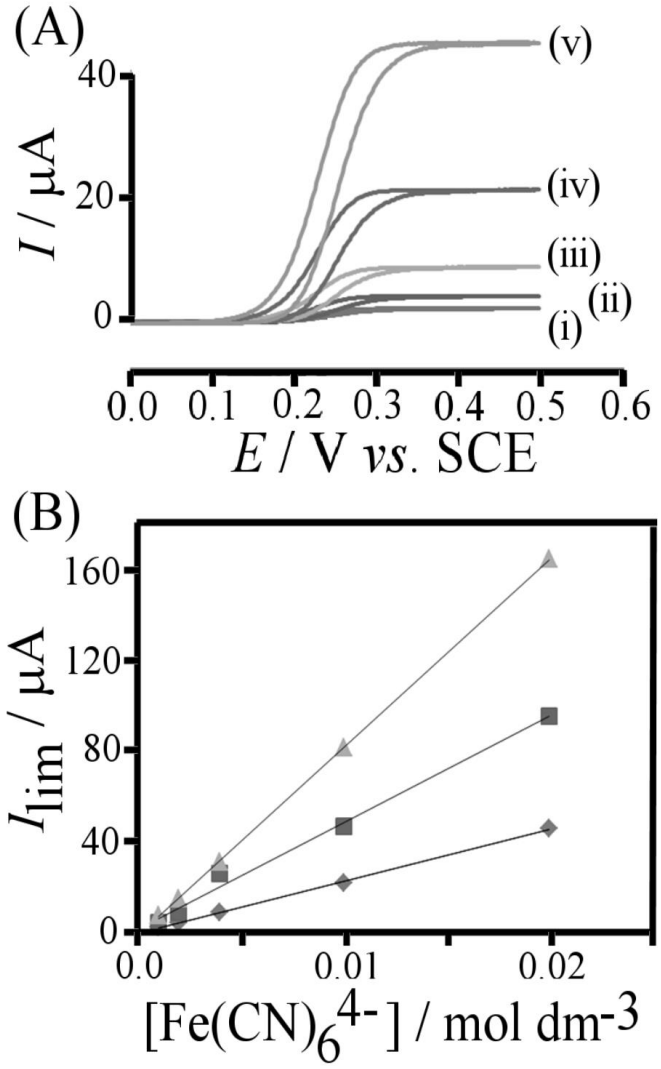

Figure 6.5. (A) Cyclic voltammogram (scan rate 10 mVs^{-1}) for the oxiation of (i) 1, (ii) 2, (iii) 4, (iv) 10, and (v) 20 mM $Fe(CN)_6^{4-}$ in 1 M KCl at a 3.2 mm diameter platinum electrode (rocking rate 1.67 Hz). (B) Plot of the mass transport limited current versus concentration.

6.4.2 Rocking Disc Electrode Voltammetry II.: Effect of Diffusion Coefficient and Viscosity

The effect of the diffusion coefficient on the RoDE limiting current was studied by working with five different redox systems (see Figure 6.6): (i) the reduction of H^+ in 1M KCl (see Figure 6.7A), (ii) the oxidation of I^- in 0.125 M H_2SO_4 (see Figure 6.7C), (iii) the reduction of $Ru(NH_3)_6^{3+}$ in 0.1 M KCl (see Figure 6.7E), (iv) the oxidation of hydroquinone in 0.1 M phosphate buffer pH 7 (see Figure 6.7G), and (v) the oxidation of $Fe(CN)_6^{4-}$ in 1M KCl. The corresponding diffusion coefficients have been reported in the literature [9]. The double logarithmic plot of the mass transport limited current (divided by the number of transferred electrons) versus D shows a trend in good agreement with the expected $D^{2/3}$ dependence.

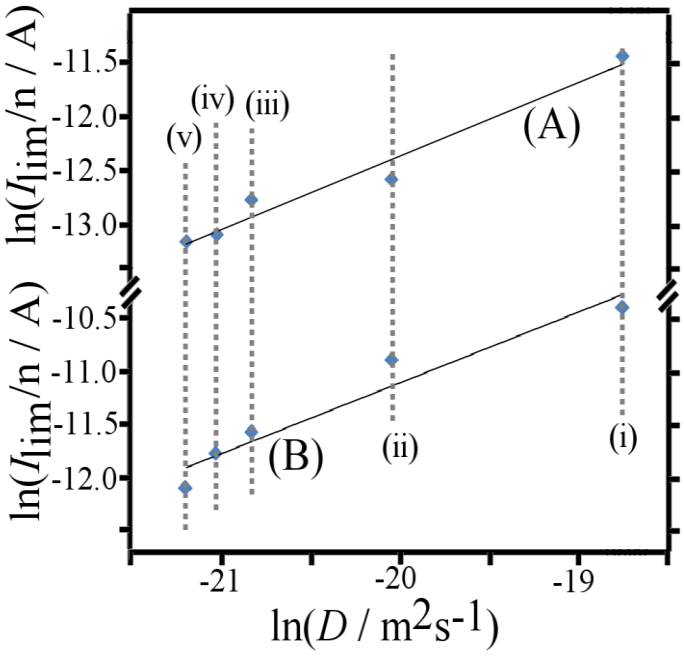

Figure 6.6. Double-logarithmic plots of the limiting current versus diffusion coefficients for (i) H^+ in 1M KCl, (ii) I^- in 0.125M H_2SO_4, (iii) $Ru(NH_3)_6^{3+}$ in 0.1M KCl, (iv) hydroquinone in 0.1 M phosphate buffer pH 7, and (v) $Fe(CN)_6^{4-}$ in 1M KCl) for (A) f_{rock} = 1.67 s^{-1} (slope=0.678, R^2=0.97, SE=0.15) and (B) 16.7 s^{-1} (slope=0.672, R^2=0.94, SE=0.20). The line of best fit in both cases shows a slope of 2/3.

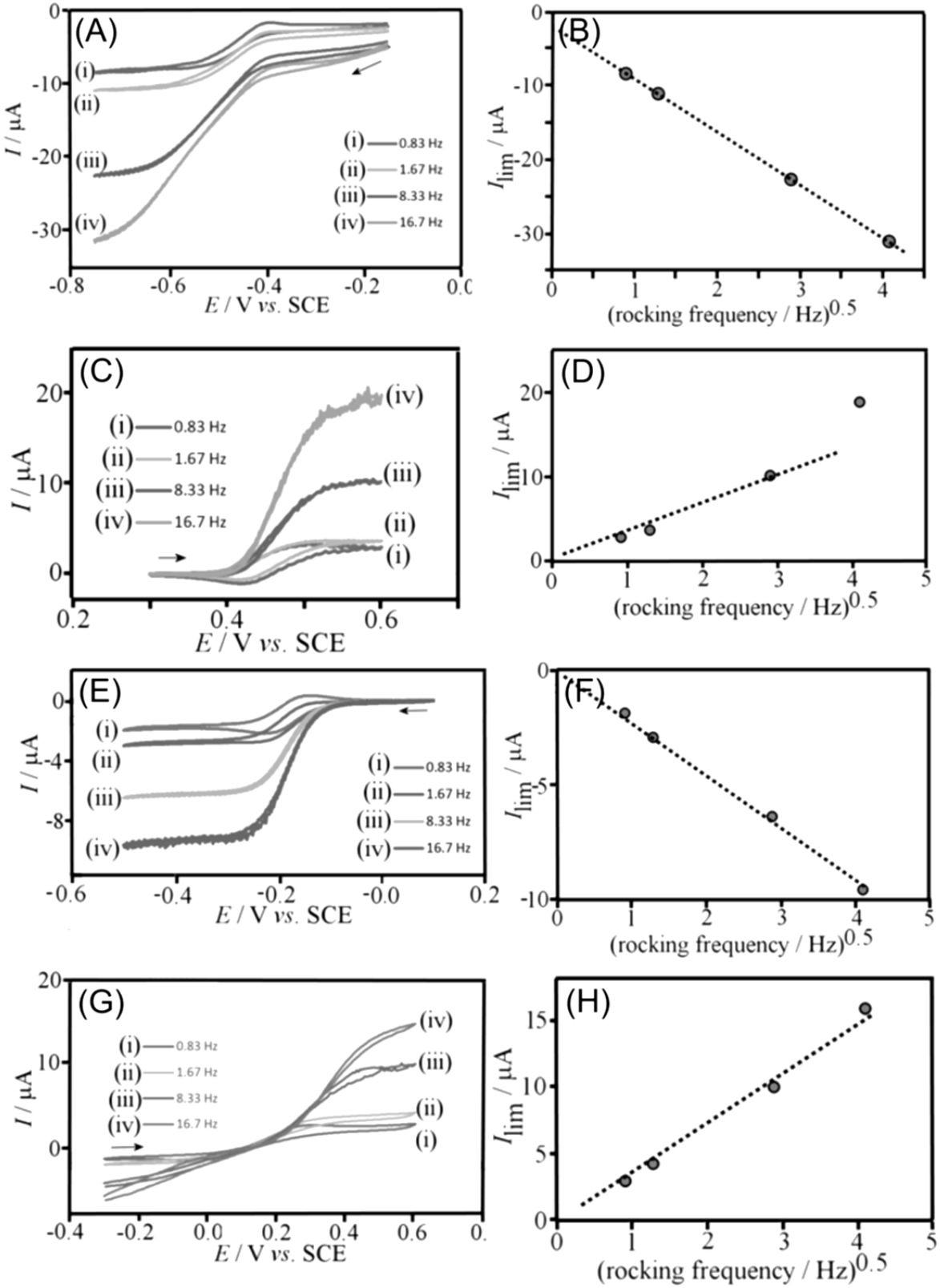

Figure 6.7. A) Cyclic voltammograms (scan rate 10 mVs^{-1}) for the reduction of 1 mM H^+ in 1 M KCl at a 1.6 mm diameter Pt disc electrode as a function of rocking frequency with B) corresponding Levich plot. C) Same as A but for 1 I^- in 0.125 M H_2SO_4 with D) corresponding Levich plot. E) Same as A but for

1mM $Ru(NH_3)_6^{3+}$ in 0.1 M KCl with F) corresponding Levich plot. G) Same as A, but for 1 mM hydroquinone in 0.1 M phosphate buffer pH 7 with H) with corresponding Levich plot.

The effect of changing viscosity is more subtle and is studied here by the addition of sucrose into the aqueous electrolyte solution. Sucrose is electrochemically inert within the potential range of the experiment and could be used to adjust the viscosity over a sufficiently large range (see Figure 6.7A). The change in viscosity of the liquid electrolyte is known to affect the diffusion coefficient of the electroactive species. The diffusion coefficient of $Fe(CN)_6^{4-}$ in 1 M KCl at different sucrose concentrations was determined by running chronoamperometry experiments utilising a micro-disc electrode with 100 μm diameter. The chronoamperometry data was analysed using simulation software package DigiElch assuming a 2D semi-infinite diffusion model to extract reliable diffusion coefficient data (see Figure 6.9B). To elucidate the effect of the kinematic viscosity on the limiting current, a normalisation accounting for the change in diffusion coefficient is applied. The double logarithmic plot of the limiting current (under rocking disc conditions) divided by $D^{2/3}$ versus kinematic viscosity is shown in Figure 6.9C (with the raw data on Figure 6.8).

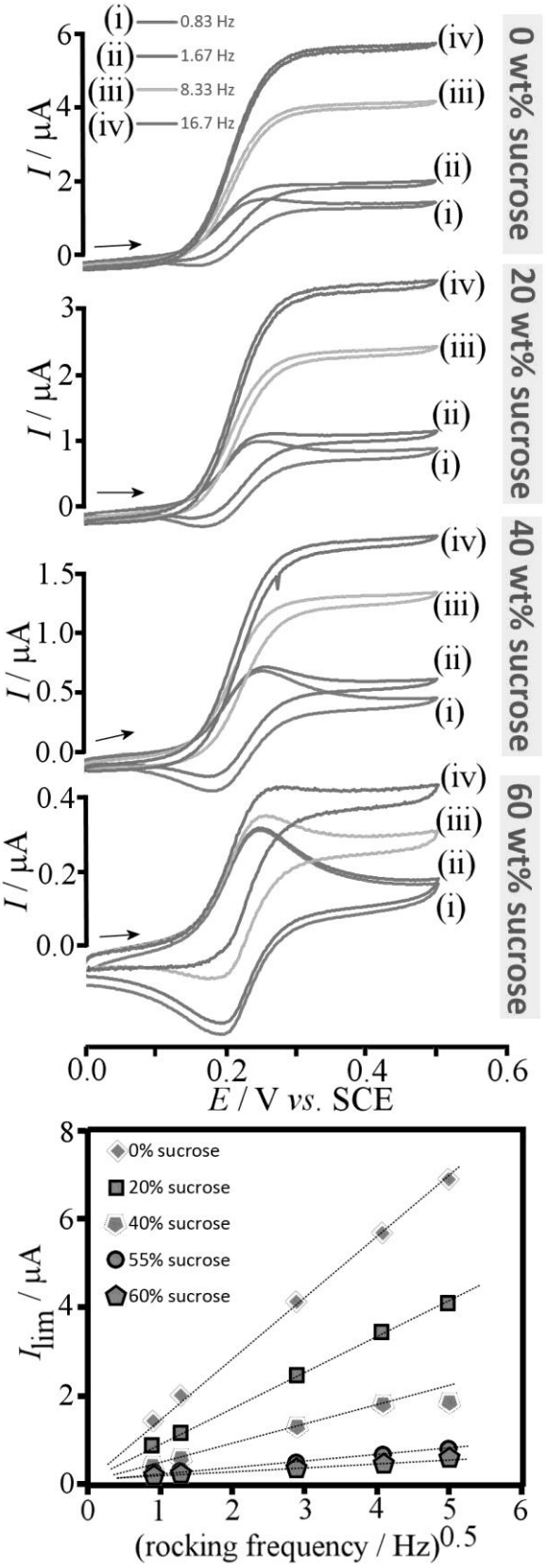

Figure 6.8. Cyclic voltammograms run at $10mVs^{-1}$ for 1 mM $Fe(CN)_6^{4-}$ in 1 M $KCl_{(aq)}$ at various rocking frequencies with A) 0 wt% sucrose content, B) 20 wt% sucrose content, C) 40 wt% sucrose content, and D) 60 wt% sucrose content. E) The corresponding 'Levich' plot for all wt% of sucrose added.

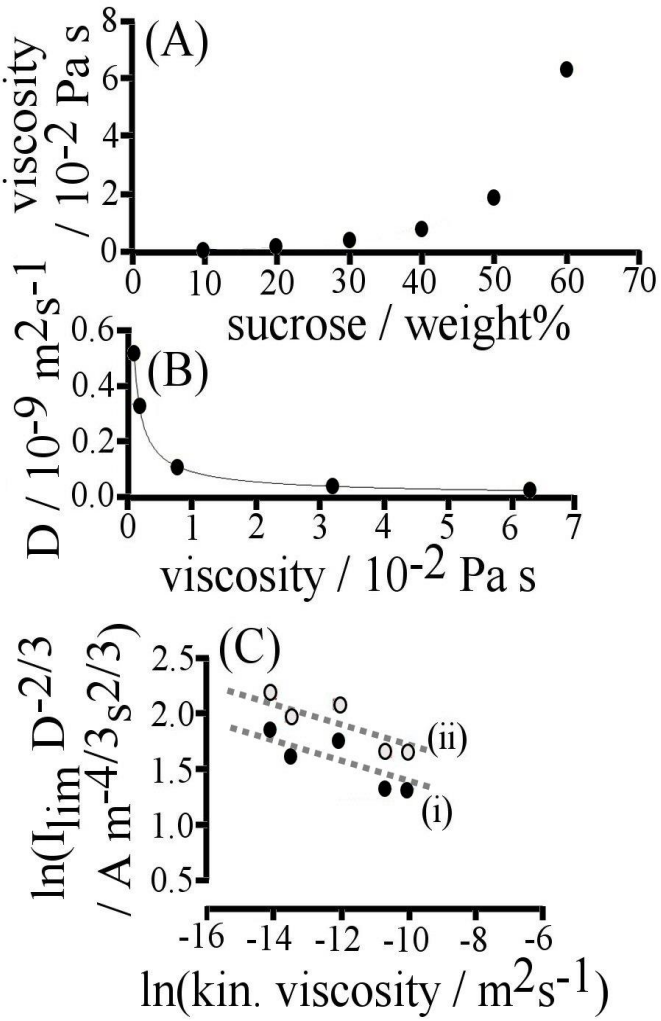

Figure 6.9. (A) Plot of the viscosity of water versus sucrose content in weight% [11]. (B) Plot of the diffusion coefficient of $Fe(CN)_6^{4-}$ in 1 M KCl (measured by micro-electrode voltammetry) versus solution viscosity. (C) Double-logarithmic plot of the $D^{2/3}$ normalised limiting current (for $Fe(CN)_6^{4-}$ in 1 M KCl) versus kinematic viscosity for (i) 8.3 Hz (slope=-0.165, R^2=0.67, SE=0.15), and (ii) 16.7 Hz (slope=-0.167, R^2=0.66, SE=0.13).

The dashed line shows the expected behaviour for $I_{\lim} \propto v^{-1/6}$ within the error of the experimental data. The rocking disc electrode limiting current appears similar to the Levich equation apart from being dependent on the rocking rate *f* and derived here for the specific case of a 90 degree rocking angle. The numerical constant 1.0 is based on fitting with the ferrocyanide redox system shown in Figure 6.4C at $10 mVs^{-1}$, where the kinematic viscosity of the electrolyte solution was assumed to be 9.16×10^{-7} cP (at 20 ^{0}C) [12].

$$I_{\lim} = 1.0(\pm 0.1) \times \frac{nFAD^{2/3}}{v^{1/6}} \sqrt{f} \qquad \text{(eq. 6.33)}$$

6.4.3 Rocking Disc Electrode Voltammetry III.: Collector-generator dual semi-disc electrode

The voltammetric response of a glassy carbon dual semi-disc electrode with a diameter of 3.5mm (with both semi-discs at the same potential) is shown in Figure 6.8A for the oxidation of 1 mM $Fe(CN)_6^{4-}$.

$$Fe(CN)_6^{4-}(aq) \rightleftharpoons Fe(CN)_6^{3-}(aq) + e^-$$

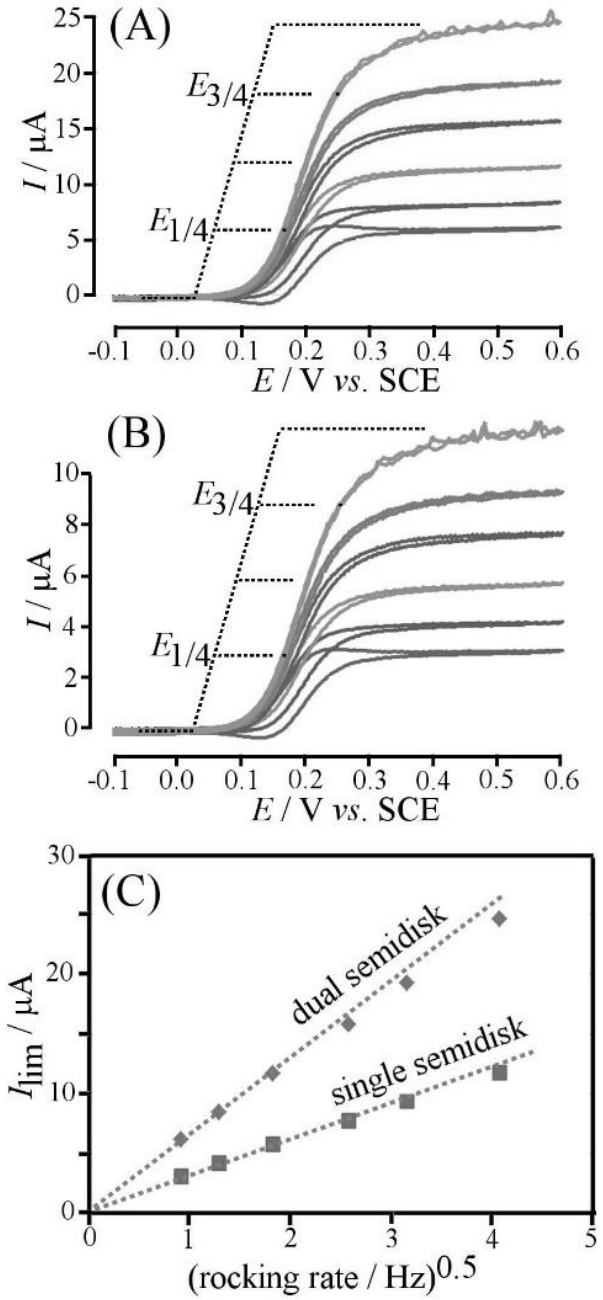

Figure 6.8. (A) Rocking disc voltammograms (scan rate 10 mVs^{-1} with rocking rates from bottom to top 0.83, 1.67, 3.33, 6.67, 10.0 and 16.67Hz) for the oxidation of 1 mM $Fe(CN)_6^{4-}$ in 0.1 M KCl at a dual semi-disc electrode. (B) As above, but only one semi-disc active. (C) Plot of the limiting current versus square root of rocking rate.

When connecting only one of the two semi-disc electrodes the mass transport controlled limiting current halves, i.e. current scales with area (see Figure 6.12C). Wave shape analysis based on the Tomeš criterion [13], $E_{3/4} - E_{1/4}$ = 84 mV at 16.67 Hz rocking rate (see Figure 6.12), suggest quasi-reversible electron transfer conditions with approximately $k^0 = \lambda \times D / \delta_{RoDE} = 2.3 \times 6.5 \times 10^{-10} / 1.8 \times 10^{-5} = 8 \times 10^{-5}$ ms^{-1} (with the λ parameter obtained from [14]) consistent with literature reports [15]. Closer inspection of the data at lower rocking rates demonstrates the switch from steady state conditions to transient conditions with a current peak emerging at a rocking rate of 0.83 Hz and a scan rate of 10 mVs^{-1}. This full transition from steady state to transient domain can be estimated from $\delta_{RoDE} = \sqrt{\frac{DRT}{v_{transition}F}}$ to occur at a transition scan rate of approximately $v_{transition}$ = 3 mVs^{-1}.

Generator-collector electrochemical systems are versatile in mechanistic analysis (e.g. detection of reaction intermediates) as well as in electroanalytical processes (e.g. avoiding capacitive background currents). For example, the rotating ring-disc electrochemical system is widely applied in electrocatalysis [16], [17], [4]. Here, the dual semi-disc electrode is employed in generator-collector configuration. In Figure 6.9A the oxidation of 1 mM $Fe(CN)_6^{4-}$ at the generator electrode is shown to be accompanied by the back-reduction at the collector electrode (held at -0.1 V vs. SCE). For both processes limiting currents are clearly defined and additional modulation effect is seen to be superimposed on the collector current response. The generator current response is changed insignificantly with or without the collector electrode being active (see Figure 6.9B), which is reminiscent to the rotating ring-disc electrode case. The flow of redox species is predominantly outward and therefore product from the collector is unlikely to diffuse back to the generator.

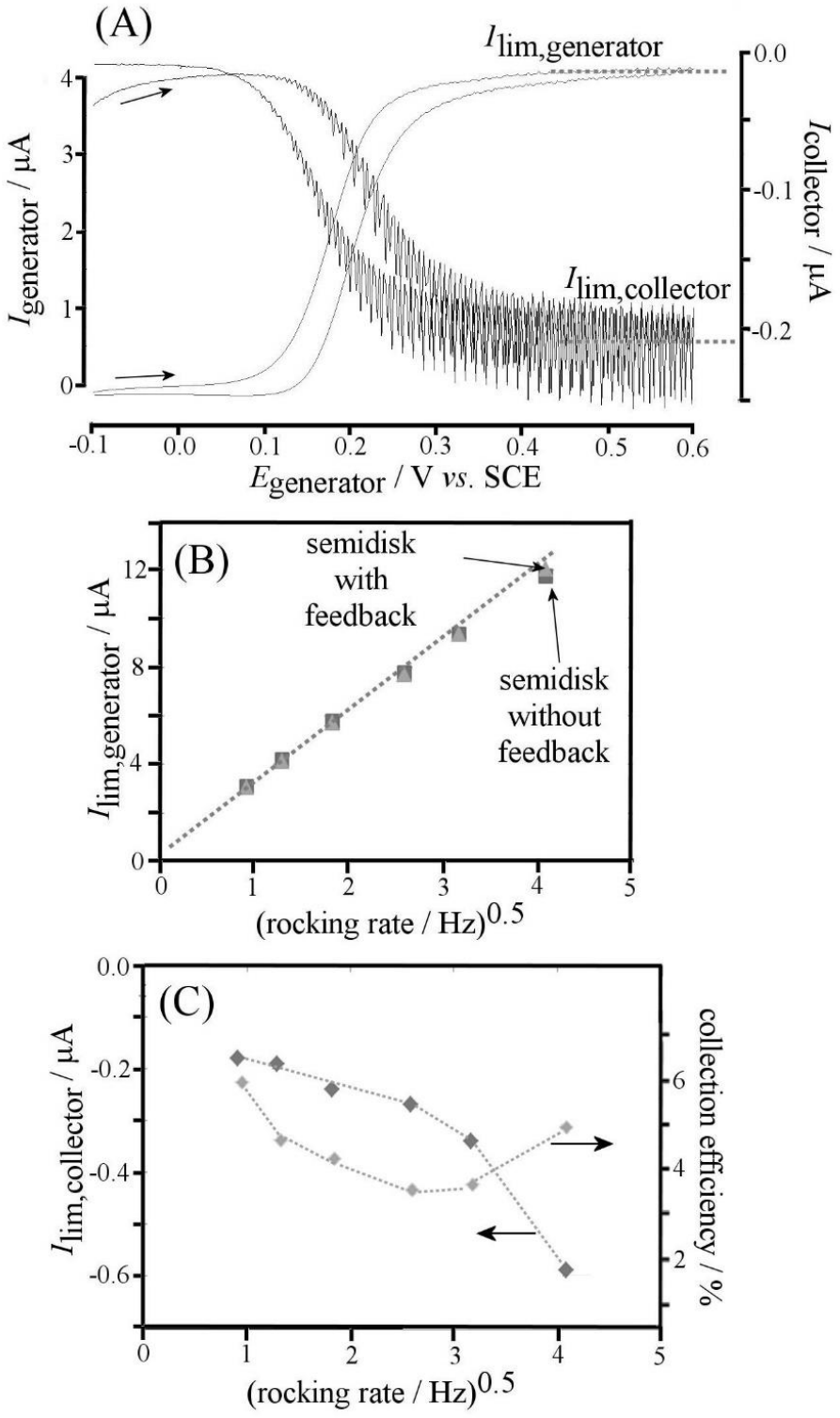

Figure 6.9. (A) Generator-collector rocking disc voltammogram (scan rate 10 mVs^{-1}, rocking rate 1.67Hz) for semi-disc generator and semi-disc collector (potential held at -0.1 V vs. SCE) for the oxidation of 1 mM $Fe(CN)_6^{4-}$ in 0.1 M KCl. (B) Plot of the limiting current at a semi-disc with or without the collector active versus rocking rate. (C) Plot of the collector limiting currents and the corresponding collection efficiencies versus square root of rocking rate.

The collector current response is significant but an order of magnitude lower compared to that for the generator. Figure 6.9C shows collector limiting current data as a function of rocking rate. The collector current increases with the square root of rocking rate, but non-linearity causes a minimum in collection efficiency at ca. 6.67 Hz rocking rate (see Figure 6.9C). This is in contrast to the rotating ring disc electrode system where the collection efficiency of the ring electrode is independent of the rotation rate. In the case of the rocking dual-semi-disc electrode, the variation in the collector efficiency with rocking rate is likely due to the (unintended) asymmetry in the construction which results in an asymmetric flow pattern (see below in Figure 6.10A). As expected for faster flow, hysteresis in both generator and collector current responses decreases with increasing rocking rate.

The collector current response is analysed in more detail in Figure 6.10. When recorded as a function of time, a regular pulse pattern is observed which is dominated by the frequency of the rocking rate. The forward and backward movement of the rocking electrode should be equivalent and therefore a symmetric alternating current is expected, but a repeating asymmetric modulation pattern is clearly observed (see Figure 6.10A-C). It is likely that a slight asymmetry in the design could induce an additional slow net angular flow of liquid over the electrode, which then causes the asymmetric pulse pattern to appear (see Figure 6.10D).

Additional information from the pulse pattern can be rationalised more effectively through Fourier transformation (see Figure 6.10E). A strong fundamental at 3.33 Hz is observed together with higher harmonics. The first harmonic should be the dominating signal, but it is suppressed relative to the fundamental due to the additional angular flow. Further harmonics contain additional information similar to cases of Fourier transform voltammetric tools developed for quiescent solution [18], [19] or for rotating disc electrode systems [20]. In future, the oscillatory components of the current may allow more detailed electron transfer of chemical rate information to be obtained or analytical sensitivity to be improved.

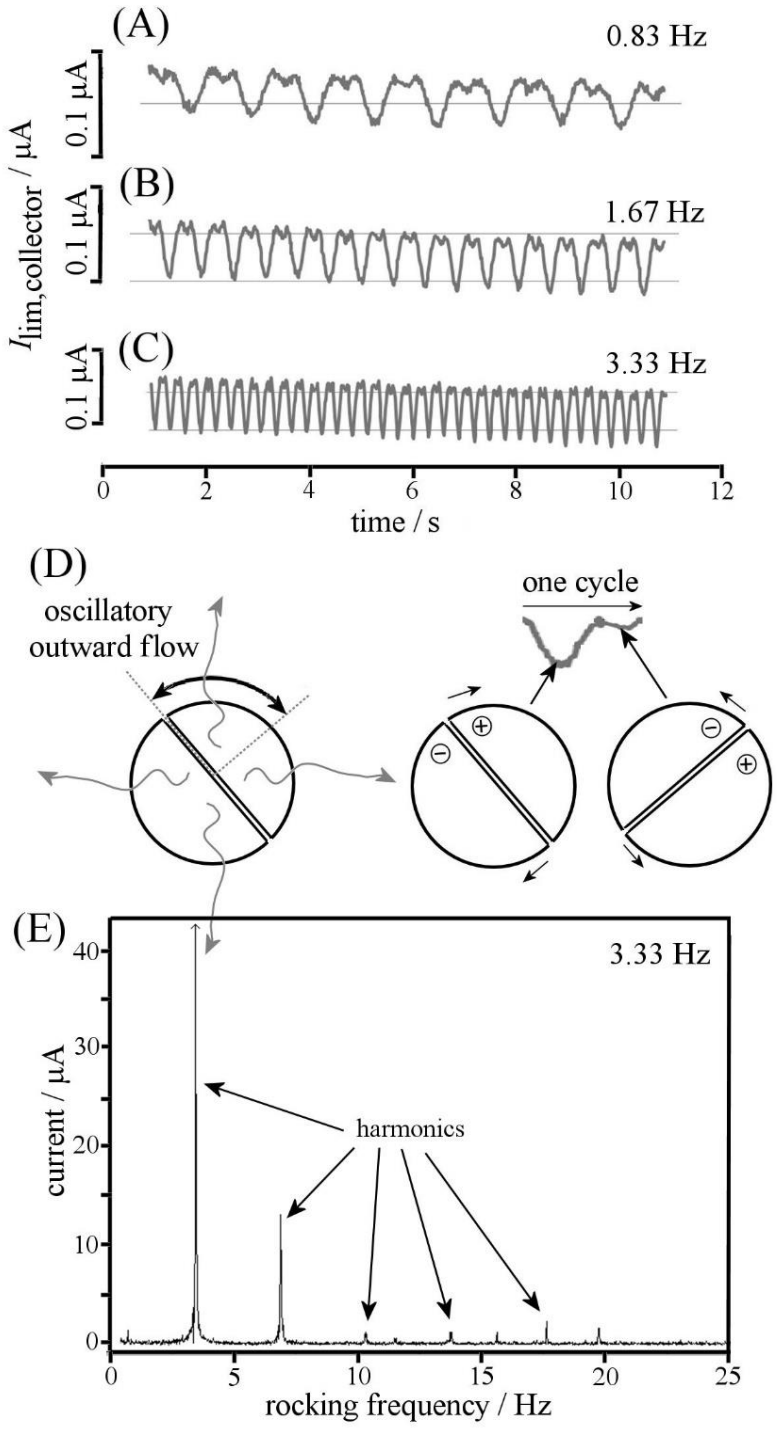

Figure 6.10. (A) Collector limiting current (rocking rate 0.83 Hz, generator potential 0.6 V vs. SCE, collector potential -0.1 V vs. SCE) as a function of time. (B) As above with rocking rate 1.67 Hz. (C) As above with rocking rate 3.33 Hz. (D) Schematic drawing of the flow pattern and the electrode movement during one cycle. (E) Fourier transformed data for a rocking rate of 3.33 Hz showing a pattern of harmonics.

6.5 Conclusion

It has been shown that for rocking frequencies up to 25 Hz for a 1.6 mm diameter inlaid platinum disc, well-defined voltammetry is possible under rocking disc voltammetry conditions. A quantitative expression, $I_{Levich,RoDE} = 0.111\, nFAD^{\frac{2}{3}} \nu^{-\frac{1}{6}} \sqrt{\Theta f}$ has been introduced based on a model and confirmed by comparison with experimental data. Intriguingly, when selecting the total rocking angle Θ = 180 degree (consistent with a full cycle for RoDE compared to RDE) the equation reverts back into the original Levich equation (with only 3% deviation) indicative of the fact that the average momentum transfer from the rocking electrode to the solution phase is similar to that induced by rotation when normalised over the angle of movement. A rocking dual-semi-disc generator-collector system is also demonstrated with a feedback response of ca. 5% collection efficiency. The rocking motion results in a superimposed current modulation with the same frequency as the rocking rate.

The potential pros and cons for RoDE experiments are as follows; (i) the RoDE system can be operated without electrical brush contacts, (ii) the rocking agitation is likely to effectively dislodge gas bubbles or particles, (iii) an approximately uniform diffusion layer allows (similar to RDE) plating of metals or thin films evenly over substrates [8,10], (iv) all methods for kinetic analysis of heterogeneous or homogeneous electrode reactions can be applied in a similar way for RoDE and RDE, and (v) electro-synthetic reactions are possible under defined diffusion layer thickness conditions. Possible problems arise from currently unknown effects of the container size and shape with significant changes in flow pattern expected for both RDE and RoDE if there is only a small gap between the container wall and the electrode [21]. For the case of non-Newtonian fluids interesting differences in RDE and in RoDE experiments should emerge. The miniaturisation of the RoDE experiment similar to that for the RDE [22] appears possible and potentially useful.

Future applications of the rocking disc voltammetry methodology are possible in plating or electro-polishing applications, where uniform mass transport and removal of bubbles from electrode surfaces are desirable. Due to the uniform accessibility of the electrode surface, the expression for the limiting current is readily adapted to apply to other electrode shapes (non-circular) and sizes. The interaction of colloid and micro-particles with the flow field in RDE experiments has been recognised to significantly affect mass transport [23]. This effect can be predicted to change under RoDE conditions possibly leading to a better interaction of the particles with the electrode surface.

6.6 References

[1] W. J. Albery and M. G. Boutelle, “The mechanism of Faradaic reactions at the thioine coated electrode,” *J. Electroanal. Chem.*, vol. 182, p. 99, 1985.

[2] J. Newman, “Schmidt number correction for the rotating disk,” *J. Phys. Chem.*, vol. 70, no. 4, pp. 1327–1328, 1966.

[3] V. G. Levich, *Physicochemical hydrodynamics*. Prentice-Hall, Englewood Cliffs, 1962.

[4] W. J. Albery, S. Bruckenstein, and D. T. Napp, “Ring-disc electrodes part 3. Current-voltage curves at the ring electrode with simultaneous currents at the disc electrode,” *Trans. Faraday Soc.*, vol. 62, pp. 1932–1937, 1966.

[5] B. Miller and S. Bruckenstein, “Theoretical and experimental study of hydrodynamically modulated current-potential curves at rotating disk electrodes under conditions of mixed electron and mass transfer control,” *J. Electrochem. Soc.*, vol. 121, no. 12, p. 1558, 1974.

[6] J. A. Cooper and R. G. Compton, “Channel electrodes - A review,” *Electroanalysis*, vol. 10, pp. 141–155, 1998.

[7] C. E. Hotchen, H. V. Nguyen, A. C. Fisher, P. E. Frith, and F. Marken, “Hydrodynamic microgap voltammetry under couette flow conditions: electrochemistry at a rotating drum in viscous poly(ethylene glycol),” *ChemPhysChem*, vol. 16, pp. 2789–2796, 2015.

[8] C. Y. Cummings, P. E. Frith, G. Zoppi, I. Forbes, K. D. Rogers, D. W. Lane, and F. Marken, “Rocking disc electro-deposition of copper films on Mo/MoSe2 substrates,” *Thin Solid Films*, vol. 519, no. 21, pp. 7458–7463, 2011.

[9] R. N. Adams, *Electrochemistry at solid electrodes*. New York: Marcel Dekker, 1969.

[10] C. Y. Cummings, G. Zoppi, I. Forbes, D. Colombara, L. M. Peter, and F. Marken, “Rocking disc electro-deposition of CuIn alloys, selenisation, and pinhole effect minimisation in CISe solar absorber layers,” *Electrochim. Acta*, vol. 79, pp. 141–147, 2012.

[11] K. Doseok, “Viscosity of sucrose aqueous solutions measured by fluorescence correlation spectroscopy,” *J. Korean Phys. Soc.*, vol. 56, no. 41, p. 1315, 2010.

[12] M. Afzal, M. Saleem, and M. Mahmood, “Temperature and concentration dependence of viscosity of aqueous electrolytes from 20.degree.C to 50.degree.C chlorides of (sodium(1+), potassium(1+), magnesium(2+), calcium(2+), barium(2+), strontium(2+), cobalt(2+), nickel(2+), copper(2+) and chromium(3,” *J. Chem. Eng. Data*, vol. 34, no. 3, pp. 339–346, 1989.

[13] K. B. Oldham and J. C. Myland, *Fundamentals of electrochemical science*. London: Academic Press, 1994.

[14] M. V Mirkin and A. J. Bard, “Simple analysis of quasi-reversible steady-state voltammograms,” no. 18, pp. 2293–2302, 1992.

[15] N. G. Ferreira, L. L. G. Silva, E. J. Corat, and V. J. Trava-Airoldi, “Kinetics study of diamond electrodes at different levels of boron doping as quasi-reversible systems,” *Diam. Relat. Mater.*, vol. 11, no. 8, pp. 1523–1531, 2002.

[16] Z. Galus and R. N. Adams, “Anodic oxidation studies of N,N-Dimethylaniline. II. Stationary and rotated disk studies at inert electrodes,” *J. Am. Chem. Soc.*, vol. 84, no. 3, pp. 2061–2065, 1962.

[17] W. J. Albery and S. Bruckenstein, “Ring-disc electrodes part 5. First order kinetic collection efficiencies at the ring electrode,” *Trans. Faraday Soc.*, vol. 62, pp. 1946–1954, 1966.

[18] C. Y. Lee, G. P. Stevenson, A. Parkin, M. M. Roessler, R. E. Baker, K. Gillow, D. J. Gavaghan, F. a. Armstrong, and A. M. Bond, “Theoretical and experimental investigation of surface-confined two-center metalloproteins by large-amplitude Fourier transformed ac voltammetry,” *J. Electroanal. Chem.*, vol. 656, no. 1–2, pp. 293–303, 2011.

[19] E. Mashkina, T. Peachey, C. Y. Lee, A. M. Bond, G. F. Kennedy, C. Enticott, D. Abramson, and D. Elton, “Estimation of electrode kinetic and uncompensated resistance parameters and insights into their significance using Fourier transformed ac voltammetry and e-science software tools,” *J. Electroanal. Chem.*, vol. 690, pp. 104–110, 2013.

[20] K. Bano, G. F. Kennedy, J. Zhang, and A. M. Bond, “Large amplitude Fourier transformed ac voltammetry at a rotating disc electrode: a versatile technique for covering Levich and flow rate insensitive regimes in a single experiment,” *Phys. Chem. Chem. Phys.*, vol. 14, no. 14, p. 4742, 2012.

[21] V.M. Chiu, P.A. Lukus, J.L. Doyle, J.O. Schenk, “Mass transport at rotating disk electrodes: effects of synthetic particles and nerve endings,” Anal. Biochem. 418 (2011) 58–65.

[22] X.P. Gao, H.S. White, “Rotating Microdisk Voltammetry,” Anal. Chem. 67 (1995) 4057-4064.

[23] R.G. Compton, C.A. Brown, “Monitoring particle sizes with rotating-disc electrodes measurement of the dissolution kinetics of calcite,” *J. Coll. Interface Sci*. 158 (1993) 243-246.

Chapter 7. Hydrodynamic Voltammetry at a Rocking Disc Electrode: EC'-type TEMPO Mediated Alcohol Oxidations

Abstract

Following on from the development and modelling of the 'rocking' disc electrode introduced in chapter 6, its application in elucidating quantitative electro-catalytic rate constants is demonstrated. Homogenous catalysis of primary alcohol oxidation using molecular catalyst 2,2,6,6-tetramethylpiperidine 1-oxyl (TEMPO) is investigated for methanol, ethanol, butan-1-ol, hexan-1-ol, benzyl alcohol, 3-pyridinemethanol, and 2-pyridinemethanol. The observed steady state catalytic currents under rocking disc conditions appear to follow an approximate EC' mechanism, where the rate limiting step was assumed to be a single chemical catalytic step between $TEMPO^+$ and the alcohol substrate. Chemical rate constants are evaluated (by varying the diffusion layer thickness) employing the DigiElch4.F simulation package. Trends in the chemical rate constants (compared with DFT calculations) suggest enhanced reactivity for methanol *versus* higher primary alcohols and for aromatic *versus* non-aromatic primary alcohols. Rocking disc voltammetry allows quantitative mechanistic analysis in the laminar flow regime.

Keywords: Levich equation, hydrodynamic voltammetry, convection, fuel cells, bio-fuels.

Acknowledgements

Antoine Buchard is gratefully acknowledged for designing and running the density functional theory calculations presented in section 7.2.5 and 7.3.5.

This work is available on 'early view' as

Ahn S.D., Fisher A.C, Buchard A., Bull S.D., Bond, A.M., Marken F., Electroanalysis, Copyright (2016). John Wiley & Sons.

Contents

7.1 Introduction

Use of hydrodynamic techniques in investigating electron transfer processes coupled to homogenous chemical processes has been widely reported [1]–[4]. The rotating disc electrode technique has been demonstrated to be able to distinguish between most cases of electro-catalytic mechanisms [5]. Use of hydrodynamic techniques in these cases is desirable to minimize current contributions from non-faradaic processes. In the specific case of an electro-catalytic EC' mechanism (outlined in Figure 7.1) the electro-catalyst precursor, A, is oxidised at the electrode surface by an applied potential. The active electro-catalyst, B, is generated which then reacts with substrate species E to re-generate catalyst precursor A and to produce product F. The true nature of the EC' process can be more complex with multi-electron transfer steps and additional comproportionation processes. To obtain reliable kinetic information on a given mechanism through voltammetric measurements, repeating experiments in a variety of settings (i.e. substrate concentration and catalyst concentration) is recommended. Along with this, modulating the rate of electro-catalyst formation (or the diffusion layer thickness) through hydrodynamic methods provides another layer of settings to test the consistency of the kinetic data obtained.

$A \rightleftharpoons B + e^-$ electrochemical step

$B + E \rightarrow F + A$ chemical step

Figure 7.1. Reaction scheme of an electro-catalytic EC' mechanism.

Further to the development of the novel hydrodynamic 'rocking' disc electrode technique introduced in Chapter 6, its application in elucidating quantitative kinetic information through the voltammetry of an electro-catalytic system is demonstrated. Use of a commercial electrochemistry simulation software package (DigiElch 4.F) is utilized to support the mechanistic analysis. Here, the electro-catalytic mechanism of 2,2,6,6-tetramethylpiperidine-1-oxyl (TEMPO) mediated alcohol oxidation is investigated (see Fig. 7.2). Unlike the electro-catalytic system utilized in chapter 5 where a TEMPO derivative is immobilized in an inert film on the electrode surface for heterogeneous catalysis, in this case the TEMPO catalyst is dissolved in an aqueous electrolyte solution to mediate homogenous catalysis of alcohol oxidation.

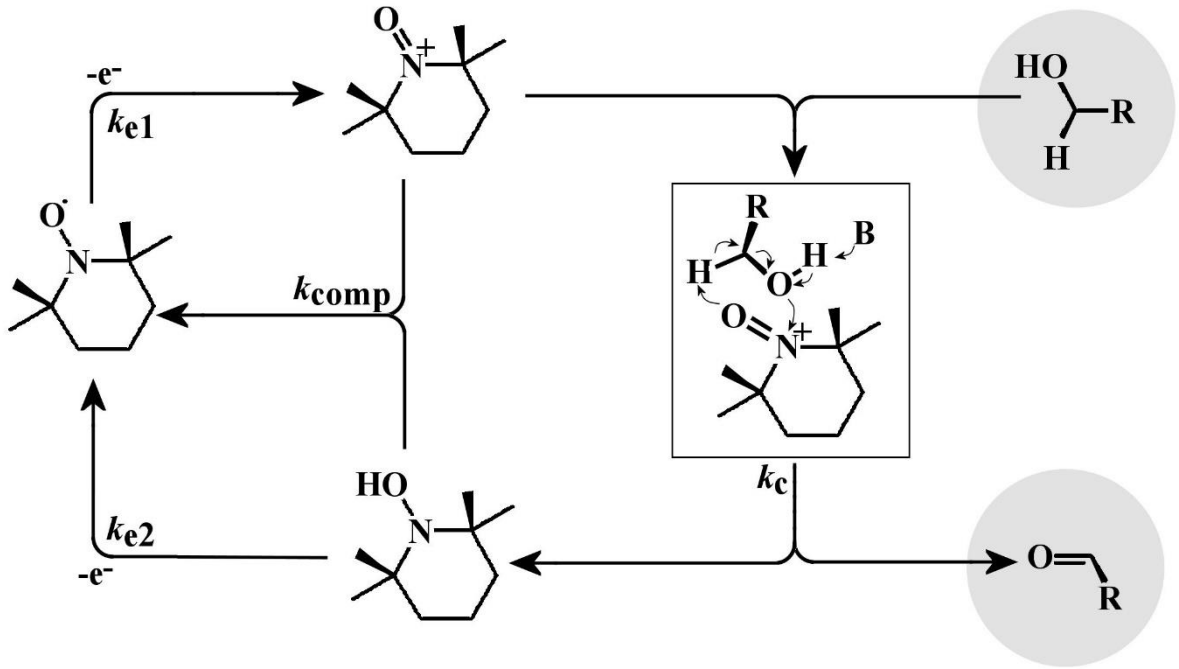

Figure 7.2. Mechanistic scheme of electrochemical TEMPO oxidation coupled to the catalytic oxidation of a primary alcohol. k_{e1} and k_{e2} are electrode kinetic constants, k_c is the chemical rate constant for alcohol oxidation and $k_{comp.}$ is the rate constant for the comproportionation of $TEMPO^-$ and $TEMPO^+$.

The electrochemistry of nitroxyl based free radicals has been introduced in chapter 5. Despite its extensive utility in oxidative catalysis [6]–[9], particularly for alcohols, mechanistic aspects of TEMPO catalysis are not fully understood. In a recent study, electrochemical TEMPO mediated alcohol oxidation have been investigated [10], and the following observations were made: (i) catalytic current was affected by the pH, (ii) catalytic current did not increase linearly with the concentration of alcohol, (iii) the rate limiting process is a chemical step (as opposed to electrochemical) and (iv) at high pH (>11), the TEMPO catalyst is irreversibly degraded by hydroxide ions. Further to these observations, it was recently reported that the nature of the electrolyte ions present in solution also affects the catalytic process though its specific role is unclear [11]. Herein, further attempts to understand the rate limiting mechanism in TEMPO oxidation of various alcohols under rocking disc conditions are attempted.

7.2 Experimental Details

7.2.1 Chemical Reagents

2,2,6,6-tetramethylpiperidine 1-oxyl (Fluka, 98%), methanol (Fisher Scientific, 99.99%), ethanol (Sigma-Aldrich, 99.8%), butan-1-ol (Sigma-Aldrich, 99%), 2-pyridinemethanol (Aldrich, 98%), 3-pyridinemethanol (Aldrich, 98%), hexan-1-ol (Aldrich, 98%), sodium bicarbonate (Sigma-Aldrich, 98%) and sodium hydroxide (Sigma-Aldrich, 99.7%) were used without further purification. Solutions were prepared in demineralized and filtered water taken from a Thermo Scientific water purification system (Barnstead Nanopure) with 18.2 MΩcm resistivity.

7.2.2 Instrumentation

For voltammetry studies, a microAutolab II potentiostat system (EcoChemie, Netherlands) was employed with a KCl-saturated calomel reference electrode (SCE, Radiometer). For all experiments, the reference electrode was placed approximately 2 mm distance from the working electrode. The working electrode was a carbon macrodisc electrode with a diameter of 3.0 mm (BAS). The counter electrode was a platinum wire. Rocking motion (90 degrees) of the working electrode was applied with an IKA Eurostar digital motor (see chapter 6.3.2). All experiments were conducted in ambient atmosphere at a temperature of 22+/- 2 ^{o}C.

7.2.3 Hydrodynamic methods: Rocking disc electrode

A recently reported novel hydrodynamic method called the 'rocking' disc electrode technique (developed as an alternative to the popular rotating disc electrode) is utilised to yield steady-state limiting currents. The current density established by the rocking motion was shown to be uniform across the electrode in a previous study [12]. The diffusion layer thickness (δ) corresponding to a rocking rate of a given system can be extracted from the steady state current (I) using equation 7.1, where n is the number of electrons transferred per electro-active molecule, F is the Faraday constant, D is the diffusion coefficient of the electro-active species, A is the electrode area, and c is the concentration of the electro-active molecule. Note that the simulation does not require any assumptions to be made about the nature of hydrodynamic flow, other than the current density being even, such that a uniform diffusion layer is established.

$$\delta = \frac{nFADc}{I} \qquad \text{(eq. 7.1)}$$

7.2.4 DigiElch Simulation Procedures

Simulations and fitting with stationary voltammetry experiment were performed using a 1D semi-infinite diffusion model on DigiElch 4.F. The diffusion coefficient of TEMPO (which was set equal to $TEMPO^-$ and $TEMPO^+$) was fitted to match the peak current magnitude for the TEMPO/$TEMPO^+$ couple. Fitting the $TEMPO^-$/TEMPO redox couple was difficult due to broadened peaks and interference from other processes in the background of the experimental data. Simulations for rocking disc experiments were performed assuming a 1D finite diffusion model (hydrodynamic conditions), using the diffusion layer thickness estimated from steady-state experimental data of pure TEMPO in aqueous carbonate buffer solution. The parameters for the catalytic mechanism were chosen as shown below (Table 7.1; see text).

Table 7.1. Processes simulated on DigiElch software with their corresponding rate constants. The transfer coefficient (α) was assumed to be 0.5 for both electron transfer steps. $E_{mid(TEMPO/TEMPO+)}$ was +0.49 V, and $E_{mid(TEMPO-/TEMPO)}$ was -0.20 V. $K_{eq.1}$ and $K_{eq.2}$ were fixed at a value of 1 x 10^{10} to simulate chemically irreversible reactions. Rate constant k_{b1} and k_{b2} represents the rate of the chemical reaction going backwards for alcohol oxidation and comproportionation reaction respectively. Rate constant k_c is represented by 'Y' which is fitted to match the simulation with the experimental data. The concentrations of TEMPO and the substrates are specified in the results and discussions section.

$TEMPO^{\bullet}$ - e^- => $TEMPO^+$	k_{e1}	1 x 10^5 cms^{-1}
$TEMPO^-$ - e^- => TEMPO	k_{e2}	3.5 x 10^{-6} cms^{-1}
$TEMPO^+$ + Alcohol => $TEMPO^-$ + Aldehyde	k_c (= $K_{eq.1}$ x k_{b1})	Y $M^{-1}s^{-1}$
$TEMPO^+$ + $TEMPO^-$ => 2 x $TEMPO^{\bullet}$	$k_{comp.}$(= $K_{eq.2}$ x k_{b2})	1 x 10^6 $mol^{-1}dm^3s^{-1}$

The electron transfer kinetic constant k_{e1} and k_{e2} were obtained experimentally (see text) by simulating and fitting cyclic voltammetry data and the separation of the oxidation and reduction peaks using DigiElch 4.F simulation software. The transfer coefficient (α) was assumed to be 0.5 for both electron transfer steps, and the equilibrium constant (K_{eq}) of both chemical steps were set high at 1 x 10^{10} to simulate irreversible reactions. The rate of comproportionation of TEMPO has been reported to be rapid in alkali phosphate buffer [13], but that study does not address the significance of buffer ion effects which were recently reported to be significant in TEMPO catalysis [11]. As there are no reported quantitative kinetic constants for TEMPO comproportionation for the conditions used for

this study to date, the rate of comproportionation is assumed to be fast such that it is not rate limiting. The rate limiting step is the chemical reaction of $TEMPO^+$ with alcohol; the chemical constant k_c is adjusted to fit the experimental data. The diffusion coefficient of substrates were approximated by literature values taken in similar conditions, and in the case none were available Wilke-Chang's method [14] was utilized for an estimate (see Table 7.2).

Table 7.2. List of substrates and their diffusion coefficients as entered into the DigiElch simulation.

Substrate	Diffusion coefficient / m^2s^{-1}	Reference
$TEMPO/TEMPO^-/TEMPO^+$	6.2×10^{-10}	Experimental data
methanol	1.4×10^{-9}	[15]
ethanol	1.2×10^{-9}	[16]
butan-1-ol	8.5×10^{-10}	[17]
hexan-1-ol	7.0×10^{-10}	Wilke-Chang estimate
benzyl alcohol	8.2×10^{-10}	[18]
2-pyridinemethanol	7.6×10^{-10}	Wilke-Chang estimate
3-pyridinemethanol	7.6×10^{-10}	Wilke-Chang estimate

7.2.5 Density Funtional Theory (DFT) Calculation of Kinetic Barriers

The reaction between oxidised $TEMPO^+$ cation, $NaCO_3^-$ anion and various primary alcohols was examined using DFT calculations. Calculations were performed with Gaussian09 suites of code [23] and protocol rB3LYP/6-311++G(d,p)/SCRF= (cpcm,solvent=water)/ temperature=298.15. The nature of all the stationary points as minima or transition states were verified by calculations of the vibrational frequency spectrum. All transition states were characterized by normal coordinate analysis revealing precisely one imaginary mode corresponding to the intended reaction, and verified by Intrinsic Reaction Coordinates. As expected, the oxidation of alcohols to aldehydes by $TEMPO^+$ is highly thermodynamically favoured. Calculations also revealed the key hydride transfer step to occur via a cyclic transition state (see Fig. 7.3), with an activation barrier low enough for the reaction to happen readily at room temperature. Table 7.3 shows the calculated free enthalpy barriers of this transition state for a series of alcohols. Figure 7.3 illustrates the proposed reaction mechanism. A two-electron transfer occurs formally as hydride transfer from the primary alcohol to the $TEMPO^+$ oxygen.

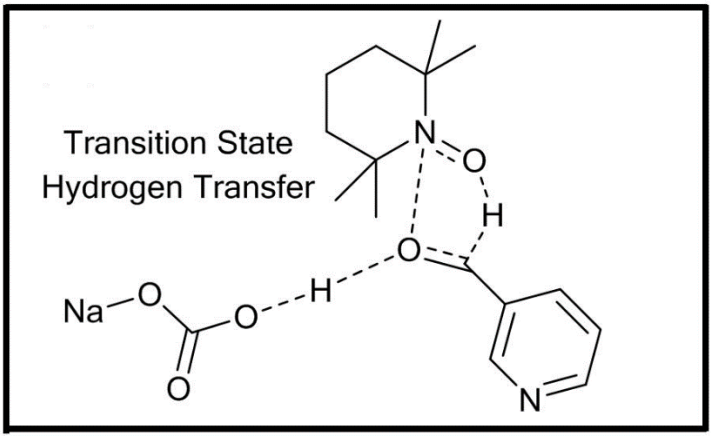

Figure 7.3. Schematic of the rate limiting transition state for which the activation energy barrier is calculated using DFT. The hydride transfer reaction occurs through cyclic transition state. Note that the calculation was completed with the inclusion of the carbonate anion.

Table 7.3. Summary of DFT calculation results in terms of the approximate activation barrier for the two-electron transfer process converting a primary alcohol to an aldehyde.

Substrate	**DFT barrier / kJmol^{-1}**
methanol	14.5
ethanol	19.7
butan-1-ol	20.7
hexan-1-ol	20.5
benzyl alcohol	12.8
2-pyridinemethanol	17.7
3-pyridinemethanol	13.1

7.3 Results and Discussion

7.3.1. Rocking Disc Electrode Voltammetry I.: Oxidation of TEMPO in Carbonate Buffer

Voltammetric data for TEMPO oxidation at a 3 mm diameter glassy carbon electrode immersed in pH 9.5 carbonate buffer was obtained (see Figure 7.4). Two prominent redox processes are observed and assigned to P1: the oxidation of the free radical TEMPO to the cation (equation 7.2) and P2: the reduction of TEMPO to the one-electron reduced and de-protonated form $TEMPO^-$ with a $pK_A \approx 6.6$ (equation 7.3).

$$\text{P1:} \quad \text{TEMPO} \rightleftharpoons \text{TEMPO}^+ + e^- \qquad \text{(eq. 7.2)}$$

$$\text{P2:} \quad \text{TEMPO}^- \rightleftharpoons \text{TEMPO} + e^- \qquad \text{(eq. 7.3)}$$

From analysis of the midpoint potentials (obtained from the peak potentials with $E_{mid} = ½\ E_{p,ox} + ½\ E_{p,red}$, see Figure 7.4) it is possible to obtain the approximate reversible potentials for process P1 (TEMPO/$TEMPO^+$ with E_{mid} of +0.49 V vs. SCE) and for process P2 ($TEMPO^-$/TEMPO with E_{mid} of -0.20 V vs. SCE). From the peak-to-peak separation for process P1, ca. 60 mV, it can be inferred that electron transfer at the electrode | solution interface is fast. In contrast, for the peak-to-peak separation for process P2, ca. 700 mV, it can be concluded that electron transfer is essentially irreversible. Further analysis of the data was carried out by comparison to simulation data (utilizing DigiElch 4.F software, see dashed line in Figure 7.4). With the concentration of TEMPO in solution known, the diffusion coefficient of TEMPO, $D_{TEMPO} = 6.0 \times 10^{-10}\ m^2s^{-1}$, was evaluated by fitting the peak currents for process P1. Next, the rate for heterogeneous electron transfer for process P1 was selected high ($10^3\ ms^{-1}$) whereas the position of the reduction and oxidation peaks for process P2 were fitted to give an apparent standard rate constant for heterogeneous electron transfer of $k_{e2} = 3.5 \times 10^{-8}\ ms^{-1}$. This treatment provides a good approximate description for the rate of the interfacial process (*vide infra*).

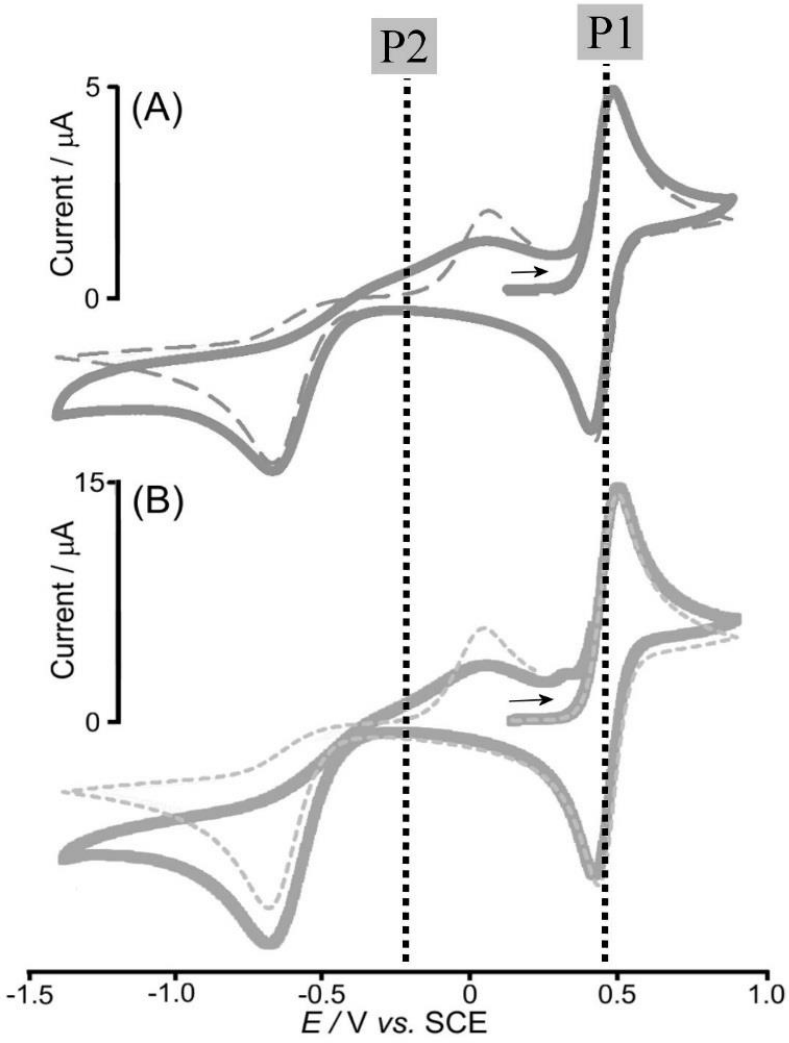

Figure 7.4. Cyclic voltammetry data obtained at 10 mVs^{-1} for (A) 1 mM and (B) 3 mM TEMPO dissolved in 0.1 M carbonate buffer pH 9.5. Comparison of experimental data (solid lines) with DigiElch simulations (dashed lines). 2D semi-infinite diffusion model with D_{TEMPO} = 6.0 x 10^{-10} m^2s^{-1}.

Table 7.4. E_{mid} and electron transfer kinetic rate constant data for the two redox forms of TEMPO. Mass transport limited voltammetry of TEMPO under hydrodynamic rocking disc electrode conditions is analysed utilizing DigiElch 4.F simulation software.

		$TEMPO^-$/TEMPO		TEMPO/$TEMPO^+$	
[TEMPO] / M	**[buffer] / M**	**E_{mid}/V**	**k_{e1}/ms^{-1}**	**E_{mid}/V**	**k_{e2}/ms^{-1}**
0.001	0.1	-0.2	$3.5x10^{-8}$	0.49	100
0.003	0.1	-0.2	$3.5x10^{-8}$	0.49	100

Under hydrodynamic conditions voltammetric processes change from transient (with peak responses) to steady state (with sigmoidal responses). Typical rocking disc electrode voltammetry data are shown in Figure 7.5A. With increasing rocking rate the shape changes and the mass transport limited current increases. A quantitative "Levich-type" expression for this type of process has been reported in Chapter 6 (equation 7.4).

$$I_{lim} = 0.111nFAcD^{2/3}v^{-1/6}(\Theta f)^{1/2} \qquad \text{(eq. 7.4)}$$

In this expression, I_{lim} is the hydrodynamic mass transport limited current, *n* is the number of electrons transferred per molecule diffusing to the electrode surface, *F* is the Faraday constant, *A* is the geometric electrode area, *D* is the diffusion coefficient, v is the kinematic viscosity, Θ is the total rocking angle in degree, and f is the rocking frequency in units of Hz. As shown in the plot in 7.5B the limiting current is linearly dependent on the square root of rocking frequency and in excellent agreement with the theory.

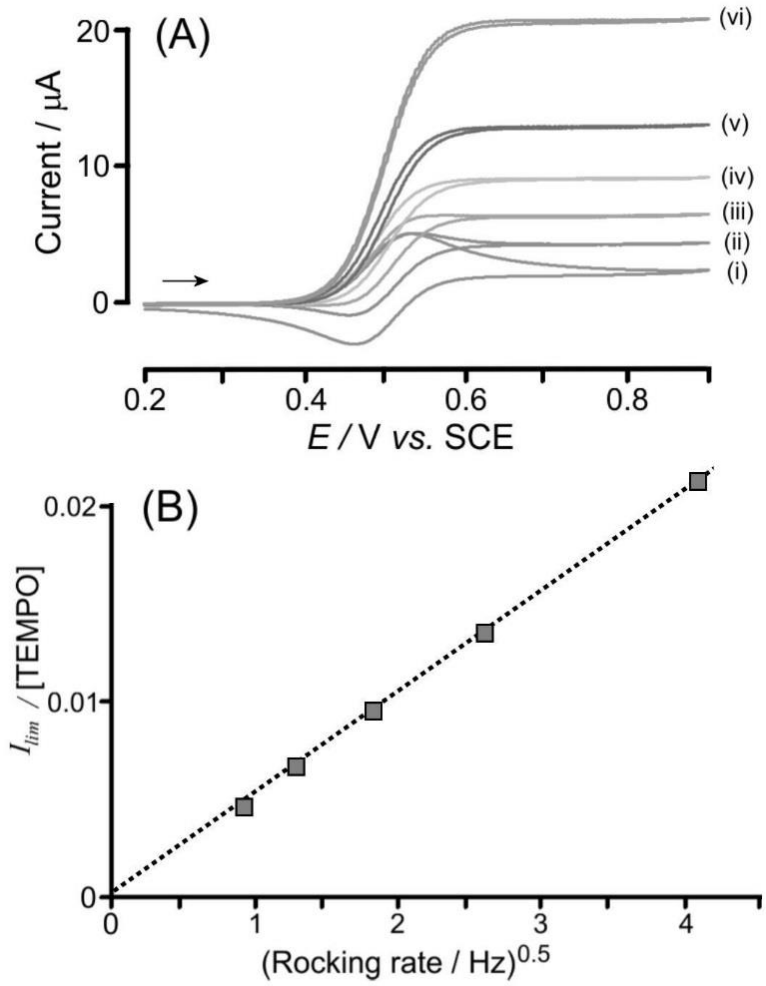

Figure 7.5. A) Cyclic voltammogram recorded at 10 mVs^{-1} of 1 mM TEMPO in 0.1M Carbonate buffer pH 9.5 at (i) 0 Hz, (ii) 0.83 Hz, (iii) 1.67 Hz, (iv) 3.33 Hz, (v) 6.67 Hz and (vi) 16.67 Hz. B) "Levich plot" of the limiting current taken from cyclic voltammograms recorded at 10 mVs^{-1} at +0.9 V vs. SCE.

Data in Figure 7.5B can be used to confirm the diffusion coefficient for TEMPO (*vide supra*). The viscosity of the electrolyte solution is approximated here to be the same as pure water (1.0×10^{-6} m^2s^{-1} at 20 ^{0}C). Taking the gradient of the linear plot in Figure 7.5B and applying equation 7.5 yields $D_{TEMPO} = 6.2\ (\pm 0.13) \times 10^{-10}$ m^2s^{-1}. This value is in good agreement with the value attained from fitting transient voltammetry data using DigiElch (*vide supra*). When evaluating the diffusion layer thickness based on equation 7.5 and employing the DigiElch simulation tool, it is now possible to model the steady state voltammetric signal as well as homogeneous reactions which may occur within the diffusion layer of the rocking disc electrode.

$$\delta_{RoDE} = \frac{9.0 D^{\frac{1}{3}} \nu^{\frac{1}{6}}}{\sqrt{\Theta f}} \qquad \text{(eq. 7.5)}$$

7.3.2 Rocking Disc Electrode Voltammetry II.: TEMPO-Mediated Oxidation of Ethanol in Carbonate Buffer

In the presence of ethanol, TEMPO-mediated 2-electron oxidation to ethanal is observed as an increase in the mass transport controlled limiting current in rocking disc voltammetry data. Figure 7.6A show the increase in current going from 0 mM to 15 mM substrate concentration. The mass transport limited current does not scale linearly with substrate concentration as would be expected for a very fast (diffusion controlled) catalytic reaction. This is consistent with literature reports for homogenous TEMPO catalysis [10] and a tell-tale sign for a chemical reaction step limiting the catalytic cycle. Figure 7.6B shows that increasing the rocking frequency (or decreasing the diffusion layer thickness) also increases the mass transport limited current. However at high rocking rates, the current due to the catalytic process relative to the mass transport limited current (for TEMPO oxidation) decreases. A convergence of limiting currents for all substrate concentrations at higher rocking rates shown in Figure 7.6D.

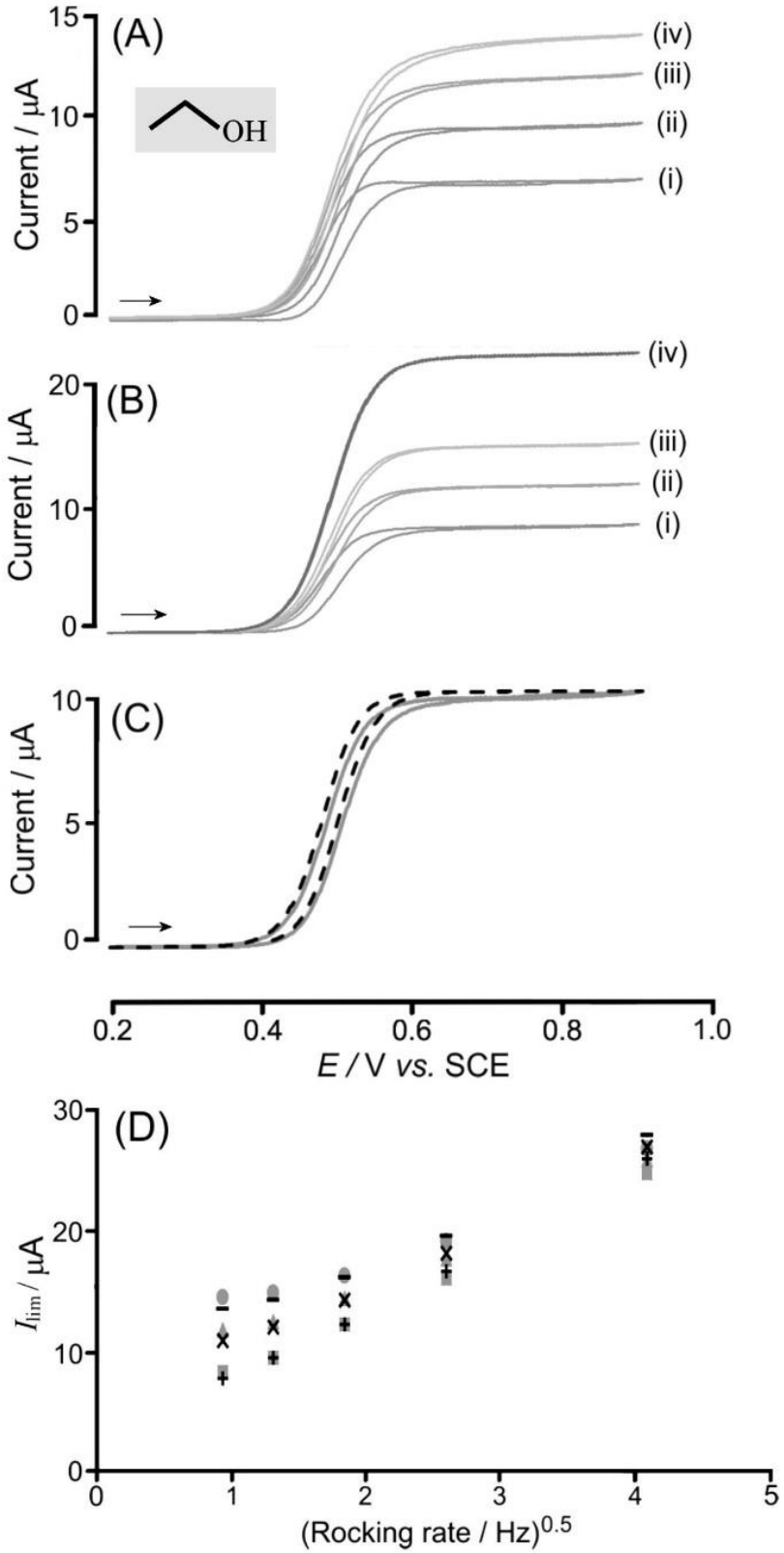

Figure 7.6. A) Cyclic voltammograms recorded at 10 mVs^{-1} of 1 mM TEMPO in 0.1 M carbonate buffer pH 9.5 at a rocking rate of 1.67 Hz, with (i) 0 mM, (ii) 5 mM, (iii) 10 mM and (iv) 15 mM ethanol. B) Cyclic voltammogram recorded at 10 mVs^{-1} of 1 mM TEMPO in 0.1 M carbonate buffer pH 9.5 with 5 mM ethanol, at a rocking rate of (i) 0.83 Hz, (ii) 3.33 Hz, (iii) 6.66 Hz and (iv) 16.67 Hz. C) Cyclic voltammograms performed at same conditions given in B but at 1.67 Hz rocking rate, with comparison

with the fitted DigiElch simulation data where $k_c = 20\ M^{-1}s^{-1}$. D) "Levich plot" of experimental limiting currents at +0.9 V vs. SCE extracted from cyclic voltammogram data plots for 5 mM (■), 10 mM (▲) and 15 mM (●) ethanol compared with currents predicted from DigiElch simulation (5 mM (+), 10 mM (x) and 15 mM (–)) assuming a rate constant of $k_c = 20\ mol^{-1}dm^3s^{-1}$ and $D_{EtOH} = 1.2 \times 10^{-9}\ m^2s^{-1}$ [16].

The proposed model for the overall reaction is shown in the reaction scheme in Figure 7.2. The rate constant k_c for the alcohol oxidation step is responsible for the additional current in the presence of ethanol and a simulation model can be used to describe the process. All parameters such as the rate of electron transfer, the comproportionation rate, all diffusion coefficients, and concentrations of all species are fixed and only the reaction rate constant k_c is used to match simulation with experimental data. Figure 7.6C shows the close to quantitative agreement for oxidation of 5 mM ethanol and a rocking frequency of 1.67 Hz. A good agreement of experiment and simulation is obtained for $k_c = 20\ mol^{-1}dm^3s^{-1}$. Data for the analysis of experiments with five different rocking rates and three different concentrations of ethanol are summarised in Figure 7.6D. The fit between experimental and simulation data (with a single set of parameters) is satisfactory as it deviates by less than 6% for all concentration of ethanol at all rocking frequencies. The deviation at the lowest rocking frequency of 0.83 Hz is the worst at around 6% deviation for all three concentrations. Generally, the trends in limiting currents with rocking rate and with concentration are reproduced by the simulation and the rate constant k_c appears valid as does the mechanism. The main error in the simulation is likely to be in the estimated (non-optimised) diffusion coefficient for the alcohol.

7.3.3 Rocking Disc Electrode Voltammetry III.: Slow TEMPO-Mediated Oxidations of Alcohols in Carbonate Buffer

In order to generate a larger data set of chemical rate constants, the rocking disc electrode voltammetry data are recorded for a wider range of primary alcohols. Data for butan-1-ol, hexan-1-ol, 3-pyridinemethanol, and benzaldehyde are shown in Figures 7.7, 7.8, 7.9, and 7.10 respectively. For butan-1-ol a relatively good match of experiment with simulation are seen for 5 mM substrate concentration with less than 3% deviation (Figure 7.7B). However, at higher substrate concentrations of 10 mM and at 15 mM butan-1-ol, the deviation increases to around 5% and 6%, respectively. The chemical rate constant for the rate limiting oxidation of butan-1-ol is $k_c = 18\ mol^{-1}dm^3s^{-1}$, which is very similar to that of ethanol.

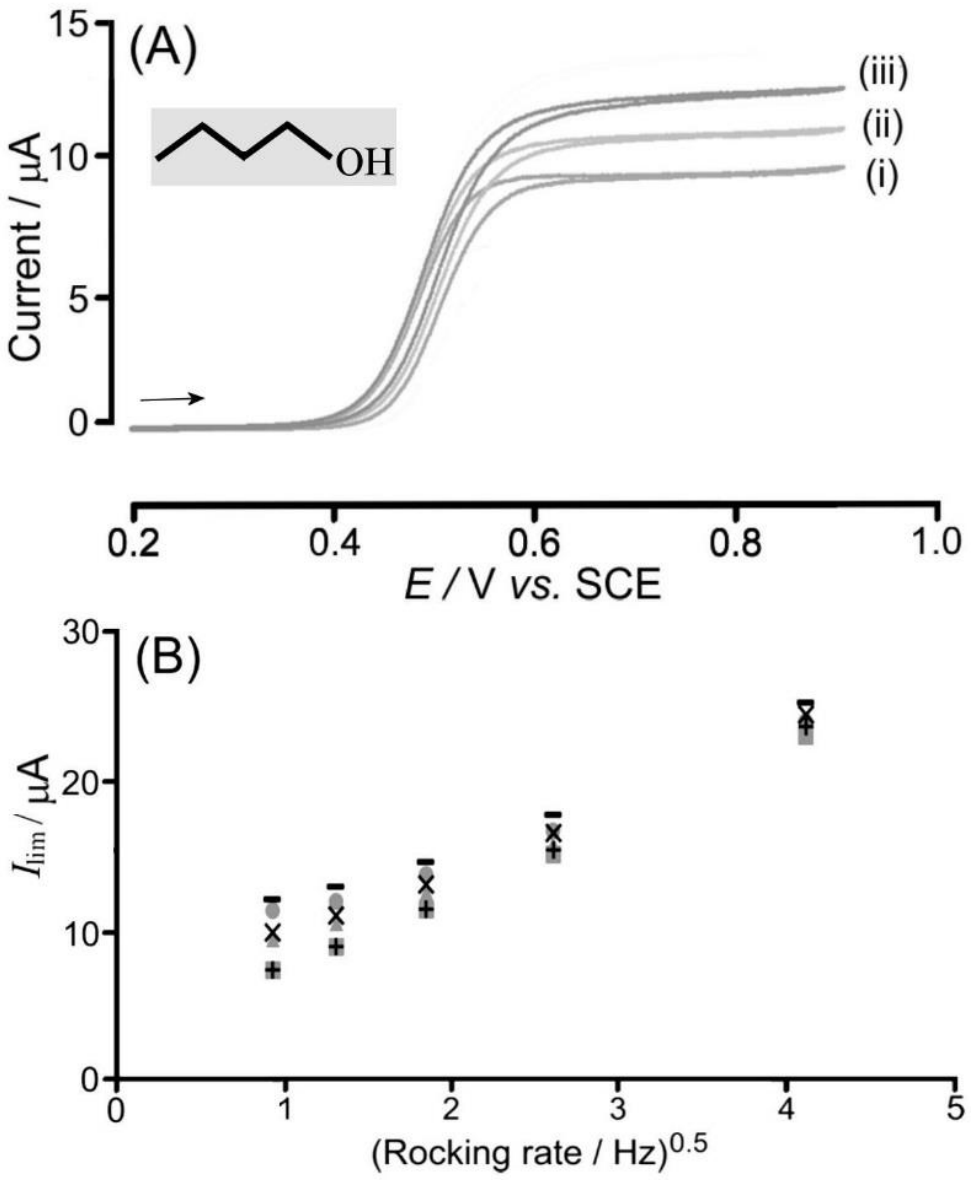

Figure 7.7. A) Cyclic voltammogram recorded at 10mVs^{-1} of 1mM TEMPO in 0.1M Carbonate buffer pH 9.5 at a rocking rate of 1.67 Hz, with (i) 5 mM, (ii) 10 mM, and (iii) 15 mM butan-1-ol. B) Levich plot of experimental limiting currents at +0.9V vs. SCE extracted from cyclic voltammogram plots for 5 mM (■), 10 mM (▲) and 15 mM (●) butan-1-ol compared with currents predicted from DigiElch simulation (5 mM (+), 10 mM (x) and 15 mM (–)) assuming a rate constant of k_c = 18 mol^{-1}dm^{3}s^{-1} and D_{BuOH} = 8.5 x 10^{-10} m^{2}s^{-1} [17].

A similar pattern of experimental data versus simulation is seen for hexan-1-ol (Figure 7.8). With approximately 4% deviation between simulation and experimental data at 5 mM substrate concentration the match of simulation with data is good. This deviation increases to 10% at 15 mM hexan-1-ol concentration for slow rocking rates. This could be an indication of substrate solubility and aggregation issues in the aqueous electrolyte solution affecting the proposed mechanistic scheme.

Most likely an error in the diffusion coefficient estimates could account for the deviation between experiment and simulation at higher substrate concentrations. However, the value of k_c = 20 $mol^{-1}dm^3s^{-1}$ is also similar with the fitted rate constant for ethanol.

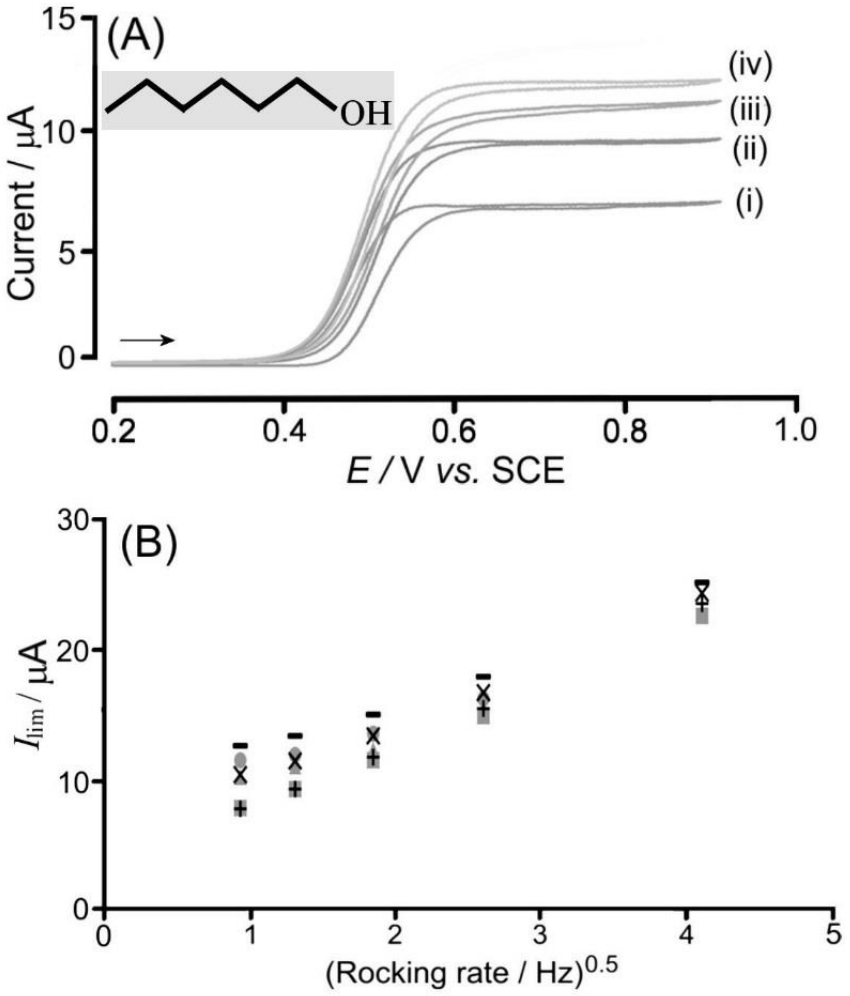

Figure 7.8. A) Cyclic voltammogram recorded at 10 mVs^{-1} of 1 mM TEMPO in 0.1 M carbonate buffer pH 9.5 at a rocking rate of 1.67 Hz, with (i) 0 mM, (ii) 5 mM, (iii) 10 mM and (iv) 15 mM hexan-1-ol. B) Levich plot of experimental limiting currents at +0.9V vs. SCE extracted from cyclic voltammogram plots for 5 mM (■), 10 mM (▲) and 15 mM (●) hexan-1-ol compared with currents predicted from DigiElch simulation (5 mM (+), 10 mM (x) and 15 mM (–)) assuming a rate constant of k_c = 19.7 $mol^{-1}dm^3s^{-1}$ and D_{HxOH} = 7 x 10^{-10} m^2s^{-1}.

For benzylalcohol (see Figure 7.9), the fit between simulation and experimental data is good for all substrate concentrations and in particular at lower rocking frequencies. There are some deviations at higher rocking frequency, which rises to around 10% at 16.7 Hz for all substrate concentrations. Inspection of rocking disc electrode voltammetric data in this case shows that for higher rocking rates

the limiting current is not fully reached, which may account for this deviation. The corresponding current suppression effect could be associated with faster mass transport affecting adsorption of substrate and product at the electrode surface or with an onset of pH gradient effects (due to the weak buffer). The rate constant, k_c = 55 $mol^{-1}dm^3s^{-1}$, evaluated for benzylalcohol is increased relative to that of ethanol.

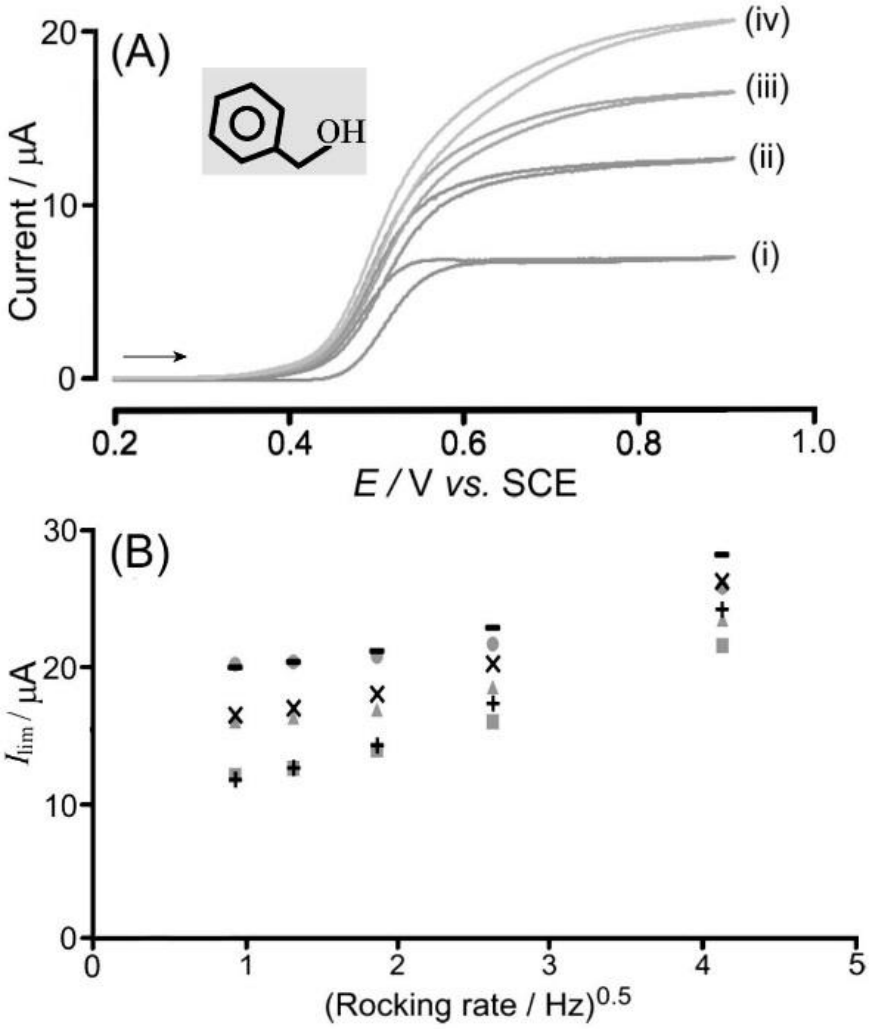

Figure 7.9. A) Cyclic voltammogram recorded at 10 mVs^{-1} of 1 mM TEMPO in 0.1 M carbonate buffer pH 9.5 at a rocking rate of 1.67 Hz, with (i) 0 mM, (ii) 4.85 mM, (iii) 9.89 mM and (iv) 14.6 mM Benzyl alcohol. B) Levich plot of experimental limiting currents at +0.9V vs. SCE extracted from cyclic voltammogram plots for 4.85 mM (■), 9.89 mM (▲) and 14.6 mM (●) Benzyl alcohol compared with currents predicted from DigiElch simulation (4.85 mM (+), 9.89 mM (x) and 14.6 mM (–)) assuming a rate constant of k_c = 55 $mol^{-1}dm^3s^{-1}$ and $D_{Benzyl\ alcohol}$ = 8.21 x 10^{-10} m^2s^{-1} [18].

When investigating 3-pyridinemethanol (Figure 7.10), the deviation between experiment and numerical simulation at lower rocking frequencies appears acceptable. The deviation again increases at the highest rocking frequencies to over 10% for all three substrate concentrations. This deviation at high rocking rates again is associated with the limiting current only very gradually increasing, possibly due to an adsorption effect when using relatively large aromatic substrate molecules in aqueous environment or the onset of pH gradient effects. The value of k_c, 122 $mol^{-1}dm^3s^{-1}$, is further increased when compared to that for benzaldehyde.

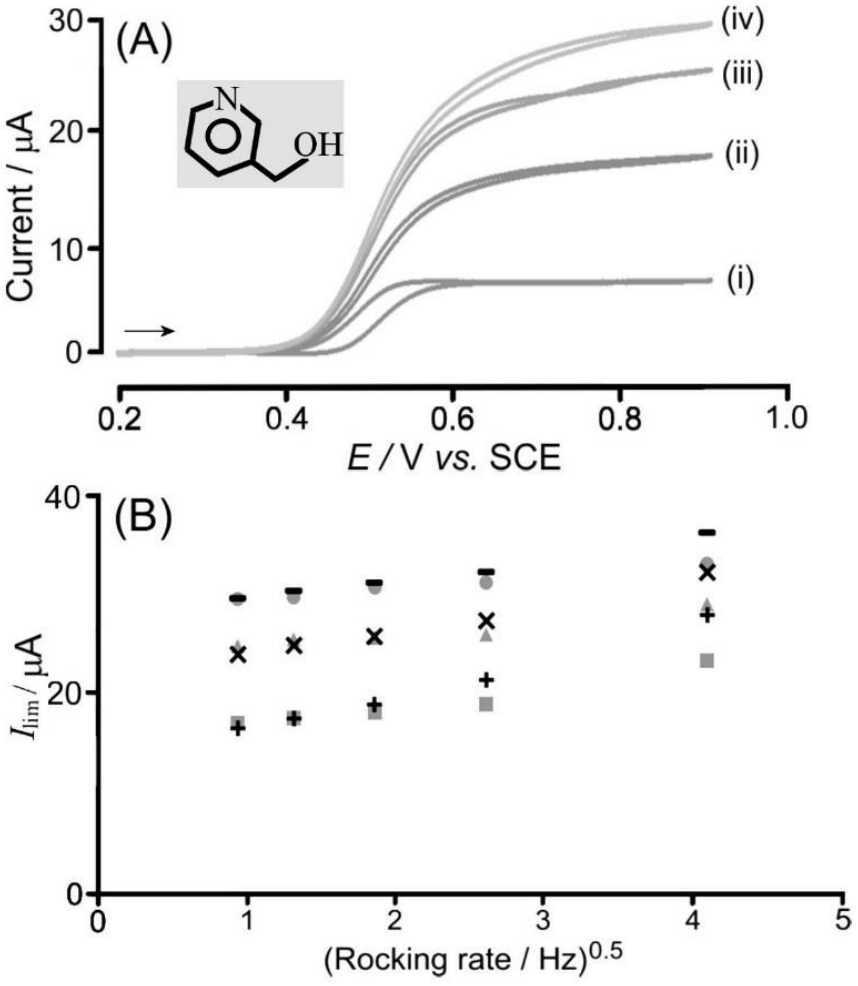

Figure 7.10. A) Cyclic voltammogram recorded at 10 mVs^{-1} of 1 mM TEMPO in 0.1M carbonate buffer pH 9.5 at a rocking rate of 1.67 Hz, with (i) 0 mM, (ii) 4.7 mM, (iii) 9.5 mM and (iv) 14 mM 3-pyridinemethanol. B) Levich plot of experimental limiting currents at +0.9V vs. SCE extracted from cyclic voltammogram plots for 4.7 mM (■), 9.5 mM (▲) and 14 mM (●) 3-pyridinemethanol compared with currents predicted from DigiElch simulation (4.7 mM (+), 9.5 mM (x) and 14 mM (–)) assuming a rate constant of k_c = 122 $mol^{-1}dm^3s^{-1}$ and D_{3PM} = 7.6 x 10^{-10} m^2s^{-1} (estimated using method in [14]).

7.3.4 Rocking Disc Electrode Voltammetry IV.: Fast TEMPO-Mediated Oxidations of Alcohols in Carbonate Buffer

Data for 2-pyridinemthanol and for methanol are presented in Figures 7.11 and 7.12. When compared to other substrates the overall fit between experimental data and simulated catalytic currents is relatively poor, although rate constants of k_c = 215 $M^{-1}s^{-1}$ and k_c = 217 $M^{-1}s^{-1}$ are obtained indicative of fast catalysis. The experimental limiting currents for both 2-pyridinemethanol and methanol appears almost independent of rocking frequency at substrate concentrations 10 mM and 15 mM (see Fig. 7.11B and 7.12B). The experimental currents are lower than that predicted by the simulation, and the deviation is more severe for higher substrate concentrations. In this case, the lack of buffer capacity for the weak carbonate buffer at pH 9.5 may play a significant role. The lack of adequate pH control is likely to impact on experimental data in particular for fast reaction rates and for higher concentrations of substrate. The values for k_c obtained here are realistic, but probably somewhat underestimate the true rate constant values.

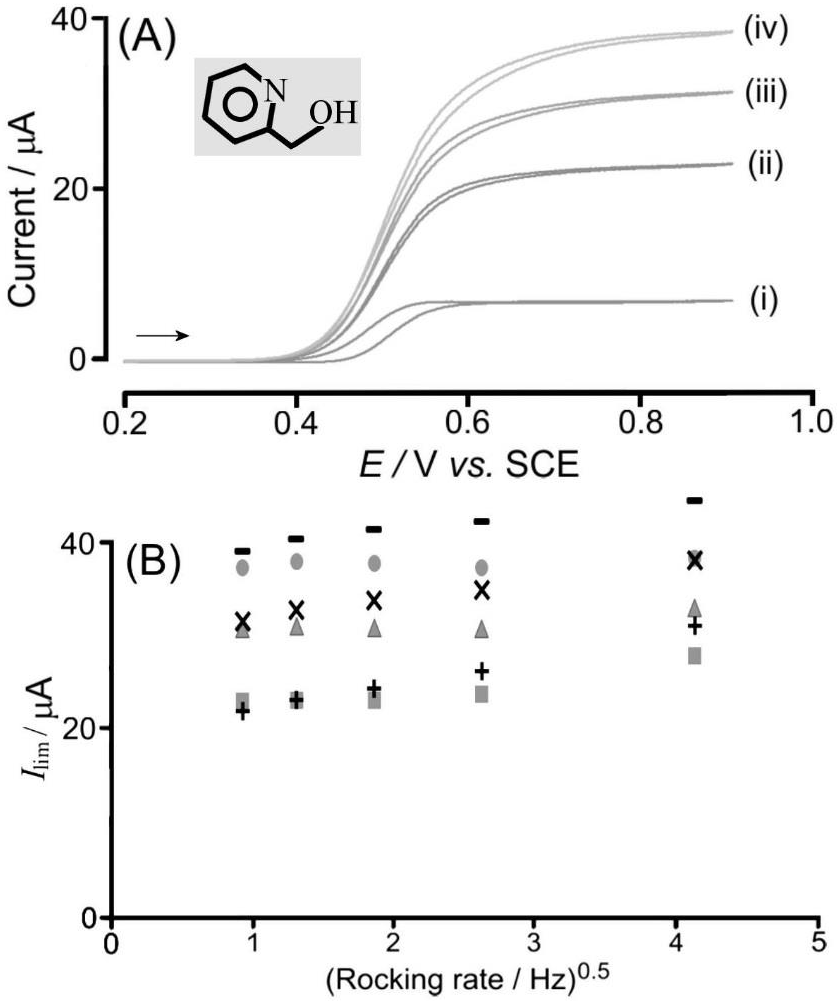

Figure 7.11. A) Cyclic voltammogram recorded at 10 mVs^{-1} of 1 mM TEMPO in 0.1 M carbonate buffer pH 9.5 at a rocking rate of 1.67 Hz, with (i) 0 mM, (ii) 5 mM, (iii) 10 mM and (iv) 15 mM 2-pyridinemethanol. B) Levich plot of experimental limiting currents at +0.9 V vs. SCE extracted from cyclic voltammogram plots for 5 mM (■), 10 mM (▲) and 15 mM (●) 2-pyridinemethanol compared with currents predicted from DigiElch simulation (5 mM (+), 10 mM (x) and 15 mM (–)) assuming a rate constant of k_c = 215 $mol^{-1}dm^3s^{-1}$ and D_{2PM} = 7.6 x 10^{-10} m^2s^{-1} (estimated using method in [14]).

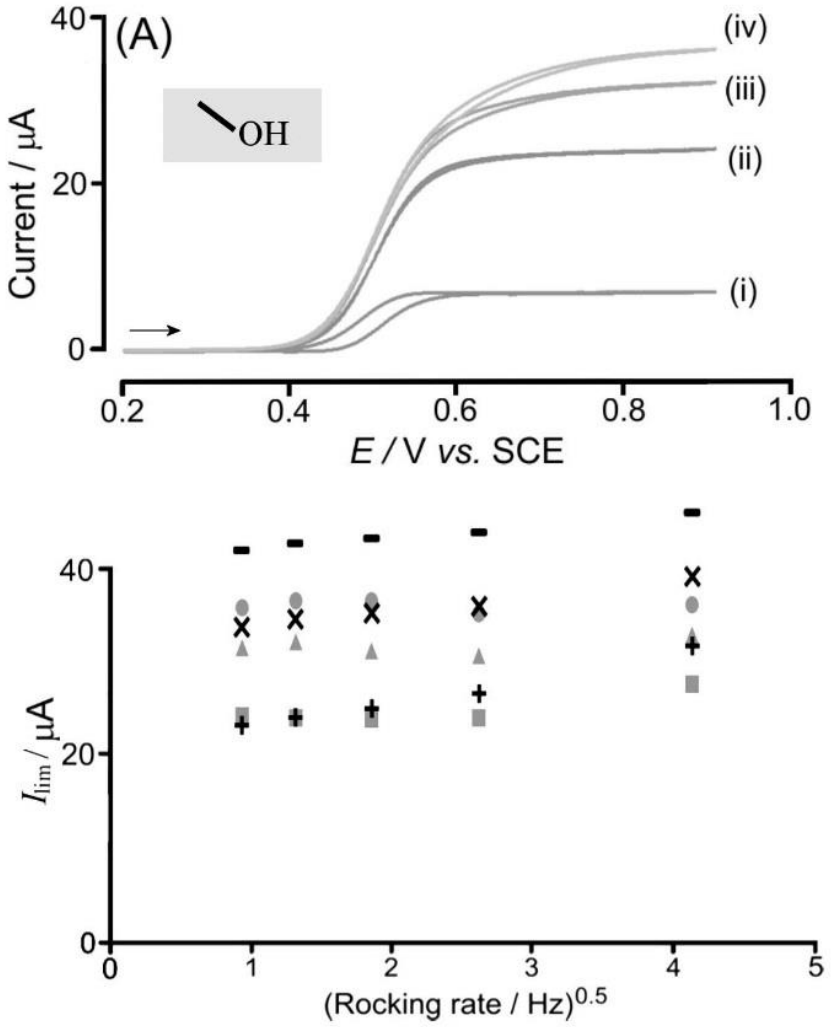

Figure 7.12. A) Cyclic voltammogram recorded at 10 mVs^{-1} of 1 mM TEMPO in 0.1 M carbonate buffer pH 9.5 at a rocking rate of 1.67 Hz, with (i) 0 mM, (ii) 5 mM, (iii) 10 mM and (iv) 15 mM methanol. B) "Levich plot" of experimental limiting currents at +0.9V vs. SCE extracted from cyclic voltammogram plots for 5 mM (■), 10 mM (▲) and 15 mM (●) methanol compared with currents predicted from DigiElch simulation (5 mM (+), 10 mM (x) and 15 mM (–)) assuming a rate constant of k_c = 217 $mol^{-1}dm^3s^{-1}$ and D_{MeOH} = 1.4 x 10^{-9} m^2s^{-1} [15].

Even with the sources of systematic error discussed earlier, the mismatch between simulation and experimental values may also suggest that there may be more complexity in the catalytic mechanism than is modelled by the simulation. The over-estimation of catalytic current may be indicative of another rate limiting process present (e.g. adsorption-desorption on glassy carbon or association of hydrophobic species in solution) that is not correctly modelled by the simulated mechanism. The catalytic model presented in section 7.2.4 assumes rapid comproportionation rates for simplification, but it is likely that it occurs at a finite rate that may become rate limiting in certain cases. An alternative mechanism where the electrochemical rate constant of $TEMPO^-$ oxidation (k_{e2}) was set to zero (such

that all the TEMPO is regenerated by the comproportionation pathway), yielded simulation data almost identical to the mechanism presented in Table 7.1 for the substrates tested in the study. This implies that the contribution of electrochemical oxidation of $TEMPO^-$ to TEMPO in the simulated catalytic mechanism is negligible in the model utilized for this study, and that the simulation results are sensitive to the specified rate of comproportionation. To the best of my knowledge, there is only one quantitative value of the second order rate constant of homogeneous comproportionation of TEMPO in literature, which was obtained for dilute aqueous phosphate buffer solutions [13]. The mechanistic model presented may show improved fit with experimental values when a comproportionation rate constant ($k_{comp.}$) obtained specifically for the set of conditions utilized for this study is applied.

7.3.5 Rocking Disc Electrode Voltammetry V: Correlation of simulated kinetic data with DFT calculations.

In order to rationalise trends in reactivity of $TEMPO^+$ towards primary alcohols, it is instructive to explore computational methods. Approximate DFT calculations are carried out to estimate the energetic activation barrier of the hydride transfer chemical step. The reaction between various primary alcohols and the $TEMPO^+$ cation, associated with a $NaCO_3^-$ anion originated from the buffer used was shown to be thermodynamically favoured. As expected from a strong oxidant, the oxidation of alcohols to aldehydes by $TEMPO^+$ was shown to be thermodynamically favoured ($\Delta G \leq -200$ kJ mol^{-1}). The calculations revealed that the key hydride transfer step from the primary alcohol to the $TEMPO^+$ cation could occur via a concerted transition state, in which the $NaCO_3^-$ buffer anion "activates" the alcohol via deprotonation, with activation barriers low enough for the reaction to happen readily at room temperature. Failing to include the buffer anion in the model resulted in activation barriers impossible to achieve at room temperature. The calculated energy barriers were used to estimate the catalytic rate constant (see Equation 7.6 below), where k is the chemical rate constant, A is the pre-exponential constant, E_A is the activation energy of the chemical process, R is the ideal gas constant and T is the temperature. Using the proposed concerted hydride transfer as the kinetic limiting step, activation energy (E_A) barrier values were obtained and plotted as Boltzmann coefficients versus the experimentally measured chemical rate constants k_c in Figure 7.13.

$$k = Aexp\frac{-E_A}{RT} \qquad \text{(Eq. 7.6)}$$

Table 7.5. Summary of rate constants extracted by fitting experimental data using DigiElch simulations.

Substrate	kinetic constant k_c / $mol^{-1}dm^3s^{-1}$	DFT barrier / $kJmol^{-1}$	Arrhenius exponential function
methanol	217	14.5	2.86×10^{-3}
ethanol	20	19.7	3.48×10^{-4}
butan-1-ol	18	20.7	2.34×10^{-4}
hexan-1-ol	20	20.5	2.50×10^{-4}
benzyl alcohol	55	12.8	5.67×10^{-3}
2-pyridinemethanol	215	17.7	8.04×10^{-4}
3-pyridinemethanol	122	13.1	5.15×10^{-3}

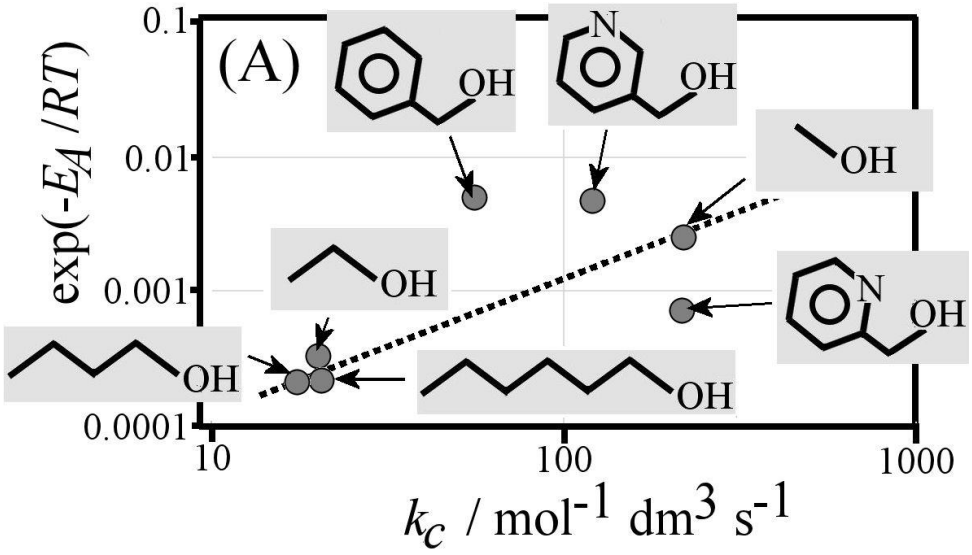

Figure 7.13. A correlation plot between the chemical rate constant k_c obtained through DigiElch fitting, with DFT kinetic calculations for (i) methanol, (ii) ethanol, (iii) butan-1-ol, (iv) hexan-1-ol, (v) benzyl alcohol, (vi) 3-pyridinemethanol and (vii) 2-pyridinemethanol.

For all simple aliphatic primary alcohols except methanol a cluster of points is observed. For methanol a significant increase in reaction rate is predicted by DFT, approximately consistent with the experimental observation. All aromatically substituted primary alcohols are predicted to be faster reacting in agreement with experiment, although no simple correlation from data is apparent. Both, experimental methods and computational methods will have to be further refined (including an in-depth investigation of other possible mechanistic pathways and solvent effects) to provide further insight into the TEMPO-mediated oxidation mechanism.

7.4. Conclusions

The rocking disc electrode technique has been utilized to investigate a complex catalytic mechanism of TEMPO-mediated oxidation of primary alcohols in aqueous carbonate buffer. A catalytic mechanism was used to obtain catalytic rate constants for methanol, ethanol, butan-1-ol, hexan-1-ol, benzyl alcohol, 2-pyridinemethanol and 3-pyridinemethanol. The rate limiting step is the chemical reaction between $TEMPO^+$ and the alcohol substrate (with assumed rapid comproportionation between $TEMPO^-$ and $TEMPO^+$ species to give 2 TEMPO). Primary alcohols with aromatic substituents and methanol are found to be more reactive than aliphatic alcohols (consistent with DFT theory). For substrates with faster chemical kinetics (3-pyridinemethanol and methanol) a greater deviation between experiment and theory is observed (less well defined limiting currents), which is likely to be caused here by insufficient pH control. Further work will be required to establish a broader portfolio of experimental values for further mechanistic analysis. The rocking disc voltammetric method promises an experimentally convenient and reliable hydrodynamic tool for kinetic studies.

7.5 References

[1] S. Bruckenstein and B. Miller, “Unraveling reactions with rotating electrodes,” *Acc. Chem. Res.*, vol. 84, no. 2, pp. 54–61, 1976.

[2] P. Beran and S. Bruckenstein, “A rotating disk electrode study of the catalytic wave produced by the reduction of iodine in the presence of iodate,” *J. Phys. Chem.*, vol. 1745, no. 15, pp. 3630–3635, 1968.

[3] S. Karp, “Homogeneous chemical kinetics with the rotating disk electrode. The ECE mechanism,” *J. Phys. Chem.*, p. 1082, 1967.

[4] R. A. Kamin and G. S. Wilson, “Rotating ring-disk enzyme electrode for biocatalysis kinetic studies and characterization of the immobilized enzyme layer,” *Anal. Chem.*, vol. 52, pp. 1198–1205, 1980.

[5] R. G. Compton, M. J. Day, M. E. Laing, R. J. Northing, J. I. Penman, and A. M. Waller, “Rotating-disc electrode voltammetry,” *J. Chem. SOC., Faraday Trans.*, vol. 84, no. 6, pp. 2013–2025, 1988.

[6] M. Zhao, J. Li, E. Mano, Z. Song, D. M. Tschaen, E. J. J. Grabowski, and P. J. Reider, “Oxidation of primary alcohols to carboxylic acids with sodium chlorite catalyzed by TEMPO and bleach,” *J. Org. Chem.*, vol. 64, no. 7, pp. 2564–2566, 1999.

[7] Z. Ma and J. M. Bobbitt, “Organic oxoammonium salts. A new convenient method for the oxidation of alcohols to aldehydes and ketones,” *J. Org. Chem.*, no. 18, pp. 6110–6114, 1991.

[8] J. M. Hoover and S. S. Stahl, “Highly practical copper(I)/TEMPO catalyst system for chemoselective aerobic oxidation of primary alcohols.,” *J. Am. Chem. Soc.*, vol. 133, no. 42, pp. 16901–10, 2011.

[9] S. D. Rychnovsky, T. L. McLernon, and H. Rajapakse, “Enantioselective oxidation of secondary alcohols using a chiral nitroxyl (n-oxoammonium salt) catalyst,” *J. Org. Chem.*, vol. 61, no. 4, pp. 1194–1195, 1996.

[10] R. a. Green, J. T. Hill-Cousins, R. C. D. Brown, D. Pletcher, and S. G. Leach, “A voltammetric study of the 2,2,6,6-tetramethylpiperidin-1-oxyl (TEMPO) mediated oxidation of benzyl alcohol in tert-butanol/water,” *Electrochim. Acta*, vol. 113, pp. 550–556, 2013.

[11] Y. Jin, K. J. Edler, F. Marken, and J. L. Scott, “Voltammetric optimisation of TEMPO-mediated oxidations at cellulose fabric,” *Green Chem.*, vol. 16, no. 6, p. 3322, 2014.

[12] C. Y. Cummings, P. E. Frith, G. Zoppi, I. Forbes, K. D. Rogers, D. W. Lane, and F. Marken, “Rocking disc electro-deposition of copper films on Mo/MoSe2 substrates,” *Thin Solid Films*, vol. 519, no. 21, pp. 7458–7463, 2011.

[13] A. Israeli, M. Patt, M. Oron, A. Samuni, R. Kohen, and S. Goldstein, “Kinetics and mechanism of the comproportionation reaction between oxoammonium cation and hydroxylamine derived from cyclic nitroxides,” *Free Radic. Biol. Med.*, vol. 38, no. 3, pp. 317–324, 2005.

[14] C. R. Wilke and P. Chang, “Correlation of diffusion coefficients in dilute solutions,” *AIChE J.*, vol. 1, no. 2, pp. 264–270, 1955.

[15] L. L. Van Loon, H. C. Allen, and B. E. Wyslouzil, “Effective diffusion coefficients for methanol in sulfuric acid solutions measured by Raman spectroscopy.,” *J. Phys. Chem. A*, vol. 112, no. 43, pp. 10758–10763, 2008.

[16] S. Parez, G. Guevara-Carrion, H. Hasse, and J. Vrabec, “Mutual diffusion in the ternary mixture of water + methanol + ethanol and its binary subsystems.,” *Phys. Chem. Chem. Phys.*, vol. 15, no. 11, pp. 3985–4001, 2013.

[17] J. Bulicka and J. Prochazka, “Diffusion coefficients in some ternary systems,” *J. Chem. Eng. …*, vol. 21, no. 4, pp. 2–6, 1976.

[18] S. E. Bialkowski, *Photothermal spectroscopy methods for chemical analysis*. John Wiley & Sons, Inc., 1996.

Chapter 8. Conclusion

In the introduction, the concept of an Integrated Chemical System was introduced where components with different functions can be synergistically combined and arranged to achieve a more complex output. In the context of electrochemistry, modifying electrodes with materials to add or improve activity, stabilise performance and to substitute more expensive materials, is desirable for enhanced control over the activity of an electrode. The thesis specifically present approaches aimed at improving the atom economy and sustainability of electrochemical processes by utilising methods that does not require post-electrolytic processing/separations. This is achieved by i) utilising triple-phase boundary systems where the electro-active species are kept in a separate phase from the source of electrons and ions, and ii) introducing methods of heterogenising the electro-catalyst from the reaction mixture by immobilising in immiscible oils or polymers of intrinsic microporosity. The first chapter began with a general overview of various electrode modification strategies pioneered throughout the last few decades as an introductory narrative for the approach taken in the thesis. Details on modification methodologies are not reviewed as the main results of the thesis utilises simple techniques in the interest of technical ease and economy. One exception to this is the first result chapter on the synthesis of carbon nanofibers.

Chapter 3 details the development of carbon nanofibers through carbonising electrospun polyacrylonitrile fibres at a much lower temperature than that commonly found in literature. Carbon nanofibers are an excellent material for mediating liquid | electrode | liquid based ion-transfer processes (or triple-phase boundary processes) as they exhibit good electronic conductivity, mechanical stability, amphiphilic properties, porosity and hence large surface area. Its utility in ion-transfer based electrochemical applications has already been demonstrated through previous work by Marken's group, where electro-synthetic transformations could be mediated in a liquid phase without intentionally added electrolyte at high yields and reasonable timeframes. This results chapter expands on this by optimizing a method to synthesize carbon nanofiber materials. Electrospun poly-acrylonitrile nanofibers were modified with graphene oxide flakes (by dip coating) before being carbonised in a vacuum furnace. Addition of graphene oxide flakes introduces surface roughness to the nanofibers which increases the surface area, and also lowers the carbonisation temperature required for the desired electrode properties from over 2000 ^{0}C to 500 ^{0}C. The chapter demonstrates proof-of-principle application of the synthesized material on triple-phase boundary microreactors for

oil analysis (redox active Manganese porphyrins dissolved in 4-phenyl-(3-propyl)-pyridine oil). Compared to microreactors previously engineered by the group, utilising carbon nanofiber materials with the low temperature method allows incorporation of relatively cheap borosilicate glass based templates, which allows more complex miniature devices to be made with ease.

Chapter 4 carries on the theme of developing triple-phase boundary interfaces, with a more conveniently prepared porous carbon material which is a composite of glassy carbon microspheres held together by polystyrene. The composite is deposited as a droplet shaped electrode on the end of a commercially available cylindrical pencil lead. Compared to carbon nanofibers, this composite material can be rapidly prepared through unsophisticated methods of mixing and drop-casting. Polystyrene functions as an inert ambient binder which provides mechanical support for the composite. Though sufficiently durable for electrochemical measurements, the mechanical properties are inferior to that of carbon nanofibers which makes it unviable for use as a free standing membrane. But as the materials and method of preparation is both cheap and easy, the composite is proposed as a readily made disposable electrode for oil analysis reminiscent of the well-known carbon paste electrode. Within the composite material, the carbon microspheres are shown to be coated with a thin layer of polystyrene that binds each microsphere to its neighbours. The carbon microspheres are shown to function effectively as an electrochemical interface despite being coated with an inert material, as demonstrated through the analysis of methyl laurate oil with redox active (and electro-catalytic) quinizarin dye dissolved inside of it. The two materials combined forms a porous electrode material shown to effectively mediate triple-phase boundary oil analysis, as supported by ex-situ fluorescence spectra of the sample before and after faradaic conversion.

Chapter 5 explores a composite of carbon microspheres with a polymer of instrinsic microporosity deposited as a film on the electrode surface. Here the polymer has a more complex function; it acts as an ambient binder, whilst its intrinsic porosity allows it to host electro-catalytic guest molecules. The carbon microspheres acts as a conducting support, and forms a macro-porous structure which provides the composite film good access to electrolyte and ions. In contrast to the previous two result chapters, the composite film is utilized to heterogenise molecular electro-catalyst as opposed to liquid based electro-active substrates. A nitroxyl based free radical electro-catalyst is hosted by the polymer of intrinsic microporosity, a comparison of the redox currents of the electro-catalyst with and without the carbon microspheres embedded in the film demonstrates the significance of the role played by carbon microspheres. Once the modified electrode is optimized for stability and activity, electro-

catalysis of various substrates with a primary alcohol group is investigated. The polymer of intrinsic microporosity is shown to exhibit host selectivity effects for substrates based on its hydrophobicity. Density functional theory and diffusion models based on the works of Albery and Hillman are utilised to justify the conclusions.

The full diagnosis following the Albery and Hillman model requires the hydrodynamic voltammetry to be utilised, however this could not be completed for the materials utilised in Chapters 3, 4 and 5 due to the degradation of the electrode material resulting from the shear force from rotating the electrode in the electrolyte solution. While forming integrated chemical systems as modifying layers on the electrode by combining materials without use of covalent bonding chemistry is convenient and economical, this came at the cost of low material durability and stability. In future, more robust materials are needed to effectively facilitate triple-phase boundary electrochemistry and heterogeneous electro-catalytic reactions. Alternatively, materials that are able to establish dynamic triple phase boundaries (as opposed to stationary) such as carbon particles freely suspended between two immiscible liquids (previously reported by McDonald et. al.) can be expanded to include newer nano-carbon materials such as graphene and carbon nanotubes. Such systems would benefit from an enhanced triple phase boundary while also being compatible with conventional methods of increasing mass transport such as rotating/rocking disc electrode and sono-chemistry.

Chapter 6 and 7 cover the development and application of a novel hydrodynamic method called the 'rocking' disc electrode which has a similar function to the popular rotating disc electrode. Unlike the rotating disc, the rocking disc undergoes a semi-rotation back and forth at an amplitude of 45 degrees at a specified frequency. It is argued that the rocking motion has the advantage of technical simplicity which negates the need for a brush or a mercury based contact. The rocking motion is also effective at dislodging gas bubbles from its surface which can be beneficial for electro-plating applications. The rocking disc electrode can be utilised to diagnose rate limiting processes in electro-catalysis within modifying film materials. In chapter 7, its application in the investigation of a complex homogenous electro-catalytic mechanism involving a nitroxyl based free radical is demonstrated. The catalytic cycle can be approximately modelled as an EC' mechanism though the fit between the model and the experimental data deviates to varying degrees depending on the substrate. The rocking disc electrode technique is a versatile diagnostic tool for investigating modified electrode processes and electro-catalysis.

The quantitative 'Levich style' model for the mass transport limited current at the rocking disc electrode presented in chapter 6 is written in a general form where the angle of rocking is introduced as another variable in the equation. In future, it is of fundamental interest to vary the angle of rocking to examine whether the hypothesized relations hold over a broader range of rocking angles. The presented equation in its current form is consistent with the Levich equation for the rotating disc electrode when normalised by the angle of rotation. This suggests that the proposed model may be valid for rocking angles greater than 45 degrees. However, it is unclear whether the relations will hold for rocking angles lower than 45 degrees. Oscillations over small rocking angles are reminiscent of vibrating wire electrodes. A systematic study of the mass transport limited current induced by rocking at a range of angles lower and also greater than the 45 degrees is not only of fundamental interest, but may also offer practical benefits of more efficient hydrodynamic agitation based on turbulent fluid flow.

The series of studies presented in the thesis offers strategies to improve the atom economy and sustainability of electrochemical processes through utilising economic materials and simple methodologies. Whilst the final outcome and devices presented are not fully optimised, they demonstrate a proof-of-principle of the main advantages of employing the modified electrodes. In future, better materials are needed to address the weaknesses of the composites investigated in the thesis to extract the full benefits offered by the electrochemical approach of chemical synthesis and analysis.